
Applied Superconductivity:

Josephson Effect and Superconducting Electronics

Manuscript to the Lecture during WS 2003/04

Prof. Dr. Rudolf Gross
and
Dr. Achim Marx

Walther-Meissner-Institut
Bayerische Akademie der Wissenschaften
and
Lehrstuhl für Technische Physik (E23)
Technische Universität München

Walther-Meissner-Strasse 8
D-85748 Garching
Rudolf.Gross@wmi.badw.de

Contents

Preface	ix
I The Josephson Effect	1
1 Foundations of the Josephson Effect	3
1.1 The Macroscopic Quantum Model	3
1.1.1 Coherent Phenomena in Superconductivity	3
1.1.2 Macroscopic Quantum Currents in Superconductors	13
1.1.3 The London Equations	19
1.2 Flux Quantization	22
1.2.1 Flux and Fluxoid Quantization	25
1.2.2 Experimental Proof of Flux Quantization	26
1.3 The Josephson Effect	29
1.3.1 The Josephson Equations	30
1.3.2 Josephson Tunneling	35
2 JJs: The Zero Voltage State	39
2.1 Basic Properties of Lumped Josephson Junctions	40
2.1.1 The Lumped Josephson Junction	40
2.1.2 The Josephson Coupling Energy	41
2.1.3 The Superconducting State	43
2.1.4 The Josephson Inductance	45
2.1.5 Mechanical Analogs	46
2.2 Short Josephson Junctions	47
2.2.1 Short Josephson Junction in an Applied Magnetic Field	47
2.2.2 The Fraunhofer Diffraction Pattern	51
2.2.3 Determination of the Maximum Josephson Current Density	55

2.2.4	Direct Imaging of the Supercurrent Distribution	60
2.2.5	Small Josephson Junction: Energy Considerations	60
2.2.6	The Motion of Josephson Vortices	63
2.3	Long Josephson Junctions	66
2.3.1	The Stationary Sine-Gordon Equation	66
2.3.2	The Josephson Vortex	68
2.3.3	Junction Types and Boundary Conditions	72
2.3.4	Josephson Current Density Distribution and Maximum Josephson Current	79
2.3.5	The Pendulum Analog	84
3	JJs: The Voltage State	87
3.1	The Basic Equation of the Lumped Josephson Junction	88
3.1.1	The Normal Current: Junction Resistance	88
3.1.2	The Displacement Current: Junction Capacitance	90
3.1.3	The Fluctuation Current	92
3.1.4	The Basic Junction Equation	93
3.2	The Resistively and Capacitively Shunted Junction Model	95
3.2.1	Underdamped and Overdamped Josephson Junctions	97
3.2.2	Response to dc Driving Sources	99
3.2.3	Response to ac Driving Sources	105
3.2.4	Effect of Thermal Fluctuations	110
3.3	Secondary Quantum Macroscopic Effects	118
3.3.1	Quantum Consequences of the Small Junction Capacitance	118
3.3.2	Macroscopic Quantum Tunneling	122
3.4	Voltage State of Extended Josephson Junctions	127
3.4.1	Negligible Screening Effects	127
3.4.2	The Time Dependent Sine-Gordon Equation	127
3.4.3	Solutions of the Time Dependent Sine-Gordon Equation	129
II	Applications of the Josephson Effect	133
4	SQUIDs	135
4.1	SQUIDs	137
4.2	The DC SQUID	138

4.2.1	The Zero Voltage State	138
4.2.2	The Voltage State	144
4.2.3	Operation and Performance of dc-SQUIDs	147
4.2.4	Practical dc-SQUIDs	151
4.3	Applications of SQUIDs	156
4.3.1	Magnetometers and Gradiometers	156
5	Digital Electronics	159
5.1	Superconductivity and Digital Electronics	160
5.1.1	Historical development	160
5.1.2	Advantages and Disadvantages of Josephson Switching Devices	161
5.2	Josephson Switching Gates	163
5.2.1	General requirements for Josephson switching devices	163
5.2.2	2-terminal and 3-terminal Devices	163
5.2.3	Operation Principle and Switching Times	163
5.2.4	Relevant Time Scales	164
5.2.5	Power dissipation	166
5.3	Josephson Logic Gates	167
5.3.1	Magnetically coupled gates	167
5.3.2	Directly Coupled Gates	168
5.3.3	Switching Delay of Logic Gates	170
5.3.4	Memory cells	171
5.3.5	Microprocessors	171
5.3.6	Problems of Josephson Logic Gates	173
5.4	RSFQ Logic	174
5.4.1	RSFQ Buffer/Amplifier Stage	175
5.5	Recent Developments	176
5.5.1	RSFQ Logic	176
5.5.2	Latching Josephson Logic	178
6	The Josephson Voltage Standard	181
7	Microwave Sources and Detectors	183

8 Superconducting Quantum Bits	185
8.1 Quantum Bits and Quantum Computers	187
8.1.1 Quantum Bits	187
8.1.2 Quantum Computing	188
8.1.3 Quantum Error Correction	192
8.1.4 What are the Problems?	194
8.2 Implementation of Quantum Bits	195
8.3 Why Superconducting Qubits	198
8.3.1 Superconducting Island with Leads	198
III Appendix	201
IV Anhang	203
A The Josephson Equations	205
B Imaging of the Maximum Josephson Current Density	209
C Numerical Iteration Method for the Calculation of the Josephson Current Distribution .	211
D Qubits	213
D.1 What is a quantum bit ?	213
D.2 Entanglement	216
D.3 Qubit Operations	218
D.4 Quantum Logic Gates	220
D.5 The No-Cloning Theorem	228
D.6 Quantum Complexity	228
D.7 The Density Matrix Representation	229
E Two-Level Systems	231
E.1 Introduction to the Problem	231
E.2 Static Properties of Two-Level Systems	232
E.3 Dynamic Properties of Two-Level Systems	236
F The Spin 1/2 System	239
F.1 Experimental Demonstration of Angular Momentum Quantization	239
F.2 Theoretical Description	240
F.3 Evolution of a Spin 1/2 Particle in a Homogeneous Magnetic Field	242
F.4 Spin 1/2 Particle in a Rotating Magnetic Field	244

G	Literature	249
H	SI-Einheiten	251
H.1	Geschichte des SI Systems	251
H.2	Die SI Basiseinheiten	253
H.3	Einige von den SI Einheiten abgeleitete Einheiten	254
H.4	Vorsätze	256
H.5	Abgeleitete Einheiten und Umrechnungsfaktoren	257
I	Physikalische Konstanten	261

Preface

The present manuscripts is addressed to students in the 7. and 8. semester of the Technical University of Munich being interested in the course on *Superconductivity and Low Temperature Physics*. The material of the lecture on *Applied Superconductivity: Josephson Effect and Superconducting Electronics* completes that of the lecture on *Foundations of Superconductivity*, which focuses on the fundamental aspects of the phenomenon superconductivity.

The present manuscript is focused on weak superconductivity, in particular the foundations of Josephson effects and their applications in superconducting devices and circuits. After a brief introduction into macroscopic quantum systems it discusses the static and dynamic properties of small and large Josephson junctions. This provides the basis for the understanding of superconducting devices such as Superconducting Quantum Interference Devices (SQUIDs), microwave mixers and oscillators as well as of simple circuits in analog and digital electronics. The manuscript also briefly addresses the fabrication of Josephson junctions based on metallic superconductors and the novel high temperature superconductors. Finally, some actual topics such as superconducting quantum bits are discussed.

The manuscript is considered as a supplement to the lecture. It contains additional material to the topics discussed during the lecture. This material is provided to those students being interested to obtain a deeper insight into the field of applied superconductivity.

The manuscript will be completed parallel to the lecture during the winter semester 2003/04. Therefore, it definitely contains in its first version a lot of typos and mistakes. The author is grateful for hints concerning mistakes or conceptual errors (e-mail: Rudolf.Gross@wmi.badw.de).

Garching, October 2003

Rudolf Gross

Part I

The Josephson Effect

Chapter 1

Foundations of the Josephson Effect

1.1 The Macroscopic Quantum Model

One of the main principles of quantum mechanics is the fact that physical quantities such as energy or momentum are, under certain conditions, quantized. That is, they can have only discrete values. However, for a long time it was believed that quantization is relevant only for microscopic objects such as nuclei, atoms or molecules. Indeed, if we are considering the behavior of macroscopic objects consisting of a large number of atoms, quantization effects cannot be observed, although every single atom obeys the laws of quantum mechanics. This is due to the fact that thermal motion masks quantum regularities. However, for a number of phenomena, in particular superconductivity, it has been found that it is possible to observe macroscopic quantization. That is, we can observe quantization of parameters that characterize macroscopic objects (for example the flux through a superconducting ring of macroscopic dimension) many orders of magnitude larger than microscopic objects like atoms. As will be discussed in the following, this is caused by the fact that the electron system in a superconductor is highly correlated due to coherence effects. Then we have to consider all superconducting electrons as a single quantum mechanical entity.

1.1.1 Coherent Phenomena in Superconductivity

Although superconductivity has been discovered already in 1911,¹ it took many decades until a modern concept for the superconducting state has been developed. The main milestones along the way towards a deeper understanding of superconductivity have been the discovery of the **Meißner effect**² by **W. Meißner** and **R. Ochsenfeld** in 1933, the development of the phenomenological theories by **Fritz** and **Heinz London**³ and **V.L. Ginzburg** and **L.D. Landau**⁴ and finally the creation of the microscopic BCS theory by **J. Bardeen**, **L.N. Cooper** and **J.R. Schrieffer**⁵ with later important contributions by **Bogolyubov** and **L.P. Gor'kov**⁶ as well as by **A.A. Abrikosov**⁷.

Although a great deal of our knowledge on superconductivity can be obtained from classical models (e.g. electrodynamics of superconductors), the classical models have just been formulated to agree with

¹H. Kammerlingh Onnes, Leiden Commun. **122b**, 124 (1911).

²Walther Meißner, R. Ochsenfeld, Naturwissenschaften **21**, 787 (1933).

³F. London, H. London, Proc. Roy. Soc. Lond. **A 149**, 71 (1935); see also F. London, *Superfluids*, Wiley, New York (1950).

⁴V.L. Ginzburg, L.D. Landau, Zh. Eksp. Teor. Fiz. **20**, 1064 (1950).

⁵Phys. Rev. **108**, 1175 (1957).

⁶see e.g. A.A. Abrikosov, L.P. Gor'kov, I.E. Dzyaloshinskii in *Quantum Field Theoretical Models in Statistical Physics*, Pergamon Press, London (1965).

⁷A.A. Abrikosov, Zh. Eksp. Teor. Fiz. **32**, 1141 (1957)

Walther Meißner (1882 -1974):

Walther Meißner was born on December 16, 1882 in Berlin.

He studied mechanical engineering at the Technische Hochschule Berlin Charlottenburg from 1901 - 1904 as well as mathematics and physics at the University of Berlin from 1904 - 1906. In 1907 he finished his Ph.D. in the group of Max Planck. Then he joined the National Bureau of Standards at Berlin. From 1922 - 1925 he set up a helium liquifier which was the third one worldwide. In 1933 he discovered the perfect diamagnetism in superconductors together with Ochsenfeld. Today, this effect therefore is denoted as Meißner-Ochsenfeld effect.

In 1934 he was offered a full professor position at the Technische Hochschule München. After the second world war Walther Meißner was the first president of the Bavarian Academy of Sciences and founded in 1946 the Commission for Low Temperature Research. The laboratories of this commission first were at Herrsching close to Munich. In 1965, the new Central Institute for Low Temperature Research was build on the research campus at Garching. On the occasion of Walther-Meißner's 100. birthday this institute is renamed Walther-Meißner-Institute in 1982.

Walther Meißner died on November 15, 1974 in Munich.



the fundamental observations, namely perfect conductance, the Meißner effect and the thermodynamic nature of the superconducting transition. That is, the classical models do not show us how these phenomena are related to each other. Historically, the theoretical predictions and experimental observation of coherent phenomena in superconductors such as flux quantization⁸ have been proven to be the key for the final formulation of the macroscopic quantum concept of superconductivity. It was already realized in 1935 by **Fritz London** that the phenomenon of superconductivity cannot be understood in terms of classical concepts. By 1948 he was able to derive the **London equations** from more fundamental ideas, if the superelectron fluid was treated as a quantum mechanical entity. London made this development, since he realized that

superconductivity is an inherently quantum phenomenon manifesting itself on a macroscopic scale.

We know that although quantum mechanics has replaced Newtonian mechanics as the appropriate physical theory, the classical laws are very good approximations on length scales much larger than the atomic dimensions. Therefore, it is not evident on first sight why quantum mechanics is required to describe the properties of a macroscopic superconductors. However, superconductivity is like the coherent light emitted by a laser. There is no way to describe the phenomenon by the laws of classical physics alone. The reason for that is that superconductivity is a **macroscopic quantum phenomenon** and this is precisely the reason why we can observe the unusual quantum phenomena on a macroscopic scale.

The macroscopic quantum model of superconductivity is based on the hypothesis that there is a macroscopic wave function $\psi(\mathbf{r}, t)$, which describes the behavior of the hole ensemble of superconducting electrons. The development and understanding of a macroscopic quantum model of superconductivity requires the sound knowledge of quantum mechanics. Therefore, in the following we briefly review the most fundamental concepts of quantum mechanics that have direct relevance to superconductivity.

Schrödinger's Equation

In 1900 **Max Planck** introduced the concept of quantization to explain the radiation emitted by a black body at a given temperature. In order to explain the experimental observations he had to abandon the

⁸R. Doll, M. Nähbauer, Phys. Rev. Lett. **7**, 51 (1961);
B.S. Deaver, W.M. Fairbank, Phys. Rev. Lett. **7**, 43 (1961).

classical concept that radiation can be emitted in arbitrarily small quanta. Instead he has to postulate that the electromagnetic field can exchange energy only in certain discrete amounts. Planck did not feel comfortable with this postulation and considered it as a mathematical trick. However, **Albert Einstein** considered Plank's departure from classical physics as something far more fundamental. In 1905 he postulated that electromagnetic radiation has to be considered as a collection of particles known as **photons**. A single photon of a known frequency ω represents the smallest amount of energy namely

$$E = \hbar\omega \quad \text{with} \quad (1.1.1)$$

$$\hbar = 1.054\,571\,596(82) \times 10^{-34} \text{ J s} \quad (\text{Planck's constant}) \quad (1.1.2)$$

that can be radiated from a black body. That is, Planck has not merely postulated a mathematical trick but discovered a very fundamental characteristic of nature.

Later on, **Louis de Broglie** realized in 1924 that, just by reasons of symmetry, it should be possible to describe classical particles as waves, in the same way as classical waves can be described as particles. In his doctoral thesis he introduced the concept of **matter waves**, which was completely outside normal experience at that time. Today, there is overwhelming experimental evidence for the **wave-particle duality** and we are used to this concept. The **de Broglie relations** linking the particle quantities energy E and momentum \mathbf{p} to the wave quantities frequency ω and wave vector \mathbf{k} , resp. wavelength λ , are given by

$$E = \hbar\omega \quad (1.1.3)$$

$$\mathbf{p} = \hbar\mathbf{k} = \frac{\hbar}{\lambda}\hat{\mathbf{k}} \quad (1.1.4)$$

with $h = 2\pi \cdot \hbar = 6.6262 \times 10^{-34} \text{ Js}$ and $\hat{\mathbf{k}} = \mathbf{k}/|\mathbf{k}|$. In both equations the constant of proportionality is related to the Planck's constant. It is due to the small value of Planck's constant that we usually do not notice quantum effects in our macroscopic world.

Based on these ideas we have to find an equation of motion for a quantum system playing the role of Newton's equation of motion for a classical system. Based on the existence of matter waves, **Erwin Schrödinger** initiated in 1926 the development of the wave mechanics by using the analogy to wave optics. According to Schrödinger a quantum particle can be described by the complex wave function $\Psi(\mathbf{r}, t)$, where in analogy to wave optics the relations

$$\Psi(\mathbf{r}, t) = A \exp[i(\mathbf{k} \cdot \mathbf{r} - \omega t)] = A \exp\left[\frac{i}{\hbar}(\mathbf{p} \cdot \mathbf{r} - Et)\right] \quad (1.1.5)$$

are valid.

We first consider the case of a free particle without any spin effects for which the potential energy $E_{\text{pot}} = 0$ and hence $E = E_{\text{kin}}$. According to the analogy to wave optics it is natural to start with the wave equation

$$\nabla^2\Psi - \frac{1}{v_{\text{ph}}^2} \frac{\partial^2\Psi}{\partial t^2} = 0 \quad (1.1.6)$$

for waves with the phase velocity v_{ph} . For stationary problems, for which \mathbf{p} and E do not vary with time, the wave function can be separated into two parts depending on space and time. Thus we can write

$$\Psi(\mathbf{r}, t) = \Psi(\mathbf{r}, 0) \exp(-i\omega t) . \quad (1.1.7)$$

Using this Ansatz in the above wave equation and by using

$$k^2 = \frac{\omega^2}{v_{\text{ph}}^2} = \frac{p^2}{\hbar^2} = \frac{2mE_{\text{kin}}}{\hbar^2} = \frac{2m\omega}{\hbar} \quad (1.1.8)$$

we obtain the expression

$$\nabla^2 \Psi = -k^2 \Psi = -\frac{2mE_{\text{kin}}}{\hbar^2} \Psi . \quad (1.1.9)$$

In the more general case the particle can move in the potential V . If the potential is conservative, we can attribute each position a potential energy E_{pot} with the total energy $E = E_{\text{kin}} + E_{\text{pot}}$ being constant. With $E_{\text{kin}} = E - E_{\text{pot}}$ we obtain from (1.1.9) the **stationary Schrödinger equation**

$$\left(-\frac{\hbar^2}{2m} \nabla^2 + E_{\text{pot}} \right) \Psi(\mathbf{r}) = E \Psi(\mathbf{r}) . \quad (1.1.10)$$

By using the time derivative of (1.1.7) we obtain

$$i\hbar \frac{\partial}{\partial t} \Psi(\mathbf{r}, t) = E_{\text{kin}} \Psi(\mathbf{r}, t) . \quad (1.1.11)$$

Then, with (1.1.9) we obtain the time dependent equation

$$i\hbar \frac{\partial}{\partial t} \Psi(\mathbf{r}, t) = -\frac{\hbar^2}{2m} \nabla^2 \Psi(\mathbf{r}, t) . \quad (1.1.12)$$

For non-stationary problems (i.e. $E_{\text{kin}} = E_{\text{kin}}(t)$ and $p = p(t)$) we can no longer express $\partial^2 \Psi / \partial t^2$ by $-\omega^2 \Psi$ and hence derive the wave equation for matter waves. Schrödinger postulated that even in the case of a time dependent potential energy the equation

$$i\hbar \frac{\partial}{\partial t} \Psi(\mathbf{r}, t) = \left(-\frac{\hbar^2}{2m} \nabla^2 + E_{\text{pot}}(\mathbf{r}, t) \right) \Psi(\mathbf{r}, t) \quad (1.1.13)$$

is valid. This general **time dependent Schrödinger equation** was noted by Schrödinger for the first time in 1926. Up to now this equation has been confirmed in a huge number of experiments and represents the basic equation of quantum mechanics. Often the Schrödinger equation is written as $i\hbar \frac{\partial}{\partial t} = \hat{H} \Psi$ with $\hat{H} \equiv -\frac{\hbar^2}{2m} \nabla^2 + E_{\text{pot}}(\mathbf{r}, t)$ being the **Hamilton operator**.

Erwin Schrödinger (1887 -1961), Nobel Price in Physics 1933:

Erwin Schrödinger was born on August 12, 1887, in Vienna. He was a highly gifted man with a broad education. After having finished his chemistry studies, he devoted himself for years to Italian painting. After this he took up botany, which resulted in a series of papers on plant phylogeny. Schrödinger's wide interests dated from his school years at the Gymnasium, where he not only had a liking for the scientific disciplines, but also appreciated the severe logic of ancient grammar and the beauty of German poetry. (What he abhorred was memorizing of data and learning from books.)

From 1906 to 1910 he was a student at the University of Vienna, during which time he came under the strong influence of Fritz Hasenöhrl, who was Boltzmann's successor. It was in these years that Schrödinger acquired a mastery of eigenvalue problems in the physics of continuous media, thus laying the foundation for his future great work. Hereafter, as assistant to Franz Exner, he, together with his friend K. W. F. Kohlrausch, conducted practical work for students (without himself, as he said, learning what experimenting was). During the First World War he served as an artillery officer.

In 1920 he took up an academic position as assistant to Max Wien, followed by positions at Stuttgart (extraordinary professor), Breslau (ordinary professor), and at the University of Zurich (replacing von Laue) where he settled for six years. In later years Schrödinger looked back to his Zurich period with great pleasure - it was here that he enjoyed so much the contact and friendship of many of his colleagues, among whom were Hermann Weyl and Peter Debye. It was also his most fruitful period, being actively engaged in a variety of subjects of theoretical physics. His papers at that time dealt with specific heats of solids, with problems of thermodynamics (he was greatly interested in Boltzmann's probability theory) and of atomic spectra; in addition, he indulged in physiological studies of colour (as a result of his contacts with Kohlrausch and Exner, and of Helmholtz's lectures). His great discovery, Schrödinger's wave equation, was made at the end of this epoch-during the first half of 1926.

It came as a result of his dissatisfaction with the quantum condition in Bohr's orbit theory and his belief that atomic spectra should really be determined by some kind of eigenvalue problem. For this work he shared with Dirac the Nobel Prize for 1933.

In 1927 Schrödinger moved to Berlin as Planck's successor. Germany's capital was then a centre of great scientific activity and he enthusiastically took part in the weekly colloquies among colleagues, many of whom "exceeding him in age and reputation". With Hitler's coming to power (1933), however, Schrödinger decided he could not continue in Germany. He came to England and for a while held a fellowship at Oxford. In 1934 he was invited to lecture at Princeton University and was offered a permanent position there, but did not accept. In 1936 he was offered a position at University of Graz, which he accepted only after much deliberation and because his longing for his native country outweighed his caution. With the annexation of Austria in 1938, he was immediately in difficulty because his leaving Germany in 1933 was taken to be an unfriendly act. Soon afterwards he managed to escape to Italy, from where he proceeded to Oxford and then to University of Ghent. After a short stay he moved to the newly created Institute for Advanced Studies in Dublin, where he became Director of the School for Theoretical Physics. He remained in Dublin until his retirement in 1955.

All this time Schrödinger continued his research and published many papers on a variety of topics, including the problem of unifying gravitation and electromagnetism, which also absorbed Einstein and which is still unsolved; (he was also the author of the well-known little book "What is Life?", 1944). He remained greatly interested in the foundations of atomic physics. Schrödinger disliked the generally accepted dual description in terms of waves and particles, with a statistical interpretation for the waves, and tried to set up a theory in terms of waves only. This led him into controversy with other leading physicists.

After his retirement he returned to an honored position in Vienna. He died on the 4th of January, 1961, after a long illness.



Probability Currents

In the last section we have seen that the Schrödinger equation governs the evolution of the wave function Ψ in space and time. The wave function Ψ is somehow descriptive of the quantum system but its interpretation is not obvious. On the first sight we might consider it as a quantum field similar to the fields encountered in electromagnetism. However, this is not the case. It is evident that Ψ cannot be a real scalar function as a result of the factor i in the Schrödinger equation. Therefore, if Ψ is a scalar function,

it must have both real *and* imaginary parts. For a plane wave this implies

$$\Psi(\mathbf{r}, t) = \Psi_0 e^{i(\mathbf{k} \cdot \mathbf{r} - \omega t)} . \quad (1.1.14)$$

In contrast, electromagnetic fields always can be represented as the real *or* imaginary part of a complex expression:

$$\mathbf{E}(\mathbf{r}, t) = \operatorname{Re} \left\{ \mathbf{E}_0 e^{i(\mathbf{k} \cdot \mathbf{r} - \omega t)} \right\} . \quad (1.1.15)$$

The fact that the quantum wavefunction is necessarily a complex quantity does not generate any problems with mathematics. However, recalling that Ψ_0 is just the amplitude of a plane wave we see from Schrödinger's equation that the absolute phase of this quantity cannot be arbitrarily. This is quite astonishing. Usually we do not discuss the absolute phase, since it does not change the physics of the problem. Schrödinger's equation in contrast seems to suggest that the absolute phase is not arbitrary but rather a measurable quantity with physical significance. To remove this problem, **Max Born** was proposing that the absolute square of the wavefunction corresponds to the probability $\rho(\mathbf{r}, t)$ of a quantum object to be at the location \mathbf{r} at time t . That is, we can write

$$\rho(\mathbf{r}, t) = |\Psi(\mathbf{r}, t)|^2 = \Psi^*(\mathbf{r}, t)\Psi(\mathbf{r}, t) \quad (1.1.16)$$

$$\int \Psi^*(\mathbf{r}, t)\Psi(\mathbf{r}, t) dV = 1 . \quad (1.1.17)$$

Here, (1.1.17) represents a normalization condition, since the probability to find the particle somewhere in space must be unity at all times.

We now will discuss how $\rho(\mathbf{r}, t)$ evolves in space and time. In order to do so we perform the following steps:

- We first multiply the Schrödinger equation from the left side by $\Psi^*(\mathbf{r}, t)$.
- We next multiply the complex conjugate of the Schrödinger equation from the left side by $\Psi(\mathbf{r}, t)$.
- We then subtract the subtract both equations from each other.

In this way we obtain

$$\frac{\partial}{\partial t}(\Psi^*\Psi) + \frac{\hbar}{2mi}(\Psi^*\Delta\Psi - \Psi\Delta\Psi^*) = 0 . \quad (1.1.18)$$

Because any scalar function f and vector field \mathbf{F} obeys the vector identity

$$\nabla \cdot (f\mathbf{F}) = f\nabla \cdot \mathbf{F} + \mathbf{F} \cdot \nabla f$$

and $\Delta \equiv \nabla \cdot \nabla$ we can rewrite (1.1.18) to

$$\frac{\partial}{\partial t}(\Psi^*\Psi) + \nabla \cdot \left[\frac{\hbar}{2mi}(\Psi^*\nabla\Psi - \Psi\nabla\Psi^*) \right] = 0 . \quad (1.1.19)$$

This equation has the form of a continuity equation for the probability

$$\frac{\partial \rho}{\partial t} + \nabla \cdot \mathbf{J}_\rho = 0 , \quad (1.1.20)$$

where the ***probability current*** \mathbf{J}_ρ is defined as

$$\mathbf{J}_\rho \equiv \frac{\hbar}{2im}(\Psi^*\nabla\Psi - \Psi\nabla\Psi^*) = \text{Re} \left\{ \Psi^* \frac{\hbar}{im} \nabla \Psi \right\} . \quad (1.1.21)$$

Equation 1.1.20 is the desired expression describing the evolution of the probability in space and time. It gives the local constraint on ρ , whereas (1.1.17) gives the global constraint on ρ . Eq.(1.1.21) says that the probability of a quantum objects at a certain point cannot change instantaneously but rather has to change in a continuous fashion by the flow of a probability current. Then, expression (1.1.20) can be viewed as a stating the ***conservation of probability***.

It is obvious that (1.1.20) resembles the familiar expression for the conservation of charge. However, this similarity is only mathematical. Whereas the electrical current is a real, physical measurable quantity the probability current is only a theoretical construct. It is not possible to measure \mathbf{J}_ρ for a single particle.

The probability current (1.1.21) describes the probabilistic flow of a quantum object which is subjected to forces varying in space and time. However, it still does not describe the situation we are interested in namely the motion of a charged particle in an electromagnetic field. This is caused by the fact that a charged particle moving in an electromagnetic field is subjected to forces depending on the motion of the particle itself. To find \mathbf{J}_ρ for this situation we first have to find the appropriate form of the Schrödinger equation. In order to do so we start with the general classical equation of motion

$$\frac{d}{dt} \mathbf{p} = -\nabla V . \quad (1.1.22)$$

Here, \mathbf{p} is the canonical momentum and V the externally applied potential, which are used in writing the total energy of the system. We will see that this formalisms is useful for the considered case, since the electromagnetic field represents a nonconservative potential making the formulation of energy relationships difficult.

We begin with the classical equation of motion for a particle of charge q and in an electromagnetic field given by the **Lorentz's law**

$$m \frac{d\mathbf{v}}{dt} = q[\mathbf{E} + (\mathbf{v} \times \mathbf{B})] . \quad (1.1.23)$$

In order to obtain the Schrödinger equation for this problem we first rewrite (1.1.23) into the form suggested by (1.1.22). The first step is to express the field quantities \mathbf{E} and \mathbf{H} in terms of potentials. According to **Gauss's law** the flux density \mathbf{B} always can be written as

$$\mathbf{B} = \nabla \times \mathbf{A} , \quad (1.1.24)$$

where \mathbf{A} is a **vector potential**. \mathbf{A} can be used to write **Faraday's law** $\nabla \times \mathbf{E} = -\partial \mathbf{B} / \partial t$ as

$$\nabla \times \left(\mathbf{E} + \frac{\partial \mathbf{A}}{\partial t} \right) = 0 . \quad (1.1.25)$$

Using the fact that the curl of the gradient of any single-valued scalar field ϕ is zero, (1.1.25) is equivalent to the statement

$$\mathbf{E} = -\frac{\partial \mathbf{A}}{\partial t} - \nabla \phi . \quad (1.1.26)$$

Then, Lorentz's law in terms of these potentials can be written as

$$m \frac{d\mathbf{v}}{dt} = -q \left(\nabla \phi + \frac{\partial \mathbf{A}}{\partial t} - \mathbf{v} \times (\nabla \times \mathbf{A}) \right) . \quad (1.1.27)$$

In order to bring this equation into the form of (1.1.22) we have to group all time derivatives together. Using the chain rule of differentiation

$$\frac{d\mathbf{A}}{dt} = \frac{\partial \mathbf{A}}{\partial t} + (\mathbf{v} \cdot \nabla) \mathbf{A} \quad (1.1.28)$$

we obtain

$$\frac{d}{dt} (m\mathbf{v} + q\mathbf{A}) = -q[\nabla\phi - (\mathbf{v} \cdot \nabla)\mathbf{A} - \mathbf{v} \times (\nabla \times \mathbf{A})] . \quad (1.1.29)$$

Now eq.(1.1.29) is close to the desired form and we can suspect that the ***canonical momentum*** is given by

$$\mathbf{p} = m\mathbf{v} + q\mathbf{A} . \quad (1.1.30)$$

To verify this we must be able to express the right hand side of (1.1.29) as the gradient of a scalar function. We therefore rewrite it in terms of the canonical momentum and obtain

$$\frac{d\mathbf{p}}{dt} = -q\nabla\phi + \frac{q}{m}(\mathbf{p} \cdot \nabla)\mathbf{A} - \frac{q^2}{m}(\mathbf{A} \cdot \nabla)\mathbf{A} + \frac{q}{m}\mathbf{p} \times (\nabla \times \mathbf{A}) - \frac{q^2}{m}\mathbf{A} \times (\nabla \times \mathbf{A}) . \quad (1.1.31)$$

Using the vector identities

$$\mathbf{a} \times (\nabla \times \mathbf{b}) = \nabla(\mathbf{a} \cdot \mathbf{b}) - (\mathbf{a} \cdot \nabla)\mathbf{b} - (\mathbf{b} \cdot \nabla)\mathbf{a} - \mathbf{b} \times (\nabla \times \mathbf{a}) \quad (1.1.32)$$

$$\mathbf{a} \times (\nabla \times \mathbf{a}) = \frac{1}{2}\nabla(\mathbf{a} \cdot \mathbf{a}) - (\mathbf{a} \cdot \nabla)\mathbf{a} \quad (1.1.33)$$

we can rewrite (1.1.31) as

$$\frac{d\mathbf{p}}{dt} = -q\nabla\phi + \frac{q}{m}\nabla(\mathbf{p} \cdot \mathbf{A}) - \frac{q^2}{2m}\nabla(\mathbf{A} \cdot \mathbf{A}) - \frac{q}{m}(\mathbf{A} \cdot \nabla)\mathbf{p} - \frac{q}{m}\mathbf{A} \times (\nabla \times \mathbf{p}) . \quad (1.1.34)$$

At this point we have to recall that we are using a set of independently specified variables (\mathbf{r}, \mathbf{p}) to describe the problem. Therefore, the spatial derivative of the canonical momentum is zero and we obtain

$$\frac{d\mathbf{p}}{dt} = -\nabla \left\{ q\phi - \frac{q}{m}(\mathbf{p} \cdot \mathbf{A}) + \frac{q^2}{2m}(\mathbf{A} \cdot \mathbf{A}) \right\} . \quad (1.1.35)$$

That is, we have achieved our initial goal of writing Lorentz's law in the generic form of eq.(1.1.22).

We briefly will discuss the physical meaning of (1.1.35). First, the canonical momentum \mathbf{p} given by (1.1.30) is composed of two parts. The first part, $m\mathbf{v}$, is the usual ***kinetic momentum*** and is associated with the momentum in elementary mechanics. The second part, $q\mathbf{A}$, is denoted as the ***field momentum***, which is a direct result of the charge of the particle. Any change of the velocity of the particle produces

an electromagnetic field that must be considered self-consistently. Therefore, the generalized potential of the problem

$$V = q\phi - \frac{q}{m}(\mathbf{p} \cdot \mathbf{A}) + \frac{q^2}{2m}(\mathbf{A} \cdot \mathbf{A}) \quad (1.1.36)$$

is not only a function of space and time but also of the canonical momentum. In this way the interaction of the externally applied field and the induced current created by the motion of the charged particle is accounted for self-consistently.

The next step in obtaining the Schrödinger equation is to use the expressions for \mathbf{p} and V to write down the total energy:

$$E = E_{\text{kin}} + E_{\text{pot}} = \frac{\mathbf{p} \cdot \mathbf{p}}{2m} + \left\{ q\nabla\phi - \frac{q}{m}(\mathbf{p} \cdot \mathbf{A}) + \frac{q^2}{2m}(\mathbf{A} \cdot \mathbf{A}) \right\} . \quad (1.1.37)$$

This purely classical expression can be rewritten as

$$E = \frac{1}{2m}(\mathbf{p} - q\mathbf{A}) \cdot (\mathbf{p} - q\mathbf{A}) + q\phi . \quad (1.1.38)$$

The last step is to replace energy and momentum by the corresponding quantum mechanical operators

$$E \Rightarrow i\hbar \frac{\partial}{\partial t} \quad \mathbf{p} \Rightarrow -i\hbar \nabla . \quad (1.1.39)$$

Using these expression we expect the quantum form of the Lorentz's law to be

$$i\hbar \frac{\partial \Psi}{\partial t} = \frac{1}{2m} \left(\frac{\hbar}{i} \nabla - q\mathbf{A} \right)^2 \Psi + q\phi \Psi . \quad (1.1.40)$$

We finally can use now eq.(1.1.40) to derive the probability current of a charged particle in an electromagnetic field to

$$\mathbf{J}_\rho = \text{Re} \left\{ \Psi^* \left(\frac{\hbar}{im} \nabla - \frac{q}{m} \mathbf{A} \right) \Psi \right\} . \quad (1.1.41)$$

In deriving this equation we have to take into account that ϕ represents a portion of the applied potential field and therefore is a real quantity. We will see in the following section that Eq.(1.1.41) is the central expression in the quantum mechanical description of superconductivity.

1.1.2 Macroscopic Quantum Currents in Superconductors

After having recalled some basic concepts of quantum mechanics we can apply these concept to superconductors. Before doing so let us first consider the situation in a normal conductor. Of course, the electron in a normal metal move according to the laws of quantum mechanics. In the usual approximation of weakly or non-interacting particles this motion can be described in terms of the ordinary Schrödinger equation

$$i\hbar \frac{\partial \Psi}{\partial t} = \hat{H}\Psi , \quad (1.1.42)$$

where

$$\Psi(\mathbf{r}, t) = \Psi_0(\mathbf{r}, t) e^{i\theta(\mathbf{r}, t)} \quad (1.1.43)$$

is the complex wave function of a particle. According to quantum mechanics $|\Psi|^2$ can be interpreted as the probability density of the particles. In the stationary situation $|\Psi|$ can be assumed constant and \hat{H} can be replaced by the energy E of the particle. As a result we can write

$$\hbar \frac{\partial \theta}{\partial t} = -E . \quad (1.1.44)$$

That is, the quantum specific character is reduced to the that of the wave function phase θ .

The important point is that in normal metals (1.1.44) does not result in quantum correlations for the macroscopic variables because the electrons obey Fermi-Dirac statistics and their energies can never be exactly equal. Therefore, according to (1.1.44) the temporal evolution of the phases of the particle wave functions differs for all particles. That is, the phases are uniformly distributed and since all macroscopic quantities are sums over all the particles the phases drop out in these quantities. We will discuss now that this is not the case for superconductor. In superconductors bound pairs of electron (Cooper pairs) are formed with opposite momenta and spins in the simplest case. These pairs with zero net spin obey the Bose-Einstein statistics and therefore can occupy the lowest energy state at low temperatures. As a result, their rates $\partial\theta/\partial t$ are identical. Furthermore, the Cooper pairs have a relatively large size of the order of 10 to 1000 nm, which is much larger than the typical distance between the pairs. Therefore, the wave functions of the individual pairs are strongly overlapping. As a result of these two factors, all the pairs are forming a **phase-locked** state that can be described by a single wave function Ψ , which is frequently denoted as the order parameter. In this situation the phases do not drop out during summation over all particles and therefore macroscopic variable, in particular current, can depend on the phase θ , which changes in a quantum manner under the action of an electromagnetic field. This quantum dependence leads not only to the zero resistance of superconductors and the Meißner effect but also to specific coherent effects such as the **flux quantization** and the **Josephson effect**.

The qualitative discussion of the previous paragraph shows that the situation for superconductors is somehow similar to the situation in atoms. For the latter, the fact that electrons can orbit the nucleus without

decaying and having the atom to collapse could not be explained classically. Only quantum mechanics provided the necessary framework. In the same way, the infinite conductivity of superconductors cannot be explained classically. If one would try to do so, one has to postulate that the superelectrons do not scatter. Although the results of this assumption are consistent with the experimental fact, it seems to be arbitrary to postulate an infinite scattering time. In the same way as Schrödinger's equation provides the explanation for stable microscopic currents created by orbiting electrons, it was hypothesized by **Fritz London** that the macroscopic currents in superconductors might be explained in a similar way. This was the starting point of the ***macroscopic quantum model*** of superconductivity.

The central hypothesis behind the macroscopic quantum model of superconductivity can be stated as follows:

There exists a macroscopic quantum wave function

$$\psi(\mathbf{r}, t) = \psi_0(\mathbf{r}, t) e^{i\theta(\mathbf{r}, t)} \quad (1.1.45)$$

that describes the behavior of the entire ensemble of superelectrons in a superconductor.

The motivation for this assumption is that superconductivity is a ***coherent phenomenon*** of all superelectrons. This situation is analogous to the quantum description of electromagnetism. According to wave-particle dualism we can envision a photon as a quantum particle. Then, when a large number of photons interact coherently such as in a laser, the entire collection of these quantum particles can be adequately described in terms of an electromagnetic field with amplitude and phase. As we will see, the macroscopic wave function ψ is a fieldlike quantity that similarly describes the whole ensemble of superelectrons.

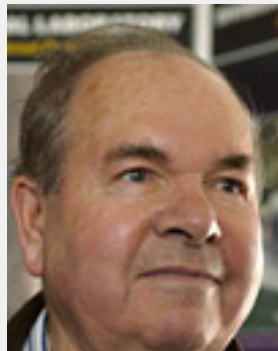
We have now to examine the consequences of postulating a macroscopic wavefunction describing the whole ensemble of superelectrons. We first discuss the meaning of $|\psi|^2$. For a single quantum particle described by the wavefunction Ψ the absolute square $|\Psi(\mathbf{r}, t)|^2$ has been interpreted as the probability to find the particle at the location \mathbf{r} at a given time t . As a result we have the global constraint or normalization condition $\int \Psi^* \Psi dV = 1$ (compare (1.1.17) stating that the particle exists somewhere in space at any time. Along this line it is natural to assume that the wavefunction ψ representing the whole ensemble of superelectrons satisfies the normalization condition

$$\int \psi^*(\mathbf{r}, t) \psi(\mathbf{r}, t) dV = N^* \quad (1.1.46)$$

$$|\psi(\mathbf{r}, t)|^2 = \psi^*(\mathbf{r}, t) \psi(\mathbf{r}, t) = n^*(\mathbf{r}, t) \quad (1.1.47)$$

Here, $n^*(\mathbf{r}, t)$ is the local density and N^* the total number of superconducting electrons. Condition (1.1.46) says that if we are searching the whole space we have to find all superelectrons. Since the superelectrons are discrete objects, there must be of course a sufficiently large density in order to make the definition of a local density sense. This concern is similar to the situation in fluid mechanics. Although we know that all fluids consist of discrete atoms or molecules, it is convenient to describe the system by a local fluid density. Due to the analogy to fluid mechanics the collection of superelectrons is often referred to as a ***charged superfluid***. Therefore, the theoretical description of superconductors (charged superfluid) and uncharged superfluids such as superfluid helium has many similarities. Indeed, the Nobel Price in Physics 2003 was given to **Vitaly L. Ginzburg, Alexei A. Abrikosov and Anthony J. Leggett** for their pioneering contributions to the theory of superconductors and superfluids.

The Nobel Price in Physics 2003 has been given to Alexei A. Abrikosov, Vitaly L. Ginzburg, and Anthony J. Leggett for their pioneering contributions to the theory of superconductors and superfluids.



Alexei A. Abrikosov



Vitaly L. Ginzburg



Anthony J. Leggett

Alexei A. Abrikosov, born 1928 (75 years) in Moscow, the former Soviet Union, American (and Russian) citizen. Doctor's degree in physics in 1951 at the Institute for Physical Problems, Moscow. Distinguished Argonne Scientist, Argonne National Laboratory, Argonne, Illinois, USA.

Vitaly L. Ginzburg, born 1916 (87 years) in Moscow, Russia (Russian citizen). Doctor's degree in physics at the University of Moscow. Former Head of the Theory Group at the P.N. Lebedev Physical Institute, Moscow, Russia.

Anthony J. Leggett, born 1938 (65 years) in London, England (British and American citizen). Doctor's degree in physics in 1964 at the University of Oxford. MacArthur Professor at the University of Illinois at Urbana-Champaign, USA.

Note that the macroscopic quantum model of superconductivity does not explain the microscopic origin of superconductivity, which will not be discussed here. That is, it does not explain the microscopic origin of the attractive interaction of electrons in a solid resulting in the formation of Cooper pairs. This mechanism, which may be different for the classical metallic superconductors, the novel high temperature superconductors or the heavy fermion superconductors is not relevant for the macroscopic quantum phenomena discussed in the following. The only relevant issue is the possibility to describe the superelectron fluid as a quantum mechanical entity irrespective of the detailed pairing mechanism.

The analogy to superfluids is powerful to establish an intuitive picture about the macroscopic quantum model. Instead of a single particle wavefunctions describing the probabilities for single particles we are now considering so many quantum objects that we have a wavefunction describing the actual location of a complete subset of the whole ensemble. Then, in the local constraint on ψ which is analogous to the continuity equation (1.1.20) we do not have a probability flow but rather a flow of particles, which is nothing more than a physical current. Following (1.1.41) we can immediately write down the macroscopic quantum current density \mathbf{J}_s in an electromagnetic field, which is equivalent to the supercurrent density. We only have to multiply the ensemble probability current describing the particle flux by the charge q^* of the superelectron:

$$\mathbf{J}_s = q^* \text{Re} \left\{ \Psi^* \left(\frac{\hbar}{im^*} \nabla - \frac{q^*}{m^*} \mathbf{A} \right) \Psi \right\} . \quad (1.1.48)$$

Here, m^* is the mass of the superelectron. This expression can be brought in a more useful form by making some assumption on ψ . According to our discussion the macroscopic wavefunction $\psi(\mathbf{r}, t)$ obeys the Schrödinger-like equation for the ensemble in an electromagnetic field:

$$i\hbar \frac{\partial \psi(\mathbf{r},t)}{\partial t} = \frac{1}{2m^*} \left(\frac{\hbar}{i} \nabla - q^* \mathbf{A}(\mathbf{r},t) \right)^2 \psi(\mathbf{r},t) + q^* \phi(\mathbf{r},t) \psi(\mathbf{r},t) . \quad (1.1.49)$$

Because of the phase factor i in this expression the macroscopic wavefunction ψ in the same way as the microscopic one is a complex quantity. Therefore, $\psi(\mathbf{r},t)$ is of the form

$$\psi(\mathbf{r},t) = \sqrt{n^*(\mathbf{r},t)} e^{i\theta(\mathbf{r},t)} . \quad (1.1.50)$$

Here, we have used an amplitude satisfying the condition that the absolute square of the wavefunction is equivalent to the density of superelectrons. We also note that θ is a real function representing the phase of the complex number.

Substitution of (1.1.50) into the expression (1.1.48) for the supercurrent we obtain the supercurrent equation

$$\mathbf{J}_s = q^* n^*(\mathbf{r},t) \left\{ \frac{\hbar}{m^*} \nabla \theta(\mathbf{r},t) - \frac{q^*}{m^*} \mathbf{A}(\mathbf{r},t) \right\} . \quad (1.1.51)$$

Since a current density always can be written as $\mathbf{J}_s = q^* n^* \mathbf{v}_s$, the expression in parentheses corresponds to the velocity of the superelectrons:

$$\mathbf{v}_s \equiv \frac{\hbar}{m^*} \nabla \theta(\mathbf{r},t) - \frac{q^*}{m^*} \mathbf{A}(\mathbf{r},t) . \quad (1.1.52)$$

Eq.(1.1.51) states that the supercurrent \mathbf{J}_s only depends on the phase of the macroscopic wavefunction and the vector potential. That is, the physical measurable quantity \mathbf{J}_s is related to two quantities which cannot be determined directly from the experiment. Moreover, because any single-valued scalar field f satisfies the condition $\nabla \times (\nabla f) = 0$, we know that for an arbitrary scalar function χ

$$\mathbf{B} = \nabla \times \mathbf{A} = \nabla \times (\mathbf{A} + \nabla \chi) . \quad (1.1.53)$$

That is, there exists an infinite number of vector potential that will describe the correct magnetic flux density. We hence can conclude that although θ and \mathbf{A} have been introduced only for mathematical convenience, eq.(1.1.51) implies that these quantities are physically measurable. However, this is not the case.

The way out of this dilemma is to recognize the fact that the relation between phase and vector potential is not arbitrary but fixed. In this way we can measure the supercurrent but still are not able to determine θ **and** \mathbf{A} . That is, we demand that expression (1.1.51) is independent of the special choice of \mathbf{A} . The specific choice of \mathbf{A} is usually referred to as the gauge and, hence, we have to make the expression for the

supercurrent ***gauge invariant***. Mathematically this is straightforward. Suppose we define a new vector potential \mathbf{A}' as

$$\mathbf{A}' \equiv \mathbf{A} + \nabla\chi . \quad (1.1.54)$$

Then, according to (1.1.53) this new vector potential correctly gives the magnetic flux density. In addition, the new vector potential also must correctly describe the electric field. Therefore, we define a new scalar potential ϕ' so that the electric field is given by

$$\mathbf{E} = -\frac{\partial \mathbf{A}'}{\partial t} - \nabla\phi' . \quad (1.1.55)$$

Comparing this expression to the original expression $\mathbf{E} = -\frac{\partial \mathbf{A}}{\partial t} - \nabla\phi$ (1.1.26) we see that the two scalar potentials are related by

$$\phi' \equiv \phi - \frac{\partial\chi}{\partial t} . \quad (1.1.56)$$

According to (1.1.54) and (1.1.56) we can separately specify the temporal and spatial dependence of a scalar function χ to generate new sets of the scalar and the vector potentials which still describe the original electric and magnetic fields.

By rewriting (1.1.49) in terms of the new potentials with the new wave function $\psi'(\mathbf{r},t) = \sqrt{n^*(\mathbf{r},t)} e^{i\theta'(\mathbf{r},t)}$ we can easily derive a new expression for the supercurrent density given by

$$\mathbf{J}_s = q^* n^*(\mathbf{r},t) \left\{ \frac{\hbar}{m^*} \nabla\theta'(\mathbf{r},t) - \frac{q^*}{m^*} \mathbf{A}'(\mathbf{r},t) \right\} . \quad (1.1.57)$$

Since the supercurrent, the experimentally measurable quantity, must be the same in (1.1.57) and (1.1.51), we have to satisfy the condition

$$\theta' = \theta + \frac{q^*}{m^*} \chi . \quad (1.1.58)$$

This in turn results in

$$\psi'(\mathbf{r},t) = \psi(\mathbf{r},t) e^{i(q^*/\hbar)\chi} . \quad (1.1.59)$$

That is, the same scalar function χ is changing both the phase and the vector potential. In this way the supercurrent always has the same value and can be measured regardless the specific gauge chosen. The important conclusion that can be drawn is that the expression for the supercurrent is gauge invariant and therefore we do no longer be concerned about this issue.

From the expression (1.1.57) and (1.1.51) for the supercurrent density we obtain the condition

$$\nabla\theta' - \frac{q^*}{\hbar}\mathbf{A}' = \nabla\theta - \frac{q^*}{\hbar}\mathbf{A} . \quad (1.1.60)$$

We therefore can introduce a *gauge invariant phase gradient*

$$\gamma = \nabla\theta - \frac{q^*}{\hbar}\mathbf{A} = \nabla\theta - \frac{2\pi}{\Phi_0}\mathbf{A} , \quad (1.1.61)$$

where

$$\Phi_0 = \frac{\hbar}{q^*} \quad (1.1.62)$$

is the flux quantum. We see that the supercurrent is than given by

$$\mathbf{J}_s = \frac{q^* n^* \hbar}{m^*} \gamma = \frac{\hbar}{q^* \Lambda} \gamma , \quad (1.1.63)$$

where

$$\Lambda \equiv \frac{m^*}{n^* q^{*2}} , \quad (1.1.64)$$

is the *London coefficient*. We see that the supercurrent density is proportional to the gauge invariant phase gradient.⁹

⁹Note that $\nabla\theta - \frac{q^*}{\hbar}\mathbf{A}$ cannot be written as $\nabla\gamma$, that is as the gradient of a gauge invariant phase. In this case we would have $\mathbf{A} \propto \nabla\theta - \nabla\gamma$ and hence $\nabla \times \mathbf{A} = \mathbf{B} = 0$.

1.1.3 The London Equations

The two **London equations** formulated by **Fritz London** to describe the behavior of superconductors based on classical physics can be easily derived from the expression (1.1.51) for the supercurrent density by assuming $n^* = \text{const.}$. Note that (1.1.51) includes the cases where the superelectron density varies in space and time.

By using the London coefficient $\Lambda = \frac{m^*}{n^* q^{*2}}$ we can rewrite (1.1.51) as

$$\Lambda \mathbf{J}_s = - \left\{ \mathbf{A}(\mathbf{r}, t) - \frac{\hbar}{q^*} \nabla \theta(\mathbf{r}, t) \right\} . \quad (1.1.65)$$

By taking the curl of this expression we obtain the **second London equation**

$$\nabla \times (\Lambda \mathbf{J}_s) = -\nabla \times \mathbf{A} = -\mathbf{B} \quad (1.1.66)$$

In order to get the first London equation from (1.1.51) we have to take the partial derivative with respect to time:

$$\frac{\partial}{\partial t} (\Lambda \mathbf{J}_s) = - \left\{ \frac{\partial \mathbf{A}(\mathbf{r}, t)}{\partial t} - \frac{\hbar}{q^*} \nabla \left(\frac{\partial \theta(\mathbf{r}, t)}{\partial t} \right) \right\} . \quad (1.1.67)$$

From the Schrödinger-like equation (1.1.49) we obtain for $n^* = \text{const}$

$$-\hbar \frac{\partial \theta}{\partial t} = \frac{1}{2n^*} \Lambda \mathbf{J}_s^2 + q^* \phi . \quad (1.1.68)$$

This expression is known as the **energy-phase relationship**, since the first term on the right hand side represents the kinetic energy ($\frac{1}{2} m^* v_s^2$) and the second the potential energy. By substituting (1.1.68) into (1.1.67) and using $\mathbf{E} = -\partial \mathbf{A}/\partial t - \nabla \phi$ we obtain the **first London equation**

$$\frac{\partial}{\partial t} (\Lambda \mathbf{J}_s) = \mathbf{E} - \frac{1}{n^* q^*} \nabla \left(\frac{1}{2} \Lambda \mathbf{J}_s^2 \right) . \quad (1.1.69)$$

Usually, the first London equation is given as

$$\frac{\partial}{\partial t} (\Lambda \mathbf{J}_s) = \mathbf{E} , \quad (1.1.70)$$

that is, without the second term on the right hand side of (1.1.69) which contains the kinetic energy of the superelectrons. Since this term does not contain \hbar , it is not of quantum mechanical origin.

In order to discuss the origin of the extra term in (1.1.69) we use the vector identity

$$\mathbf{a} \times (\nabla \times \mathbf{a}) = \frac{1}{2} \nabla(\mathbf{a} \cdot \mathbf{a}) - (\mathbf{a} \cdot \nabla)\mathbf{a} \quad (1.1.71)$$

to write $\frac{1}{2} \Lambda \mathbf{J}_s^2 = \mathbf{J}_s \times (\nabla \times \mathbf{J}_s) + (\mathbf{J}_s \cdot \nabla) \mathbf{J}_s$. Then, by using the second London equation we can rewrite (1.1.69) as

$$\frac{\partial}{\partial t}(\Lambda \mathbf{J}_s) = \mathbf{E} - \frac{1}{n^* q^*} (\mathbf{J}_s \cdot \nabla)(\Lambda \mathbf{J}_s) + \frac{1}{n^* q^*} (\mathbf{J}_s \times \mathbf{B}) . \quad (1.1.72)$$

By using $\frac{d}{dt}(\Lambda \mathbf{J}_s) = \frac{\partial}{\partial t}(\Lambda \mathbf{J}_s) + (\mathbf{v}_s \cdot \nabla)(\Lambda \mathbf{J}_s)$ and $\mathbf{J}_s = n^* q^* \mathbf{v}_s$ we obtain

$$m^* \frac{d\mathbf{v}_s}{dt} = q^* \mathbf{E} + q^* \mathbf{v}_s \times \mathbf{B} , \quad (1.1.73)$$

This expression corresponds to the Lorentz's law. From this we can conclude that

- the nonlinear first London equation results from the Lorentz's law and the second London equation. Therefore, (1.1.69) must be the exact form of the expression describing the phenomenon of zero dc resistance in superconductors.
- The first London equation is derived using the second London equation. This shows that the Meißner effect is the more fundamental property of superconductors than the vanishing dc resistance.¹⁰

Since the nonlinear first London equation represents the correct expression the question arises, whether conclusions derived from the more frequently used linear London equation (1.1.70) are wrong. Fortunately, the answer is no, since in most cases the nonlinear term can be neglected. However, one has to be aware that we cannot always neglect the nonlinear term. In some cases it even plays an important role.

In order to elucidate the relevance of the nonlinear term in the first London equation we can state the following:

1. Situations dealing with superconductors in an applied magnetic field (e.g. slab in a parallel field) we usually can treat without using the first London equation. Electric fields are not important in this case. They are derived using Faraday's law after having calculated the magnetic fields and the corresponding currents. The first London equation only would yield small corrections to the supercurrent density distribution.

¹⁰Since the vanishing dc resistance has been discovered already in 1911, whereas the Meißner effect was found only in 1933, the phenomenon was not denoted as "superdiamagnetism" but as superconductivity.

Fritz London (1900 -1954):

Fritz London was born on March 7, 1900 in Breslau, Germany (now Wroclaw, Poland). He was a German-American physicist who, with Walter Heitler, devised (1927) the first quantum mechanical treatment of the hydrogen molecule. London was educated at the universities of Bonn, Frankfurt, Göttingen, Munich (Ph.D., 1921), and Paris. He was a Rockefeller research fellow at Zürich and Rome and a lecturer at the University of Berlin. From 1933 to 1936 he was a research fellow at the University of Oxford and then went to the University of Paris as master and director of research.

In 1939 he immigrated to the United States to become professor of theoretical chemistry at Duke University, Durham, N.C., and from 1953 he was James B. Duke professor of chemical physics there. He became a U.S. citizen in 1945. His publications include two volumes on Superfluids (1950, 1954).

London's theory of the chemical binding of homopolar molecules marked the beginning of modern quantum mechanical treatment of the hydrogen molecule and is considered one of the most important advances in modern chemistry. With his brother, Heinz London, he developed (1935) the phenomenological theory of superconductivity, providing a new foundation for the understanding of molecular forces and clarifying the connection between pure quantum phenomena and many of the most striking facts of chemistry.

London died on March 30, 1954, at Durham, N.C., USA.



2. It is evident from eq.(1.1.69) that the nonlinear term can always be neglected if

$$|\mathbf{E}| \gg \left| \frac{1}{n^* q^*} \nabla (\Lambda \mathbf{J}_s^2) \right|. \quad (1.1.74)$$

Assuming that the spatial variation of the supercurrent occurs on a length scale ℓ , we have $\nabla \cdot \mathbf{J}_s \sim J_s/\ell$. Then, the condition can be written as

$$|\mathbf{E}| \gg |\mathbf{v}_s| \left| \frac{\Lambda \mathbf{J}_s}{\ell} \right|. \quad (1.1.75)$$

With the same assumption we obtain

$$\left| \frac{\Lambda \mathbf{J}_s}{\ell} \right| \sim |\mathbf{B}| \quad (1.1.76)$$

from the second London equation. As a result, we obtain the condition

$$|\mathbf{E}| \gg |\mathbf{v}_s| |\mathbf{B}| \quad (1.1.77)$$

for neglecting the nonlinear term. This is not surprising, since this condition is equivalent to the usually made assumption that the magnetic contribution to the Lorentz's law can be neglected compared the electric one in deriving the first London equation.

1.2 Flux Quantization

In the previous section we have shown that the macroscopic quantum model of superconductivity is consistent with the phenomenological laws deduced using classical reasoning. We now examine the quantum mechanical consequences of the model. The first example is ***fluxoid quantization*** in multiply connected superconductors (see Fig. 1.1).

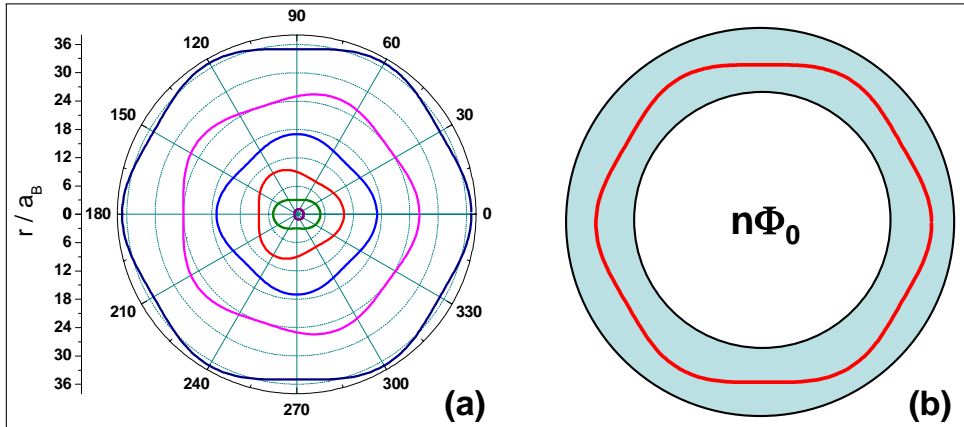


Figure 1.1: Stationary quantum states: (a) The standing electron wave around the nucleus of an atom at $r = 0$ resulting in the Bohr-Sommerfeld quantization of the angular momentum. (b) The standing wave of the macroscopic wavefunction representing the superconducting state in a superconducting cylinder resulting in flux quantization.

We start our discussion with a simple ***Gedanken*** experiment. We take a superconducting ring and generate (just by magnetic induction) a supercurrent in the ring. Since the superconductor has zero dc resistance this supercurrent should be stable, that is, the considered system is in a stationary state. Of course we can change this state by changing the induction process generating the supercurrent. Classically we would expect that in this way we can generate arbitrary supercurrents in the ring. However, after having learnt that we have to consider the superconductor as a macroscopic quantum system, we have to revise the expectation. The quantum mechanical treatment of microscopic systems teaches us that stationary states are determined by certain quantum conditions. Within Bohr's model for atoms the stationary states for the electrons are determined by the quantization condition for the angular momentum. As shown in Fig. 1.1a this is equivalent to the requirement that the electron wave is not interfering destructively. In the same way we expect a stationary state for the supercurrent along the ring only if the macroscopic wave function describing the whole ensemble of superelectrons is not interfering destructively (see Fig. 1.1b). Therefore, we immediately expect a quantization condition. This has been first supposed by **Fritz London**.¹¹ He came to the conclusion that the magnetic flux enclosed by a superconducting ring can only have discrete values given by multiples of a flux quantum Φ_0^L . London suggested the value

$$\Phi_0^L = \frac{h}{e} \simeq 4 \times 10^{-15} \text{ Vs} . \quad (1.2.1)$$

London derived this value for the flux quantum, since he presumed that single electrons are carrying the supercurrent. The fact that Cooper pairs are carrying the supercurrent became clear only after the development of the BCS theory in 1957.¹²

¹¹F. London, *Superfluids*, Wiley, New York (1950).

¹²J. Bardeen, L.N. Cooper, J.R. Schrieffer, Phys. Rev. **108**, 1175 (1957).

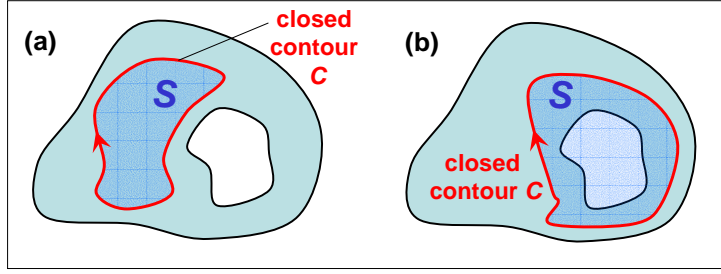


Figure 1.2: Different possibilities for closed contours within a superconducting medium: (a) The path is in a simply connected superconducting region. (b) The path is in a multiply connected region.

Before discussing the experimental observation of flux quantization, we use the macroscopic quantum model of superconductivity to mathematically derive the quantization condition. For simplicity we will assume a homogeneous and isotropic superconductor. We start with the expression (1.1.65) for the supercurrent density

$$\Lambda \mathbf{J}_s = - \left\{ \mathbf{A}(\mathbf{r}, t) - \frac{\hbar}{q^*} \nabla \theta(\mathbf{r}, t) \right\} \quad (1.2.2)$$

and integrate this expression around a closed contour C . From **Stoke's theorem** we know that

$$\oint_C \mathbf{A} \cdot d\mathbf{l} = \int_S (\nabla \times \mathbf{A}) \cdot d\mathbf{s} = \int_S \mathbf{B} \cdot d\mathbf{s} , \quad (1.2.3)$$

where S is the surface defined by the closed contour C (see Fig. 1.2) and \mathbf{B} is the flux density associated with the vector potential \mathbf{A} . Using Stoke's theorem we can rewrite (1.2.2) as

$$\oint_C (\Lambda \mathbf{J}_s) \cdot d\mathbf{l} + \int_S \mathbf{B} \cdot d\mathbf{s} = \frac{\hbar}{q^*} \oint_C \nabla \theta \cdot d\mathbf{l} . \quad (1.2.4)$$

We first evaluate the integral on the right hand side of (1.2.4). We know from the vector calculus that the integral of the gradient of a scalar function along the path defined by points \mathbf{r}_1 and \mathbf{r}_2 is given by

$$\int_{\mathbf{r}_1}^{\mathbf{r}_2} \nabla \theta \cdot d\mathbf{l} = \theta(\mathbf{r}_2, t) - \theta(\mathbf{r}_1, t) . \quad (1.2.5)$$

We see that if $\mathbf{r}_1 \rightarrow \mathbf{r}_2$ such that a closed path is formed the integral is zero. However, in general this is not true, since the specific value of the phase of ψ is not well defined. Indeed there exists an infinite

amount of possible phase values, because for integer values of n all values $\theta_n = \theta_0 + 2\pi n$ give the same value of

$$\psi(\mathbf{r}, t) = \sqrt{n^*} e^{i(\theta_0 + 2\pi n)} . \quad (1.2.6)$$

That is, although the macroscopic wavefunction ψ is well defined, this is not the case for the phase:

$$\theta(\mathbf{r}, t) = \theta_0(\mathbf{r}, t) + 2\pi n . \quad (1.2.7)$$

The phase is specified only within modulo 2π of its principal value θ_0 ranging in the interval $[-\pi, \pi]$. Since θ_0 is single valued, we obtain for the integral of the phase gradient along a closed contour

$$\oint_C \nabla \theta \cdot d\mathbf{l} = \lim_{\mathbf{r}_2 \rightarrow \mathbf{r}_1} [\theta(\mathbf{r}_2, t) - \theta(\mathbf{r}_1, t)] = 2\pi n . \quad (1.2.8)$$

With this result (1.2.4) becomes

$$\oint_C (\Lambda \mathbf{J}_s) \cdot d\mathbf{l} + \int_S \mathbf{B} \cdot d\mathbf{s} = n \Phi_0 \quad (1.2.9)$$

$$\Phi_0 = \frac{2\pi\hbar}{|q^*|} = \frac{\hbar}{|q^*|} = 2.067\,833\,636(81) \times 10^{-15} \text{ Vs} \quad (\text{flux quantum}). \quad (1.2.10)$$

Here, we have replaced $-n$ by n with no loss of generality. The quantity Φ_0 represents the flux quantum and is the smallest amount of flux included by the closed contour line.

The consequences of (1.2.9) can be easily seen by considering Fig. 1.2:

1. We first consider the case (a), where the surface S defined by the contour C is in a simply connected superconducting region (see Fig. 1.2a). We have to recall that we are performing the integration along the closed contour by imagining a line integration between two points \mathbf{r}_1 and \mathbf{r}_2 including the limit $\mathbf{r}_2 \rightarrow \mathbf{r}_1$. Since (1.2.9) holds for all contour lines, we also have to include the case where the size of the contour just has shrunk to zero. In this case both integrals in (1.2.9) vanish and we find $n = 0$ for the simply connected superconductor.¹³ This result is expected since the condition $n = 0$ just yields the integral form of the second London equation.
2. We next consider the case of a multiply connected superconductor as illustrated in Fig. 1.2b. Here, the important point is that the surface S defined by the contour C now contains both superconducting and nonsuperconducting regions (in the most simple case the nonsuperconducting region is just a hole). Thus, if we are closing the line integral by applying the limit $\mathbf{r}_2 \rightarrow \mathbf{r}_1$, we somehow have built in a “memory” in our path: We know that we have enclosed a nonsuperconducting region into the contour. In other words, the phases at the points \mathbf{r}_2 and \mathbf{r}_1 are now distinct. Therefore, although the principal value of the two phases is the same, the difference between them is $2\pi n$.

¹³Of course this is only true, if there are no singularities in the supercurrent density \mathbf{J}_s or the flux density \mathbf{B} .

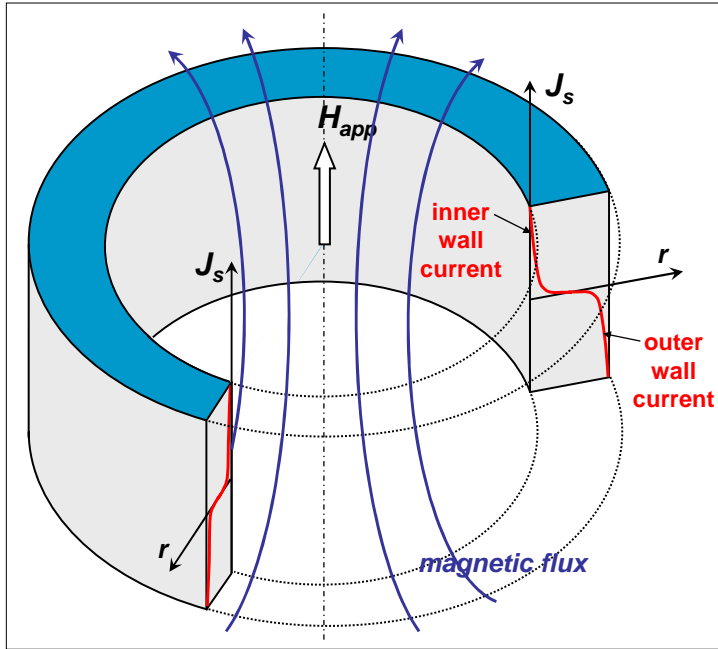


Figure 1.3: Sketch of a superconducting cylinder in the presence of an applied magnetic field along the cylinder axis. Also shown is the expected supercurrent distribution in the wall of the cylinder. For a wall thickness much larger than the superconducting screening length λ_L , the supercurrent density in the center of the wall becomes negligibly small.

1.2.1 Flux and Fluxoid Quantization

Fluxoid Quantization

The left-hand side of (1.2.9) is denoted as the **fluxoid** and hence this equation is a statement of **fluxoid quantization**. Note that the externally applied magnetic flux is not necessarily quantized. However, we have to take into account **both** the external applied flux **and** the flux generated by the induced supercurrent in our calculation. Then, the total flux threading the multiply connected superconductor cannot be arbitrary but must have discrete values corresponding to integer multiples of the flux quantum.

Flux Quantization

We now discuss a superconducting cylinder as sketched in Fig. 1.3. We assume that the wall of the cylinder is much thicker than the London penetration depth λ_L . If we apply a small magnetic field (much smaller than the critical field of the superconducting material) after cooling down the cylinder below the transition temperature of the superconducting material, no flux will thread the superconducting cylinder. There are screening currents flowing on the outer surface of the cylinder wall screening the magnetic field.

The more interesting case is obtained by applying the magnetic field during cooling down. In this case below the transition temperature a screening current flows on the outer surface of the cylinder to expel the applied magnetic field from the superconducting material. In the same way, a screening current with opposite direction is flowing on the inner surface of the cylinder to keep the applied magnetic field outside the superconducting material.

We now use (1.2.9) to analyze the amount of flux trapped in the superconducting cylinder. In the classical case the currents flowing on the inner surface would be constraint only by Ampère's law. Then, classi-

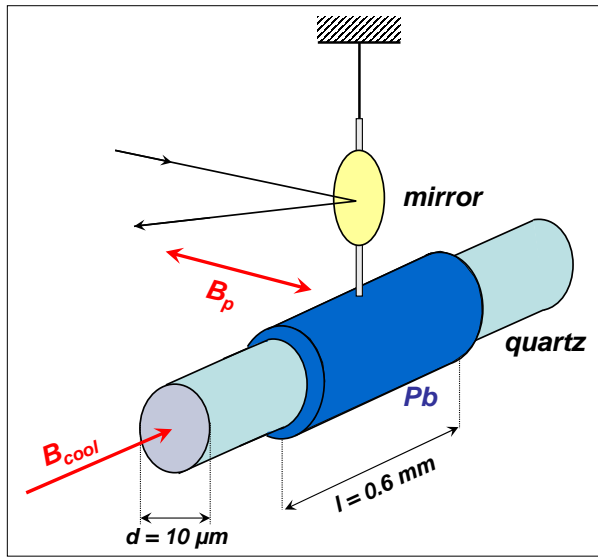


Figure 1.4: Sketch of the experimental configuration used by Doll and Näbauer in 1961 for the determination of the flux quantization in a superconducting cylinder (according to R. Doll, M. Näbauer, Phys. Rev. Lett. 7, 51 (1961)).

cally we could trap arbitrary amounts of magnetic flux in the cylinder by simply varying the magnetic field applied during cooling down. However, in an exact quantum mechanical treatment we have to satisfy also the fluxoid quantization condition (1.2.9). Since the thickness of the superconducting material is much thicker than the London penetration depth λ_L , we can choose a close contour deep inside the superconducting material, where in very good approximation we have $\mathbf{J}_s = 0$. The fluxoid quantization condition then simplifies to

$$\int_S \mathbf{B} \cdot d\mathbf{s} = n \Phi_0 . \quad (1.2.11)$$

That means, if we are removing the applied magnetic field after cooling down, the magnetic flux trapped in the cylinder exactly is an integer multiple of the flux quantum. Therefore, (1.2.11) can be considered as a statement of ***flux quantization***.

1.2.2 Experimental Proof of Flux Quantization

In 1961 the flux quantization in superconducting cylinders has been experimentally proved by two groups, **R. Doll** and **M. Näbauer** at the Walther-Meißner-Institute in Munich and **B. S. Deaver** and **W. M. Fairbank** at Stanford.¹⁴ These very difficult experiments not only have demonstrated the quantization of magnetic flux in a superconducting cylinder but also for the first time proved the existence of Cooper pairs with charge $q^* = 2e$ thereby confirming the prediction of the microscopic theory developed by **John Bardeen**, **Leon Cooper** and **Robert Schrieffer** (BCS-theory) in 1957.

The aim of the experiments was to show that the flux enclosed by a superconducting cylinder of wall thickness $d \gg \lambda_L$ can have only discrete values $\Phi_n = n \cdot \Phi_0$. In order to do so different amounts of

¹⁴R. Doll, M. Näbauer, Phys. Rev. Lett. 7, 51 (1961).
B. S. Deaver, W. M. Fairbank, Phys. Rev. Lett. 7, 43 (1961).

magnetic flux have to be frozen in during cooling down the cylinder in an applied magnetic field B_{cool} and then the amount of trapped flux has to be measured with a precision much better than a single flux quantum. In order to obtain a large relative change of the magnetic flux from measurement to measurement only small values of B_{cool} have to be used resulting in a small number of trapped flux quanta. Since $\Phi = B \cdot S$, both small applied fields and a small cross-sectional area S , resp. diameter d of the cylinder has to be used. Note that for a cylinder area of $S = 1 \text{ mm}^2$ a flux density B of only about 10^{-9} T is required to generate one flux quantum. This flux density is much smaller than that due to the earth magnetic field $B_e \simeq 2 \times 10^{-5} \text{ T}$.

Both experimental groups were using small hollow cylinders with an outer diameter of the order of $10 \mu\text{m}$. For such diameter, a flux density of $B \simeq 2 \times 10^{-5} \text{ T}$ is required to generate one flux quantum $\Phi_0 = 2 \times 10^{-15} \text{ T m}^2$. Since this flux density is of the same order of magnitude as the one due to the earth magnetic field, a careful shielding of the earth magnetic field and other perturbing fields was necessary.

In the experiment of Doll and N  bauer a hollow Pb cylinder was used (see Fig. 1.4). The cylinder was obtained by evaporating Pb on a quartz fiber. In this cylinder they were trapping magnetic flux by cooling down the sample below the transition temperature in a small magnetic field applied parallel to the axis of the cylinder. The magnitude of the trapped magnetic flux has been determined by measuring the torque $\mathbf{D} = \mu \times \mathbf{B}_p$ due to a probe field B_p applied perpendicular to the cylinder axis. Here, μ is the magnetic moment of the trapped magnetic flux. The measurement has been done by hanging up the cylinder using a thin quartz thread. The rotation of the cylinder has been measured by shining light on a mirror attached to the quartz thread. Since the torque is very small, static measurements of the torque could not be performed. Therefore, Doll and N  bauer used a so-called self-resonance method. In this method they were using the small torque created by the probe field B_p for the excitation of a torque vibration of the system. In case of resonance the resulting resonance amplitude is becoming large enough to be measured. The resonance amplitude is proportional to the exciting torque, which in turn is proportional to the flux trapped in the cylinder. Of course, in order to excite the vibration the direction of the probe field B_p has to be switched at the resonance frequency.

In the experiment by Deaver and Fairbank a tiny Sn tube with a length of about 0.9 mm, an inner diameter of $13 \mu\text{m}$ and a wall thickness of $1.5 \mu\text{m}$ was used. The cylinder was vibrated in the axial direction at

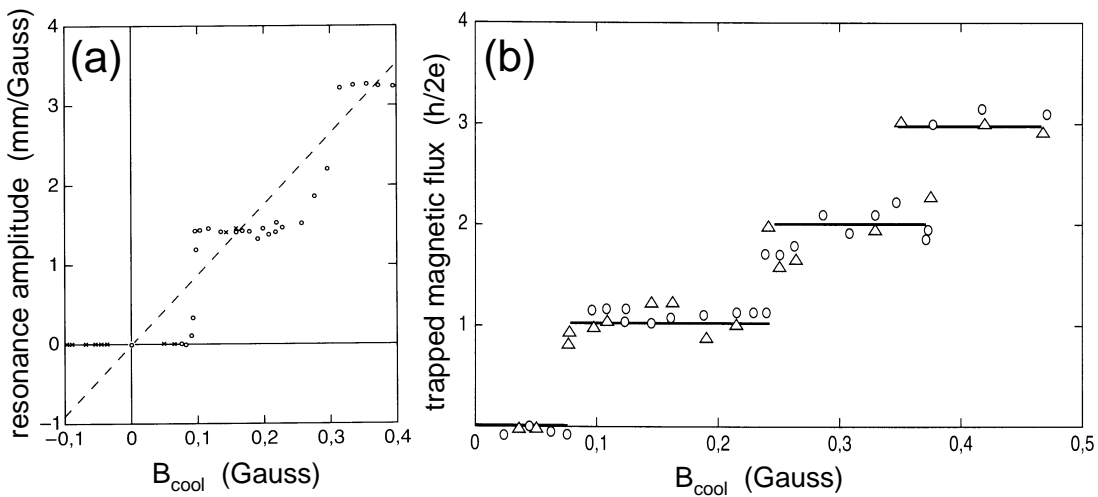


Figure 1.5: Magnetic flux trapped in a superconducting cylinder as a function of the applied magnetic flux density during cooling down the cylinder below the superconducting transition temperature. (a) Experiment by Doll and N  bauer (according to R. Doll, M. N  bauer, Phys. Rev. Lett. 7, 51 (1961)). (b) Experiment by Deaver and Fairbank (according to B. S. Deaver, W. M. Fairbank, Phys. Rev. Lett. 7, 43 (1961)).

a frequency of about 100 Hz and the resulting rf signal was detected via a pair of pick-up coils. The experimental results of both experiments are shown in Fig. 1.5. The results of both experiments were essentially identical and convincing. Although the cylinders were cooled down in different magnetic fields, the net magnetic flux trapped in the cylinder always occurred in quantized amounts. In this way the two experimental groups experimentally demonstrated the limitations of a purely classical treatment of superconductivity.

1.3 The Josephson Effect

In section 1.2 we have discussed the fluxoid quantization in multiply connected superconductors as the first consequence of the macroscopic quantum model of superconductivity. It became evident that this phenomenon is a direct manifestation of the macroscopic quantum coherence of the superconducting state. In this section we discuss the ***Josephson effect*** as a second coherent phenomenon. The Josephson effect has been predicted by **Brian D. Josephson** in 1962 and is equally important as flux quantization.¹⁵ Today, the Josephson effect is used for many applications of superconductivity in electronics, sensors and high frequency devices. The Josephson effect is observed, if two superconductors are weakly connected by an electrical contact. Such contact can be established in many different ways. Prominent examples are tunnelling barriers, point contacts or normal conducting layers connecting the two superconducting electrodes. In the following we will denote such contact as ***Josephson junction***. The initial theoretical work by Josephson has considered only superconductor-insulator-superconductor (SIS) junctions.

Suppose we consider a SIS contact between two identical superconductors as sketched in Fig. 1.6. For a normal metal-insulator- normal metal (NIN) tunnel junction it is well known that for a thin enough tunneling barrier the normal electrons can tunnel through the barrier with the tunneling current density decaying exponentially with increasing barrier thickness. Now, for a SIS tunnel junction at zero temperature we do no longer have normal electrons at the Fermi level. Therefore, we expect that there is no tunnelling current as long as the applied voltage V is smaller than twice the energy gap voltage $2\Delta/e$. For $eV \geq 2\Delta$ Cooper pairs can be broken up into normal electrons, which in turn can tunnel through the barrier. As will be discussed later, this effect is indeed observed.

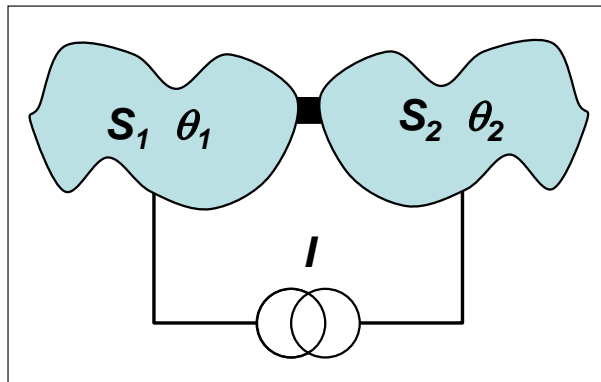


Figure 1.6: The Josephson effect: coherent phenomenon for two weakly coupled superconductors S_1 and S_2 with wave functions $\psi_1 = \sqrt{n_1^*} e^{\theta_1}$ and $\psi_2 = \sqrt{n_2^*} e^{\theta_2}$.

We also have to ask ourselves, whether or not it is possible for Cooper pairs to tunnel through a thin insulating barrier. The consensus in 1962 was that such events would not happen often enough to be measurable. The reason for that seems to be evident. Even the probability of a single electron to tunnel through a thin barrier is very small. Typically the tunneling probability is $p_t \lesssim 10^{-4}$. Then, for a Cooper pair one would expect a probability p_t^2 , which again is orders of magnitude smaller. However, in 1962 Brian Josephson changed this common reasoning. He discovered that the probability of a Cooper pair tunneling through the barrier is the same as that for a single electron. The reason is that the tunneling of Cooper pairs is a coherent process. That is, we should not consider the Cooper pair as two incoherent electron waves leaking through the barrier. Instead, it is the macroscopic wave function describing the entire ensemble of superconducting electrons that is tunneling through the barrier. Only one year later,

¹⁵Brian Josephson, Phys. Rev. Lett. **1**, 251 (1962). For his theoretical predictions of the properties of a supercurrent through a tunnel barrier, in particular those phenomena which are generally known as the Josephson effects, Brian Josephson received the Nobel Price in physics in 1973 together with **Leo Esaki** and **Ivar Giaever**.

Brian David Josephson (born 1940):

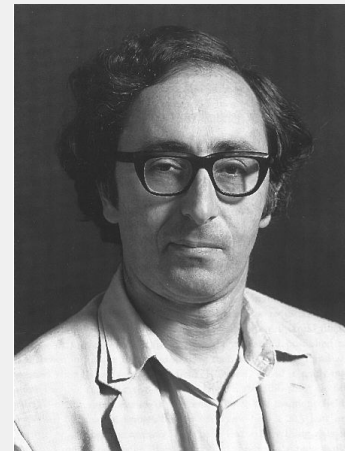
Brian David Josephson was born on January 4, 1940 in Cardiff, Glamorgan, Wales. He is a British physicist whose discovery of the Josephson effect while a 22-year-old graduate student won him a share (with Leo Esaki and Ivar Giaever) of the 1973 Nobel Prize for Physics.

He entered Trinity College, Cambridge, in pursuit of an education in physics and received his bachelor's (1960) and master's and Ph.D. degrees (1964) there, publishing his first work while still an undergraduate. It dealt with certain aspects of the special theory of relativity and the Mößbauer effect. He was elected a fellow of Trinity College in 1962. He was a brilliant and assured student; one former lecturer recalled a special need for precision in any presentation to a class that included Josephson – otherwise, the student would confront the instructor politely after class and explain the mistake.

While still an undergraduate, Josephson became interested in superconductivity, and he began to explore the properties of a junction between two superconductors that later came to be known as a Josephson junction. Josephson extended earlier work in tunneling, the phenomenon by which electrons functioning as radiated waves can penetrate solids, done by Esaki and Giaever. He showed theoretically that tunneling between two superconductors could have very special characteristics, e.g., flow across an insulating layer without the application of a voltage. If a voltage is applied, the current stops flowing and oscillates at high frequency. This was the Josephson effect. Experimentation confirmed it, and its confirmation in turn reinforced the earlier BCS theory of superconductor behavior. Applying Josephson's discoveries with superconductors, researchers at International Business Machines Corporation had assembled by 1980 an experimental computer switch structure, which would permit switching speeds faster than those possible with conventional silicon-based chips, increasing data processing capabilities by a vast amount.

He went to the United States to be a research professor at the University of Illinois in 1965-66 and in 1967 returned to Cambridge as assistant director of research. He was appointed reader in physics in 1972 and professor of physics in 1974. He was elected a fellow of the Royal Society in 1970.

A few years before the Nobel award, Josephson grew interested in the possible relevance of Eastern mysticism to scientific understanding. In 1980 he and V.S. Ramachandran published an edited transcript of a 1978 international symposium on consciousness at Oxford under the title *Consciousness and the Physical World*.



Philip Anderson and **John Rowell** had experimentally confirmed the prediction of Brian Josephson, which again is a direct consequence of the macroscopic quantum nature of the superconducting state.

1.3.1 The Josephson Equations

First Josephson Equation: current-phase relation

We first speculate what determines the supercurrent between two weakly connected superconductors. It certainly can depend on the Cooper pair densities $|\psi_1|^2 = n_1^*$ and $|\psi_2|^2 = n_2^*$ in the junction electrodes. However, since the coupling between the two superconductors is weak and, hence, the supercurrent density between them is small, we can assume that the supercurrent density between the two junction electrodes is not changing $|\psi|^2$. However, although the amplitude of the wave functions in the electrodes does not play a role, the supercurrent density certainly is expected to depend on the phase of the wave functions.

We already have learnt that the supercurrent density in a bulk superconductor depends on the gauge invariant phase gradient (compare (1.1.63)) as

$$J_s(\mathbf{r}, t) = \frac{q^* n^*(\mathbf{r}, t) \hbar}{m^*} \gamma(\mathbf{r}, t) . \quad (1.3.1)$$

We simplify our discussion by assuming that (i) the current density can be considered homogeneous. We will see later that this assumption can be always made if the junction area is small enough. We are now applying expression (1.3.1) to the case of two weakly connected superconductors. Doing so, we make the further assumption that (ii) the magnetic vector potential is zero, as it would be in the absence of any electric and magnetic field. Below we will relax this simplifying assumption. We further assume that (iii) the phase is varying negligibly in the superconducting electrodes. This is always a good assumption as long as the supercurrent density across the Josephson junction is low. Then, we can replace the phase gradient $\gamma = \nabla\theta - \frac{2\pi}{\Phi_0}\mathbf{A}$ of the gauge invariant phase just by $\varphi = (\theta_2 - \theta_1)/d$, where d is the thickness of the coupling region (see Fig. 1.6). Hence, according to (1.3.1) we expect the supercurrent density J_s to be a function only of φ , that is, $J_s = J_s(\varphi)$. Actually, according to (1.3.1) we expect $J_s \propto \varphi$. However, we have to take into account that any phase change of 2π in the wave functions of the junction electrodes results in the same wave function $\psi_{1,2}$. From this we can conclude that $J_s(\varphi)$ should not be a linear but a 2π -periodic function:

$$J_s(\varphi) = J_s(\varphi + n 2\pi) . \quad (1.3.2)$$

Finally, in the absence of any current both electrodes form a single superconductor with a common phase. That is, in this case we have $\theta_1 = \theta_2$ and hence

$$J_s(0) = J_s(n 2\pi) = 0 . \quad (1.3.3)$$

Summarizing our discussion we can conclude that the supercurrent density between the two junction electrodes in the most general case should have the form

$$J_s(\varphi) = J_c \sin \varphi + \sum_{m=2}^{\infty} J_m \sin(m\varphi) . \quad (1.3.4)$$

Here, J_c is the **critical or maximum Josephson current density**, which is determined by the coupling strength between the two junction electrodes. Expression (1.3.4) is the general formulation of the **1. Josephson equation**. It also is denoted as the **current-phase relation**, since it relates the supercurrent density to the phase difference. Rigorous theoretical treatment shows that in most cases (in particular in the case of weak coupling) the second term on the right hand side can be neglected. Then, (1.3.4) obtains the form

$$J_s(\varphi) = J_c \sin \varphi , \quad (1. Josephson equation) \quad (1.3.5)$$

which was derived by Josephson in his original paper for the particular case of an insulating barrier. Here, due to the rapid decay of the wave function in the insulator, weak coupling was explicitly assumed. We will discuss this case in more detail in section 1.3.2.

The basic essence of (1.3.5) can be summarized as follows:

The supercurrent density through a Josephson junction varies sinusoidally with the phase difference $\varphi = \theta_2 - \theta_1$ across the junction in the absence of any scalar and vector potentials.

Above we have made the assumption of a homogenous supercurrent density allowing a one-dimensional treatment. This assumption can be relaxed by noting that the argument given above still holds if applied *locally* to each point (y, z) of the junction area. In particular, we can generalize the critical current density J_c to $J_c(y, z)$ (the junction area extends in the yz -plane, see Fig. 1.7). The current flow is always in x -direction so that there is no divergence of current density. That is, for any given y and z the supercurrent is flowing straight across the junction area. However, the current density given by (1.3.5) may now depend on y and z and we have to generalize the current-phase relation to

$$J_s(y, z, t) = J_c(y, z) \sin \varphi(y, z, t) . \quad (1.3.6)$$

In deriving the current-phase relation (1.3.5) we have assumed a vanishingly small vector potential in the junction to represent the vanishing magnetic flux density in the junction. We therefore have to analyze now the more general case of a non-vanishing vector potential. In general, we can choose the magnetic vector potential to be written as

$$\mathbf{A}(\mathbf{r}, t) = -\nabla \chi(\mathbf{r}, t) \quad (1.3.7)$$

to ensure $\mathbf{B} = 0$ in the junction. Here, $\chi(\mathbf{r}, t)$ is an arbitrary single-valued function. We now can use a new gauge

$$\mathbf{A}'(\mathbf{r}, t) = \mathbf{A}(\mathbf{r}, t) + \nabla \chi(\mathbf{r}, t) = 0 , \quad (1.3.8)$$

so that for this new gauge the vector potential vanishes. Then, in this gauge we obtain the same current-phase relation as given by (1.3.5):

$$J_s = J_c \sin(\theta'_2 - \theta'_1) = J_c \sin \varphi . \quad (1.3.9)$$

Here, θ'_2 and θ'_1 are the phases of the wavefunction in the gauge with \mathbf{A}' . We now can use expression (1.1.58), which relates the phases of the wavefunction in the two gauges:

$$\theta' = \theta - \frac{2\pi}{\Phi_0} \chi , \quad (1.3.10)$$

where we have used $q^* = -2e$ and $\Phi_0 = h/2e$. We therefore obtain

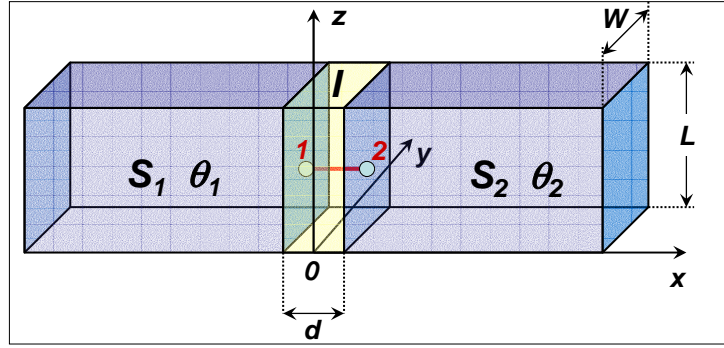


Figure 1.7: Sketch of a superconductor-insulator-superconductor (SIS) Josephson junction with a current source driving a current through the junction.

$$\theta'_2 - \theta'_1 = \theta_2 - \theta_1 + \frac{2\pi}{\Phi_0}(\chi_2 - \chi_1) . \quad (1.3.11)$$

We now use the fact that the difference of a scalar function $f(r)$ between two points can be written as a line integral between these two points:

$$f(\mathbf{r}_2) - f(\mathbf{r}_1) = \int_{\mathbf{r}_1}^{\mathbf{r}_2} \nabla f \cdot d\ell . \quad (1.3.12)$$

Then the difference $\chi_2 - \chi_1$ can be expressed as a line integral from point 1 in superconductor 1 to point 2 in superconductor 2 of the gradient of χ :

$$\chi_2 - \chi_1 = \int_1^2 \nabla \chi \cdot d\ell = - \int_1^2 \mathbf{A}(\mathbf{r}, t) \cdot d\ell . \quad (1.3.13)$$

With $\varphi = \theta'_2 - \theta'_1$ and (1.3.11) we obtain the **gauge-invariant phase difference** φ as

$$\varphi(\mathbf{r}, t) = \theta_2(\mathbf{r}, t) - \theta_1(\mathbf{r}, t) - \frac{2\pi}{\Phi_0} \int_1^2 \mathbf{A}(\mathbf{r}, t) \cdot d\ell . \quad (1.3.14)$$

We note that the integration path is along the direction of current (see Fig. 1.7). That is, for a SIS-type Josephson junction the path is across the insulating barrier from the superconductor one with phase θ_1 to the superconductor 2 with phase θ_2 . For the geometry of Fig. 1.7 the integration path is from $-d/2$ to $+d/2$ and the differential line element is $d\ell$.

We emphasize that the current-phase relation (1.3.5) and the expression for the gauge invariant phase difference (1.3.14) have been derived for the special case of a vanishing flux density \mathbf{B} in the junction. However, it is plausible that these relations also hold in the case of $\mathbf{B} \neq 0$. This can be seen by considering the limiting case $d \rightarrow 0$. In this limit we obtain $J_s \propto -\nabla\theta - \frac{2\pi}{\Phi_0}\mathbf{A}$, that is we recover the general expression for the supercurrent density J_s (compare (1.1.51)), which is valid when \mathbf{B} is nonzero. Therefore, it is plausible to assume that expressions for the current-phase relation and the gauge-invariant phase difference also hold for nonzero \mathbf{B} . However, we will not prove this here.

Second Josephson Equation: voltage-phase relation

In order to derive the 2. Josephson equation we use the time derivative of the gauge invariant phase difference

$$\frac{\partial\varphi}{\partial t} = \frac{\partial\theta_2}{\partial t} - \frac{\partial\theta_1}{\partial t} - \frac{2\pi}{\Phi_0} \frac{\partial}{\partial t} \int_1^2 \mathbf{A}(\mathbf{r},t) \cdot d\ell . \quad (1.3.15)$$

Substitution of the energy-phase relation (1.1.68)

$$-\hbar \frac{\partial\theta}{\partial t} = \frac{1}{2n^\star} \Lambda \mathbf{J}_s^2 + q^\star \phi \quad (1.3.16)$$

into (1.3.15) yields

$$\frac{\partial\varphi}{\partial t} = -\frac{1}{\hbar} \left(\frac{\Lambda}{2n^\star} [\mathbf{J}_s^2(2) - \mathbf{J}_s^2(1)] + q^\star [\phi(2) - \phi(1)] \right) - \frac{2\pi}{\Phi_0} \frac{\partial}{\partial t} \int_1^2 \mathbf{A} \cdot d\ell . \quad (1.3.17)$$

Since the supercurrent density across the junction is continuous, we can use $\mathbf{J}_s(2) = \mathbf{J}_s(1)$ and obtain

$$\frac{\partial\varphi}{\partial t} = \frac{2\pi}{\Phi_0} \int_1^2 \left(-\nabla\phi - \frac{\partial\mathbf{A}}{\partial t} \right) \cdot d\ell . \quad (1.3.18)$$

Here, we have expressed the difference in the scalar potential ϕ as a line integral of its gradient. Since the term in parentheses is just the electric field (compare (1.1.55)), we can write

$$\frac{\partial\varphi}{\partial t} = \frac{2\pi}{\Phi_0} \int_1^2 \mathbf{E}(\mathbf{r},t) \cdot d\ell \quad (2. \text{ Josephson equation}) . \quad (1.3.19)$$

This equation is known as the ***second Josephson equation*** or ***voltage-phase relation***. Together with the ***current-phase relation*** (1.3.5) and the ***gauge-invariant phase difference*** (1.3.14) the ***voltage-phase relation*** represents the set of basic equations governing the behavior of Josephson junctions.

We note that $\int_1^2 \mathbf{E}(\mathbf{r}, t) \cdot d\ell$ corresponds to a voltage drop across the junction. That is, if a constant voltage V is applied to the Josephson junction we obtain

$$\frac{\partial \varphi}{\partial t} = \frac{2\pi}{\Phi_0} V . \quad (1.3.20)$$

and the phase difference is growing linearly in time:

$$\varphi(t) = \varphi_0 + \frac{2\pi}{\Phi_0} V \cdot t . \quad (1.3.21)$$

Then, the Josephson current $I_s(t) = I_c \sin \varphi(t)$ is oscillating at the ***Josephson frequency***

$$\frac{\nu}{V} = \frac{\omega}{2\pi V} = \frac{1}{\Phi_0} \simeq 483\,597.898(19) \frac{\text{MHz}}{\mu\text{V}} . \quad (1.3.22)$$

We see that the Josephson junctions can be considered as a voltage controlled oscillator that can be used to generate very high frequencies (500 GHz at 1 mV). The linewidth and the power that can be achieved with Josephson junctions will be discussed later, when we are discussing applications of the Josephson effect.

1.3.2 Josephson Tunneling

So far we have not discussed the magnitude of the ***maximum Josephson current density*** J_c . In this subsection we derive an expression of this quantity for the case of Josephson junction with an insulating tunneling barrier of thickness d . That is, we consider the supercurrent density across a superconductor-insulator-superconductor Josephson junction as sketched in Fig. 1.7. To solve the problem we are using the so-called ***wave matching method***. Here, we solve the Schrödinger equation in the three regions, namely the two superconducting electrodes and the insulating barrier. The solutions will contain coefficients that can be determined by matching the solutions at the boundaries between the three regions.

We first start with the wavefunction in the superconducting electrodes. The supercurrent density at the edges of the junction electrodes at the positions $x = \pm d/2$ is given by the supercurrent density equation (1.1.51)

$$\mathbf{J}_s = q^\star n^\star(\mathbf{r}, t) \left\{ \frac{\hbar}{m^\star} \nabla \theta(\mathbf{r}, t) - \frac{q^\star}{m^\star} \mathbf{A}(\mathbf{r}, t) \right\} . \quad (1.3.23)$$

We already have found the relationship between the current density at the boundary to the insulator and the phase of the wavefunctions at each boundary. It is given by the current-phase relation. In order to derive the magnitude of the maximum Josephson current density J_c we make the same assumptions as in section 1.3.1. That is, we assume a uniform tunneling barrier. We further assume that the junction area $L \cdot W$ is small enough, so that the Josephson current density can be assumed uniform within the junction area. It will be discussed later, up to which length scale this approximation is valid.

We start our discussion with the energy-phase relation (1.1.68) for the superconducting electrodes, which directly follows from the Schrödinger equation. In the absence of any electric and magnetic field this equation can be written as

$$-\hbar \frac{\partial \theta}{\partial t} = \frac{\Lambda}{2n^*} \Lambda \mathbf{J}_s^2 . \quad (1.3.24)$$

The term on the right hand side corresponds to the kinetic energy $E_0 = m^* v_s^2 / 2$ of the moving superelectrons and therefore we can write

$$\frac{\partial \theta}{\partial t} = -\frac{E_0}{\hbar} . \quad (1.3.25)$$

Consequently, the time dependent macroscopic wave function can be written as

$$\psi(\mathbf{r}, t) = \psi(\mathbf{r}) e^{-i(E_0/\hbar)t} , \quad (1.3.26)$$

where $\psi(\mathbf{r})$ is the time independent amplitude of the wave function.

We must now determine the wavefunction within the insulating barrier of thickness d . The barrier height V_0 is assumed larger than E_0 . Then, the variation of the potential along the x -direction is given by a step-like function $V(x)$, which is zero outside and V_0 inside the barrier region (see Fig. 1.8). We know that classically for $V_0 > E_0$ the superelectrons cannot penetrate the barrier region. However, quantum mechanically the situation is different. Here, the superelectrons can tunnel through the barrier. In our discussion we consider only elastic processes, that is, the superelectrons maintain their energy. Therefore, the time evolution of the wavefunction is the same outside and inside the barrier and we have to consider only the time independent part. Moreover, since within the barrier we are in a region of constant potential energy V_0 , the time dependent Schrödinger-like equation (1.1.49) can be written as the time independent Schrödinger equation

$$-\frac{\hbar^2}{2m^*} \nabla^2 \psi(\mathbf{r}) = (E_0 - V_0) \psi(\mathbf{r}) . \quad (1.3.27)$$

Using now our simplifying assumptions of a homogeneous barrier and homogeneous supercurrent flow we have to consider only the x -dependence, i.e. we have to solve only a one-dimensional problem.

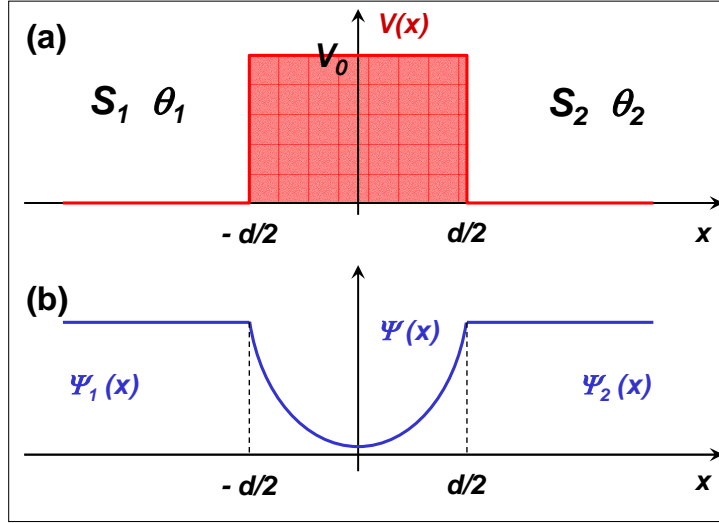


Figure 1.8: (a) Sketch of the model potential $V(x)$ of a superconductor-insulator-superconductor Josephson junction. (b) Time independent part of the wave function.

The solution of (1.3.27) can be written as a sum of decaying and growing exponentials or equivalently as

$$\psi(x) = A \cosh(\kappa x) + B \sinh(\kappa x), \quad (1.3.28)$$

where the ***characteristic decay constant*** κ is determined by the barrier properties and is given by

$$\kappa = \sqrt{\frac{2m^*(V_0 - E_0)}{\hbar^2}}. \quad (1.3.29)$$

The coefficients A and B are determined by the boundary conditions at $x = \pm d/2$:

$$\psi(-d/2) = \sqrt{n_1^*} e^{i\theta_1} \quad (1.3.30)$$

$$\psi(+d/2) = \sqrt{n_2^*} e^{i\theta_2}. \quad (1.3.31)$$

Here, $\sqrt{n_{1,2}^*}$ and $\theta_{1,2}$ are the magnitude and the phase of the wavefunction at the boundaries $x = \pm d/2$.

With these boundary conditions we obtain from (1.3.28)

$$\sqrt{n_1^*} e^{i\theta_1} = A \cosh(\kappa d/2) - B \sinh(\kappa d/2) \quad (1.3.32)$$

$$\sqrt{n_2^*} e^{i\theta_2} = A \cosh(\kappa d/2) + B \sinh(\kappa d/2) \quad (1.3.33)$$

and hence by solving for A and B

$$A = \frac{\sqrt{n_1^*} e^{i\theta_1} + \sqrt{n_2^*} e^{i\theta_2}}{2 \cosh(\kappa d/2)} \quad (1.3.34)$$

$$B = \frac{\sqrt{n_1^*} e^{i\theta_1} - \sqrt{n_2^*} e^{i\theta_2}}{2 \sinh(\kappa d/2)} . \quad (1.3.35)$$

We now have to recall the supercurrent density is given by (compare (1.1.41))

$$\mathbf{J}_s = \frac{q^*}{m^*} \Re \left\{ \psi^* \left(\frac{\hbar}{i} \nabla \right) \psi \right\} . \quad (1.3.36)$$

With the wavefunction from (1.3.28) the current density is obtained to

$$\mathbf{J}_s = \frac{q^*}{m^*} \kappa \hbar \Im \{ A^* B \} . \quad (1.3.37)$$

Substituting (1.3.34) and (1.3.35) in (1.3.37) yields the supercurrent density

$$\mathbf{J}_s = \mathbf{J}_c \sin(\theta_2 - \theta_1) \quad (1.3.38)$$

with the **maximum Josephson current density**

$$\mathbf{J}_c = -\frac{q^*}{m^*} \kappa \hbar \frac{\sqrt{n_1^* n_2^*}}{2 \sinh(\kappa d/2) \cosh(\kappa d/2)} = -\frac{q^* \hbar \kappa}{2 m^*} \frac{\sqrt{n_1^* n_2^*}}{2 \sinh(\kappa d)} . \quad (1.3.39)$$

We see that from our analysis we not only obtain the value for the maximum Josephson current density but also the current-phase relation, which has been derived from our qualitative discussion above.

In real junctions the barrier height V_0 typically is of the order of a few eV and therefore the decay length $1/\kappa$ less than a nanometer. Since the thickness of the tunnel barrier is usually a few nanometer, we have $\kappa d \gg 1$. In this case we can use the approximation $\sinh(\kappa d) \simeq \frac{1}{2} \exp(\kappa d)$. Hence, the maximum Josephson current density decays exponentially with increasing thickness of the tunneling barrier.

We note that the Josephson equations also can be derived by considering two separate quantum mechanical systems that are weakly coupled by a coupling Hamilton operator (transfer Hamiltonian approach). This derivation is discussed in Appendix A

Chapter 2

Physics of Josephson Junctions: The Zero Voltage State

In this chapter we discuss the physics of Josephson junctions in the zero voltage state. In this situation the Josephson current density J_s always is smaller than the maximum Josephson current density J_c so that the current is always flowing as supercurrent that can be described by the macroscopic quantum approach. The voltage state of Josephson junctions will be discussed in chapter 3. In the case of a finite junction voltage the situation is more complex, since besides the Josephson current other types of current such as a normal current or a displacement current have to be taken account. These currents vanish in the zero voltage state and hence make the treatment of this situation simple.

In section 2.1 we first restrict ourselves to cases where the junction area is small enough so that the junction can be considered as a zero-dimensional or lumped element. Then the current rather than the current density is sufficient to describe the Josephson junction properties. We will introduce the ***Josephson coupling energy*** and the ***Josephson inductance*** as well as mechanical analogs for lumped Josephson junctions.

In sections 2.2 and 2.3 we then relax the restriction on the junction area and discuss the junctions as distributed systems, where the currents have a spatial dependence inside the junction itself. Here, the discussion of the magnetic field dependence of the Josephson current density is the main topic.

2.1 Basic Properties of Lumped Josephson Junctions

In many superconducting devices and circuits Josephson junctions with very small spatial dimensions are used. Such small Josephson junctions can be understood by considering the gauge invariant phase difference and the current density to be uniform over the junction area. We will show later (see sections 2.2 and 2.3) that small means that the spatial extension of the junction area must be much smaller than a characteristic screening length, the so-called ***Josephson penetration depth*** λ_J . This screening length of a weak superconducting system is the analog of the ***London penetration depth*** λ_L of a bulk superconductor and sets the length scale over which variations of the supercurrent density occur. Therefore, the supercurrent density across a Josephson junction can be assumed to be constant, if the junction area is much smaller than this screening length. In the same way the supercurrent density in a bulk superconductor always can be assumed constant, if the spatial dimensions of the bulk superconductor are much smaller the London penetration depth.

Note that the London penetration depth $\lambda_L = \sqrt{\frac{m^*}{\mu_0 n^* q^{*2}}}$ defines the length scale over which an applied field can penetrate a bulk superconductor. Equivalently, it defines the surface layer, in which the screening currents are flowing. This length scale typically ranges between several 10 nm and about 1 μm for most superconductors. For a weak superconducting system as a Josephson junction the equivalent screening length is much larger. This can be understood simply by the fact that in the weak region connecting two bulk superconductors the density of Cooper pairs is strongly reduced. Since the screening length is proportional to $1/\sqrt{n^*}$, the corresponding screening length λ_J is strongly increased. It easily can be larger than 100 μm . That is, even Josephson junctions with spatial dimensions of the order of several 10 μm can be considered small.

2.1.1 The Lumped Josephson Junction

We call Josephson junctions with spatially homogeneous supercurrent density and phase difference ***lumped junctions***. Such junctions can be described by a supercurrent

$$I_s = \int_S \mathbf{J}_s \cdot d\mathbf{s} . \quad (2.1.1)$$

The region of integration is the junction area. The current-phase relation (1.3.6) can be rewritten in terms of the currents as

$$I_s(t) = I_c \sin \varphi(t) . \quad (2.1.2)$$

The gauge-invariant phase difference is still given by

$$\varphi(t) = \theta_2(t) - \theta_1(t) - \frac{2\pi}{\Phi_0} \int_1^2 \mathbf{A}(\mathbf{r}, t) \cdot d\ell . \quad (2.1.3)$$

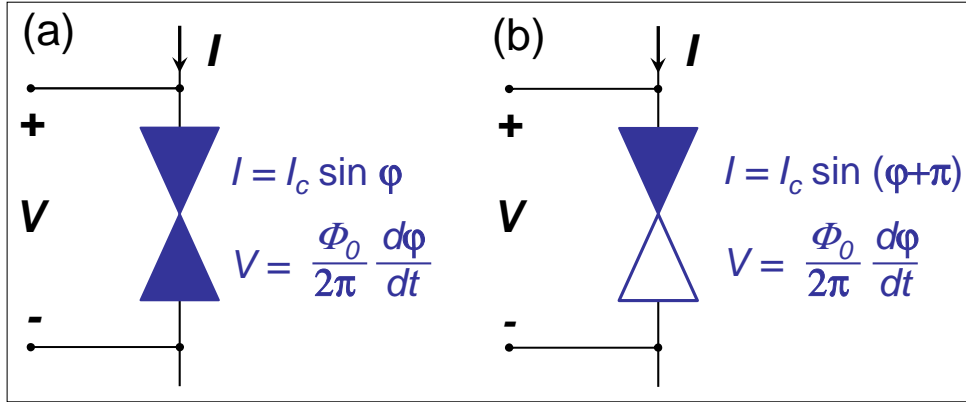


Figure 2.1: The Josephson junction as a lumped circuit element, which is characterized by the crossed symbol in circuit diagrams and is governed by the two Josephson equations. Left: “0”-junction, right: “ π ”-junction

The voltage-phase relation $\frac{\partial \phi}{\partial t} = \frac{2\pi}{\Phi_0} \int_1^2 \mathbf{E}(\mathbf{r}, t) \cdot d\ell$ can be simplified by noting that $\int_1^2 \mathbf{E}(\mathbf{r}, t) \cdot d\ell$ is just the voltage $V(t)$ across the junction. The voltage is well defined for a lumped junction, since the integration path is well defined across the junction parallel to the current direction. Furthermore, for a lumped junction the electric field is independent of y and z . Here we are assuming that the current flow is in x -direction and the junction area extends in the yz -plane. The voltage-phase relation then becomes

$$\frac{d\phi}{dt} = \frac{2\pi}{\Phi_0} V . \quad (2.1.4)$$

Note that we are now using the total derivative because for a lumped junction the phase difference ϕ does not depend on any spatial coordinate.

Fig. 2.1) shows the symbol for a lumped Josephson junction along with the two equations describing the junction. We distinguish between “0”-junctions, for which the current is flowing in the direction of the applied current for $\phi = 0$, and “ π ”-junctions, for which the current is flowing in the direction of the applied current for $\phi = \pi$. In the following subsections we discuss how energy can be stored in this lumped junctions and how it behaves when it is driven by external current or voltage sources.

2.1.2 The Josephson Coupling Energy

Due to the zero junction voltage, no energy will be dissipated in the junction residing in the S state. However, there is a finite energy stored in the junction. This becomes immediately evident by considering the process of increasing the junction current from zero to a finite value I . Let the initial value of the phase difference ϕ be zero at zero junction current. As we are increasing the current, according to the current-phase relation also the phase difference ϕ has to change. Furthermore, according to the voltage-phase relation a changing phase difference corresponds to a finite junction voltage. That is, on increasing the current the external source has to supply energy that is determined by the integral of the power $I \cdot V$ during the current increase. Although the superelectrons can flow across the junction without causing any resistance, on increasing the current we have to accelerate the superelectrons in the sample and this requires a certain amount of energy. This energy is then stored by the moving superelectrons.

In order to calculate the energy stored in the Josephson junction we have to integrate the power from time $t = 0$ when we start the current increase to time $t = t_0$ when we are stopping the increase:

$$E_J = \int_0^{t_0} I_s V dt . \quad (2.1.5)$$

Here, V is the voltage generated during increasing the current from zero at $t = 0$ to the final value I at time t_0 . Using the current-phase and the voltage-phase relation we obtain

$$E_J = \int_0^{t_0} (I_c \sin \varphi') \left(\frac{\Phi_0}{2\pi} \frac{d\varphi'}{dt} \right) dt . \quad (2.1.6)$$

With the phase difference $\varphi(0) = 0$ and $\varphi(I) = \varphi$ we can write the integral as

$$E_J = \frac{\Phi_0 I_c}{2\pi} \int_0^\varphi \sin \varphi' d\varphi' . \quad (2.1.7)$$

Integration gives the energy stored in the junction as

$$E_J = \frac{\Phi_0 I_c}{2\pi} (1 - \cos \varphi) = E_{J0} (1 - \cos \varphi) . \quad (2.1.8)$$

This energy is usually denoted as the ***coupling energy***. Similar to the binding energy of a molecule this energy results from the overlap (or coupling) of the wavefunctions of the two superconducting electrodes.

In Fig. 2.2 we plot the coupling energy and the Josephson current as a function of the phase difference. The energy is lowest, if no current flows and φ is zero or a multiple of 2π . Therefore, such junctions are denoted as “0” junctions. There are also other junctions (e.g. junctions with ferromagnetic barrier layers) for which the state of lowest coupling energy is obtained for a phase difference of π or $(2n+1)\pi$. These junctions are named “ π ” junctions.

We briefly discuss the order of magnitude of the Josephson coupling energy. For a junction with a typical critical current of 1 mA we have $E_{J0} \simeq 3 \times 10^{-19}$ J what corresponds to the thermal energy $k_B T$ at around 20.000 K. Therefore, thermal smearing effects are negligible. However, for junctions with very small critical current this is different. For example, for $I_c = 1 \mu$ A the coupling energy corresponds to the thermal energy at around 20 K and, hence, thermal smearing effects become prominent as discussed in chapter 3.

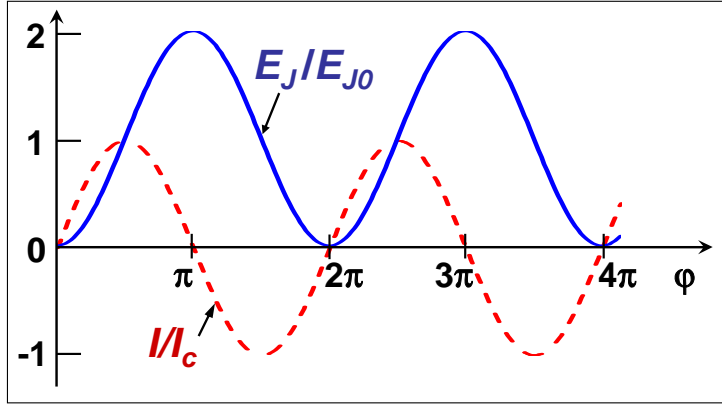


Figure 2.2: The normalized Josephson current I_s/I_c and the normalized coupling energy E_J/E_{J0} plotted versus the phase difference φ .

2.1.3 The Superconducting State

According to the current-phase relation (2.1.1) a constant dc current imposed on a Josephson junction by an external current source results in a constant phase difference

$$\varphi = \varphi_n = \arcsin\left(\frac{I}{I_c}\right) + 2\pi n \quad (2.1.9)$$

$$\varphi = \varphi'_n = \pi - \arcsin\left(\frac{I}{I_c}\right) + 2\pi n \quad (2.1.10)$$

for

$$-I_c \leq I \leq +I_c . \quad (2.1.11)$$

The constant phase difference results in $d\varphi/dt = 0$. Hence, each of the solutions corresponds to zero junction voltage and describes the superconducting state. We will call this situation the *zero voltage state* or stationary (*S*) state.

In order to analyze the stability of the zero voltage state we use the potential energy E_{pot} of the system Josephson junction + current source. To find E_{pot} we use the rule, which is general for any subsystem (the Josephson junction in our case) under the action of a constant external force F (the applied current in our case), saying that the total energy G^1 is equal to the difference of the two terms:

$$G = E - F \cdot x . \quad (2.1.12)$$

¹Note that in thermodynamics G is called the Gibbs energy (potential) of the subsystem, which has to be distinguished from the free energy (Helmholtz energy) E .

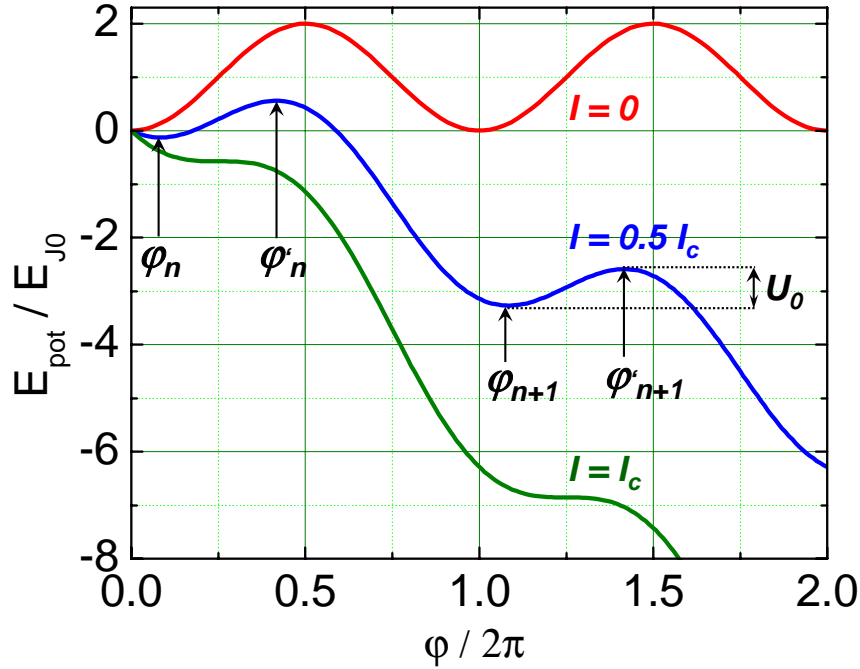


Figure 2.3: The potential energy $E_{\text{pot}}(\varphi)$ of a current biased lumped Josephson junction at various values of the applied current. The potential is named tilted washboard potential.

Here, E is the intrinsic (free) energy of the subsystem and x is its generalized coordinate corresponding to the generalized force $F = I$. The coordinate should be chosen in a way that the product $F\dot{x}$ gives the power P flowing into the subsystem. Since for the Josephson junction the latter product equals to $I \cdot V$, the desirable coordinate is

$$x = \int V dt = \frac{\hbar}{2e}\varphi + c = \frac{\Phi_0}{2\pi}\varphi + c , \quad (2.1.13)$$

where c is an integration constant. The potential energy of the system is thus given by

$$E_{\text{pot}}(\varphi) = E_J - I \left(\frac{\Phi_0}{2\pi}\varphi + c \right) = E_{J0} \left[1 - \cos \varphi - \frac{I}{I_c}\varphi \right] + c' . \quad (2.1.14)$$

As shown by Fig. 2.3 the function $E_{\text{pot}}(\varphi)$ has the shape of a tilted washboard and is therefore often called the **tilted washboard potential**. The washboard has minima and maxima for the values of the phase difference given by (2.1.9) and (2.1.10), respectively. It is evident that the former solutions are stable and the latter are unstable. We further note that the states corresponding to different n are physically equivalent and therefore we usually only refer to the $n = 0$ solution.

By analyzing the tilted washboard potential we can easily derive from (2.1.14) the difference $U_0 = E_{\text{pot}}(\varphi_n) - E_{\text{pot}}(\varphi'_n)$ and the curvature $k \equiv \partial^2 E_{\text{pot}} / \partial \varphi^2$ of the potential at the potential minimum. We obtain²

²Here we use the equality $\arcsin(x) = \arccos \sqrt{1 - x^2}$.

$$U_0 \equiv E_{\text{pot}}(\varphi_n) - E_{\text{pot}}(\varphi'_n) = 2E_{J0} \left[\sqrt{1 - \left(\frac{I}{I_c} \right)^2} - \frac{I}{I_c} \arccos \left(\frac{I}{I_c} \right) \right] \quad (2.1.15)$$

$$k \equiv \frac{\partial^2 E_{\text{pot}}}{\partial \varphi^2} = E_{J0} \sqrt{1 - \left(\frac{I}{I_c} \right)^2}. \quad (2.1.16)$$

We see that these quantities approach zero for $I \rightarrow I_c$. Close to the critical current we have $\alpha \equiv 1 - I/I_c \ll 1$ and can use the following approximations

$$\varphi_0 = \frac{\pi}{2} - \sqrt{2\alpha} \quad \varphi'_0 = \frac{\pi}{2} + \sqrt{2\alpha} \quad (2.1.17)$$

$$U_0 = \frac{2}{3} E_{J0} (2\alpha)^{2/3} \quad (2.1.18)$$

$$k = E_{J0} (2\alpha)^{1/2}. \quad (2.1.19)$$

We will see in chapter 3 that the tilted washboard potential is very useful for describing the dynamics of Josephson junctions at $I > I_c$. It is evident from (2.1.14) and Fig. 2.3 that in this case there are no longer any minima in the potential and consequently the phase will continuously increase resulting in a finite junction voltage. The dynamics can be described by considering the phase as a particle moving down the tilted washboard potential. However, in order to describe this process we have to determine the mass of the particle and the damping of the motion. This can be done only after introducing the other current components as the normal current and the displacement current in chapter 3.

2.1.4 The Josephson Inductance

Energy storage and conservation in the Josephson junction suggests that it can be considered as a ***non-linear reactance***. In order to clarify this we consider the time derivative of the current-phase relation:

$$\frac{dI_s}{dt} = I_c \cos \varphi \frac{d\varphi}{dt}. \quad (2.1.20)$$

Using the voltage-phase relation we obtain

$$\frac{dI_s}{dt} = I_c \cos \varphi \frac{2\pi}{\Phi_0} V. \quad (2.1.21)$$

This immediately shows that for small variations of the current around the value $I_s = I_c \sin \varphi$ the Josephson junction behaves as an inductance

$$L_s = \frac{\Phi_0}{2\pi I_c \cos \varphi} = L_c \frac{1}{\cos \varphi} \quad \text{with} \quad L_c = \frac{\hbar}{2eI_c} . \quad (2.1.22)$$

A very unusual property of this **Josephson inductance** is the fact that it can have negative values in the intervals $\pi/2 + 2\pi n < \varphi < 3\pi/2 + 2\pi n$. Note that from the electrotechnical point of view the energy E_J can be considered as stored in the inductance L_s . The fact that the Josephson inductance can have negative values results in a behavior that is completely different from an ordinary nonlinear inductance. This is immediately seen, if we apply constant voltage V to the Josephson junction. In this case we have obtain an oscillating Josephson current as discussed already in section 1.3.1. Note that for an ordinary inductance the current would not oscillate but just gradually increase. The oscillations of the supercurrent are called **Josephson oscillations** and have been predicted in the original paper by Brian Josephson. These oscillations accompany most processes in Josephson junctions and are of particular importance for their dynamics as we will see in chapter 3.

2.1.5 Mechanical Analogs

The unusual properties of the supercurrent has stimulated the search for mechanical analogs that can be used to better understand the dynamics of the Josephson junction. The first example is a plane mechanical pendulum in a uniform gravity field. Here, the phase difference φ plays the role of the angle of the pendulum with respect to its equilibrium position. The supercurrent corresponds to the torque and the voltage to the angular velocity of the pendulum.

A second useful analog is a particle moving along the coordinate φ with velocity $v \propto d\varphi/dt \propto V$ in a potential given by (2.1.14).

2.2 Short Josephson Junctions

So far we only have considered zero-dimensional Josephson junctions with a spatially homogeneous supercurrent density. These lumped elements we could describe by the integral Josephson current I_s with its maximum value I_c and the gauge-invariant phase difference φ . In this section we relax the condition of spatially homogeneous values of the Josephson current density and the gauge-invariant phase difference and allow now for spatial variations $J_s(\mathbf{r})$ and $\varphi(\mathbf{r})$ of these quantities. We refer to such junctions as *extended Josephson junctions*.

Discussing the physics of extended Josephson junctions we have to distinguish between two cases:

- *Short Josephson junctions:*

For short junctions the magnetic field generated by the Josephson current itself (self-field) is negligible compared to the externally applied magnetic field. We will show that junctions can be considered as short junctions, if the spatial dimensions of the junction area are smaller than a characteristic length scale named ***Josephson penetration depth*** λ_J .

- *Long Josephson junctions:*

For long Josephson junctions the magnetic field generated by the Josephson current itself is no longer negligible. Long Josephson junctions have spatial dimensions larger than the ***Josephson penetration depth*** λ_J .

2.2.1 Short Josephson Junction in an Applied Magnetic Field

We consider the cross section of an extended Josephson junction as sketched in Fig. 2.4. The two junction electrodes are separated by a thin insulating barrier of thickness d . The junction area $L \cdot W$ extends in the yz -plane and the current is flowing in the x -direction. We assume $W, L \gg d$ so that effects of the edges of the junction can be neglected. Each superconducting electrode is assumed to have a thickness t_1 and t_2 much larger than the London penetration depth λ_{L1} and λ_{L2} of the electrode material, respectively. An external magnetic field is applied parallel to the y -direction, that is, $\mathbf{B}_e = (0, B_y, 0)$. Since the applied field penetrates the superconducting electrode up to a thickness given by the London penetration depth, we can define a magnetic thickness of the junction given by $t_B = d + \lambda_{L1} + \lambda_{L2}$.

In order to discuss the effect of the applied magnetic field on the Josephson current density J_s we have to determine the phase shift introduced between positions P and Q along the z -axis separated by an infinitesimal distance dz . The gauge-invariant phase difference between the two points can be determined by considering the line integral along the contour shown in Fig. 2.4. We have to demand that the total phase change along the close contour in $2\pi n$, that is

$$\oint_C \nabla \theta \cdot d\ell = (\theta_{Q_b} - \theta_{Q_a}) + (\theta_{P_c} - \theta_{Q_b}) + (\theta_{P_d} - \theta_{P_c}) + (\theta_{Q_a} - \theta_{P_d}) = n2\pi \quad (2.2.1)$$

For the determination of the different terms we use (compare (1.1.65))

$$\nabla \theta = \frac{2\pi}{\Phi_0} (\Lambda \mathbf{J}_s + \mathbf{A}) \quad (2.2.2)$$

and the gauge-invariant phase difference (compare (1.3.14))

$$\varphi = \theta_2 - \theta_1 - \frac{2\pi}{\Phi_0} \int_1^2 \mathbf{A} \cdot d\ell . \quad (2.2.3)$$

The first and third term in (2.2.1) are the differences across the Josephson junction barrier and directly follow from (2.2.3):

$$\theta_{Q_b} - \theta_{Q_a} = +\varphi(Q) + \frac{2\pi}{\Phi_0} \int_{Q_a}^{Q_b} \mathbf{A} \cdot d\ell \quad (2.2.4)$$

$$\theta_{P_d} - \theta_{P_c} = -\varphi(P) + \frac{2\pi}{\Phi_0} \int_{P_c}^{P_d} \mathbf{A} \cdot d\ell . \quad (2.2.5)$$

The second and fourth term are differences in the superconducting material and are found from the supercurrent equation (2.2.2) for $\nabla\theta$:

$$\theta_{P_c} - \theta_{Q_b} = \int_{Q_b}^{P_c} \nabla\theta \cdot d\ell = +\frac{2\pi}{\Phi_0} \int_{Q_b}^{P_c} \Lambda \mathbf{J}_s \cdot d\ell + \frac{2\pi}{\Phi_0} \int_{Q_b}^{P_c} \mathbf{A} \cdot d\ell \quad (2.2.6)$$

$$\theta_{Q_a} - \theta_{P_d} = \int_{P_d}^{Q_a} \nabla\theta \cdot d\ell = +\frac{2\pi}{\Phi_0} \int_{P_d}^{Q_a} \Lambda \mathbf{J}_s \cdot d\ell + \frac{2\pi}{\Phi_0} \int_{P_d}^{Q_a} \mathbf{A} \cdot d\ell . \quad (2.2.7)$$

Substituting (2.2.4) – (2.2.7) into (2.2.3) yields

$$\varphi(P) - \varphi(Q) = 2\pi n + \frac{2\pi}{\Phi_0} \oint_C \mathbf{A} \cdot d\ell + \frac{2\pi}{\Phi_0} \int_{Q_b}^{P_c} \Lambda \mathbf{J}_s \cdot d\ell + \frac{2\pi}{\Phi_0} \int_{P_d}^{Q_a} \Lambda \mathbf{J}_s \cdot d\ell . \quad (2.2.8)$$

The integration of \mathbf{A} is around a close contour and therefore is equal to the total flux Φ inside the area enclosed by the contour. The integration of \mathbf{J}_s follows the same contour C but excludes the integration over the insulating barrier. We rewrite this integral as an integral along the incomplete contour C' :

$$\oint_{C'} \Lambda \mathbf{J}_s \cdot d\ell = \int_{Q_b}^{P_c} \Lambda \mathbf{J}_s \cdot d\ell + \int_{P_d}^{Q_a} \Lambda \mathbf{J}_s \cdot d\ell . \quad (2.2.9)$$

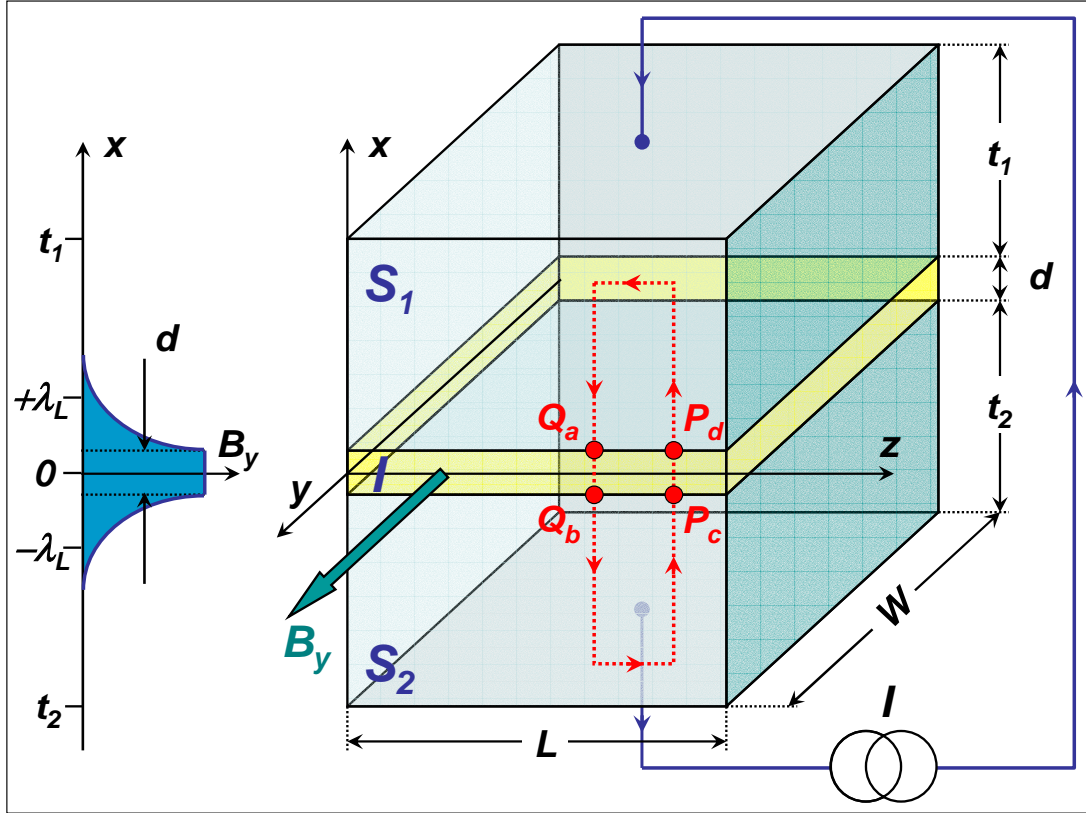


Figure 2.4: Cross section of an extended Josephson junction. The current flows in x -direction, the magnetic field is applied in y -direction. The broken line indicated the closed contour. On the left hand side the decay of the magnetic field in the junction electrodes over the length scale λ_L is indicated.

Then, the difference of the gauge-invariant phase difference between point Q and P is obtained to

$$\varphi(P) - \varphi(Q) = 2\pi n + \frac{2\pi\Phi}{\Phi_0} + \frac{2\pi}{\Phi_0} \oint_{C'} \Lambda \mathbf{J}_s \cdot d\ell . \quad (2.2.10)$$

Discussing the magnitude of the line integral of the current density we can note the following: First, the integration of the current density along one segment of the path in x -direction cancels with the contribution of the adjacent path, which is only an infinitesimal distance dz away. Second, each part of the integration in the z -direction is taken deep inside ($\gg \lambda_L$) the superconducting electrode, where the current density induced by the applied field is exponentially small. Furthermore, the applied current is in the negative x -direction. That is, it is perpendicular to the integration path along z and therefore contributes nothing to the integral of the current density. Therefore, the line integral of the current density vanishes and we obtain

$$\varphi(P) - \varphi(Q) = \frac{2\pi\Phi}{\Phi_0} , \quad (2.2.11)$$

where the phase difference is measured modulo 2π .

Since the magnetic Field decays exponentially into each superconducting electrodes the total flux enclosed by the contour line is

$$\Phi = B_y(d + \lambda_{L1} + \lambda_{L2})dz = B_e t_B \delta z . \quad (2.2.12)$$

Then, with $\varphi(P) - \varphi(Q) = \frac{\partial \varphi}{\partial z} \delta z$ we obtain

$$\frac{\partial \varphi}{\partial z} = \frac{2\pi}{\Phi_0} B_y t_B \quad (2.2.13)$$

We can use a similar argument by choosing point Q and P at an infinitesimal distance dy in the y -direction and obtain

$$\frac{\partial \varphi}{\partial y} = -\frac{2\pi}{\Phi_0} B_z t_B . \quad (2.2.14)$$

In general, we can write

$$\nabla \varphi(\mathbf{r}, t) = -\frac{2\pi}{\Phi_0} t_B [\mathbf{B}(\mathbf{r}, t) \times \hat{\mathbf{x}}] , \quad (2.2.15)$$

where $\hat{\mathbf{x}}$ is the unit vector in x -direction, that is perpendicular to the junction area resp. parallel to the current flow.

Integration of (2.2.13) gives

$$\varphi(z) = \frac{2\pi}{\Phi_0} B_y t_B z + \varphi_0 , \quad (2.2.16)$$

where the integration constant φ_0 is the phase difference at $z = 0$. Using the current-phase relation we obtain the supercurrent density flowing in x -direction to

$$J_s(y, z, t) = J_c(y, z) \sin \left(\frac{2\pi}{\Phi_0} t_B B_y z + \varphi_0 \right) = J_c(y, z) \sin(kz + \varphi_0) \quad (2.2.17)$$

with $k = \frac{2\pi}{\Phi_0} t_B B_y$.

So far we have assumed the the thickness of the junction electrodes is much larger than the London penetration depth. If $t_1 < \lambda_{L1}$ and $t_2 < \lambda_{L2}$ the magnetic field penetrates the complete electrode and the Meißner shielding currents are less than those in thick electrodes. As a result the effective value of the magnetic thickness of the junction increases and the magnetic thickness t_B should be replaced by

$$\tilde{t}_B = d + \lambda_{L1} \coth \frac{t_1}{\lambda_{L1}} + \lambda_{L2} \coth \frac{t_2}{\lambda_{L2}} . \quad (2.2.18)$$

2.2.2 The Fraunhofer Diffraction Pattern

In this subsection we discuss, how the integral current $I_s = \iint J_s(y, z) dy dz$ across the junction depends on the applied magnetic field. We first integrate the maximum Josephson current density $J_c(y, z)$ in the direction of the applied magnetic field. If the external field is in y -direction ($\mathbf{B}_e = (0, B_y, 0)$) we obtain

$$i_c(z) = \int_{-W/2}^{W/2} J_c(y, z) dy . \quad (2.2.19)$$

With this expression we obtain according to (2.2.17)

$$I_s(B_y) = \int_{-L/2}^{L/2} i_c(z) \sin(kz + \varphi_0) dz . \quad (2.2.20)$$

This expression is equivalent to

$$I_s(B_y) = \Im \left\{ e^{i\varphi_0} \int_{-\infty}^{\infty} i_c(z) e^{ikz} dz \right\} , \quad (2.2.21)$$

where $k = \frac{2\pi}{\Phi_0} t_B B_y$. Since $i_c(z)$ is zero outside the junction, i.e. for $|z| > L/2$, we have replaced the integration limits by $\pm\infty$ and obtain

In general, the integral in (2.2.21) is a complex number having both a magnitude and a phase. When the integral is multiplied by $e^{i\varphi_0}$, only the phase but not the magnitude changes. Therefore, the maximum Josephson current I_s^m is just given by the magnitude of the integral, that is by

$$I_s^m(B_y) = \left| \int_{-\infty}^{\infty} i_c(z) e^{ikz} dz \right| . \quad (2.2.22)$$

This integral represents a Fourier integral, that is, the magnetic field dependence of the maximum Josephson current, I_s^m , is given by the Fourier transform of the function $i_c(z)$. This is completely analogous to optics, where the intensity of the light behind a slit of width L and transmission function $i_c(z)$ is given by the Fourier transform of the transmission function.

If the maximum Josephson current density $J_c(y, z)$ of the junction is spatially homogeneous, the magnitude of $i_c(z)$ is constant for $-L/2 \leq z \leq +L/2$ and zero for $|z| > L/2$. In this case the $I_s^m(B_y)$ dependence is equivalent to the diffraction pattern of a slit of width L with constant transmission i_c . The diffraction pattern is the well known **Fraunhofer diffraction pattern** shown by Fig. 2.5:

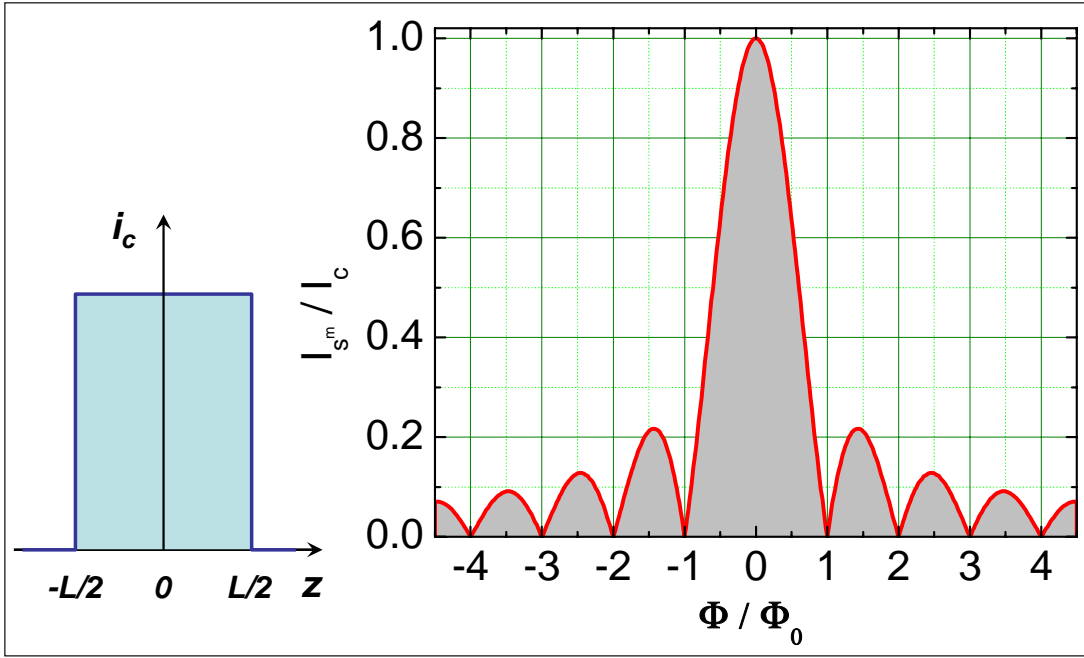


Figure 2.5: Magnetic field dependence of the maximum Josephson current I_s^m of a short Josephson junction. On the left the maximum current density integrated along the magnetic field direction, $i_c(z) = \int J_c(y, z) dy$, is shown for the case of a spatially homogeneous maximum current density $J_c(y, z)$.

$$I_s^m(\Phi) = I_c \left| \frac{\sin \frac{kL}{2}}{\frac{kL}{2}} \right| = I_c \left| \frac{\sin \frac{\pi\Phi}{\Phi_0}}{\frac{\pi\Phi}{\Phi_0}} \right|. \quad (2.2.23)$$

Here, $\Phi = B_y t_b L$ is the flux through the junction and $I_c = i_c L$. We note that the experimental observation of the Fraunhofer diffraction pattern like $I_s^m(\Phi)$ dependence was very important to prove the Josephson tunneling of Cooper pairs. From the experimental point of view it was unclear whether or not the measured supercurrent in a superconductor/insulator/superconductor tunnel junction is flowing as a homogeneous Josephson tunneling current or just through small pinholes in the tunneling barrier. However, if the latter would have been true, no Fraunhofer diffraction pattern would have been observed for the $I_s^m(\Phi)$ dependence.

To understand the shape of the $I_s^m(\Phi)$ dependence we consider the spatial distribution of $i_s(z) = \int J_s(y, z) dy$ along the z -direction for a magnetic field applied in y -direction. For zero field, that is $\Phi = 0$ the gauge-invariant phase difference is constant, $\varphi(z) = \varphi_0$, and hence $i_s(z) = \text{const}$. The maximum Josephson current is obtained for $\varphi_0 = -\pi/2$, that is, $J_s(y, z) = -J_c(y, z)$ (note that the current is flowing in negative x -direction, see Fig. 2.6a). If we feed a current less than the maximum Josephson current through the junction, we have $\varphi \neq \pi/2$ and the local current density is just $J_s(y, z) = J_c(y, z) \sin \varphi_0 < J_c(y, z)$.

We next consider the case of an externally applied magnetic flux of $\Phi = \Phi_0/2$. In this case according to (2.2.16) the gauge-invariant phase difference $\varphi(z)$ varies as

$$\varphi(z) = \frac{2\pi\Phi}{\Phi_0} \frac{z}{L} + \varphi_0 = \frac{\pi z}{L} + \varphi_0. \quad (2.2.24)$$

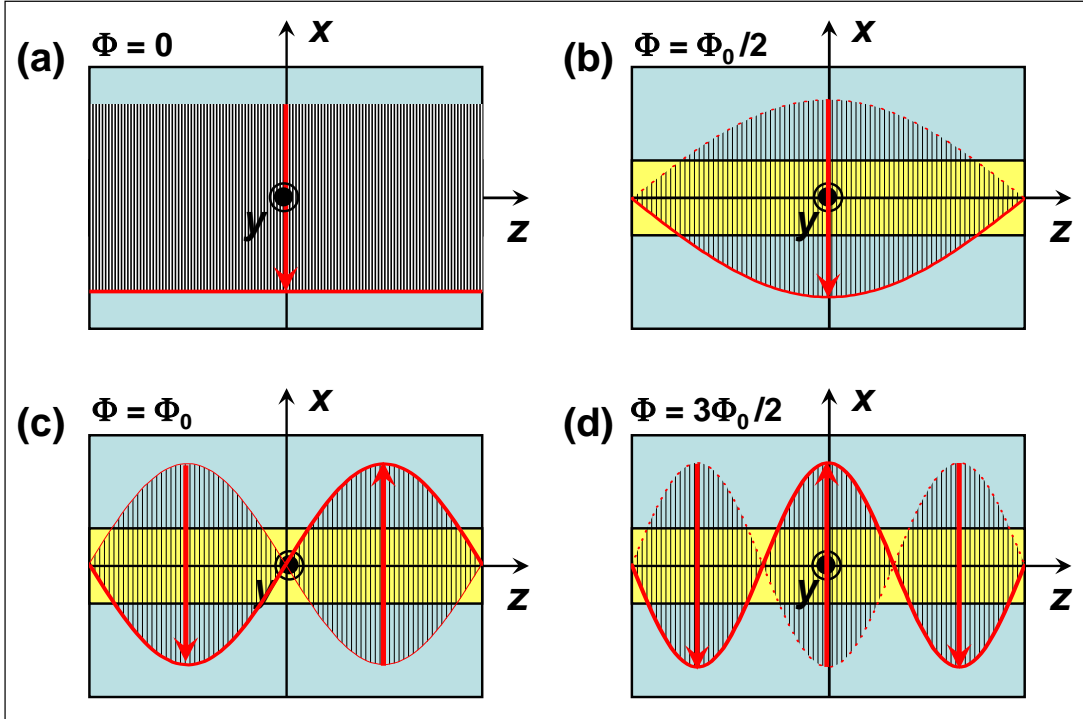


Figure 2.6: The Josephson current density distribution along a small Josephson junction extending from $-L/2$ to $+L/2$ in z -direction. (a) $\Phi = 0$, $\phi_0 = -\pi/2$ (b) $\Phi = \frac{1}{2}\Phi_0$, $\phi_0 = -\pi/2$, (c) $\Phi = \Phi_0$, $\phi_0 = 0$ and (d) $\Phi = \frac{3}{2}\Phi_0$, $\phi_0 = +\pi/2$. The magnetic field is applied in y -direction. The external current is applied in negative x -direction.

Therefore, the supercurrent density varies sinusoidally with z . The difference of the phases between the two edges of the junction is

$$\varphi(L/2) - \varphi(-L/2) = \pi. \quad (2.2.25)$$

That means that half of a full oscillation period fits into the junction. This situation is shown in Fig. 2.6b. Which half period to put into the junction depends on the choice of φ_0 . In Fig. 2.6b we have made the choice $\varphi_0 = -\pi/2$. In this case the phase difference increases from $-\pi$ at $z = -L/2$ to 0 at $z = +L/2$. This choice gives the maximum possible Josephson current I_c^m in negative x -direction. Note that for $\varphi = 0$ we obtain a vanishing total Josephson current.

In Fig. 2.6c and d we show the situation for $\Phi = \Phi_0$ and $\Phi = \frac{3}{2}\Phi_0$, respectively. For $\Phi = \Phi_0$ the total phase difference from one edge of the junction to the other is 2π and a complete oscillation period of the Josephson current density fits into the junction. In this case the total Josephson current is zero irrespective of the choice of φ_0 . For $\Phi = \frac{3}{2}\Phi_0$ the total phase difference from one edge to the other is 3π and one and a half oscillation periods of the Josephson current density fit into the junction. The current from the full period is zero and the total current is determined by a half period. Of course, the total current is smaller than for $\Phi = \Phi_0/2$ when a half period fits the whole junction. This shows that the Josephson current generally tends to decrease with increasing applied magnetic field as shown in Fig. 2.5.

We discuss in more detail the situation for $\Phi = \Phi_0$ shown in Fig. 2.6c. Evidently in this situation the Josephson current density flows in negative and positive x -direction on the left and right side of the junction, respectively. The question is, how the supercurrent density can have such pattern across

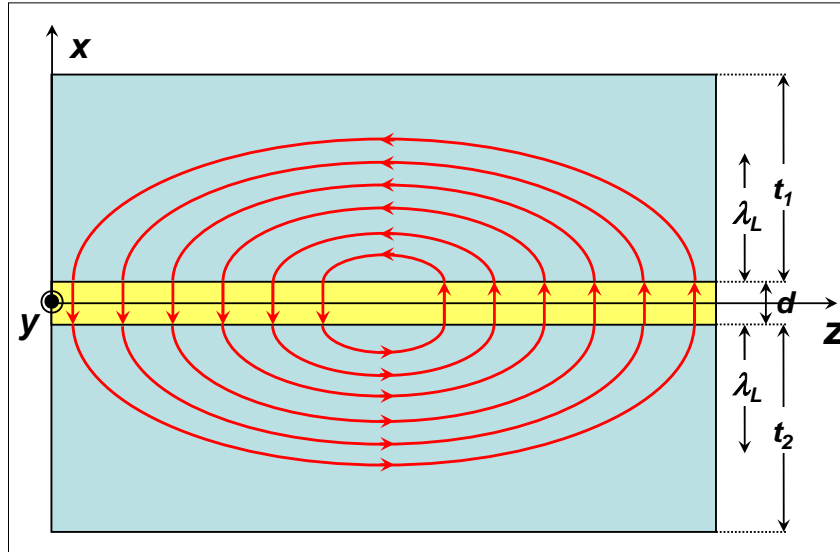


Figure 2.7: The supercurrent distribution in the superconducting electrodes and across the insulator for the case $\Phi = \Phi_0$. The pattern is known as the Josephson vortex.

the insulating barrier and still have no net driving current. The solution is shown in Fig. 2.7. The supercurrent on the left side turns around in the bottom electrode so as to match the supercurrent density in the insulator on the right side. Actually the supercurrent has to bend to avoid the penetration of the applied magnetic field into the electrode material over a length scale larger than the London penetration depth. The resulting supercurrent density pattern resembles the pattern of an Abrikosov vortex in a type-II superconductor and is known as **Josephson vortex**. Note that in contrast to an Abrikosov vortex the Josephson vortex does not need to have a normal core, since the supercurrent density in the center is zero.

Arbitrary Magnetic Field Direction

We consider a short Josephson junction as shown in Fig. 2.4 and let the applied magnetic field lie in an arbitrary direction within the plane of the junction barrier so that

$$\mathbf{B}_e = B_y \hat{\mathbf{y}} + B_z \hat{\mathbf{z}} . \quad (2.2.26)$$

Here, $\hat{\mathbf{y}}$ and $\hat{\mathbf{z}}$ are the unit vector in y - and z -direction. By generalizing the arguments given above, for this situation the magnetic field dependence of the maximum Josephson current can be expressed as

$$I_s^m(\Phi) = I_c \left| \frac{\sin \frac{\pi \Phi_y}{\Phi_0}}{\frac{\pi \Phi_y}{\Phi_0}} \right| \left| \frac{\sin \frac{\pi \Phi_z}{\Phi_0}}{\frac{\pi \Phi_z}{\Phi_0}} \right| , \quad (2.2.27)$$

where $\Phi_y = B_y t_b L$ and $\Phi_z = B_z t_b W$. Equivalently, we can write

$$I_s^m(\mathbf{B}_e) = \left| \int_A J_c(y, z) e^{i\mathbf{k} \cdot \mathbf{r}} dA \right|. \quad (2.2.28)$$

Here, $A = L \cdot W$ is the junction area, \mathbf{r} the position vector in the two-dimensional yz -plane, and dA the differential surface area in that plane.

2.2.3 Determination of the Maximum Josephson Current Density

In real Josephson junctions usually critical current density $J_c(y, z)$ is spatially inhomogeneous due imperfections of the fabrication process or a spatially varying thickness of the tunneling barrier. That is, this quantity usually is not known. Therefore, for researchers fabricating Josephson junctions it would be very desirable to be able to determine the spatial distribution $J_c(y, z)$ experimentally. A suitable method would be the measurement of the $I_s^m(\Phi)$ dependence. However, it is evident from (2.2.22) or (2.2.23) that the distribution $J_c(y, z)$ cannot be derived from the measured $I_s^m(\Phi)$ dependence by performing an inverse Fourier transformation. The reason for that is that in a measurement only the amplitude of the complex function $I_s^m(\Phi)$ is measured but not the phase. Therefore, the back transformation of $I_s^m(\Phi)$ to obtain $i_c(z)$ is not possible.³

By making some assumptions about the properties of the function $i_c(z)$ one can restore $i_c(z)$ approximately from the measured $I_s^m(\Phi)$ dependence. For example, if $i_c(z)$ is symmetrical with respect to the junction midpoint, we obtain

$$i_c(z - L/2) = \frac{1}{\pi} \int_0^\infty |I_s^m(k)| \cos(kz) (-1)^{n(k)} dk, \quad (2.2.29)$$

where $k = \frac{2\pi}{\Phi_0 t_B B_y}$ and n is the number of zeros of $|I_s^m(k)|$ between 0 and k . Analyzing this equation we see that the secondary maximums of the diffraction pattern are increased or reduced, if $i_c(z)$ increases or decreases towards the junction edges, respectively.⁴ Note that $i_c(z)$ is determined by applying the field in y -direction and measuring $I_s^m(\Phi)$. In the same way, we can determine $i_c(y)$ by applying the magnetic field in z -direction and measuring the corresponding $I_s^m(\Phi)$. The two-dimensional distribution $J_c(y, z)$ can be determined by measuring $I_s^m(\Phi)$ for various field directions.

Note that in order to get information on $J_c(y, z)$ on a very small length scale, we have to measure the $I_s^m(\Phi)$ dependence up to high fields. If we could do a Fourier back transformation the spatial resolution would be given by $2\pi/k$. With $k = \frac{2\pi}{\Phi_0 t_B B_y}$ and $\Phi = B_y t_B L$ we obtain

$$\frac{2\pi}{k} = \frac{\Phi_0}{t_B} \frac{1}{B_y} = L \frac{\Phi_0}{\Phi}. \quad (2.2.30)$$

³We note that in principle also the phase can be measured directly using specific junction configurations. However, this has not yet been used in experiments. See e.g. L. D. Jackel, R. A. Buhrman, W. W. Webb, Phys. Rev. **B 10**, 2782 (1974); J. R. Waldrum, J. M. Lumley, Rev. Phys. Appl. **10**, 7 (1975); J. E. Meservey, P. W. Tedrow, D. Paraskevopoulos, IEEE Trans. Magn. **11**, 720 (1975); R. Rifkin, B.S. Deaver, Phys. Rev. **B 13**, 3894 (1976).

⁴A. Barone, G. Paterno, M. Russo, R. Vaglio, Phys. Status Solidi **A 41**, 393 (1977).

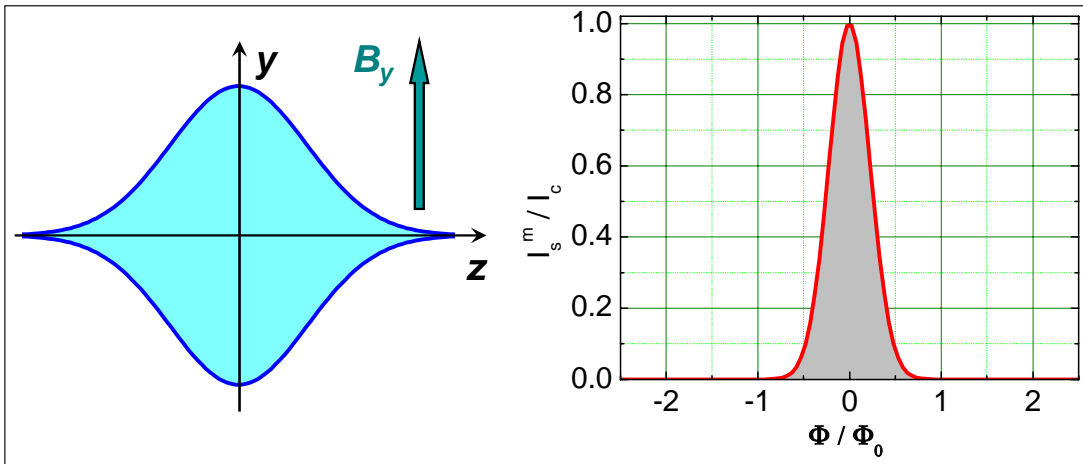


Figure 2.8: Left: Gaussian shaped junction area extending in the yz -plane. For spatially homogeneous $J_c(y, z)$ the current density integrated in y -direction, $i_c(z) = \int J_c(y, z) dy$ corresponds to a Gaussian profile. Right: Magnetic field dependence of the maximum Josephson current as a function of the flux through junction. The magnetic field is applied in y -direction.

We see that the spatial resolution is proportional to $1/B_y$. If we are measuring the $I_s^m(\Phi)$ dependence only up to $\Phi/\Phi_0 = 1$, we obtain a spatial resolution only of the order of the junction length L .

In some applications of Josephson junction (e.g. x-ray detectors) the Josephson current has to be suppressed by an applied magnetic field. Therefore, a $I_s^m(\Phi)$ dependence having only a central maximum and vanishing side lobes is desirable. This can be achieved by generating a $i_c(z)$ dependence that is close to a Gauss profile

$$i_c(z) = i_c(0) \exp\left(-\frac{z^2}{2\sigma^2}\right). \quad (2.2.31)$$

Since the Fourier transform of a Gauss profile again is a Gauss profile, we obtain a $I_s(\Phi)$ dependence that has no side lobes

$$I_s^m(\Phi) = \sqrt{\frac{1}{2\pi}} i_c(0) L \exp(-\sigma k^2) = \sqrt{\frac{1}{2\pi}} i_c(0) L \exp\left(-\sigma \frac{4\pi^2}{L^2} \frac{\Phi^2}{\Phi_0^2}\right). \quad (2.2.32)$$

As shown in Fig. 2.8 a Gaussian profile of $i_c(z)$ can be achieved by not choosing a rectangular shaped junction geometry but a shape that well approaches a Gauss curve. For homogeneous $J_c(y, z)$ then $i_c(z)$ is close to a Gauss profile resulting in a good suppression of the side lobes of the $I_s^m(\Phi)$ curve.

The Supercurrent Auto-correlation Function

We briefly compare the measurement of the maximum Josephson current as a function of an applied magnetic field to an optical diffraction experiment (see Fig. 2.9). In the optical diffraction experiment a plane wave is illuminating an object (e.g. a slide) with a transmission function $P_0(z)$. This transmission

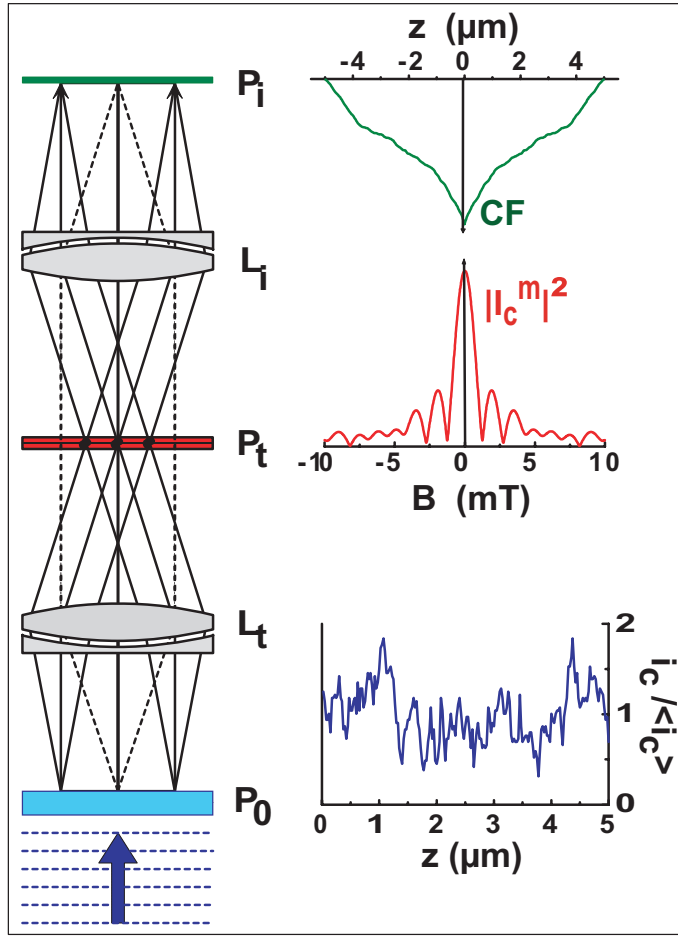


Figure 2.9: Comparison of the measurement of the maximum Josephson Current (right) and an optical diffraction experiment (left). Note that in optics the second Fourier transformation recovers an image P_i of the transmission function P_0 .

function corresponds to the spatial distribution $i_c(z)$ of the maximum Josephson current density integrated along the field direction (y-direction for the situation shown in Fig. 2.9). In the simplest case the transmission function is that of an ideal slit, which is constant inside and zero outside the slit. This would correspond to an ideal rectangular shaped junction with spatially homogeneous $J_c(y, z)$. In the more general case the transmission probability or equivalently $i_c(z)$ may vary along z as shown in Fig. 2.9.

For the optics experiment, the measurement of the $I_c^m(B_y)$ dependence corresponds to the observation of the square root of the light intensity P_t in the focal plane after the first lens system L_t . However, in optics in the focal plane both the amplitude and the phase are recovered and, hence, a back-transformation of P_t can be made by a second lens system L_i resulting in an image P_i of the original transmission function P_0 . This is just the well known optical imaging process. The spatial resolution of this imaging process depends on how many diffraction orders are used for reconstructing the image. In Fig. 2.9 we only have shown the 0th as well as the ±1st order for simplicity. For the $I_c^m(B_y)$ measurement, in principle the same process could be performed, if both the amplitude and the phase of $I_c^m(B_y)$ could be measured. Then, in the imaging process the spatial resolution of the $i_c(z)$ image would be given by the number of side lobes of the diffraction pattern used for the reconstruction process. However, as already discussed above, in an experiment we are only measuring the amplitude of $I_c^m(B_y)$ and not the phase. Therefore, in a second Fourier transformation we can back-transform only the intensity $(I_c^m)^2(B_y)$. As we discuss now,

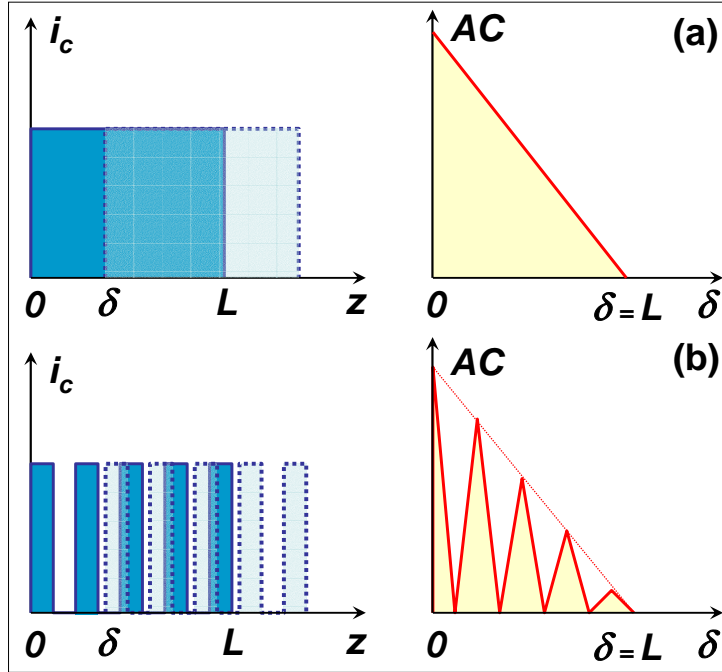


Figure 2.10: (a) The supercurrent auto-correlation function for a ideal slit function $i_c(z)$ obtained for a rectangular shaped Josephson junction with homogeneous critical current density $J_c(y, z)$. (b) The supercurrent auto-correlation function for a periodic function $i_c(z)$. The auto-correlation function shows a modulation with the periodicity of the periodic function.

the Fourier transform of the intensity distribution is just the auto-correlation function of the supercurrent distribution along the junction.

In general, the auto-correlation function is defined as

$$AC(\delta) = \int_{-\infty}^{\infty} i_c(z) i_c(z + \delta) dz . \quad (2.2.33)$$

This expression shows, that the auto-correlation function is just obtained by calculating the overlap between the function $i_c(z)$ and the same function shifted by δ . This is shown in Fig. 2.10a, where we have plotted the auto-correlation function for a simple slit function. It is evident that the auto-correlation function is a linearly decreasing function. If the function $i_c(z)$ is not constant across the width L of the slit but varies strongly as schematically shown in Fig. 2.10b, the auto-correlation function no longer shows a linear decrease but a rich fine structure. Only the envelop shows a linear decay.

Using the **Wiener-Khintchine theorem**⁵ ⁶ we can express the auto-correlation function of the supercurrent distribution $i_c(z)$ in terms of the intensity of the $I_s^m(B_y)$ dependence:

$$AC(\delta) = \int_{-\infty}^{\infty} |I_s^m(k)|^2 e^{ik\delta} dk , \quad (2.2.34)$$

⁵N. Wiener, *Generalized harmonic analysis*, Acta Mathematica **55**, 117 (1930).

⁶A. Khintchine, *Korrelationstheorie der stationären stochastischen Prozesse*, Math. Ann. **109**, 604 (1934).

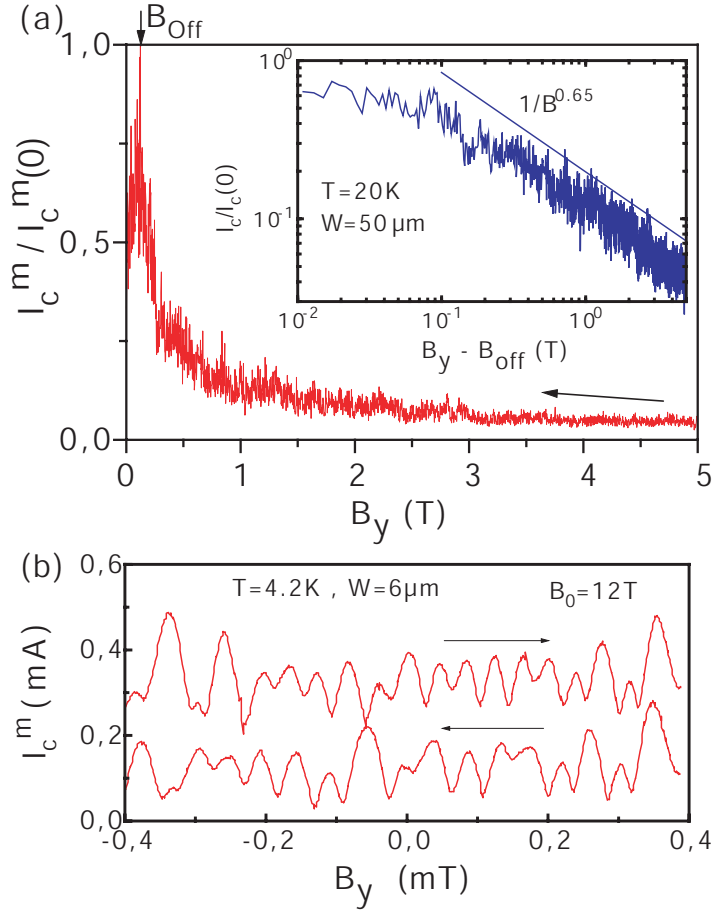


Figure 2.11: (a) I_c^m vs B_y dependence of a $\text{YBa}_2\text{Cu}_3\text{O}_{7-\delta}$ grain boundary Josephson junction recorded for decreasing magnetic field at $T = 20 \text{ K}$. The inset shows I_c^m vs $B_y - B_{\text{off}}$ on a log-log scale. (b) Modulation of I_c^m with varying B_y for opposite sweep directions as indicated by the arrows at a base field $B_0 = 12 \text{ T}$. The curve for increasing field is shifted vertically by $0.2 \mu\text{A}$ for clarity (from O. Fröhlich *et al.*, Appl. Phys. Lett. **66**, 2289 (1995)).

where $k = \frac{2\pi}{\Phi_0} t_B B_y = \frac{1}{L} 2\pi \frac{\Phi}{\Phi_0}$. We immediately see that the spatial information contained in the autocorrelation function depends on the k , or equivalently the magnetic field interval, used in the measurement of the $I_c^m(B_y)$ dependence. According to (2.2.30) we have the spatial resolution $2\pi/k = L \frac{\Phi_0}{\Phi}$. That is, recording the $I_c^m(B_y)$ dependence up to the 100^{th} side lobe (equivalent to $\frac{\Phi_0}{\Phi} = 0.01$) we have a spatial resolution of 0.01 times the junction width.

Note that already the envelop of the $|I_c^m(B_y)|^2$ curve contains valuable statistical information on the supercurrent distribution.⁷ If we have for example inhomogeneities of $i_c(z)$, which have a probability

⁷see e.g. O. M. Fröhlich, H. Schulze, A. Beck, R. Gerdemann, R. Gross, R. P. Huebener, IEEE Trans. Appl. Supercond. **5**, 2188 (1995); O. M. Fröhlich, H. Schulze, A. Beck, B. Mayer, L. Alff, R. Gross, R. P. Huebener, Appl. Phys. Lett. **66**, 2289 (1995).

distribution $p(a) \propto 1/a$, that is, if the probability times the characteristic length scale a of the inhomogeneity is constant, then the envelop of the $|I_c^m(B_y)|^2$ curve follows a $1/B_y$ dependence. Therefore, we speak about “spatial $1/f$ noise”.⁸ The presence of such inhomogeneities can be checked easily in the experiment by plotting $\log |I_s^m(B_y)|^2$ versus $\log B_y$. In such plot one should obtain a straight line with a slope of -1 . If, in contrast, the supercurrent distribution would be formed by a random distribution of filaments of width a , then the envelop of the autocorrelation function should be a constant function up to $k = 2\pi/a$ and then should fall off proportional to $1/B_y^2$. In this case we speak of “spatial shot noise”.⁹ These two examples show that the analysis of the autocorrelation function can yield valuable statistical information on inhomogeneities of the critical current density.

An experimental example is shown in Fig. 2.11. Here, the $I_c^m(B_y)$ dependence of a $\text{YBa}_2\text{Cu}_3\text{O}_{7-\delta}$ grain boundary Josephson junction has been measured up to an applied magnetic field of 5 Tesla. In a $\log |I_s^m(B_y)|$ versus $\log B_y$ plot one obtains a slope of about -0.65 corresponding to $\log |I_s^m(B_y)|^2 \propto 1/B_y^{1.3}$. From this observation one can conclude that there are spatial inhomogeneities in the supercurrent distribution that have a probability distribution $p(a) \propto 1/a^{1.5}$. That is, inhomogeneities with smaller characteristic length scale a have higher probability.

2.2.4 Direct Imaging of the Supercurrent Distribution

Since it is difficult to derive the spatial distribution of the maximum Josephson current density from measurements of $I_c^m(\Phi)$, direct imaging methods have been developed.¹⁰ In these imaging methods the Josephson junction is scanned by a focused electron or laser beam and the change $\delta I_c^m(y, z)$ of the maximum Josephson current is measured as a function of the beam position (y, z) . As discussed in more detail in Appendix B, the measured change $\delta I_c^m(y, z)$ of the global junction current in first approximation is directly proportional to the local critical current density $J_c(y, z)$. Hence, by scanning the junction and measuring $\delta I_c^m(y, z)$ simultaneously, a two-dimensional image of $J_c(y, z)$ is obtained.

The local perturbation of the focused electron or laser beam can be modelled in most cases by a local thermal heating effect. Therefore, the spatial resolution of the imaging technique is not determined by the diameter of the focused electron or laser beam but by the so-called thermal healing length, which determines the diameter of the heated sample region. Typically, for superconducting thin film structures this length scale is of the order of $1 \mu\text{m}$.

2.2.5 Small Josephson Junction: Energy Considerations

After having found the spatial distribution of the maximum Josephson current density we now discuss the energy E associated with a short Josephson junction. Doing so, we derive a criterion for the notation “short”. We will see that short means smaller than a characteristic length scale λ_J , the ***Josephson penetration depth***.

The junction energy is given by the sum

⁸In the analysis of fluctuating time signals one is plotting the intensity of the Fourier transform of the time signal (the power spectral density S) versus frequency and often obtains a $1/f$ dependence. This is the signature of so-called $1/f$ noise that is ubiquitous in nature. The power spectral density $S(f)$ corresponds to $|I_c^m(B_y)|^2$.

⁹In the analysis of time signals the random appearance of spikes of constant width δt is known to appear due to the discrete nature of physical quantities (e.g. the electronic charge in charge transport). The resulting noise is called shot noise. This noise is white, that is frequency independent, up to high frequencies $f \propto 1/\delta t$ and then falls off as $1/f^2$.

¹⁰for a review see *Low Temperature Scanning Electron Microscopy of Superconducting Thin Films and Josephson Junctions*, R. Gross, D. Kölle, Reports on Progress in Physics **57**, 651-741 (1994).

$$E = E_S + E_I , \quad (2.2.35)$$

where E_S is the energy stored in the superconducting electrodes and E_I the energy stored in the insulating barrier. The energy stored in the superconducting electrodes is the sum of the magnetic field energy and the kinetic energy of the superelectrons. It is given by

$$E_S = \frac{1}{2\mu_0} \int_{V_s} (\mathbf{B}^2 + \mu_0 \Lambda \mathbf{J}_s^2) dV , \quad (2.2.36)$$

where the integration is over the superconducting volume V_s . This expression, which can be derived from the first London equation, is not valid for the insulating barrier. Here, instead of the kinetic energy of the superelectrons we have to use the Josephson coupling energy E_J . We obtain

$$E_I = \frac{1}{2\mu_0} \int_{V_i} \mathbf{B}^2 dV + \int_{V_i} \frac{1}{d} \frac{E_J}{A_i} dV . \quad (2.2.37)$$

Here, $V_i = A_i \cdot d$ is the volume of the insulator with A_i the junction area and d the barrier thickness. With $E_J/A_i = \frac{\Phi_0 J_c}{2\pi} (1 - \cos \varphi)$ (compare (2.1.8)) we obtain

$$E_I = \frac{1}{2\mu_0} \int_{V_i} \mathbf{B}^2 dV + \int_{A_i} \frac{\Phi_0 J_c(y, z)}{2\pi} (1 - \cos \varphi(z)) dy dz . \quad (2.2.38)$$

Here, the second term has been integrated over the barrier thickness d thus leaving only an integral over the junction area A_i extending in the yz -plane.

With (2.2.36) and (2.2.38) we obtain the total energy

$$E = \frac{1}{2\mu_0} \int_{V_s+V_i} \mathbf{B}^2 dV + \frac{1}{2} \int_{V_s} \Lambda \mathbf{J}_s^2 dV + \int_{A_i} \frac{\Phi_0 J_c(y, z)}{2\pi} (1 - \cos \varphi(z)) dy dz . \quad (2.2.39)$$

We are now able to give a definition of a short junction by comparing the different energy contributions. We will call a junction short, if the energy E_B stored in the junction due to the external field (first and second term on the right hand side) is much larger than the energy E_J due to the flowing currents (third term on the right hand side), that is $E_B \gg E_J$.

We first consider E_B given by the first two integrals in (2.2.39). If the thickness of the superconducting electrodes is larger than the London penetration depth, the first integral dominates so that

$$E_B = \frac{1}{2\mu_0} \int_{V_s+V_i} \mathbf{B}^2 dV . \quad (2.2.40)$$

Note that the magnetic flux density penetrates the superconducting electrodes only up to a length given by the London penetration depth. Therefore, the integration volume is given by $W \cdot L \cdot (d + 2\lambda_L) = A_i \cdot t_B$ (compare Fig. 2.4). Therefore, we obtain

$$E_B = \frac{1}{2\mu_0} B_y^2 WL t_B = \frac{1}{2\mu_0} \frac{\Phi^2 W}{t_B L} , \quad (2.2.41)$$

where we have used $\Phi = B_y L t_B$.

We next consider the energy due to the currents in the junction given by the last integral in (2.2.39). If we assume for simplicity a spatially homogeneous $J_c(y, z)$, we obtain

$$\begin{aligned} E_J &= \frac{\Phi_0 I_c}{2\pi} - \int_{-W/2}^{W/2} \int_{-L/2}^{L/2} \frac{\Phi_0 J_c(y, z)}{2\pi} \cos \varphi(z) dy dz \\ &= \frac{\Phi_0 I_c}{2\pi} - \int_{-L/2}^{L/2} \frac{\Phi_0 i_c(z)}{2\pi} \cos \varphi(z) dz = \frac{\Phi_0 I_c}{2\pi} - \frac{\Phi_0 I_c}{2\pi} \frac{\sin \frac{\pi \Phi}{\Phi_0}}{\frac{\pi \Phi}{\Phi_0}} \cos(\varphi(0)) , \end{aligned} \quad (2.2.42)$$

where we have used $\varphi(z) = \frac{2\pi\Phi}{\Phi_0} \frac{z}{L} + \varphi_0$ (compare (2.2.24)).

Comparing E_J and E_B for the typical flux of one flux quantum in the junction area, the condition $E_B \gg E_J$ can be written as

$$\frac{1}{2\mu_0} \frac{\Phi_0^2 W}{t_B L} \gg \frac{\Phi_0 I_c}{2\pi} . \quad (2.2.43)$$

With the critical current density $J_c = I_c/WL$ this inequality can be expressed as

$$L \ll \tilde{\lambda}_J \equiv \sqrt{\frac{\pi\Phi_0}{\mu_0 J_c t_B}} . \quad (2.2.44)$$

Hence, a junction is considered short, if its length L is small compared to the characteristic length scale $\tilde{\lambda}_J$. This length is equal to the so-called **Josephson penetration depth** λ_J introduced in section 2.3 within a factor of the order of unity. In the discussion of long Josephson junctions in section 2.3 we will see, how λ_J is entering the equations describing these junction as a natural length scale.

2.2.6 The Motion of Josephson Vortices

Above we have seen that vortices can be used to visualize the Josephson current density in a current driven junction. We now discuss the situation, where Josephson vortices are moving along the junction in z -direction at a constant velocity v_z .

For a short Josephson junction the magnetic field due to the Josephson current density itself can be neglected compared to the external field and we can therefore assume that the flux density in the junction is given by the external field $\mathbf{B}_e = (0, B_y, 0)$. Hence, the gauge-invariant phase difference must satisfy equation (2.2.14):

$$\frac{\partial \varphi}{\partial y} = \frac{2\pi}{\Phi_0} B_y t_B . \quad (2.2.45)$$

Due to the motion of the vortices a temporal change of the phase difference at a specific position is obtained. Since the passage of a complete vortex with flux content Φ_0 changes the phase difference by 2π we can write

$$\frac{\partial \varphi}{\partial t} = \frac{2\pi}{\Phi_0} \frac{\partial \Phi}{\partial t} . \quad (2.2.46)$$

With the magnetic flux given by $\Phi = B_y t_B z$ we obtain

$$\frac{\partial \varphi}{\partial t} = \frac{2\pi}{\Phi_0} B_y t_B \frac{\partial z}{\partial t} = \frac{2\pi}{\Phi_0} B_y t_B v_z . \quad (2.2.47)$$

The solution to (2.2.45) and (2.2.47) is

$$\varphi(z, t) = \frac{2\pi}{\Phi_0} B_y t_B (z - v_z t) + \varphi(0) . \quad (2.2.48)$$

That is, the gauge-invariant phase difference is increasing linearly in space and time. This situation is shown in Fig. 2.12a, where we have plotted $\varphi(z)$ for several fixed times. In order to obtain the temporal and spatial evolution of the Josephson current density, we have to use the current-phase relation and obtain

$$J_s(y, z, t) = J_c(y, z) \sin \varphi [k(z - v_z t)] . \quad (2.2.49)$$

Comparing (2.2.49) to (2.2.17) shows that the current density through the junction has the same spatial pattern as for the stationary vortices but the pattern itself moves at a constant velocity v_z according to our assumption (see Fig. 2.12b).

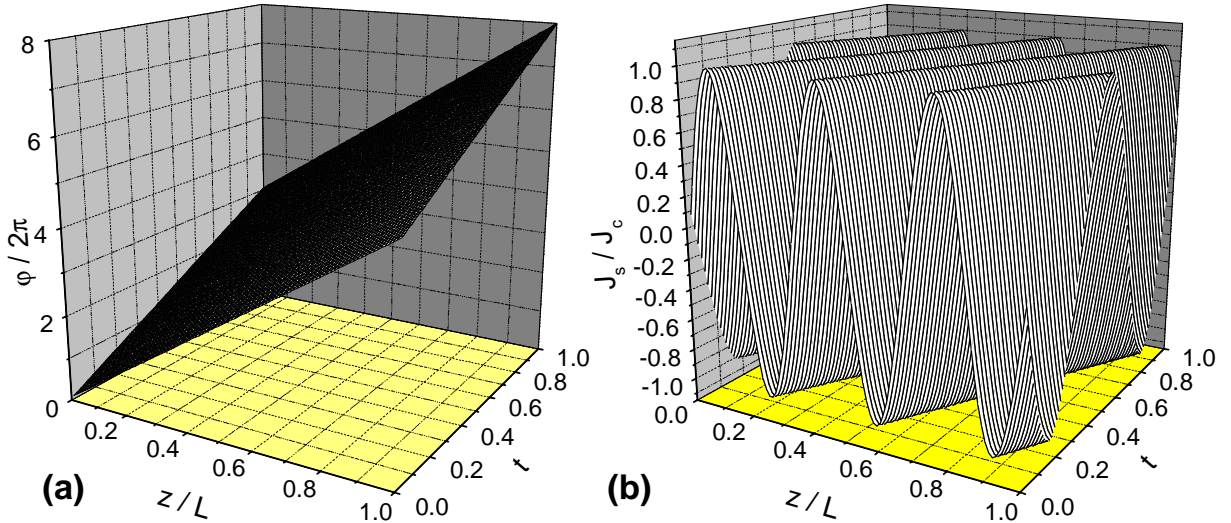


Figure 2.12: (a) The linear increase of the gauge-invariant phase difference along the junction and with increasing time. (b) The corresponding Josephson current density J_s along the junction as a function of time.

The current density pattern can be considered as a vortex with a period $p = L\frac{\Phi_0}{\Phi}$. That is, if the flux in the junction corresponds to one flux quantum, $\Phi = \Phi_0$, the period is L . For $\Phi > \Phi_0$ and $\Phi < \Phi_0$ the period is smaller and larger than the junction length L , respectively. With the period p we can define the number of vortices in the junction as

$$N_V = \frac{L}{p} = \frac{\Phi}{\Phi_0} . \quad (2.2.50)$$

The amount $\Delta\varphi$ the gauge-invariant phase difference changes along the junction is given by

$$\Delta\varphi = 2\pi \frac{\Phi}{\Phi_0} = 2\pi N_V . \quad (2.2.51)$$

That is, the change of φ is just given by 2π times the number of vortices in the junction. We can now consider the rate, at which vortices are passing the junction. This rate is given by

$$\frac{dN_V}{dt} = \frac{1}{2\pi} \frac{d\Delta\varphi}{dt} . \quad (2.2.52)$$

Since according to the voltage-phase relation a temporal change of the gauge-invariant phase difference is equal to $\frac{2\pi}{\Phi_0}V$, where V is the junction voltage, we obtain

$$\frac{dN_V}{dt} = \frac{V}{\Phi_0} . \quad (2.2.53)$$

That is, the constant motion of the vortices across the junction is causing a constant junction voltage that is proportional to the rate, at which vortices are moving across the junction. We note that this relationship is completely analogous to the motion of Abrikosov vortices across a type-II superconductor perpendicular to the current direction resulting in the so-called flux-flow voltage.

2.3 Long Josephson Junctions

In section 2.2 we have neglected the self-field effect by the Josephson current density. This is possible only if the spatial dimensions W, L of the junction are small compared to the Josephson penetration depth. In this section we will relax this assumption and discuss long Josephson junctions with spatial dimensions larger than the Josephson penetration depth.

2.3.1 The Stationary Sine-Gordon Equation

We again consider the junction geometry shown in Fig.2.4. We also note that the derivation of expression (2.2.15) describing the spatial variation of the gauge-invariant phase difference due to a magnetic flux density is general. That is, for the geometry shown in Fig.2.4 with the external magnetic field applied parallel to the y -direction we can write

$$\frac{\partial \varphi}{\partial z} = \frac{2\pi}{\Phi_0} B_y t_B . \quad (2.3.1)$$

However, in contrast to short junctions now the magnetic flux density results both from the externally applied field **and** the Josephson current density and must satisfy Ampère's law. With $\mathbf{B} = \mu_0 \mathbf{H}$ and $\mathbf{D} = \epsilon_0 \mathbf{E}$ we obtain

$$\nabla \times \mathbf{B} = \mu_0 \mathbf{J} + \epsilon \epsilon_0 \mu_0 \frac{\partial \mathbf{E}}{\partial t} . \quad (2.3.2)$$

Here, μ_0 and ϵ_0 are the permeability and permittivity in vacuum, respectively, and ϵ is the dielectric constant of the barrier material.

As in section 2.2 we only consider the zero voltage state, that is, we have $\partial \mathbf{E} / \partial t = 0$. Then, for the geometry of Fig.2.4 Ampère's law gives

$$\frac{\partial B_y(z)}{\partial z} = -\mu_0 J_x(z) . \quad (2.3.3)$$

With this expression we can write the spatial derivative of (2.3.1) as

$$\frac{\partial^2 \varphi(z)}{\partial z^2} = -\frac{2\pi t_B}{\Phi_0} \frac{\partial B_y(z)}{\partial z} = -\frac{2\pi \mu_0 t_B}{\Phi_0} J_x(z) . \quad (2.3.4)$$

Assuming that $J_c(y, z) = \text{const}$ and remembering that the current is flowing in negative x -direction, that is, $J_x(y, z) = -J_s(y, z)$ so that $J_x(z) = -J_c \sin \varphi(z)$ expression (2.3.4) can be rewritten as

$$\frac{\partial^2 \varphi(z)}{\partial z^2} = \frac{2\pi\mu_0 t_B J_c}{\Phi_0} \sin \varphi(z) = \frac{1}{\lambda_J^2} \sin \varphi(z) \quad (2.3.5)$$

$$\lambda_J \equiv \sqrt{\frac{\Phi_0}{2\pi\mu_0 t_B J_c}}. \quad (2.3.6)$$

Here, λ_J is the ***Josephson penetration depth***, which is equal to the characteristic length scale $\tilde{\lambda}_J$ derived in section 2.2 (see (2.2.44)) within a factor of the order unity. Equation (2.3.5) shows that the gauge-invariant phase difference follows a nonlinear differential equation called ***stationary Sine-Gordon equation*** (SSGE).¹¹ Formally, solutions of this equation can be expressed in terms of elliptic Jacobi functions.¹² A typical boundary problem for this equation admits, however, several such solutions and only some of them can be realized. In many situations, the stationary Sine-Gordon equation has to be solved numerically.

We close this subsection by emphasizing that for a two-dimensional junction we have the two-dimensional ***stationary Sine-Gordon equation***

$$\frac{\partial^2 \varphi(y)}{\partial y^2} + \frac{\partial^2 \varphi(z)}{\partial z^2} = \frac{1}{\lambda_J^2} \sin \varphi(y, z). \quad (2.3.7)$$

Analytical Solutions of the SSGE

We consider a few simple cases where we can solve the SSGE (2.3.5) analytically. First we note that we can linearize (2.3.5) for small arguments. Then, with $\sin \varphi \simeq \varphi$ we have

$$\frac{\partial^2 \varphi(z)}{\partial z^2} = \frac{1}{\lambda_J^2} \varphi(z) \quad (2.3.8)$$

with the solution

$$\varphi(z) = \varphi(0) e^{-z/\lambda_J}. \quad (2.3.9)$$

Then, from (2.3.1) we obtain for the magnetic field $B_y(z)$ along the junction to

$$B_y(z) = -\frac{\varphi(0)}{2\pi} \frac{\Phi_0}{\lambda_J t_B} e^{-z/\lambda_J}. \quad (2.3.10)$$

¹¹J. Rubinstein, J. Math. Phys. **11**, 258 (1970).

¹²I.O. Kulik, Sov. Phys. JETP **51**, 1952 (1966); C.S. Owen, D.J. Scalapino, Phys. Rev. **164**, 538 (1967).

This expression shows that λ_J is a decay length for the magnetic field justifying the expression penetration depth.

With $\frac{\partial B_y(z)}{\partial z} = -\mu_0 J_x(z)$ we obtain for the current flowing at the edges of the junction

$$J_x(z=0) = \frac{1}{\lambda_J} \frac{B_y(z=0)}{\mu_0} . \quad (2.3.11)$$

Since the junction can stay in the Meißner state as long as $J_x \leq J_c$, Meißner solutions are possible for

$$B_y(z=0) \leq \mu_0 J_c \lambda_J . \quad (2.3.12)$$

We next consider the case of a small junction with $L \ll \lambda_J$. Equation (2.3.5) can then be approximated by $\frac{\partial^2 \varphi(z)}{\partial z^2} \simeq 0$ resulting in $\frac{\partial \varphi(z)}{\partial z} \simeq \text{const}$. That is, we obtain the well known result of the short junction. Note that according to (2.3.4) the approximation $\frac{\partial^2 \varphi(z)}{\partial z^2} \simeq 0$ is equivalent to neglecting the self-field effect of the current. This again demonstrates that the condition for a short junction is equivalent to the assumption of neglecting self-fields.

2.3.2 The Josephson Vortex

A possible solution of the SSGE is the particular solution

$$\varphi(z) = \pm 4 \arctan \left\{ \exp \left(\frac{z-z_0}{\lambda_J} \right) \right\} + 2\pi n \quad (2.3.13)$$

which can be verified by substitution into (2.3.5). The corresponding magnetic field can be found from (2.3.1) to

$$B_y(z) = \pm \frac{\Phi_0}{\pi \lambda_L t_B} \frac{1}{\cosh \left(\frac{z-z_0}{\lambda_J} \right)} . \quad (2.3.14)$$

The Josephson current density is obtained from (2.3.3) to

$$J_x(z) = -J_s(z) = \pm \frac{\Phi_0}{\pi \mu_0 \lambda_L^2 t_B} \frac{\sinh \left(\frac{z-z_0}{\lambda_J} \right)}{\cosh \left(\frac{z-z_0}{\lambda_J} \right)} \quad (2.3.15)$$

$$= \pm 2J_c \frac{\sinh \left(\frac{z-z_0}{\lambda_J} \right)}{\cosh \left(\frac{z-z_0}{\lambda_J} \right)} . \quad (2.3.16)$$

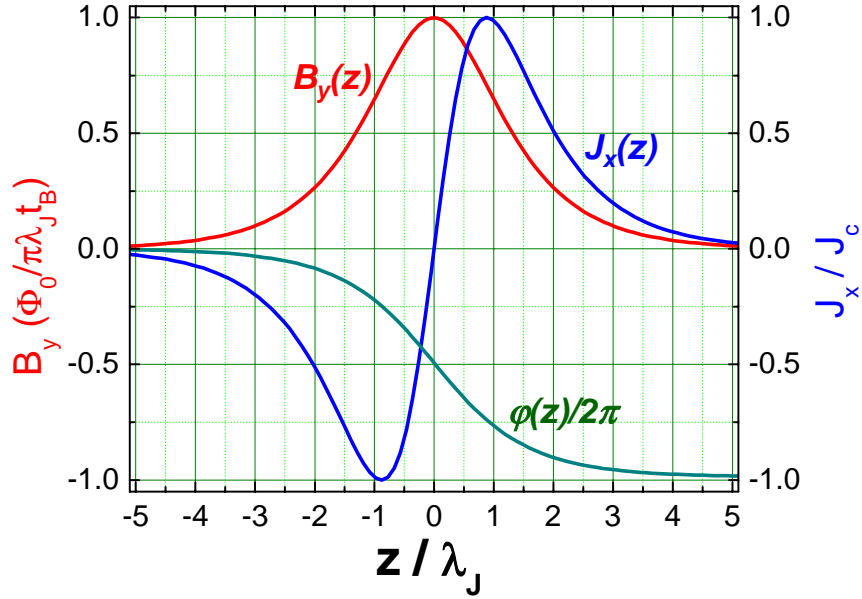


Figure 2.13: Magnetic flux and current density distribution as well as the variation of the gauge-invariant phase difference for a the Josephson vortex solution of the stationary Sine-Gordon equation.

Note that for a general solution of a differential equation we not only have to know the particular solution but also the homogeneous solutions in order to match the boundary conditions. However, we will restrict ourselves here to those cases where only the particular solution is needed.

A particularly important example is the case where the origin is chosen at z_0 and $\varphi(z)$ is chosen to vanish at $z = \pm\infty$ in a junction of infinite length. In this case the particular solution is the full solution satisfying the boundary conditions. The corresponding magnetic field and current distribution is shown in Fig. 2.13. The magnetic field and the Josephson current density decay with the characteristic length scale λ_J . Interestingly, the Josephson current density does not have a maximum at the position where the magnetic field has its maximum. Integrating the magnetic flux density and the current density along the junction we see that the total Josephson current is zero and the total flux is equal to Φ_0 . That is, we have a situation similar to that shown in Fig. 2.6c and Fig. 2.7. Therefore, we can interpret this special solution of the SSGE as a **Josephson vortex** in a long Josephson junction. The different signs in (2.3.13) – (2.3.16) correspond to different orientations or polarizations of the vortex. It is evident that the Josephson vortex is confined to a length of the order of the Josephson penetration depth λ_J .

Energy of the Josephson Vortex Solution

As we have done for a short junction, we can calculate the energy E for a long Josephson junction. In fact the expression (compare (2.2.39))

$$E = \frac{1}{2\mu_0} \int_{V_s+V_i} \mathbf{B}^2 dV + \frac{1}{2} \int_{V_s} \Lambda \mathbf{J}_s^2 dV + \int_{A_i} \frac{\Phi_0 J_c(y, z)}{2\pi} (1 - \cos \varphi(z)) dy dz \quad (2.3.17)$$

also holds for long Josephson junctions with the energy (compare (2.2.36))

$$E_s = \frac{1}{2\mu_0} \int_{V_s} (\mathbf{B}^2 + \mu_0 \Lambda \mathbf{J}_s^2) dV \quad (2.3.18)$$

stored in the superconductor and the energy (compare (2.2.38))

$$E_I = \frac{1}{2\mu_0} \int_{V_i} \mathbf{B}^2 dV + \int_{A_i} \frac{\Phi_0 J_c(y, z)}{2\pi} (1 - \cos \varphi(z)) dy dz . \quad (2.3.19)$$

stored in the insulator.

We are now calculating the stored energy for the vortex solution of the long junction. Here we again assume that the junction electrodes are much thicker than the London penetration depth so that in the expression for E_s the first term dominates. Then we have

$$E = \frac{1}{2\mu_0} \int_{V_s+V_i} \mathbf{B}^2 dV + \int_{A_i} \frac{\Phi_0 J_c(y, z)}{2\pi} (1 - \cos \varphi(z)) dy dz . \quad (2.3.20)$$

Using $\partial \varphi / \partial z = 2\pi B_y t_B / \Phi_0$ to express the magnetic flux density B_y in terms of the gauge-invariant phase difference φ we obtain after integrating over y and x ¹³

$$E = \frac{\Phi_0 J_c W}{2\pi} \int_{-\infty}^{\infty} \left\{ \frac{1}{2} \lambda_J^2 \left(\frac{\partial \varphi(z)}{\partial z} \right)^2 + (1 - \cos \varphi(z)) \right\} dz . \quad (2.3.21)$$

With the expression (2.3.13) for $\varphi(z)$ we can now calculate the energy stored in the vortex solution. In order to do so we use the trigonometric identity $1 - \cos \varphi = 2 \sin^2(\varphi/2)$. With $\varphi(z) = 4 \arctan \left\{ \exp \left(\frac{z-z_0}{\lambda_J} \right) \right\} = -2 \sin^{-1}(1/\cosh(z/\lambda_J))$ we obtain

$$1 - \cos \varphi(z) = 2 \frac{1}{\cosh^2 \left(\frac{z}{\lambda_J} \right)} . \quad (2.3.22)$$

Furthermore, the first term in the integral can be simplified by using (2.3.14):

¹³We obtain $B_y^2 / 2\mu_0 = (\partial \varphi / \partial z)^2 \Phi_0^2 / 8\pi^2 t_B^2 \mu_0 = (\partial \varphi / \partial z)^2 (\Phi_0 J_c / 2\pi t_B) \frac{1}{2} \lambda_J^2$. Integration over y gives just the junction width W and integration over x gives the magnetic thickness t_B . That is $\iint (\Phi_0 J_c / 2\pi t_B) \frac{1}{2} \lambda_J^2 dx dy = (\Phi_0 J_c W / 2\pi) \frac{1}{2} \lambda_J^2$.

$$\frac{1}{2} \lambda_J^2 \left(\frac{\partial \varphi}{\partial z} \right)^2 = 2 \frac{1}{\cosh^2 \left(\frac{z}{\lambda_J} \right)} . \quad (2.3.23)$$

Hence, we obtain

$$E = \frac{\Phi_0 J_c W}{\pi} \int_{-\infty}^{\infty} \frac{1}{\cosh^2 \left(\frac{z}{\lambda_J} \right)} dz = \frac{4\Phi_0 J_c W \lambda_J}{\pi} . \quad (2.3.24)$$

With this expression we can write down the energy per unit length of the Josephson vortex to

$$E_{\text{Vortex}} = \frac{E_I}{W} = \frac{4\Phi_0 J_c \lambda_J}{\pi} . \quad (2.3.25)$$

Note that the energy of the vortex is positive. That is, its formation is impossible without external fields and/or currents.

With expression (2.3.25) for the vortex energy per unit length we can find the magnetic flux density B_{c1} at which the vortex will first enter the junction in complete analogy to the lower critical field of a type-II superconductor.¹⁴ For a type-II superconductor the lower critical field is given by

$$B_{c1} = \frac{1}{\mu_0} \frac{E_{\text{Vortex}}}{\Phi_0} . \quad (2.3.26)$$

Hence, in analogy the lower critical field of a long Josephson junction is

$$B_{c1} = \frac{4\mu_0 J_c \lambda_J}{\pi} = \frac{4\Phi_0}{\pi^2 \lambda_J t_B} . \quad (2.3.27)$$

This result can be understood intuitively. B_{c1} is just about the magnetic flux density of a single flux quantum distributed over an area $t_B \cdot \lambda_J$.

¹⁴see e.g. T. P. Orlando, K. A. Delin, *Foundations of Applied Superconductivity*, Addison-Wesley, New York (1991); section 6.5.

2.3.3 Junction Types and Boundary Conditions

If we consider the stationary Sine-Gordon equation (SSGE) we see that only the properties of the tunneling barrier (barrier thickness d or equivalently J_c) and the junction electrodes (London penetration depth λ_L) are entering. In contrast, the geometry of the junction electrodes are not entering the differential equation. However, the geometry of the junction electrodes determine how the current is flowing into the junction area and therefore is entering the boundary conditions.

In order to solve the SSGE we have to know the magnetic flux density at the edges of the junction. That is, we have to know the boundary conditions

$$\frac{\partial \varphi}{\partial z} \Big|_{z=0} = \frac{2\pi t_B}{\Phi_0} B_y \Big|_{z=0} \quad (2.3.28)$$

$$\frac{\partial \varphi}{\partial z} \Big|_{z=L} = \frac{2\pi t_B}{\Phi_0} B_y \Big|_{z=L} \quad (2.3.29)$$

$$\frac{\partial \varphi}{\partial y} \Big|_{y=0} = -\frac{2\pi t_B}{\Phi_0} B_z \Big|_{y=0} \quad (2.3.30)$$

$$\frac{\partial \varphi}{\partial y} \Big|_{y=W} = -\frac{2\pi t_B}{\Phi_0} B_z \Big|_{y=W}. \quad (2.3.31)$$

The main problem is that the magnetic flux density is determined by both the external applied flux density \mathbf{B}^{ex} **and** the flux density \mathbf{B}^{el} of the current density in the junction electrodes:

$$\mathbf{B} = \mathbf{B}^{ex} + \mathbf{B}^{el}. \quad (2.3.32)$$

In contrast to short junctions we no longer can neglect \mathbf{B}^{el} . Unfortunately, in many cases the geometry of the junction electrodes is complicated and, hence, it is difficult to calculate the magnetic flux density at the junction edges. Moreover, the current density distribution in the junction electrodes is determined by the spatial distribution of the Josephson current density itself. That is, the boundary conditions depend on the solution of the SSGE itself. Therefore, in many cases numerical iteration methods have to be used to solve the SSGE.¹⁵

In the following we discuss the boundary conditions for a few simple one-dimensional junction geometries. Here, one-dimensional means that the junction dimension in one direction (the y -direction in the following) is much smaller than the Josephson penetration depth. Then, for this junction direction self-field effects of the current can be usually neglected. In the following subsections we classify the junctions into three main types, namely

- *overlap junctions,*

¹⁵see e.g. *Calculation of the Josephson Current Distribution in Two-dimensional Tunnel Junctions*, J. Mannhart, J. Bosch, R. Gross, R. P. Huebener, Phys. Lett. **A 121**, 241 (1987); *Spatial Distribution of the Maximum Josephson Current in Superconducting Tunnel Junctions*, J. Mannhart, J. Bosch, R. Gross, R. P. Huebener, J. Low Temp. Phys. **70**, 459 (1988); *Nonlocal Response of Grain Boundary Type Josephson Junctions to Local Perturbation*, B. Mayer, H. Schulze, G. M. Fischer, R. Gross, Phys. Rev. **B 52**, 7727 (1995).

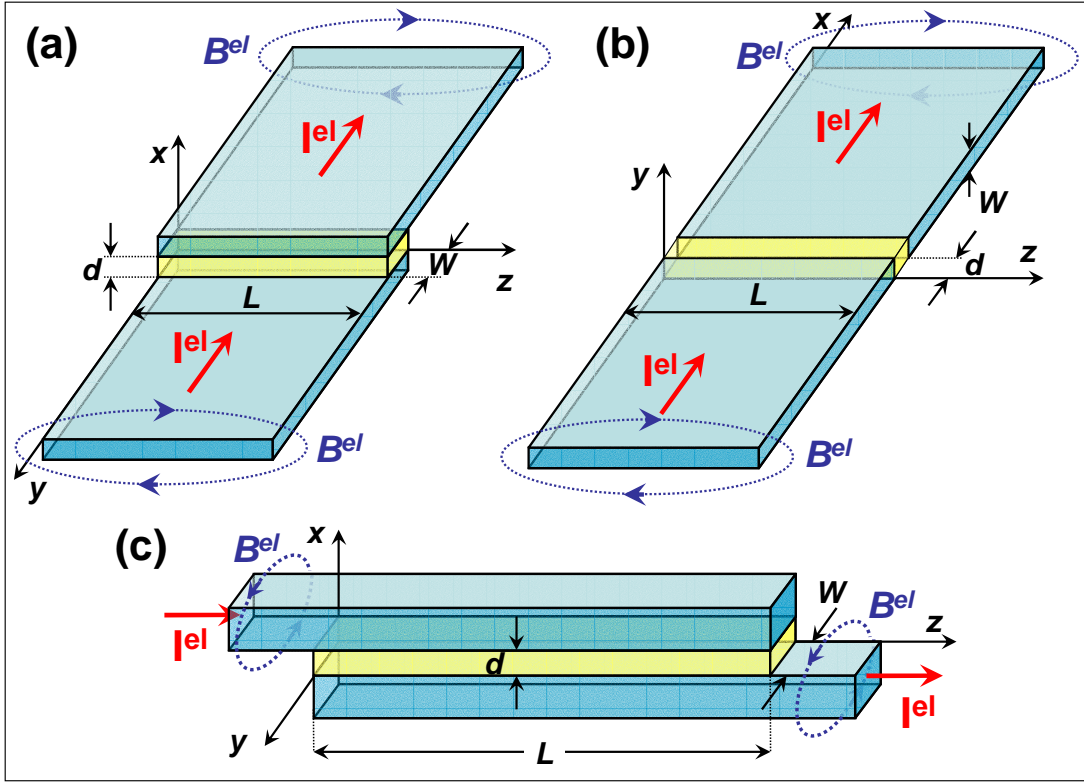


Figure 2.14: The geometry of the overlap (a), the grain boundary (b) and the inline Josephson junction. The junction plane always extends in the yz -plane. The width W of the junction is small, whereas the length L of the junction is large compared to the Josephson penetration depth λ_J . Also indicated is the direction of the electrode current I^{el} and the resulting magnetic field B_{el} .

- *inline junctions* and
- *grain boundary junctions*.

We then discuss the boundary conditions for these junction types and the resulting stationary Sine-Gordon equation.

The geometry of the three main junction types is shown in Fig. 2.14. For the *overlap junction* the junction area is formed by a short overlap of width W of the bottom and the top junction electrodes extending in the x -direction. The one-dimensional junction of length L extends in z -direction, that is, perpendicular to the direction of the current flow in the electrodes (x -direction). Therefore, the magnetic field B^{el} generated by the electrode current I^{el} at the junction edges is parallel to the z -direction and, hence, perpendicular to the short side of the junction. Therefore, the magnetic flux $\Phi^{el} = B^{el}Wt_B$ is negligibly small due to the very small width W of the junction. Note that the field component B_x^{el} is perpendicular to the junction area and has no influence on the gauge-invariant phase difference (compare (2.2.15)).

For the *inline junction* the situation is different. Here, the junction area is formed by a long overlap of length L of the bottom and the top junction electrodes extending in the z -direction. The width W again is very small so that we have a one-dimensional junction extending in the z -direction. The important point is that in contrast to the overlap junction the long side of the junction now is parallel to the direction of the current flow in the electrodes (z -direction). Therefore, the magnetic field B^{el} generated by the electrode current I^{el} at the junction edges is parallel to the x -direction and, hence, perpendicular to the long side of the junction. Therefore, the magnetic flux $\Phi^{el} = B^{el}Lt_B$ is significant due to the large length $L \gg \lambda_J$.

of the junction and has to be taken into account. As for the overlap junction the field component B_x^{el} is perpendicular to the junction area and therefore has no influence on the gauge-invariant phase difference.

For the **grain boundary junction** geometry we have somehow a mixture of the overlap and inline geometry. Here, the junction area is not formed by an overlap of the bottom and the top electrode, but both electrodes are attached to each other face to face. This junction configuration has been widely used for the high temperature superconductors. For these materials a Josephson junction could be obtained by putting an epitaxial film on a bicrystalline substrate. Since the high temperature superconducting film takes the in-plane orientation of the bicrystalline substrate, an individual grain boundary could be introduced into the epitaxial film with the grain boundary angle determined by the substrate. This artificial grain boundary was found to act as junction barrier resulting in a Josephson junction.¹⁶ Therefore, this junction type is called grain boundary Josephson junction. In the grain boundary geometry the junction area extending in the yz -plane is not parallel to the surface of the electrodes (xz -plane) as for the overlap and inline geometry but perpendicular to it. Therefore, the electrode current I^{el} is now flowing perpendicular to the junction area and not parallel to it as for the overlap and inline geometry. The width W of the junction is small and the length L of the junction large compared to the Josephson penetration depth resulting in a one-dimensional junction extending in the z -direction. In contrast to the overlap and inline geometry now both the y - and z -component of the magnetic field B^{el} generated by the electrode current I^{el} lie in the junction plane. Whereas the component B_z^{el} can be neglected due to the small width W of the junction, the component B_y^{el} has to be taken into account, since it is perpendicular to the long side of the junction.

Overlap Junctions

For the overlap junction the magnetic field B_z^{el} due to the electrode current flowing in the bottom and top electrode can be expressed as¹⁷

$$B_z^{el} \simeq \pm \frac{\mu_0}{2} \frac{I^{el}}{L} . \quad (2.3.33)$$

We see that the electrode current is generating only a field component in z -direction. With the external magnetic field applied in y -direction, the total field in z -direction is only determined by B_z^{el} and we can write the boundary conditions (2.3.30) and (2.3.31) as¹⁸

$$\left. \frac{\partial \varphi}{\partial y} \right|_{y=0} = + \frac{2\pi t_B}{\Phi_0} B_z^{el} \Big|_{y=0} = + \frac{1}{\lambda_J^2} \frac{I^{el}}{2J_c L} \quad (2.3.34)$$

$$\left. \frac{\partial \varphi}{\partial y} \right|_{y=W} = - \frac{2\pi t_B}{\Phi_0} B_z^{el} \Big|_{y=W} = - \frac{1}{\lambda_J^2} \frac{I^{el}}{2J_c L} . \quad (2.3.35)$$

With $W \ll \lambda_J$, the gauge-invariant phase difference φ can have only a very small variation in y -direction. Therefore, we can use the Ansatz

¹⁶For a review see R. Gross: Grain Boundary Josephson Junctions in the High Temperature Superconductors in *Interfaces in High-T_c Superconducting Systems*, S. L. Shinde and D. A. Rudman eds., Springer Verlag, New York (1994), pp. 176-210.

¹⁷We use $\oint B ds = \mu_0 I^{el}$ and $\oint B ds \simeq B_z^{el} \cdot 2L$. We also assume that the current distribution in the electrodes is homogeneous. The case of an inhomogeneous current distribution will be discussed below in the subsection on mixed overlap and inline junction geometries.

¹⁸Note that B_z^{el} is in negative z -direction for $y = 0$ and in positive z -direction for $y = W$.

$$\varphi(y, z) = \varphi(z) + f(y) .$$

With the boundary conditions (2.3.34) and (2.3.35) we obtain for an arbitrary y position between the two edges

$$\frac{\partial f}{\partial y} = \frac{2\pi t_B}{\Phi_0} \frac{\mu_0 I^{el}}{2L} \left(1 - \frac{2y}{W} \right)$$

and hence

$$\frac{\partial^2 \varphi}{\partial y^2} = -\frac{2\pi t_B}{\Phi_0} \frac{\mu_0 I^{el}}{LW} = -\frac{2\pi t_B \mu_0 J_c}{\Phi_0} \frac{I^{el}}{I_c} = -\frac{1}{\lambda_J^2} \frac{I^{el}}{I_c} = -\frac{1}{\lambda_J^2} \gamma , \quad (2.3.36)$$

where $\gamma \equiv I^{el}/I_c$. With the solution for $\frac{\partial^2 \varphi}{\partial y^2}$ we obtain from (2.3.7)

$$\frac{\partial^2 \varphi(z)}{\partial z^2} - \frac{1}{\lambda_J^2} \sin \varphi(y, z) = \frac{1}{\lambda_J^2} \gamma . \quad (2.3.37)$$

For the field component in y -direction we have $B_y = B_y^{ex}$ and we obtain the boundary conditions

$$\frac{\partial \varphi}{\partial z} \Big|_{z=0} = +\frac{2\pi t_B}{\Phi_0} B_y^{ex} \Big|_{z=0} \quad (2.3.38)$$

$$\frac{\partial \varphi}{\partial z} \Big|_{z=L} = +\frac{2\pi t_B}{\Phi_0} B_y^{ex} \Big|_{z=L} . \quad (2.3.39)$$

Inline Junctions

For the inline junction the magnetic field B_y^{el} due to the electrode current flowing in the bottom and top electrode can be expressed as

$$B_y^{el} \simeq \pm \frac{\mu_0}{2} \frac{I^{el}}{W} . \quad (2.3.40)$$

We see that the electrode current is generating only a field component in y -direction. With the external magnetic field applied in y -direction, the total field in y -direction is then determined by the sum $B_y^{ex} + B_y^{el}$.

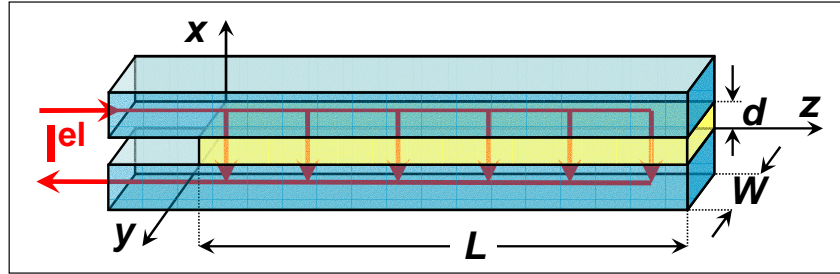


Figure 2.15: The geometry of an asymmetric inline junction. In contrast to the symmetric inline junction the electrode currents in the top and bottom electrode are flowing in opposite direction. At $z = L$ the electrode current density becomes zero, since along the junction length the current injected at $z = 0$ in the top electrode is tunneling to the bottom electrode and flowing back in opposite direction.

Since $W \ll \lambda_J$ and since we have no magnetic field component in z -direction, we can assume $\frac{\partial^2 \varphi}{\partial y^2} \simeq 0$ and we arrive at the differential equation for the inline junction

$$\frac{\partial^2 \varphi(z)}{\partial z^2} - \frac{1}{\lambda_J^2} \sin \varphi(y, z) = 0 . \quad (2.3.41)$$

For the field parallel to the y -direction we have $B_y = B_y^{ex} + B_y^{el}$ and we can write the boundary conditions (2.3.28) and (2.3.29) as¹⁹

$$\left. \frac{\partial \varphi}{\partial z} \right|_{z=0} = +\frac{2\pi t_B}{\Phi_0} \left(B_y^{ex} - \frac{\mu_0 I^{el}}{2W} \right)_{z=0} \quad (2.3.42)$$

$$\left. \frac{\partial \varphi}{\partial z} \right|_{z=L} = +\frac{2\pi t_B}{\Phi_0} \left(B_y^{ex} + \frac{\mu_0 I^{el}}{2W} \right)_{z=L} . \quad (2.3.43)$$

These are the boundary conditions for a so-called symmetric inline junction where the current in the top and bottom electrode are flowing in the same direction. In an **asymmetric inline junction** the current in the top and bottom electrode are flowing in opposite direction as shown in Fig. 2.15. In this case we have the boundary conditions

$$\left. \frac{\partial \varphi}{\partial z} \right|_{z=0} = +\frac{2\pi t_B}{\Phi_0} \left(B_y^{ex} - \frac{\mu_0 I^{el}}{W} \right)_{z=0} \quad (2.3.44)$$

$$\left. \frac{\partial \varphi}{\partial z} \right|_{z=L} = +\frac{2\pi t_B}{\Phi_0} (B_y^{ex})_{z=L} . \quad (2.3.45)$$

These boundary conditions are evident, since now the field at $z = 0$ is twice of that of the symmetric inline junction whereas the field at $z = L$ vanishes.

¹⁹Note that the field due to the electrode current is in negative y -direction at $z = 0$ and in positive y -direction for $z = L$.

Mixed Overlap and Inline Junctions

We can have two situations, where we obtain an inline admixture to an overlap junction geometry:

1. Overlap junctions for which the width of the junction electrodes is larger or smaller than the junction length L .
2. The electrode current is not distributed homogeneously over the cross-section of the electrode. This is the case, if the thickness of the electrodes is larger than the London penetration depth λ_L . Then, the current density distribution in the junction electrodes is peaked at the edges of the junctions (see Fig. 2.16c).

Note that for the overlap geometry the electrode current always was flowing only in x -direction resulting in a magnetic field component B_z^{el} which is perpendicular to the short side of the junction. However, as shown in Fig. 2.16 for the two cases mentioned above there is always a finite electrode current I_z^{el} at the edges of the junction area, which is parallel to the z -direction and results in a magnetic field component B_y^{el} in y -direction. This field component is perpendicular to the long side of the junction and corresponds to the field component of the inline geometry. Therefore, for the situations shown in Fig. 2.16 we speak about a ***mixed overlap and inline geometry***.

The inline admixture to an overlap type junction can be formally characterized by a dimensionless parameter s which ranges between 0 and 1. Here, $s = 0$ corresponds to a pure overlap junction and $s = 1$ to a pure inline junction. With this parameter we obtain the stationary Sine-Gordon equation to

$$\frac{\partial^2 \varphi(z)}{\partial z^2} - \frac{1}{\lambda_J^2} \sin \varphi(z) = (1-s) \frac{1}{\lambda_J^2} \gamma \quad (2.3.46)$$

with $\gamma \equiv I^{el}/I_c$. The boundary conditions are

$$\left. \frac{\partial \varphi}{\partial z} \right|_{z=0} = + \frac{2\pi t_B}{\Phi_0} \left(B_y^{ex} - s \frac{\mu_0 I^{el}}{2W} \right)_{z=0} \quad (2.3.47)$$

$$\left. \frac{\partial \varphi}{\partial z} \right|_{z=L} = + \frac{2\pi t_B}{\Phi_0} \left(B_y^{ex} + s \frac{\mu_0 I^{el}}{2W} \right)_{z=L} \quad (2.3.48)$$

Grain Boundary Josephson Junctions

In grain boundary junctions the junction area is perpendicular to the direction of the electrode currents. This is different to overlap and inline junctions, where the junction area is parallel to the direction of the electrode currents. In contrast to the overlap junction for the grain boundary junctions geometry we have to take into account the y -component of the magnetic field B^{el} due to the electrode currents:

$$B_y^{el} \simeq \pm \frac{\mu_0}{2} \frac{I^{el}}{L} \quad (2.3.49)$$

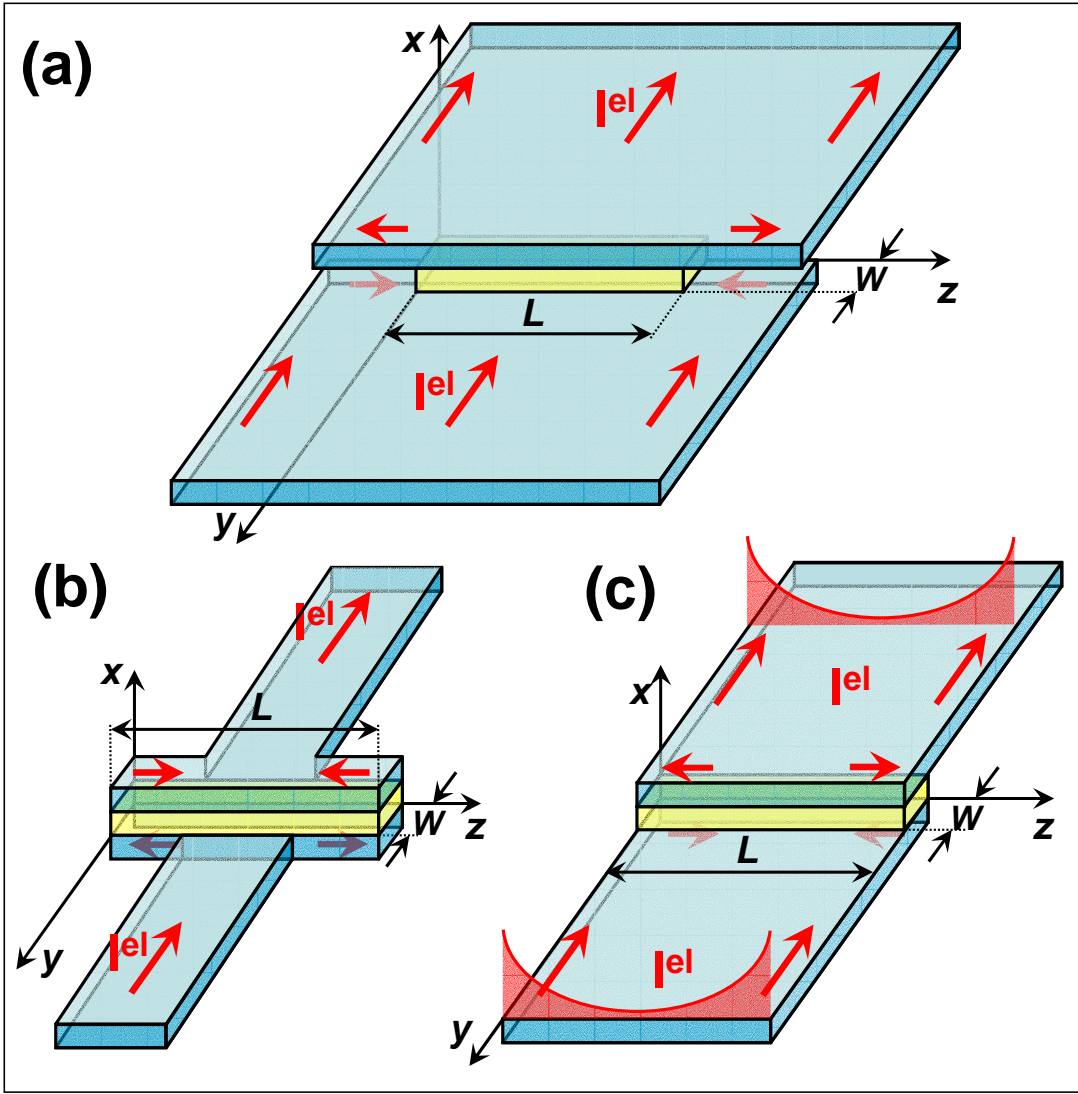


Figure 2.16: The geometry of mixed overlap and inline junctions. In (a) and (b) the width of the electrodes is larger and smaller than the junction length L , respectively, resulting in an electrode current parallel to the z -direction both in the bottom and top electrode. In (c) an electrode current density peaked at the electrode edges results in an electrode current parallel to the z -direction at the edges of the junction area.

For the overlap geometry this field was perpendicular to the junction area and has no effect on the gauge-invariant phase difference. In contrast, for the grain boundary junctions B_y^{el} is parallel to the junction area. The field component B_y^{el} results in a finite inline admixture. Writing B_y^{el} as

$$B_y^{el} \simeq \pm \frac{\mu_0}{2} \frac{W}{L} \frac{I^{el}}{W} = s \frac{\mu_0}{2} \frac{I^{el}}{W} \quad (2.3.50)$$

we see by comparison with (2.3.47) and (2.3.48) that the amount of inline admixture is just $s = W/L \ll 1$, since usually the length L of the grain boundary junction is usually much larger than the width W . Our analysis shows that the grain boundary junction can be considered as a overlap junction with a small inline admixture. Therefore we can use the expression for the mixed overlap and inline geometry and the stationary Sine-Gordon equation can be written as

$$\frac{\partial^2 \varphi(z)}{\partial z^2} - \frac{1}{\lambda_J^2} \sin \varphi(z) = \left(1 - \frac{W}{L}\right) \frac{1}{\lambda_J^2} \gamma = (1-s) \frac{1}{\lambda_J^2} \gamma . \quad (2.3.51)$$

The boundary conditions are

$$\left. \frac{\partial \varphi}{\partial z} \right|_{z=0} = \frac{2\pi t_B}{\Phi_0} \left(B_y^{ex} + \frac{W}{L} \frac{\mu_0 I^{el}}{2W} \right)_{z=0} \quad (2.3.52)$$

$$\left. \frac{\partial \varphi}{\partial z} \right|_{z=L} = \frac{2\pi t_B}{\Phi_0} \left(B_y^{ex} - \frac{W}{L} \frac{\mu_0 I^{el}}{2W} \right)_{z=L} . \quad (2.3.53)$$

We note that for an electrode thickness larger than the London penetration depth λ_L the electrode current is peaked at the junction edges. This results in an additional inline admixture as already discussed above.

2.3.4 Josephson Current Density Distribution and Maximum Josephson Current

After having found the stationary Sine-Gordon equation and the boundary conditions for the various junction types we can calculate the Josephson current distribution $J_s(y, z)$ in the junction as well as the maximum Josephson current. We will do this calculation only for a few simple cases assuming that the critical current density $J_c(y, z)$ is homogeneous across the junction. We will start with the zero field case.

Overlap Junction: $\mathbf{B}^{ex} = 0$

We first consider an overlap junction with a spatially homogeneous electrode current distribution. For zero external magnetic field we have $\partial \varphi / \partial z = 0$ at both junction edges according to (2.3.38) and (2.3.39). Therefore, $\partial^2 \varphi / \partial z^2 = 0$ and we obtain the following trivial solution of the SSGE (2.3.36)

$$\varphi(z) = \arcsin(\gamma) + 2\pi n = const \quad (2.3.54)$$

and hence for the Josephson current density

$$J_s(z) = J_c \sin \varphi(z) = const \quad (2.3.55)$$

The maximum Josephson current in this case is

$$I_s^m = \int_{A_i} J_s dA = J_c \cdot LW = J_c \cdot A_i . \quad (2.3.56)$$

Here, $A_i = LW$ is the junction area.

For the overlap junction we obtain the important result that for zero applied magnetic field the Josephson current density is constant across the junction area and that the maximum Josephson current is increasing linearly with increasing junction area.

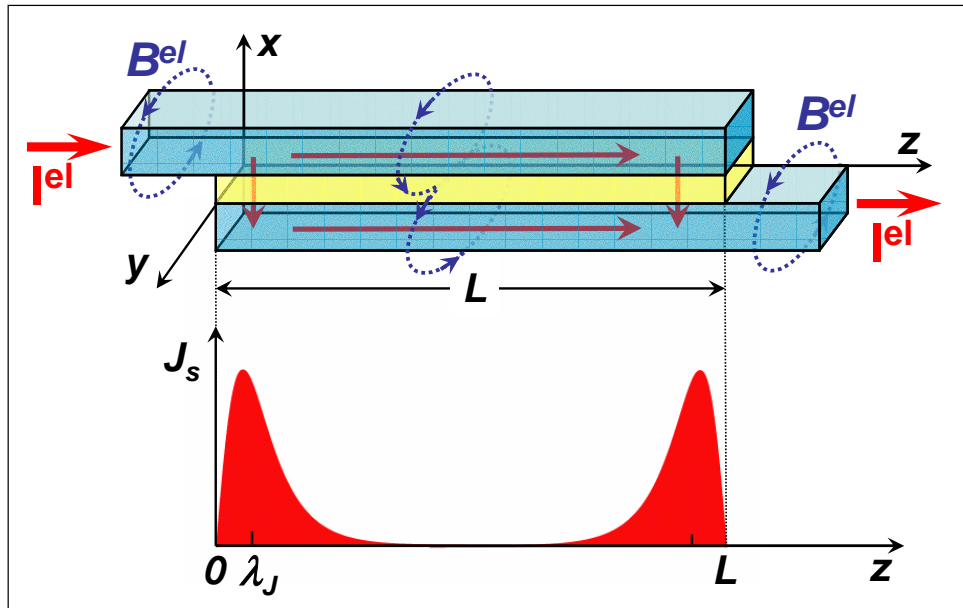


Figure 2.17: The geometry (a) and the Josephson current distribution of a long inline Josephson junction. The Josephson current density J_s is restricted to the boundaries of the junction thereby resulting in the Meißner state of the long inline Josephson junction.

Inline Junction: $\mathbf{B}^{ex} = 0$

In contrast to the overlap junction for the inline junction we have to take into account the magnetic field due to the electrode current. Qualitatively, we can find the current distribution by recalling that a superconducting system always wants to stay in the Meißner state, that is, it wants to expel the magnetic field. As shown in Fig. 2.17, in an inline junction the Meißner state can be achieved by restricting the Josephson current density to the left and right edge of the junction. Then, the electrode current flowing in the top and bottom electrode are the same along the junction and their magnetic fields cancel each other. In this way the inner of the junction resides in the Meißner state. This situation is similar to a bulk superconductor, where the supercurrent density is flowing only on the surface of the sample and decays exponentially away from the surface. Here, the characteristic decay length is the London penetration depth λ_L . For a Josephson junction an exponential decay is obtained only in the linear approximation (compare (2.3.8) to (2.3.10)). However, due to the nonlinearity of the Sine-Gordon equation the Josephson current density is zero at the edges, increases to the maximum value J_c at a depth equal to about λ_J and then decays again so that the Josephson current density is restricted to an edge regime with a length of about $2\lambda_J$. A detailed calculation shows that the integral maximum Josephson current is

$$I_s^m = \int_{A_i} J_s dA = J_c \cdot 4W\lambda_J . \quad (2.3.57)$$

That is, in contrast to the overlap junction, for which the maximum Josephson current increases linearly with the junction length, the maximum Josephson current of an inline junction is independent of the junction length L . This is evident from Fig. 2.17. Since the Josephson current density is restricted to the edges of the junction, an increase of the junction length above a value of about $L = 4\lambda_J$ does no longer increase the integral junction current.

Grain Boundary Junction: $\mathbf{B}^{ex} = 0$

For the grain boundary junction we have a overlap type geometry with a certain amount of inline admixture. If the thickness t of the electrodes of the grain boundary Josephson junction is smaller than the London penetration depth, the current distribution in the electrodes is quite homogeneous and, hence, the inline admixture is $s = W/L = t/L$ (compare (2.3.50) and Fig. 2.14). Since usually $t/L \ll 1$ the inline admixture is small and the maximum Josephson current is expected to increase linearly with increasing junction length.

As shown in Fig. 2.18 this has been indeed observed experimentally. The experimental data obtained for the grain boundary junctions follow the theoretical estimate for the overlap junction. Fig. 2.18 also shows that with increasing inline admixture the increase of the maximum Josephson current with increasing junction length L is becoming more flat and finally vanishes for a pure inline junction.

In Fig. 2.18 we also show the effect of a spatially inhomogeneous current distribution in the junction electrodes. Assuming for an overlap junction an electrode current distribution

$$J^{el}(z) = \frac{L}{\pi\sqrt{z(L-z)}} , \quad (2.3.58)$$

which is peaked at the edges of the junction, we obtain

$$I_s^m(L) = 2.35 \sqrt{L} . \quad (2.3.59)$$

That is, the maximum Josephson current does no longer increase linearly with L but proportional to the square root of the junction length.

The Magnetic Field Dependence of the Maximum Josephson Current

The magnetic field dependence of the maximum Josephson current in the presence of an applied magnetic field has to be calculated numerically in most cases.²⁰ A convenient way to calculate the local Josephson current density as well as the integral maximum Josephson current is the use of an iteration method as described in Appendix C.

Fig. 2.19a and b show the magnetic field dependence of the maximum Josephson current for a symmetric overlap junction with a reduced junction length of $L/\lambda_J = 5$ and 10. Qualitatively, we can understand the $I_s^m(B^{ex})$ dependence of the symmetric junction as follows: For small applied fields the junction can screen the applied external field by a circulating screening current. This current flows in opposite direction at both junction edges and adds to the external applied transport current. Since the local Josephson current density cannot exceed J_c , the integral maximum Josephson current of the junction is decreasing, since at one junction edge the screening current is flowing in the same direction as the transport current. This is shown in Fig. 2.19d where we have plotted the $J_s(z)$ dependence of an overlap junction for increasing

²⁰see e.g. A. Barone and G. Paterno, *Physics and Application of the Josephson Effect*, John Wiley & Sons, New York (1982); S. Pagano, B. Ruggiero and E. Sarnelli, Phys. Rev. B **43**, 5364 (1991); S. Pagano, B. Ruggiero, M. Russo and E. Sarnelli, in *Nonlinear Superconductive Electronics and Josephson Devices*, G. Constabile, S. Pagano, N. F. Pedersen, and M. Russo eds., Plenum Press, New York, 369 (1991).

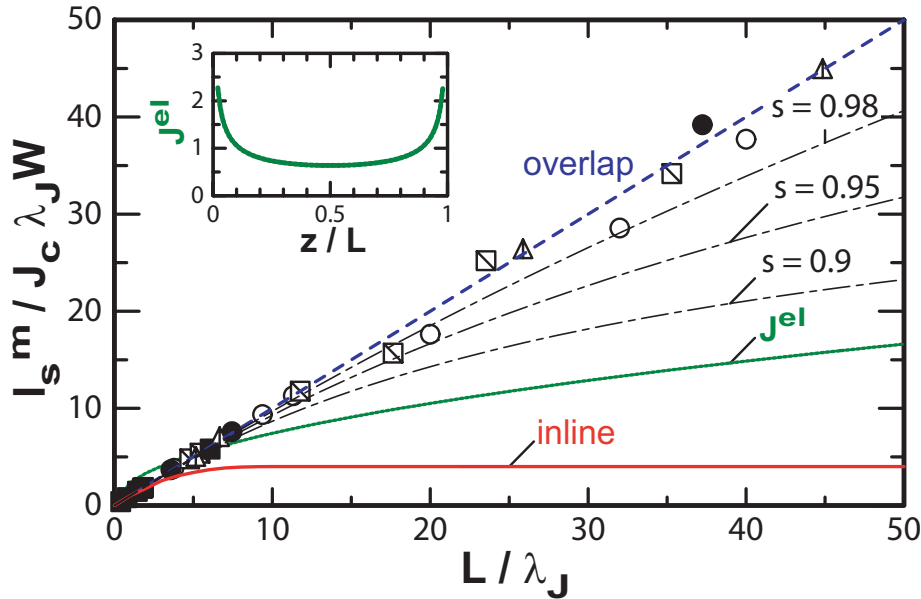


Figure 2.18: The maximum Josephson current I_s^m plotted as a function of the junction length for a pure overlap and inline geometry as well as for different amount s of an inline admixture to the pure overlap geometry. Also shown is the $I_s^m(L)$ dependence for an overlap junction with an inhomogeneous electrode current distribution $J^{el}(z)$ according to (2.3.58).

applied field. On the left junction edge the screening current is in the same direction as the applied current whereas it is opposite on the right edge. It can be seen that with increasing applied field the screening current is increasing until it reaches the critical value at the right edge. Then vortices start to penetrate the junction resulting in an oscillating $J_s(z)$ dependence.

We can use Ampère's law $\partial B_y(z)/\partial z = -\mu_0 J_x(z)$ to estimate the maximum field value that can be screened by the junction. Assuming for simplicity an exponential decay of the applied field in the junction, $B_y^{ex}(z) \propto \exp(-z/\lambda_J)$ (linear approximation), we obtain $\partial B_y(z)/\partial z = -\frac{1}{\lambda_J} B_y^{ex}(z) = -\mu_0 J_x(z)$ and

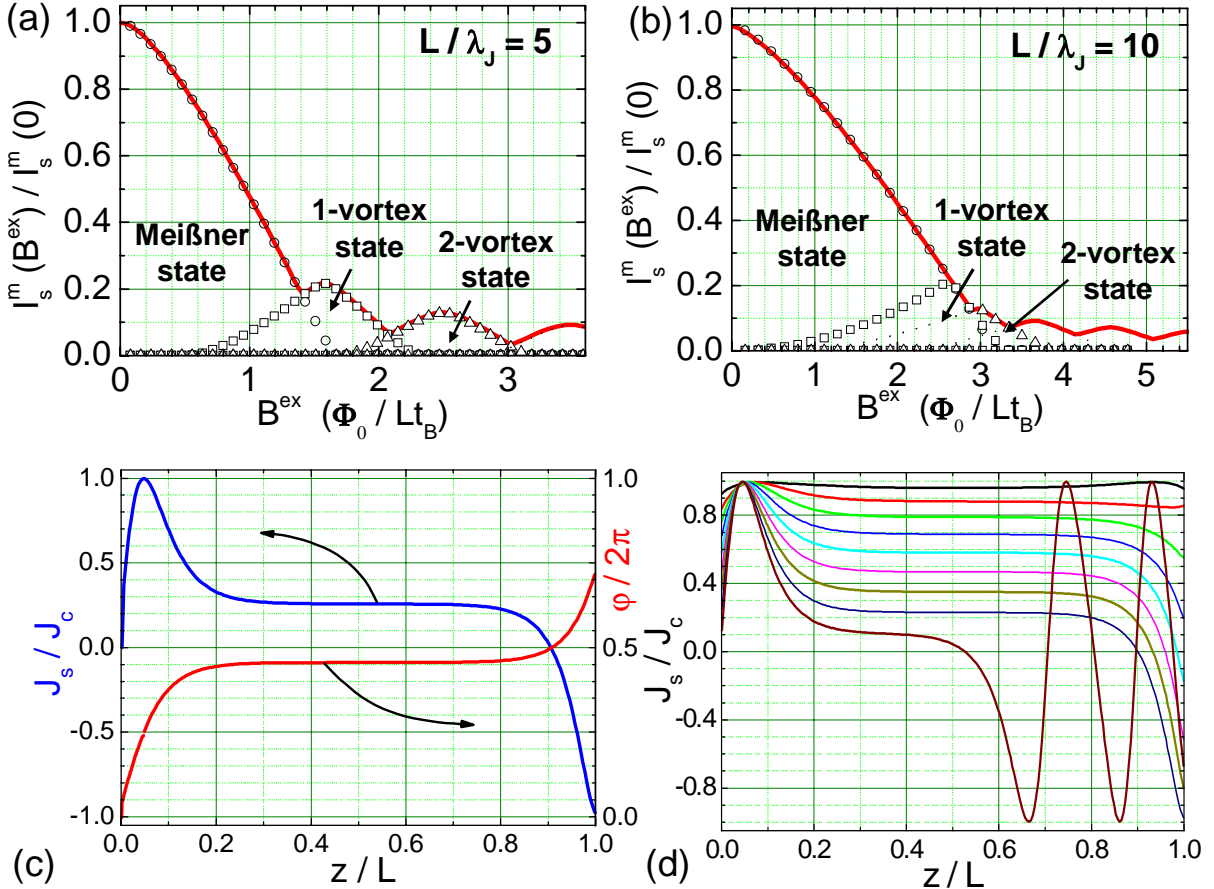


Figure 2.19: I_s^m plotted versus the applied magnetic field B^{ex} for symmetric overlap junction with $L/\Lambda_J = 5$ (a) und $L/\Lambda_J = 10$ (b). The symbols mark the solutions for the different vortex states. The solid line shows the envelop of the different solution. In (b) $J_s(z)$ as well as $\varphi(z)$ is shown along the junction for a magnetic field close to B_{c1} . In (d) the change of $J_s(z)$ with increasing applied magnetic field is shown. Only for the highest field vortices can penetrate the junction as can be seen by the oscillating $J_s(z)$ dependence.

hence $J_x = \frac{1}{\lambda_J} \frac{B_y^{ex}}{\mu_0}$. Since $J_x \leq J_c$ we can estimate the maximum field value that can be screened by the junction to $B_c = \mu_0 J_c \lambda_L$. Within a factor of unity this rough estimate is equal to the lower critical field B_{c1} of a long Josephson junction (compare (2.3.27)). Indeed, for $B^{ex} \geq B_{c1} = \frac{4}{\pi} \mu_0 J_c \lambda_J$ a state with one vortex in the junction is energetically more favorable.

The state with no vortex in the junction is called the Meissner state of the junction. For fields larger than the lower critical field B_{c1} a state with one or more vortices inside the junction is more favorable. This can be seen in Fig. 2.19, where the symbols mark the maximum Josephson current values for the different vortex states. It can be seen that for a certain external field the 1-vortex solution has a higher maximum Josephson current than the Meissner state solution, that is, the 1-vortex solution is energetically more favorable. Note that on increasing the magnetic field starting from zero, so that the junction is in its Meissner state initially, the penetration of vortices will start only at a field $B_{max} > B_{c1}$. This relation can be understood in terms of vortex pinning at the sharp edges of the uniform junction. It can be shown that $B_{max} = \frac{\pi}{2} B_{c1} = 2 \mu_0 J_c \Lambda_J$ for an infinitely long junction.²¹

Note that the variation of the gauge invariant phase difference along the junction is nonlinear (see Fig. 2.19c). Recall that for short junctions we had a linear increase of the phase difference along the junction resulting in a sinusoidal variation of the Josephson current density. The reason for this behavior

²¹ K. K. Likharev, *Dynamics of Josephson Junctions and Circuits*, Gordon and Breach Science Publishers, New York (1986).

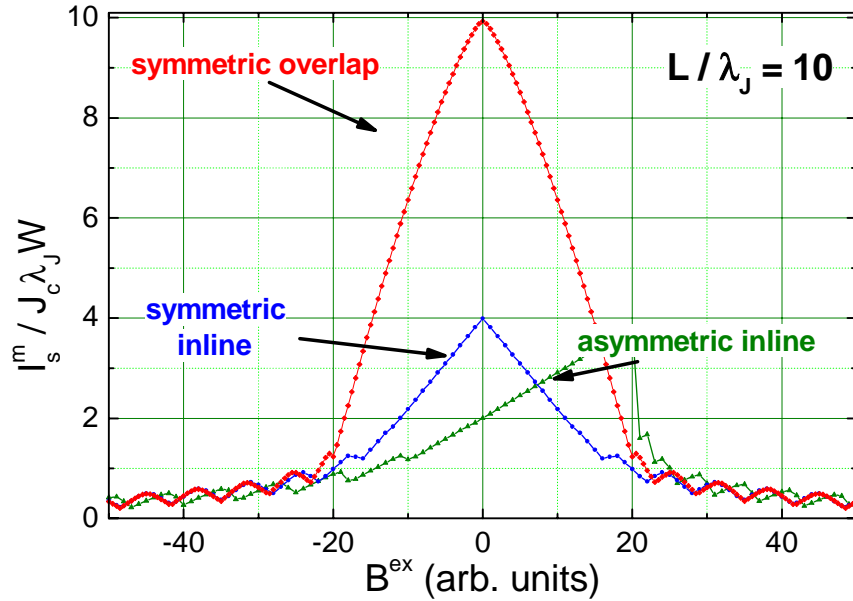


Figure 2.20: I_s^m plotted versus the applied magnetic field B^{ex} for a symmetric overlap and inline junction as well as for an asymmetric inline junction with $L/\lambda_J = 10$. T

was the fact that we could neglect the magnetic field of the current and therefore had a spatially homogeneous total magnetic field $B = B^{ex}$. For long junctions we have to take into account the field of the current what results in a spatially varying total field $B = B^{ex} + B^{el}$. Therefore, the spatial variation of $\varphi(z)$ along the junction and, in turn, of the Josephson current density $J_s(z) = J_c \sin \varphi(z)$ is more complicated.

In Fig. 2.20 we have plotted the magnetic field dependence of the maximum Josephson current for symmetric overlap and inline junctions as well as for an asymmetric inline junction. The junction have a reduced length $L/\lambda_J = 10$. It can be seen that the overlap junction has the highest zero field Josephson current, since here the maximum Josephson current is proportional to the junction length, $I_s^m = J_c W L$. In contrast, as discussed above for the inline junction the maximum Josephson current saturates as a $I_s^m = 4J_c W \lambda_J$. The asymmetric inline junction shows a highly asymmetric $I_s^m(B^{ex})$ dependence. This can be understood as follows (compare Fig. 2.15): The magnetic fields generated by the electrode currents flowing in the bottom and top electrode point in the same direction for the asymmetric inline junction. Now, this field direction can be parallel or anti-parallel to the external field. For anti-parallel orientation the external magnetic field is compensating the field of the electrode currents thereby causing a reduction of the total magnetic field. Therefore the maximum Josephson current is increasing with increasing applied field. In contrast, for parallel orientation the applied field in adding to the field of the electrode currents causing an increase of the total field and, hence, the maximum Josephson current is decreasing with increasing applied field.

2.3.5 The Pendulum Analog

In order to get some insight into the nature of solutions for φ we recall that the stationary Sine-Gordon equation has the same form as the differential equation for a pendulum. If we make the transcriptions $z \rightarrow t$, $\varphi \rightarrow \theta$ and $1/\lambda_J^2 \rightarrow \omega_0^2 = g/L$ where θ is the angle of the pendulum measured from the top of its circular orbit, and ω_0 is its natural frequency. In terms of this transcription, the solutions for φ found by neglecting the effect of the electrode currents corresponds to the motion of the pendulum whirling around and around with so much kinetic energy that gravitational acceleration is negligible. In the Sine-Gordon equation this limit corresponds to $\lambda_J \rightarrow \infty$ so that $d^2\varphi/dz^2 = 0$ and $d\varphi/dz = const$ resulting in

a sinusoidal variation of the Josephson current density.

If we consider now a pendulum moving with less energy, but still sufficient energy to have nonzero kinetic energy at the top of the circle, the motion of $\theta(t)$, which is equivalent to $\varphi(z)$, will be periodic but anharmonic. This leads to a non-sinusoidal, periodically reversing current distribution $J_s(z)$. Each cycle of the oscillating current contains one flux quantum. Unlike the sinusoidal case these Josephson vortices are actually localized entities, since they are spaced with a separation exceeding λ_J .

We finally discuss the Meißner limit of a junction of length L . The Meißner solution corresponds to pendulum moving with an energy that is just sufficient to go over the top. In this case, starting with an initial angular velocity $(d\theta/dt)_0$ from an initial angle $-\theta_0$ at the time t corresponding to $-L/2$, the pendulum decelerates nearly exponentially as it rises. It moves very slowly for a long time (corresponding to the interior length of the junction), while going over the top, and then exponentially accelerates down the other side, recovering the initial angular velocity at θ_0 (at a time t corresponding to $+L/2$).

If the angular velocity at the top is negligible compared to the initial value, then θ_0 and $(d\theta/dt)_0$ are connected by the conservation of energy and are not independent. Translating back to the junction problem we see that the corresponding initial condition is

$$\left(\frac{2\pi}{\Phi_0}B_y t_B\right)^2 = \left(\frac{d\varphi}{dz}\right)_0^2 = \frac{2}{\lambda_J^2} (1 - \cos \varphi_0) . \quad (2.3.60)$$

Solving this equation for $\cos \varphi_0$ we obtain

$$\cos \varphi_0 = 1 - \frac{1}{2} \left(\frac{B_y}{\mu_0 J_c \lambda_J}\right)^2 . \quad (2.3.61)$$

Thus, for small fields we can use the approximation $\cos x = 1 - \frac{1}{2}x^2$ and the phase difference φ_0 at the edges of the junction is given by

$$\varphi_0 = \frac{B_y}{\mu_0 J_c \lambda_J} . \quad (2.3.62)$$

If we want to estimate the strongest field that can be screened by the junction, we have to consider the case at which the pendulum is starting from the bottom, that is, $\varphi_0 = \pi$. Then we obtain

$$B_{\max} = 2\mu_0 J_c \lambda_J . \quad (2.3.63)$$

This field is just the highest field for which the Meißner solution is possible. Actually, the screening at B_{\max} is only metastable. The maximum value for which screening is thermodynamically stable has been derived above to $B_{c1} = 4\mu_0 J_c \lambda_J / \pi$ (compare (2.3.27)). Note that for fields close to B_{c1} screening is no longer exponential but rather becomes so in the interior when φ has become small.

Chapter 3

Physics of Josephson Junctions: The Voltage State

In Chapter 2 we have considered only Josephson junctions, for which the current was less than the maximum Josephson current I_s^m . Then, the junction was in the zero voltage state. In this chapter we now generalize our discussion and also discuss the situation where the junction current is larger than the maximum Josephson current. In this situation the applied current can no longer be carried completely by the Josephson current. That is, in addition to the Josephson current we have to include other current channels carrying the excess current. One additional current channel is the **resistive channel**. At temperatures above zero temperature there is a finite probability for Cooper pairs to break up by thermal excitation thereby generating unpaired “normal” electrons. In the presence of a finite voltage across the junction these normal electrons contribute to the current. In contrast to the Josephson current the normal current channel will be resistive. The second current channel is due to the finite capacitance of the Josephson junction. For example, a tunneling type superconductor/insulator/superconductor junction just represents a parallel plate capacitor. In the present of a time varying junction voltage we have a finite displacement current across this capacitor. Finally, noise is taken into account by adding a fluctuation current.

In this chapter we first describe the additional current channels in the voltage state of a Josephson junction and then discuss models for the description of the current-voltage characteristics. In particular, we discuss Josephson junctions, when they are driven by dc and ac sources.

3.1 The Basic Equation of the Lumped Josephson Junction

If we want to derive the basic equation describing the Josephson junction in the voltage state, we have to consider the additional current channels relevant in the voltage state. In the following we will consider the resistive and capacitive channel as well as an additional channel due to fluctuations (noise). In our discussion we will first consider lumped Josephson junction that can be characterized by the integral current values. Extended junctions will be discussed later in section 3.4.

3.1.1 The Normal Current: Junction Resistance

If the temperature is larger than zero there is a finite density of normal electrons due to thermal breaking of Cooper pairs. The presence of the condensate of paired electrons makes the properties of these “normal” electrons somewhat different from those in the normal state. We call them *quasiparticles*.

In the zero-voltage state of a Josephson junction the quasiparticles do not contribute to the junction current. However, if the gauge-invariant phase difference changes in time resulting in a nonvanishing junction voltage V according to the second Josephson equation, $d\varphi/dt = 2eV/\hbar$, then a then a quasiparticle component of the total current, the *normal* I_N , is obtained. This current is a resistive current and therefore the *voltage-state* of a Josephson junction is also called the *resistive state*.

We briefly discuss the temperature and voltage dependence of the normal current. First, if $T \lesssim T_c$ the binding energy 2Δ (Δ : energy gap) of the Cooper pairs is small and $k_B T$ is large. Therefore, almost all Cooper pairs are broken up and the concentration of quasiparticles is close to that in the electron density in the normal state. In this case we expect that the current-voltage characteristic (IVC) is close to the usual Ohm’s law

$$I_N = G_N V , \quad (3.1.1)$$

where $G_N = 1/R_N$ is the *normal conductance* of the Josephson junction.

Second, if the junction voltage is above the so-called *gap voltage*

$$V_g = \frac{\Delta_1(T) + \Delta_2(T)}{e} , \quad (3.1.2)$$

the external circuit provides sufficient energy to break up Cooper pairs. Here, $\Delta_1(T)$ and $\Delta_2(T)$ are the energy gaps in the two junction electrodes. A Cooper pair is broken up in one of the electrodes and the two newly formed quasiparticles pass to the other electrode. This process can set in only above the gap voltage because a minimum energy $\Delta_1(T) + \Delta_2(T)$ is required for this process. Hence, for $|V| > V_g$ the IVC is expected to be close to an ohmic dependence independent of the temperature.

Third, for $T \ll T_c$ and $|V| < V_g$ there should be a vanishing normal current, since neither the thermal energy $k_B T$ nor the energy eV supplied by the external circuit are sufficient to break up Cooper pairs. That is, the quasiparticle density and hence the normal current is vanishingly small.

The IVC expected from our discussion is shown schematically in Fig. 3.1. For $T > T_c$ and $|V| > V_g$ an ohmic dependence is obtained. For $T < T_c$ and $|V| < V_g$ the IVC depends on the sweeping direction and

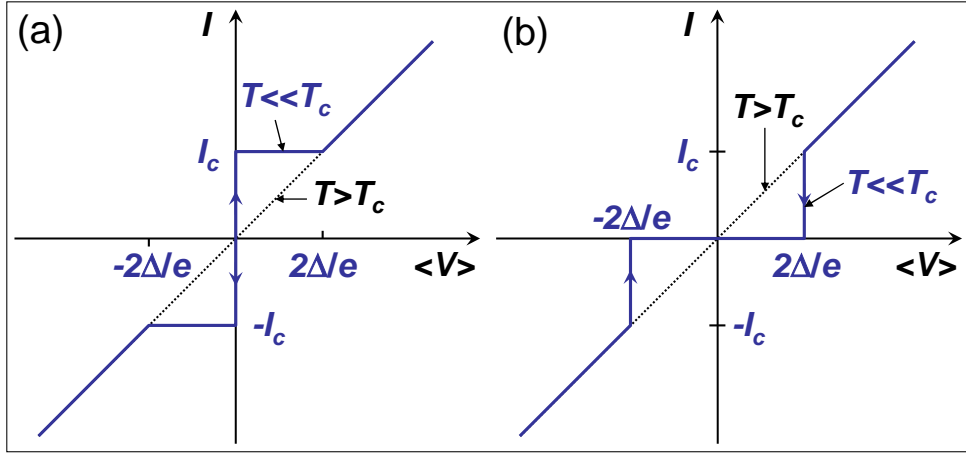


Figure 3.1: Current-voltage characteristics (IVC) of a Josephson junction driven by a constant current source. The voltage represents the time-averaged voltage. Curve (a) is for increasing and curve (b) for decreasing driving current.

on the type of the external source (current or voltage source). Here, for a current source a hysteretic IVC is obtained. The detailed reason for that will be discussed later in section 3.2.1. We note that if the junction is driven by a current source, the total current of the junction, $I = I_s + I_N$ is constant. Since in the voltage state the supercurrent $I_s = I_c \sin \varphi$ is varying in time, due to the time evolution of φ , also the normal current has to vary in time to keep the total current constant. Then, also the junction voltage $V = I_N/G_N$ is varying in time. The voltage shown in the IVCs of Fig. 3.1 is the time-averaged voltage $\langle V \rangle$.

Summarizing our discussion we see that in the voltage state of a Josephson junction we have to take into account the quasiparticle current. The quasiparticles are generated either by thermal excitation at finite temperature or due to breaking up of Cooper pairs by the junction voltage even at zero temperature. A circuit model that incorporates both the Josephson current and the normal current channel is shown in Fig. 3.2.

At $T = 0$, the equivalent conductance for the normal channel is given by

$$G_N(V) = \begin{cases} 0 & \text{for } |V| < 2\Delta/e \\ \frac{1}{R_N} & \text{for } |V| \geq 2\Delta/e \end{cases}. \quad (3.1.3)$$

At finite temperatures thermally excited quasiparticles can tunnel already at voltages smaller than the gap voltage resulting in a finite resistance $R_{sg}(T)$ called **sub-gap resistance**. The magnitude of the sub-gap resistance, or equivalently the sub-gap conductance, is determined by the amount of thermally excited quasiparticles and can be expressed as

$$G_{sg}(T) = \frac{1}{R_{sg}(T)} = \frac{n(T)}{n_{tot}} G_N. \quad (3.1.4)$$

Here, $n(T)$ is the density of excited quasiparticles at temperature T and n_{tot} is the total density of electrons in the normal state. Hence, at $T > 0$ we expect that the normal conductance channel can be characterized by the voltage and temperature dependent conductance

$$G_N(V, T) = \begin{cases} \frac{1}{R_{sg}(T)} & \text{for } |V| < 2\Delta(T)/e \\ \frac{1}{R_N} & \text{for } |V| \geq 2\Delta(T)/e \end{cases} . \quad (3.1.5)$$

Here, the fact that the energy gap and thereby the gap voltage is temperature dependent has been included. It is evident that the normal channel results in a channel results in a **nonlinear conductance** $G_N(V, T)$ that depends voltage and on temperature.

Our discussion shows that the equivalent circuit of the Josephson junction including the Josephson current and the normal current channel is characterized by a natural current scale I_c and a natural resistance R_N . Therefore, we can define a **characteristic voltage**

$$V_c \equiv I_c R_N = \frac{I_c}{G_N} , \quad (3.1.6)$$

which usually is called the $I_c R_N$ -product of the Josephson junction. According to the second Josephson equation this characteristic voltage defines defines a **characteristic frequency** of the Josephson junction

$$\omega_c = \frac{1}{\tau_c} \equiv \frac{2e}{\hbar} V_c = \frac{2\pi}{\Phi_0} V_c \quad \text{or} \quad f_c = \frac{V_c}{\Phi_0} . \quad (3.1.7)$$

With the Josephson inductance $L_c = \frac{\hbar}{2eI_c}$ (compare (2.1.22)) we can rewrite (3.1.7) as

$$\omega_c = \frac{R_N}{L_c} \quad \text{or} \quad \tau_c = \frac{1}{\omega_c} = \frac{L_c}{R_N} . \quad (3.1.8)$$

This shows that ω_c is just the inverse relaxation time in a system consisting of a normal current and a supercurrent.

We close this subsection by noting that we did not take into account any frequency dependence of the normal conductance. Of course, at high frequency the normal electrons have to be accelerated resulting in an inductive component of the normal channel and hence in a frequency dependent conductance. However, in most cases the inductance of the superelectron channel dominates over that of the normal channel and therefore we only use a frequency independent conductance for modelling the normal current channel. Finally, we should emphasize that our discussion was focused on Josephson tunnel junctions and did not include other junction types where the Josephson coupling is achieved by a normal metal, a semiconductor, a micro-constriction, etc..

3.1.2 The Displacement Current: Junction Capacitance

In situations where not only V but also its time derivative dV/dt is nonzero, the displacement current I_D plays an important role. For most practical junctions the displacement current can be represented in the usual form

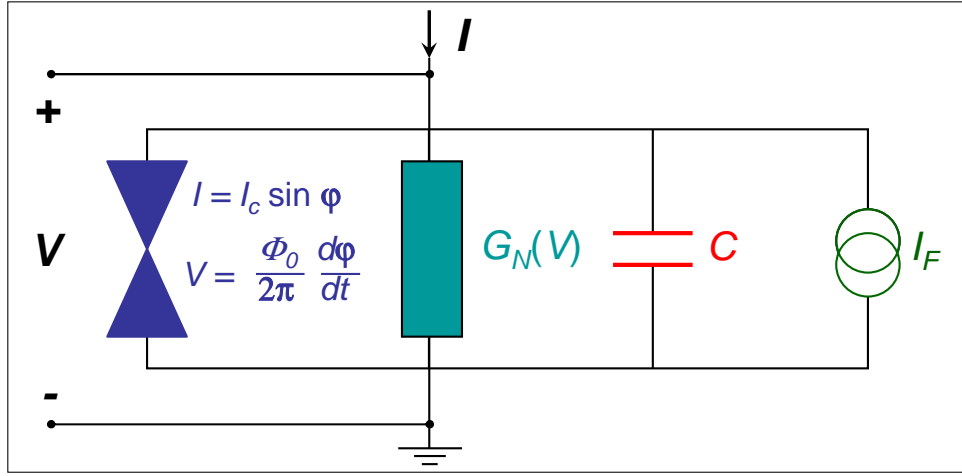


Figure 3.2: Equivalent circuit for a Josephson junction including the Josephson current channel as well as the normal current and the displacement current channel. Furthermore, noise is taken into account by a noise source providing a fluctuation current.

$$I_D = C \frac{dV}{dt} . \quad (3.1.9)$$

Here, C is the junction capacitance, which is just the same in the normal and the superconducting state. The capacitance depends on the junction type and its size. For a planar tunnel junction with area A_i and an insulating barrier of thickness d the junction capacitance is just given by

$$C = \frac{\epsilon \epsilon_0 A_i}{d} , \quad (3.1.10)$$

where ϵ is the dielectric constant of the barrier material. The displacement current results in an additional current channel parallel to the Josephson and the normal current channel.

With $V = L_s \dot{I}_s$, $I_N = V G_N$ and $I_D = C \dot{V}$ we can compare the current values in the three different current channels at a given frequency. With $L_s = L_c / \cos \varphi \geq L_c$ and $G_N(V, T) \leq 1/R_N$ we have

$$I_s \leq \frac{V}{\omega L_c} \quad I_N \leq \frac{V}{R_N} \quad I_D \simeq \omega C V . \quad (3.1.11)$$

It is evident from the equivalent circuit in Fig. 3.2 that with the additional capacitive channel we have an additional characteristic frequency

$$\omega_p \equiv \frac{1}{\sqrt{L_c C}} = \sqrt{\frac{2eI_c}{\hbar C}} . \quad (3.1.12)$$

This is the **plasma frequency** of the junction. Evidently, for $\omega < \omega_p$ the displacement current is smaller than the Josephson current.

A further characteristic frequency is defined by the $R_N C$ **time constant**

$$\omega_{RC} = \frac{1}{\tau_{RC}} \equiv \frac{1}{R_N C} = \frac{\omega_p^2}{\omega_c} \quad (3.1.13)$$

of the equivalent circuit. Evidently, the displacement current is smaller than the normal current for $\omega < 1/\tau_{RC}$.

In order to characterize the capacitance effect at all frequencies up to the frequency ω_c corresponding to the characteristic junction voltage $V_c = I_c R_N$ one can use the dimensionless parameter

$$\beta_C \equiv \frac{\omega_c^2}{\omega_p^2} = \omega_c \tau_{RC} = \frac{2e}{\hbar} I_c R_N^2 C . \quad (3.1.14)$$

This parameter has been introduced by McCumber¹ and Stewart² and therefore is referred to as the **Stewart-McCumber parameter**. Junctions with $\beta_C \ll 1$ are small capacitance and/or small resistance. These junctions have small $R_N C$ time constants ($\tau_{RC} \omega_p \ll 1$) and therefore are highly damped. In contrast, junctions with $\beta_C \gg 1$ are those with large capacitance and/or large resistance and hence have a large $R_N C$ time constant ($\tau_{RC} \omega_p \gg 1$). These junctions are weakly damped.³

3.1.3 The Fluctuation Current

In many problems it is important to take into account fluctuations (noise). In most cases, this can be done by using the **Langevin method**^{4,5} that is, by including in the system equation a random force that describes the fluctuation sources. As we will see below, for Josephson junction the system equation arises from summing up the different current contributions. Therefore, the random force is just some fluctuation current $I_F(t)$. As shown in the equivalent circuit of Fig. 3.2, the noise can be represented by a current source providing the fluctuation current.

There are three different types of fluctuations, namely thermal fluctuation, shot noise and $1/f$ noise. According to the Johnson-Nyquist formula^{6,7} for **thermal noise** the power spectral density of the current fluctuations are given by

$$S_I(f) = \frac{4k_B T}{R_N} . \quad (3.1.15)$$

We note that this expression only holds for an Ohmic resistor at

¹D.E. McCumber, J. Appl. Phys. **39**, 3113 (1968).

²W.C. Stewart, Appl. Phys. Lett. **12**, 277 (1968).

³Note that for large R_N the conductance of the resistive channel is small and hence results in small damping due to a small normal current.

⁴P. Langevin, *Sur la theorie du mouvement brownien*, Comptes Rendus **146**, 604 (1908).

⁵Sh. Kogan, *Electronic Noise and Fluctuations in Solids*, Cambridge University Press (1996).

⁶H. Nyquist, *Thermal agitation of electric charge in conductors*, Phys. Rev. **32**, 110 (1928).

⁷J.B. Johnson, *Thermal agitation of electricity in conductors*, Phys. Rev. **32**, 97 97 (1928).

$$k_B T \gg eV, \hbar\omega . \quad (3.1.16)$$

The relative intensity of the thermal noise current can be expressed by the dimensionless parameter given by the ratio of the thermal energy and the coupling energy of the Josephson junction

$$\gamma \equiv \frac{k_B T}{E_J} = \frac{2e}{\hbar} \frac{k_B T}{I_c} . \quad (3.1.17)$$

This equation can be rewritten into the form

$$\gamma \equiv \frac{I_T}{I_C} \quad \text{with} \quad I_T = \frac{2e}{\hbar} k_B T . \quad (3.1.18)$$

Here, I_T is the **thermal noise current**. Putting in numbers we see that $I_T \simeq 0.15 \mu\text{A}$ at liquid helium temperature ($T = 4.2 \text{ K}$).

If the voltage across the junction is large so that $eV \gg k_B T$ ($V > 0.5 \text{ mV}$ ($V > 0.5 \text{ mV}$ at 4.2 K)), then **shot noise** is of major importance and use the Schottky formula^{8,9} to express the power spectral density of the current fluctuations:

$$S_I(f) = 2eI_N \quad \text{at} \quad eV \gg k_B T, \hbar\omega . \quad (3.1.19)$$

At low frequencies **$1/f$ noise** often is the dominant noise source. In contrast to thermal or shot noise the physical nature of $1/f$ noise is often not clear.^{10,11,12} Typically, for Josephson junctions $1/f$ noise becomes dominant only below about 1 kHz. Therefore, in the following we will not consider the effect of $1/f$ noise, since its effect in most cases is negligible compared to the other noise sources.

3.1.4 The Basic Junction Equation

According to the discussion of the last subsections there are four essential components in the net current I flowing through the Josephson junction. Kirchhoff's law then requires that

$$I = I_s + I_N + I_D + I_F . \quad (3.1.20)$$

⁸W. Schottky, Über spontane Stromschwankungen in verschiedenen elektrischen Leitern, Ann. Physik **57**, 541 (1918).

⁹W. Schottky, Small-shot effect and flicker effect, Phys. Rev. **28**, 74 (1926).

¹⁰Sh. Kogan, *Electronic Noise and Fluctuations in Solids*, Cambridge University Press (1996).

¹¹P. Dutta, P.M. Horn, Rev. Mod. Phys. **53**, 497 (1981)

¹²F.N. Hooge, T.G.M. Kleipenning, L.K.J. Vandamme, Rep. Prog. Phys. **44**, 532 (1981).

This equation together with the voltage-phase relation

$$\frac{d\varphi}{dt} = \frac{2e}{\hbar} V \quad (3.1.21)$$

forms the basic equation for the Josephson junction. From (3.1.20) and (3.1.21) we can calculate $I(t)$ provided that $V(t)$ is known and vice versa. In principle, after writing down this equation with concrete expressions for the different current contributions the solid state physics part of the problem has been solved.

With the expressions derived above for the normal, the displacement and the fluctuation current we can express (3.1.20) as

$$I = I_c \sin \varphi + G_N(V)V + C \frac{dV}{dt} + I_F . \quad (3.1.22)$$

Using (3.1.21) we obtain

$$I = I_c \sin \varphi + G_N(V) \frac{\Phi_0}{2\pi} \frac{d\varphi}{dt} + C \frac{\Phi_0}{2\pi} \frac{d^2\varphi}{dt^2} + I_F . \quad (3.1.23)$$

This equation is nonlinear with nonlinear coefficients. Due to these nonlinearities concepts such as superposition fail. Furthermore, a nonintuitive behavior is obtained. For example, a dc driving current results in a time dependent voltage. In general, the behavior of the Josephson junction in the voltage state is governed by a complex differential equation, which in most cases has to be solved numerically. In the following we will make some simplifying assumptions to arrive at simple solutions of (3.1.23).

3.2 The Resistively and Capacitively Shunted Junction Model

To gain some insight into the dynamics of the Josephson junction we simplify the model by taking the conductance to be constant. That is, we assume

$$G(V) = G = \frac{1}{R} = \text{const} . \quad (3.2.1)$$

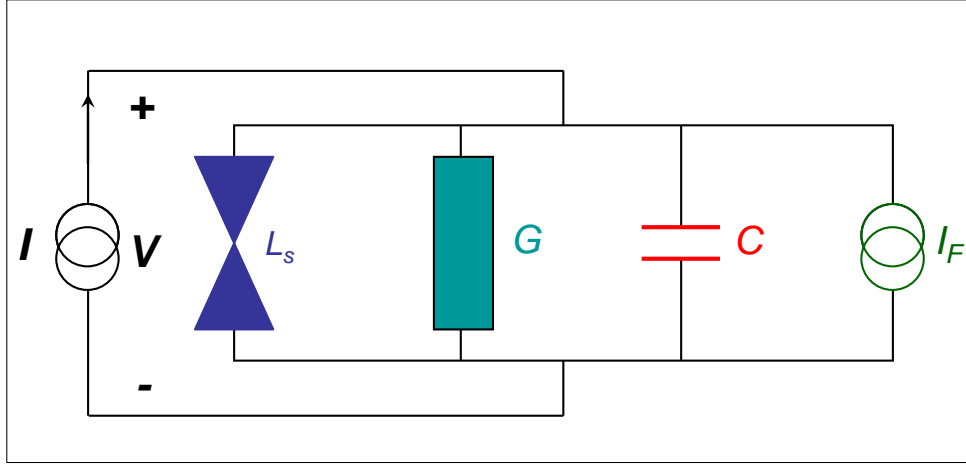


Figure 3.3: Equivalent circuit for the Resistively and Capacitively Shunted Junction Model. The Josephson junction can be characterized by the inductance $L_s = L_c / \cos \varphi$ with $L_c = \hbar / 2eI_c$, the resistive channel is approximated by a voltage independent conductance G .

We then arrive at the ***Resistively and Capacitively Shunted Junction*** (RCSJ) model. The equivalent circuit of this model is shown in Fig. 3.3. The Josephson junction is characterized by the Josephson inductance $L_s = L_c / \cos \varphi$ with $L_c = \hbar / 2eI_c$ and the resistance R is usually taken to be the normal resistance of the junction. However, more generally we can interpret R to be given by (3.1.5), so that the resistance is given by R_{sg} , if the average junction voltage is below the gap voltage, and is R_N , when the average voltage is above the gap voltage. Of course this description can only be approximate, since the junction voltage is time dependent. Nevertheless, the RCSJ-model will result in the still nonlinear but tractable differential equation. Rewriting (3.1.23) we obtain

$$\left(\frac{\hbar}{2e}\right)C \frac{d^2\varphi}{dt^2} + \left(\frac{\hbar}{2e}\right)\frac{1}{R} \frac{d\varphi}{dt} + I_c \left\{ \left[\sin \varphi - \frac{I}{I_c} + \frac{I_F(t)}{I_c} \right] \right\} = 0 . \quad (3.2.2)$$

Multiply by $\frac{\hbar}{2e}$ and using the Josephson coupling energy $E_{J0} = \hbar I_c / 2e$ and the normalized currents

$$i = \frac{I}{I_c} \quad i_F(t) = \frac{L(t)}{I_c} \quad (3.2.3)$$

we obtain

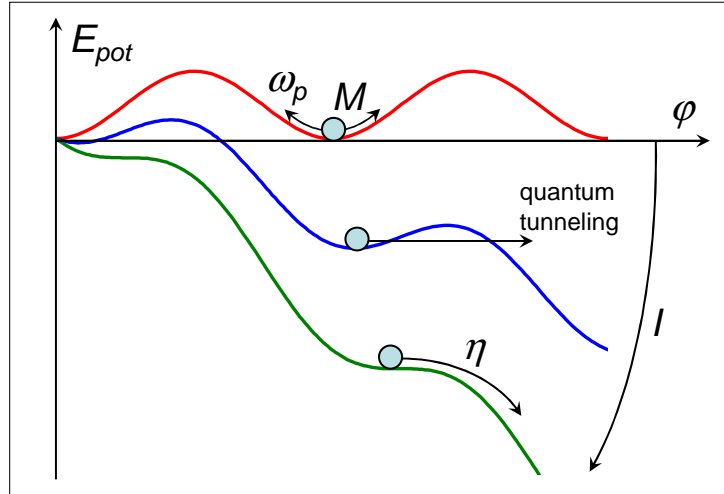


Figure 3.4: Analogy between the motion of the gauge-invariant phase difference of a Josephson junction and the damped motion of a particle of mass M in the tilt washboard potential. Note that the applied currents result in a tilt of the potential.

$$\left(\frac{\hbar}{2e}\right)^2 C \frac{d^2\varphi}{dt^2} + \left(\frac{\hbar}{2e}\right)^2 \frac{1}{R} \frac{d\varphi}{dt} + \frac{d}{d\varphi} \{E_{J0}[1 - \cos\varphi - i\varphi + i_F(t)\varphi]\} = 0 . \quad (3.2.4)$$

In order to interpret this equation of motion we compare it to the equation of motion of a particle with mass M and damping η in the potential U ,

$$M \frac{d^2x}{dt^2} + \eta \frac{dx}{dt} + \nabla U = 0 . \quad (3.2.5)$$

We immediately see that the equation of motion of the gauge-invariant phase difference of a Josephson junction is equivalent to the motion of a particle of mass M and damping η in a potential U with

$$M = \left(\frac{\hbar}{2e}\right)^2 C \quad (3.2.6)$$

$$\eta = \left(\frac{\hbar}{2e}\right)^2 \frac{1}{R} \quad (3.2.7)$$

$$U = E_{J0}(1 - \cos\varphi - i\varphi + i_F(t)\varphi) . \quad (3.2.8)$$

This situation is visualized in Fig. 3.4. We see that the mass of the potential is proportional to the capacitance and the damping proportional to $1/R$. Furthermore, the potential U is nothing else than the **tilt washboard potential** introduced in (compare (2.1.14)).

Equation (3.2.4) is often written in reduced units. By using the normalized time

$$\tau \equiv \frac{t}{\tau_c} \quad (3.2.9)$$

as well as the Stewart-McCumber parameter β_C we can write the basic equation (3.2.4) describing the Josephson junction within the RCSJ approximations as

$$\beta_C \frac{d^2\varphi}{d\tau^2} + \frac{d\varphi}{d\tau} + \sin \varphi - i - i_F(t) = 0 . \quad (3.2.10)$$

We can use the analogy between the motion of the phase and that of a particle to discuss the meaning of the plasma frequency.¹³ If we neglect damping and consider the case of zero driving current (horizontal potential in Fig. 3.4) and small amplitudes ($\sin \varphi \simeq \varphi$), we can write (3.2.10) as

$$\beta_C \frac{d^2\varphi}{d\tau^2} + \varphi = 0 . \quad (3.2.11)$$

The solution of this equation is

$$\varphi = c \cdot \exp \left(i \frac{\tau}{\sqrt{\beta_C}} \right) = c \cdot \exp \left(i \frac{t}{\sqrt{\beta_C} \tau_c} \right) = c \cdot \exp(i \omega_p t) . \quad (3.2.12)$$

That is, the plasma frequency represents the oscillation frequency of the particle around the potential minimum at small amplitudes.

We also note that there is a finite probability of the particle to tunnel through the potential well. This process is known as the macroscopic quantum tunneling of the gauge-invariant phase difference and has been observed experimentally. Furthermore, the phase particle can escape from the potential well by thermal activation. These processes will be discussed in sections 3.3.2 and 3.2.4.

3.2.1 Underdamped and Overdamped Josephson Junctions

The analogy between the motion of a “phase” particle in the tilt washboard potential and the motion of the gauge-invariant phase difference of a Josephson junction can be used to discuss the difference between underdamped and overdamped Josephson junctions. For underdamped Josephson junctions ($\beta_C = 2eI_cR^2C/\hbar \gg 1$) the junction capacitance and/or the resistance are large. That means that the mass $M \propto C$ of the particle is large and/or the damping $\eta \propto 1/R$ is small. In contrast, for overdamped junctions ($\beta_C = 2eI_cR^2C/\hbar \ll 1$) the junction capacitance and/or the resistance are small, that is, the mass M of the particle is small and/or the damping η is large.

¹³The expression plasma oscillation is used, since the oscillations show the same dispersion as plasma oscillations.

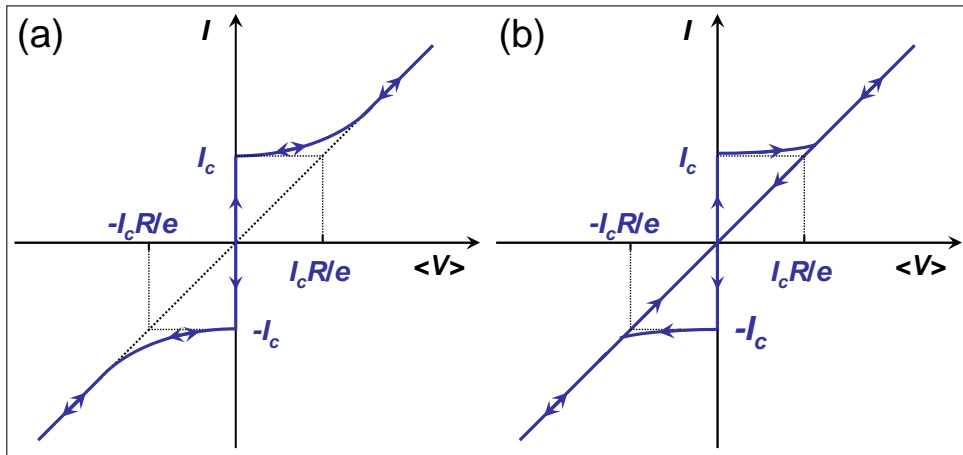


Figure 3.5: Current-voltage characteristic of an overdamped (a) and underdamped (b) Josephson junction. The arrows indicate the direction of the current variation.

Discussing the motion of the phase particle for this two limiting cases we start at an applied current larger than the critical current, that is, at a strong tilt of the potential so that the particle can move freely down the potential. Reducing the current we are reducing the tilt of the potential until at $I < I_c$ local minima are obtained. In the case of strong damping the particle will immediately stop its motion and will be trapped in one of the local minima. This is due to the small mass or equivalently small kinetic energy of the particle and the large damping. For the Josephson junction this means that the phase does no longer evolve in time and the junction switches into the zero voltage state as soon as the applied current is reduced below I_c (see Fig. 3.5a). The situation is completely different in the case of small damping. In this case the massive particle has sufficient kinetic energy and due to the small damping can easily move down the potential well even if there are local minima. In order to stop the particle, we have to bring the potential almost to the horizontal position. For the Josephson junction this means that we have to reduce the current almost to zero to achieve the zero voltage state of the junction (see Fig. 3.5b).

Starting from the zero voltage state at zero applied current and then increasing the current, both the under- and overdamped junction stay in the zero voltage state until the critical current is reached. In both cases the kinetic energy of the particle is zero and there is no reason why it should move down the potential well (we are neglecting thermally activated processes or quantum tunneling of the phase). However above the critical current the behavior is different again. Whereas in the strongly damped case the particle is moving slowly (corresponding to small voltage) at currents slightly above I_c due to the strong damping, in the underdamped case the particle is immediately accelerating to an average velocity corresponding to the average slope of the potential and the amount of damping.

This different behavior results in different current-voltage characteristics of under- and overdamped Josephson junctions. Whereas for underdamped junctions the same IVC is obtained for increasing and decreasing current, for the underdamped junction the IVC depends on whether one is decreasing or increasing the current. Decreasing the current the underdamped junction stays in the voltage state also below I_c due to the large kinetic energy and the small damping of the moving phase. Increasing the current from zero current the underdamped junction stays in the zero voltage state until the critical current because now the particle has no kinetic energy and will therefore stay in the potential minimum even at small damping. In summary, this results in a hysteretic IVC of the underdamped Josephson junction as shown schematically in Fig. 3.5b. In contrast, for overdamped junctions the mass of the phase particle and, hence, its kinetic energy is small and/or the damping is large. Therefore, the motion of the phase particle is the same for increasing and decreasing the applied current. That is, overdamped junction do not have hysteretic IVCs.

In the following subsections we will use the RCSJ-model to discuss the response of a Josephson junction to external driving sources.

3.2.2 Response to dc Driving Sources

Response to a dc Current Source

In this subsection we discuss the response of a Josephson junction to a dc current source. We first discuss the time average voltage of the junction in the presence of an applied dc current. We recall that in the voltage state we have an oscillating Josephson current. With the oscillation period T we can write

$$\langle V \rangle = \frac{1}{T} \int_0^T V(t) dt = \frac{1}{T} \int_0^T \frac{\hbar}{2e} \frac{d\varphi}{dt} dt = \frac{1}{T} \frac{\hbar}{2e} [\varphi(T) - \varphi(0)] = \frac{\Phi_0}{T}. \quad (3.2.13)$$

Here, we have used the fact that during one oscillation period the phase difference changes by 2π , that is, $\varphi(T) - \varphi(0) = 2\pi$. We see that the time-averaged voltage of the junction is determined by the flux quantum divided by the oscillation period.

We have to recall that for a driving dc current source the total current of the junction has to be constant and equal to the driving current. That is, we have

$$I = I_s(t) + I_N(T) + I_D(t) = I_c \sin \varphi(t) + \frac{V(t)}{R} + C \frac{dV(t)}{dt} = \text{const}, \quad (3.2.14)$$

where

$$\varphi(t) = \int_0^t \frac{2e}{\hbar} V(t') dt'. \quad (3.2.15)$$

We see, that for $I > I_c$ part of the current has to flow as normal or displacement current. This is only possible of course at a finite junction voltage. The finite junction voltage, in turn, results in a time varying Josephson current and, since the total current is fixed, in a temporal variation of the sum of the normal and displacement current. This results in a time varying voltage $V(t)$ and an even more complicated non-sinusoidal oscillation of the Josephson current. The oscillating voltage has to be calculated self-consistently. We immediately see that the oscillation period is $T = \Phi_0/\langle V \rangle$. The oscillation frequency is then $f = \langle V \rangle / \Phi_0$, which is just the Josephson frequency for a junction with an applied voltage equal to the average junction voltage. Of course the normal current has the same periodicity, since the sum of the currents is fixed by the applied current.

Fig. 3.6 shows the oscillating junction voltage for an applied current slightly above the critical current and for $I \gg I_c$. For $I \gtrsim I_c$ we have a highly non-sinusoidal oscillation with a long oscillation period. The time averaged voltage, which is proportional to $1/T$ is very low. In the case $I \gg I_c$ most of the current has to flow as a normal current resulting in a more constant junction voltage, that is, relative oscillation of the junction voltage is small. Then, the oscillation of the Josephson current and, in turn, the normal current is almost sinusoidal resulting in an almost sinusoidal variation of the junction voltage. Note that for a sinusoidal oscillation of the Josephson current the time-average of the Josephson current is zero. This results in a linear dependence of the time averaged voltage on the current, that is, in an ohmic IVC.

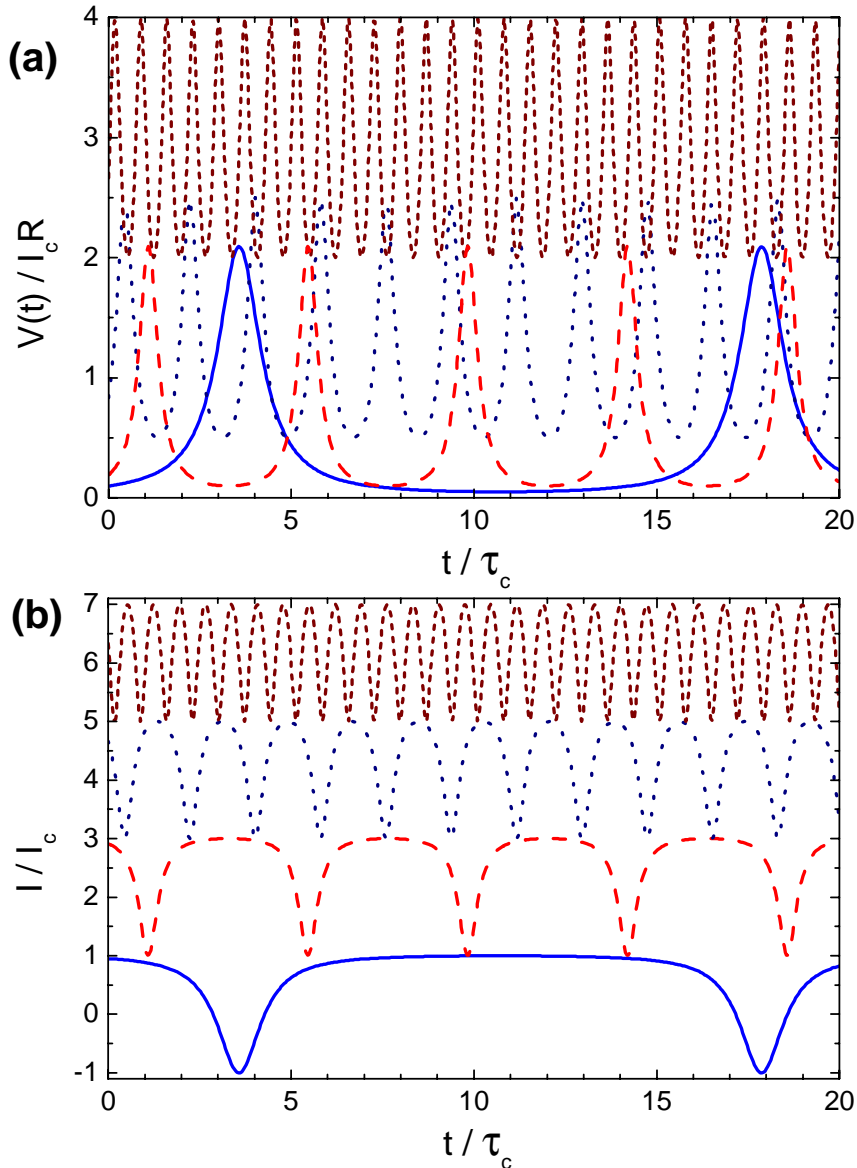


Figure 3.6: The variation of the junction voltage (a) and the Josephson current (b) with time for a current biased Josephson junctions at different values of the applied current: $I/I_c = 1.05, 1.1, 1.5$, and 3.0 . The time is normalized to $\tau_c = \hbar/2eI_c R$. In (b) the curves for $I/I_c = 1.1, 1.5$, and 3.0 are displaced vertically by 2, 4, and 6, respectively.

Current-Voltage Characteristic: Strong Damping

For strong damping, $\beta_C \ll 1$, and neglecting the noise current we can rewrite (3.2.10) as

$$\frac{d\varphi}{d\tau} + \sin \varphi - i = 0 . \quad (3.2.16)$$

If $I \leq I_c$ (i.e. $i \leq 1$) we expect that all current is flowing as supercurrent. Indeed we see that

$$\varphi = \sin^{-1} i \quad \text{for } i \leq 1 \quad (3.2.17)$$

is a solution, since φ does not depend on time. The voltage-phase relation then implies that the junction is in the zero voltage state.

When $i > 1$, the current can no longer flow as a pure supercurrent. Some of the current has to flow through the resistive channel creating a finite junction voltage that will cause a temporal evolution of the phase. Then, the full time dependence of (3.2.16) is required. Equation (3.2.16) can be solved by rewriting it as

$$d\tau = \frac{d\varphi}{i - \sin \varphi} . \quad (3.2.18)$$

Integration results in a periodic function $\varphi(t)$ with period¹⁴

$$T = \frac{2\pi\tau_c}{\sqrt{i^2 - 1}} . \quad (3.2.19)$$

With $\langle V(t) \rangle = \frac{1}{T} \int_0^T V(t) dt = \frac{\Phi_0}{T}$ (compare (3.2.13) we obtain by using $\tau_c = \frac{\Phi_0}{2\pi} \frac{1}{I_c R}$

$$\langle V(t) \rangle = IR \sqrt{1 - \left(\frac{I_c}{I}\right)^2} \quad \text{for } \frac{I}{I_c} > 1 . \quad (3.2.20)$$

This current versus time-averaged voltage curve is shown in Fig. 3.7. For $I \leq I_c$ the gauge-invariant phase difference increases according to (3.2.17), but the voltage remains zero. As the applied current exceeds the critical current I_c , part of the current must flow as a normal current through the resistive channel thereby creating a nonvanishing voltage across the junction. This results in an oscillation of the Josephson current and, in turn, of the normal current, since the total current is fixed by the external circuit. In total this results in a complex oscillation of the junction voltage as shown in Fig. 3.6. The time-averaged junction voltage is just given by the flux quantum divided by the oscillation period T .

¹⁴From the table of integrals we know that for $a^2 > 1$ we have

$$\int \frac{dx}{a - \sin x} = \frac{2}{\sqrt{a^2 - 1}} \tan^{-1} \left(\frac{-1 + a \tan(x/2)}{\sqrt{a^2 - 1}} \right) .$$

Integration of (3.2.18) then yields

$$\tau - \tau_0 = \frac{2}{\sqrt{i^2 - 1}} \tan^{-1} \left(\frac{-1 + i \tan(\varphi/2)}{\sqrt{i^2 - 1}} \right) \quad \text{for } i > 1 .$$

Here, τ_0 is an integration constant. Recalling that $\tau = t/\tau_c$ and setting the integration constant equal to zero, we can solve this equation for the gauge-invariant phase difference:

$$\varphi(t) = 2 \tan^{-1} \left\{ \sqrt{1 - \frac{1}{i^2}} \tan \left(\frac{t\sqrt{i^2 - 1}}{2\tau_c} \right) + \frac{1}{i} \right\} .$$

Although this equation is quite complex we see that $\varphi(t)$ is periodic with a period

$$T = \frac{2\pi\tau_c}{\sqrt{i^2 - 1}} .$$

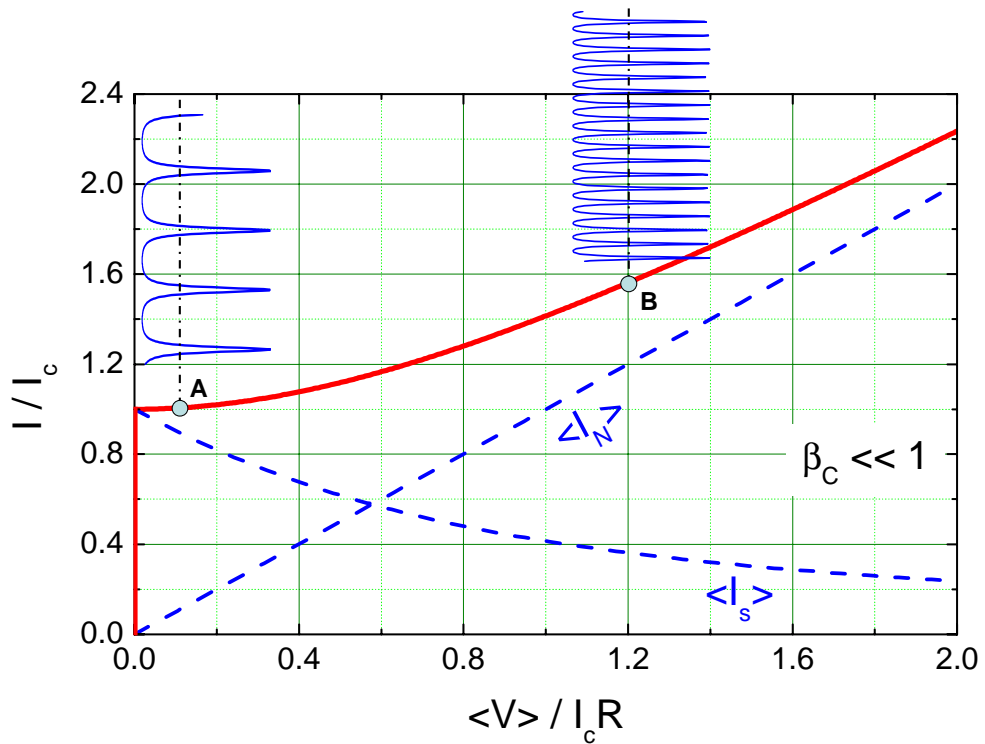


Figure 3.7: Current versus time-averaged voltage for an overdamped Josephson junction ($\beta_C \ll 1$). Also shown is the time evolution of the junction voltage $V(t)$ for two bias points A and B on the IVC.

Current-Voltage Characteristic: Weak Damping

In the underdamped case, $\beta_C \gg 1$, the characteristic frequency $\omega_{RC} = 1/R_N C$ is very small. Therefore, at almost all frequencies the large junction capacitance is effectively shunting the oscillating part of the junction voltage so that the junction voltage is almost constant: $V(t) \simeq \bar{V}$. Accordingly, the time evolution of the phase is almost linear

$$\varphi(t) = \frac{2e}{\hbar} \bar{V} t + \text{const} . \quad (3.2.21)$$

The almost linear time dependence of the gauge-invariant phase difference results in an almost sinusoidal oscillation of the Josephson current with a vanishing mean value

$$\overline{I_s(t)} = \overline{I_c \sin \left(\frac{2e}{\hbar} \bar{V} t + \text{const} \right)} \simeq 0 . \quad (3.2.22)$$

Thus, the total current has to be carried almost completely by the resistive channel and the IVC is given by an ohmic dependence

$$\bar{I} = I_N(\bar{V}) = \frac{\bar{V}}{R} \quad (3.2.23)$$

down to low voltages $\bar{V} \simeq \hbar\omega_{\text{RC}} \ll V_c = I_c R_N$. Since the related current is $\bar{I} \ll I_c$, this results in a hysteretic IVC as already discussed qualitatively above. Of course, in a real junction $R = R(V)$ and the IVC is determined by the voltage dependence of the normal resistance.

Current-Voltage Characteristic: Intermediate Damping

For $\beta_C \sim 1$ the calculation of the IVC cannot be carried out analytically even for the simplest model. Examples for numerical calculations can be found in literature.¹⁵ These calculations show that with increasing McCumber parameter the IVCs become more hysteretic (see Fig. 3.8a). The so-called **return-current** I_R , at which the junction switches back to the state is decreasing with increasing β_C . With finite damping, the return current is determined by the washboard tilt at which the energy dissipated in advancing the phase from one minimum to the adjacent exactly equals the work done by the drive current during this same motion. Using this criterion, we can calculate the normalized return current $i_R = I_R/I_c$ analytically for $\beta_C \gg 1$.

If the applied current I is close to I_R and thus for $\beta_C \gg 1$ much smaller than I_c , we can neglect both the current and the damping in zero order approximation. The junction equation then reads as $I = I_c \sin \varphi + C \frac{\phi_0}{2\pi} \frac{d^2\varphi}{dt^2}$. In this case the energy is conserved and is equal to the work $\int F dx$ (compare section 2.1.3) done by the drive current. Here the generalized force is given by the current and the generalized coordinate x by $\frac{\phi_0}{2\pi} \varphi$. That is, the energy is given by the first integral of the junction equation:

$$\begin{aligned} E &= \frac{\phi_0}{2\pi} \int_0^\varphi I d\varphi' = \frac{\phi_0}{2\pi} \int_0^\varphi \left(I_c \sin \varphi + C \frac{\phi_0}{2\pi} \frac{d^2\varphi}{dt^2} \right) d\varphi' = \frac{\Phi_0 I_c}{2\pi} \left[(1 - \cos \varphi) + \frac{1}{\omega_p^2} \int_0^t \frac{d^2\varphi}{dt'^2} \frac{d\varphi}{dt'} dt' \right] \\ &= E_{J0} \left\{ \frac{1}{2} \frac{1}{\omega_p^2} \left(\frac{d\varphi}{dt} \right)^2 + (1 - \cos \varphi) \right\}. \end{aligned} \quad (3.2.24)$$

Here, we have used $E_{J0} = \frac{\Phi_0 I_c}{2\pi}$ and $\omega_p^2 = \frac{2\pi I_c}{\Phi_0 C}$. Using this equation the energy dissipation can be expressed explicitly. Within the RSJ model we obtain

$$\begin{aligned} W_{\text{diss}} &= \int_0^T I_N V dt = \int_0^T I_N \frac{\hbar}{2e} \frac{d\varphi}{dt} dt = \int_0^{2\pi} \frac{V}{R} \frac{\hbar}{2e} d\varphi = \int_0^{2\pi} \left(\frac{d\varphi}{dt} \right) \left(\frac{\hbar}{2e} \right)^2 \frac{1}{R} d\varphi \\ &= \frac{\Phi_0 V_p}{2\pi R} \int_0^{2\pi} \left\{ 2 \left(\frac{E}{E_{J0}} - 1 + \cos \varphi \right) \right\}^{1/2} d\varphi. \end{aligned} \quad (3.2.25)$$

Here, we have used the plasma voltage

$$V_p = \omega_p \frac{\Phi_0}{2\pi} = \omega_p \frac{\hbar}{2e} = \frac{V_c}{\sqrt{\beta_C}}. \quad (3.2.26)$$

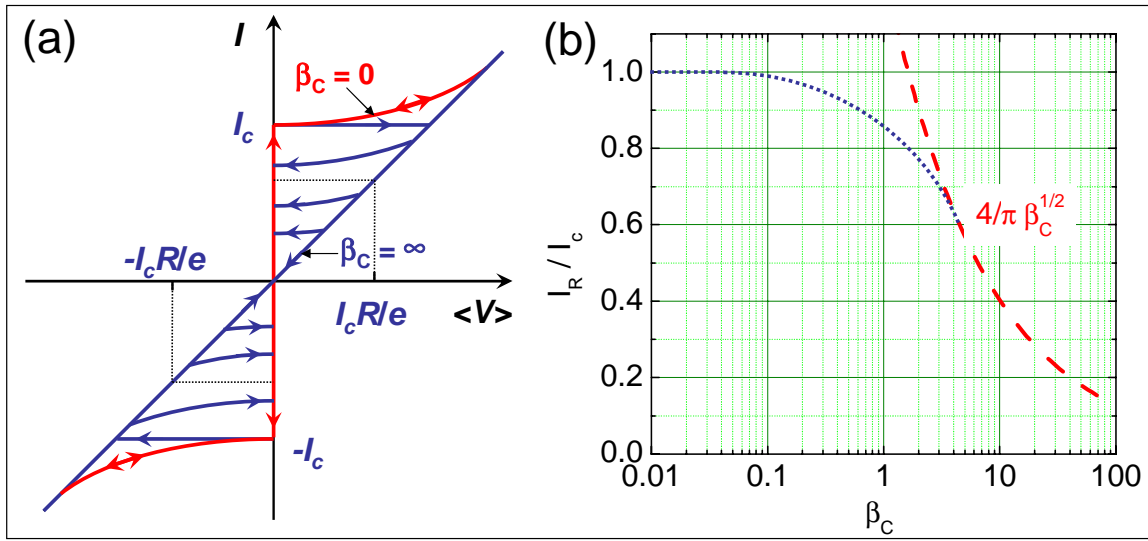


Figure 3.8: (a) RCSJ model IVCs at intermediate damping. (b) The normalized return current I_R/I_c plotted versus the Stewart-McCumber parameter β_C . The dashed line shows the large β_C approximation according to equation (3.2.28). The dotted line qualitatively shows the behavior at large damping (low β_C).

The resistive state is only possible, if the minimum value of the junction kinetic energy is positive, that is, if $E \geq 2E_{J0}$. Thus, the limit $I = I_R$ corresponds to $E = 2E_{J0}$. In this limit the right hand side of (3.2.25) can be calculated resulting in

$$W_{\text{diss}} = 4 \frac{\Phi_0 I_c}{\pi} \frac{1}{\sqrt{\beta_C}} \quad (3.2.27)$$

and hence in

$$\frac{I_R}{I_c} = \frac{4}{\pi} \frac{1}{\sqrt{\beta_C}} . \quad (3.2.28)$$

This result is plotted in Fig. 3.8b. Note that it is valid only for $\beta_C \gg 1$.

Response to a dc Voltage Source

If we drive the junction by a dc voltage source, the phase difference will evolve linearly in time as $\varphi(t) = \frac{2e}{\hbar} V_{dc} t + \text{const}$ and, in turn, the Josephson current $I_s(t) = I_c \sin \varphi(t)$ will oscillate sinusoidally. Then, the time average of the Josephson current is zero. Furthermore, since $dV/dt = 0$, also the displacement current is zero. Accordingly, the total current has to be carried by the normal current resulting in the IVC

$$I = \frac{V_{dc}}{R_N} . \quad (3.2.29)$$

¹⁵K. K. Likharev, *Dynamics of Josephson Junctions and Circuits*, Gordon and Breach Science Publishers, New York (1986).

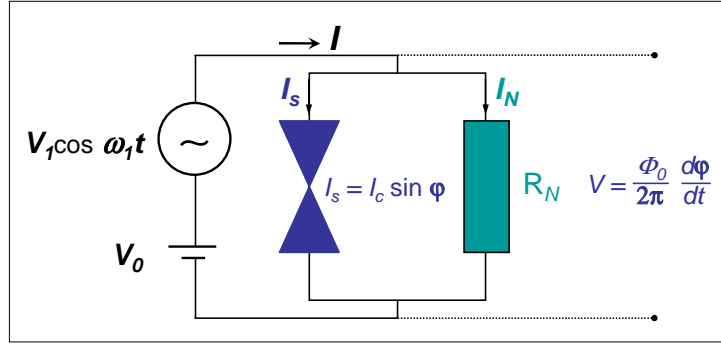


Figure 3.9: A dc and ac voltage source applied to an overdamped Josephson junction. The capacitance of the junction is assumed to be small (large damping, $\beta_C \ll 1$) so that it can be neglected.

That is, within the RCSJ model we obtain an ohmic dependence. In the more general case we have a voltage dependent resistance $R_N(V)$ and hence a nonlinear IVC.

3.2.3 Response to ac Driving Sources

In the previous section we have considered the response of a Josephson junction when it was driven by a dc source. We now use the RCSJ model to analyze the dynamics of a Josephson junction driven both by an ac and dc source. We will see that the response of the supercurrent gives rise to constant-voltage constant-voltage *Shapiro steps*¹⁶ in the IVCs, whereas the *photon-assisted tunneling* response of the quasiparticle gives rise to shifted images of the energy gap structure in the IVCs.

Response to a Voltage Source, Large Damping

We first consider the most simple case of large damping, $\beta_C \ll 1$, and an applied voltage

$$V(t) = V_{dc} + V_1 \cos \omega_1 t . \quad (3.2.30)$$

The equivalent circuit for this situation is shown in Fig. 3.9.

From the integration of the voltage-phase relation we obtain

$$\varphi(t) = \varphi_0 + \frac{2\pi}{\Phi_0} V_{dc} t + \frac{2\pi}{\Phi_0} \frac{V_1}{\omega_1} \sin \omega_1 t , \quad (3.2.31)$$

where φ_0 is an integration constant. Putting this into the current-phase relation we obtain

$$I_s(t) = I_c \sin \left\{ \varphi_0 + \frac{2\pi}{\Phi_0} V_{dc} t + \frac{2\pi}{\Phi_0} \frac{V_1}{\omega_1} \sin \omega_1 t \right\} . \quad (3.2.32)$$

¹⁶S. Shapiro, Phys. Rev. Lett. (1963).

We see that the frequency of the current is a superposition of the constant frequency $\omega_{dc} = \frac{2\pi}{\Phi_0} V_{dc}$ and a sinusoidally varying phase. Therefore, the frequency of the current is not the same as that of the driving ac voltage source. The reason for that is that the nonlinear current-phase relation can couple different frequencies with the driving frequency.

In order to analyze the time dependence of the Josephson current we rewrite (3.2.32) as a Fourier series. In order to do so we use the Fourier-Bessel series identity

$$e^{ib \sin x} = \sum_{n=-\infty}^{+\infty} J_n(b) e^{inx} . \quad (3.2.33)$$

Here, J_n is the n^{th} order Bessel function of first kind. It is evident from (3.2.32) that the argument of the sine function is of the form $(a + b \sin x)$. Hence, in order to use the identity (3.2.33) we write

$$\sin(a + b \sin x) = \Im \left\{ e^{i(a+b \sin x)} \right\} . \quad (3.2.34)$$

The Fourier-Bessel series together with the fact that $J_{-n}(b) = (-1)^n J_n(b)$ allows us to write

$$e^{i(a+b \sin x)} = \sum_{n=-\infty}^{+\infty} J_n(b) e^{i(a+nx)} = \sum_{n=-\infty}^{+\infty} (-1)^n J_n(b) e^{i(a-nx)} . \quad (3.2.35)$$

Finally, the imaginary part of (3.2.34) then gives

$$\sin(a + b \sin x) = \sum_{n=-\infty}^{+\infty} (-1)^n J_n(b) \sin(a - nx) . \quad (3.2.36)$$

With $x = \omega_1 t$, $b = \frac{2\pi V_1}{\Phi_0 \omega_1}$ and $a = \varphi_0 + \omega_{dc} t = \varphi_0 + \frac{2\pi}{\Phi_0} V_{dc} t$ we can rewrite the current equation (3.2.32) as

$$I_s(t) = I_c \sum_{n=-\infty}^{+\infty} (-1)^n J_n \left(\frac{2\pi V_1}{\Phi_0 \omega_1} \right) \sin [(\omega_{dc} - n\omega_1)t + \varphi_0] . \quad (3.2.37)$$

We see that due to the nonlinear current-phase relation we obtain a current response, in which the frequency ω_{dc} couples to multiples of the driving frequency ω_1 .

The most interesting aspect of (3.2.37) is the fact that the ac voltage source driving the junction can result in a dc current (denoted as Shapiro steps), if the argument of the sine function becomes zero. That is, we obtain a dc current response for

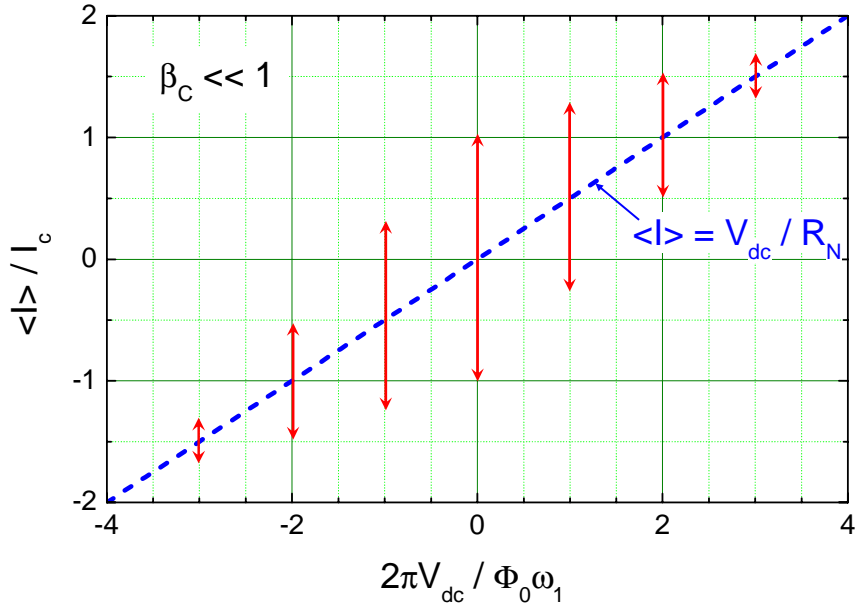


Figure 3.10: The dc component of the current plotted versus the applied dc voltage for an RSJ model junction driven by a voltage source $V(t) = V_{dc} + V_1 \cos \omega_1 t$. At the voltages $V_n = n \frac{\Phi_0}{2\pi} \omega_1$ current steps, the so called Shapiro steps appear.

$$\omega_{dc} = n\omega_1 \quad \text{or} \quad V_{dc} = V_n = n \frac{\Phi_0}{2\pi} \omega_1 . \quad (3.2.38)$$

For a specific n the amplitude of the average dc current is

$$|\langle I_s \rangle| = I_c J_n \left(\frac{2\pi V_1}{\Phi_0 \omega_1} \right) \quad (3.2.39)$$

with the detailed value depending on the initial value φ_0 .

For all other voltages $V_{dc} \neq V_n$ we have a series of sinusoidally time dependent terms with a vanishing dc component. Thus, for $V_{dc} \neq V_n$ we have

$$\langle I \rangle = \frac{V_{dc}}{R_N} + \langle \frac{V_1}{R_N} \cos \omega_1 t \rangle = \frac{V_{dc}}{R_N} . \quad (3.2.40)$$

We see that all the current has to be carried by the normal current resulting in an ohmic behavior. Only for $V_{dc} = V_n$ an average dc Josephson current appears. With respect to the IVCs this means that we have an ohmic dependence with sharp current spikes at $V_{dc} = V_n$ (see Fig. 3.10). The amplitude of the current spikes is given by (3.2.39) and depends on the amplitude V_1 of the ac source. The appearance of current steps at fixed voltages V_n has been also predicted by **B. Josephson** is due to the formation of higher harmonics of the signal frequency due to the nonlinearity of the Josephson junction. The n^{th} step corresponds to the phase locking of the junction oscillation by this n^{th} harmonic.

When we are applying for example an ac driving voltage source with $\omega_1/2\pi = 10 \text{ GHz}$ for various values of the applied dc voltage V_{dc} , a constant dc current will appear at $V_{dc} = 0$ and $V_n = n \frac{\Phi_0}{2\pi} \omega_1 \simeq n \cdot 20 \mu\text{V}$. That is, we obtain current steps in the IVCs which have constant spacing $\delta V = \frac{\Phi_0}{2\pi} \omega_1 \simeq 20 \mu\text{V}$. Note that the spacing only depends on the frequency of the ac voltage source and on fundamental constants.

Response to a Current Source, Large Damping

In most experimental arrangements the external source has a larger impedance than the Josephson junction and therefore represents a current source. In this case Kirchhoff's law allows us to write

$$I_c \sin \phi + \frac{1}{R_N} \frac{\Phi_0}{2\pi} \frac{d\phi}{dt} = I_{dc} + I_1 \sin \omega_1 t . \quad (3.2.41)$$

Here, we again have neglected the displacement current what is possible only in the limit of strong damping ($\beta_C \ll 1$) and did not take into account fluctuations.

The nonlinear differential equation (3.2.41) is difficult to solve. In order to understand what is going on we use the tilt washboard potential to perform a qualitative discussion. We recall that the current tilts the washboard potential. Therefore, the dc current can be considered to result in a constant tilt angle, whereas the ac current results in oscillations around this tilt angle with the amplitude given by the amplitude I_1 of the ac current. If we increase I_{dc} from zero at a constant ac amplitude I_1 we expect that the junction stays in the zero voltage state as long as $I_{dc} + I_1 \leq I_c$ at all times. In this case the tilt angle is always small enough so that there is a local minimum in the tilt washboard potential.

As soon as $I_{dc} + I_1 > I_c$, the phase particle can leave the local minimum and move down the washboard potential. However, due to the ac current the total current varies between $I_{dc} + I_1 > I_c$ and $I_{dc} - I_1 < I_c$. Therefore, for some part of the ac cycle the phase particle can move, whereas for the rest of the cycle it is trapped again in a local minimum. In total the motion of the particle is complicated and therefore it is difficult to calculate the resulting time-averaged voltage. An interesting situation appears when the average junction voltage reaches the values $V_n = n \frac{\Phi_0}{2\pi} \omega_1$ (compare (3.2.38)). For these values the motion of the phase particle in the tilt washboard potential is synchronized by the ac driving current. For example, if the phase particle moves from one local minimum to the adjacent one during each cycle $T = 2\pi/\omega_1$ of the ac source, there is a phase change $\phi/T = 2\pi/T = \omega_1$. This corresponds to an average voltage $\langle V \rangle = \frac{\Phi_0}{2\pi} \dot{\phi} = \frac{\Phi_0}{2\pi} \omega_1$. We see that this exactly corresponds to the voltage V_n of (3.2.38) for $n = 1$. We can generalize our discussion and assume that during each cycle of the ac source the phase particle is moving down n local minima. Then the phase change is

$$\phi = n \frac{2\pi}{T} = n \omega_1 . \quad (3.2.42)$$

This results in an average dc voltage of

$$\langle V \rangle = n \frac{\Phi_0}{2\pi} \omega_1 = V_n . \quad (3.2.43)$$

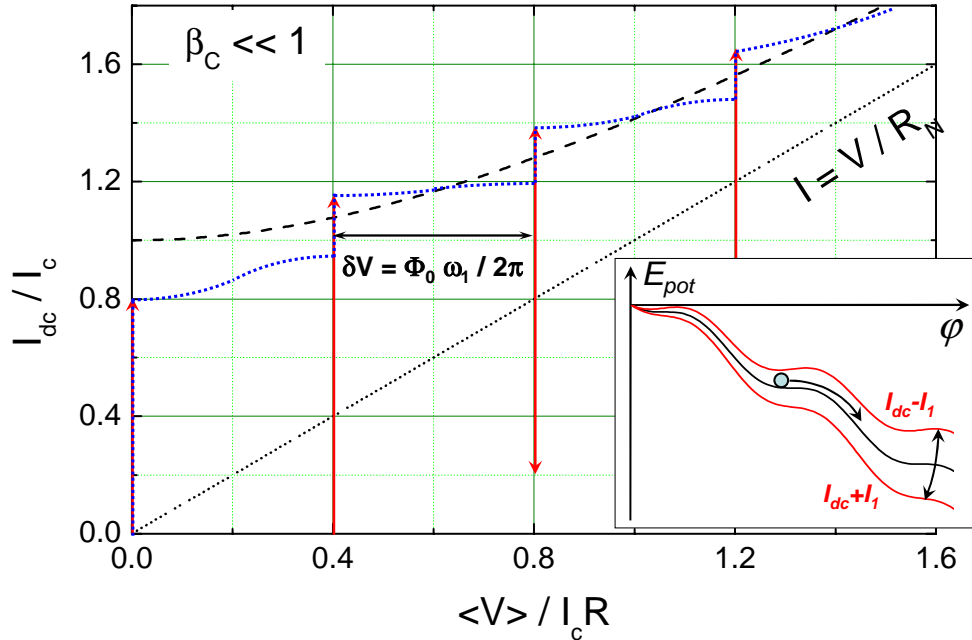


Figure 3.11: The time -averaged junction voltage plotted versus the applied dc current for an RSJ model junction driven by a current source $I(t) = I_{dc} + I_1 \sin \omega_1 t$ (dotted line). The dashed line shows the RSJ model IVC without ac driving current. The inset shows the tilt washboard potential. Due to the finite ac amplitude the tilt angle varies during one rf cycle.

We see that for the voltages V_n given by (3.2.38) the phase particle is moving down the potential well by a fixed number of minima during each cycle. That is we have a synchronization of the phase change by the external ac source. This synchronization is not only possible for a particular value of the dc current but for a complete interval of dc current. The maximum value of the dc current is given by the amplitude of the current spike according to (3.2.39).

The resulting IVC is shown schematically in Fig. 3.11 for an overdamped junction. Note that the rise of the voltage occurs at precisely the values V_n given by (3.2.38).

Response to ac Driving Sources: Intermediate Damping

So far we have discussed only the effect of strong damping by neglecting the junction capacitance. The most visible effect of the junction capacitance on the IVCs is between the current steps rather than upon the steps themselves. With the increase of β_C the supercurrent contribution to the IVCs at $\langle V \rangle \neq V_n$ decreases, so that the IVCs become hysteretic in the vicinity of each step.¹⁷

Photon-Assisted Tunneling

In the discussion of the Shapiro steps we have approximated the normal resistance by an ohmic resistance R_N . However, in a superconducting tunnel junction the normal resistance $R(V)$ is highly nonlinear with a sharp step at the gap voltage $V_g = 2\Delta/e$ manifesting itself as a strong increase of the quasiparticle current at V_g . Therefore, instead of using the simple approximation $I = V/R_N$ it is more appropriate to use the quasiparticle tunneling current $I_{qp}(V)$. However, in the $I_{qp}(V)$ curve we have to take into account the

¹⁷see e.g. K. K. Likharev, *Dynamics of Josephson Junctions and Circuits*, Gordon and Breach Science Publishers, New York (1986).

effect of the ac source on the quasiparticle tunneling. This can be done by the method introduced by **P.K. Tien and J.P. Gordon**¹⁸. They assumed that the effect of the rf driving voltage has no effect on the internal energy levels of the two electrodes but shifts these levels up or down in one electrode with respect to those in the other electrode. That means, that the energy of a quasiparticle becomes $E_{qp} + eV_1 \cos \omega_1 t$ so that the quantum mechanical phase factor $\exp(-iEt/\hbar)$ becomes frequency modulated. It can be written as

$$\exp\left(-\frac{i}{\hbar}\int(E_{qp} + eV_1 \cos \omega_1 t)dt\right) = \exp\left(-\frac{i}{\hbar}E_{qp}t\right) \cdot \exp\left(-i\frac{eV_1}{\hbar\omega_1} \sin \omega_1 t\right). \quad (3.2.44)$$

Using the Bessel function identity as discussed above we can write the factor containing V_1 as a sum of terms of the form $\mathcal{J}_n(eV_1/\hbar\omega_1)e^{-in\omega_1 t}$. This result can be interpreted as a splitting up of the quasiparticle levels into many levels at $E_{qp} \pm n\hbar\omega_1$ with probabilities given by the amplitude coefficient $\mathcal{J}_n(eV_1/\hbar\omega_1)$. With this modified density of states the quasiparticle tunneling current is obtained to

$$I_{qp}(V) = \sum_{n=-\infty}^{+\infty} \mathcal{J}_n^2\left(\frac{eV_1}{\hbar\omega_1}\right) I_{qp}^0(V + n\hbar\omega_1/e). \quad (3.2.45)$$

We see that the sharp increase of the quasiparticle tunneling current at the gap voltage is broken up into many steps of smaller current amplitude at the voltages $V_g \pm n\hbar\omega_1/e$.

Note that the steps in the quasiparticle tunneling curve resemble the Shapiro steps that occur at voltages $V_n = n\hbar\omega_1/2e$. However, there are profound differences. First, the voltage separation of the quasiparticle steps is just twice of that of the Shapiro steps because e and not $2e$ appears in the denominator. Second, the steps have no constant voltage. The sharpness of the voltage is determined by the sharpness of the increase of the quasiparticle tunneling curve at the gap voltage. Third, their amplitude varies as the square of the Bessel function of the half argument.

3.2.4 Effect of Thermal Fluctuations

In the previous subsections we have discussed the response of an RCSJ model Josephson junction to external voltage or current sources. However, in our discussion we did not take into account fluctuations. Therefore, in this section we analyze the effect of additional fluctuations. We will restrict our discussion to thermal fluctuations, which have a correlation function¹⁹

$$\langle I_F(t)I_F(t+\tau) \rangle = \frac{2k_B T}{R_N} \delta(\tau). \quad (3.2.46)$$

If the fluctuations are small, their effect are small phase fluctuations around the equilibrium value. Here, small means that the mean square of the phase fluctuations $\langle \bar{\varphi}^2 \rangle$ is much less than the width

¹⁸P.K. Tien, J.P. Gordon, Phys. Rev. **129**, 647 (1963).

¹⁹Note that according to the Wiener-Khintchine theorem the spectral density $S(f)$ of the fluctuation is twice the Fourier transform of the correlation function. That is, (3.2.46) is equivalent to $S(f) = 4k_B T/R_N$.

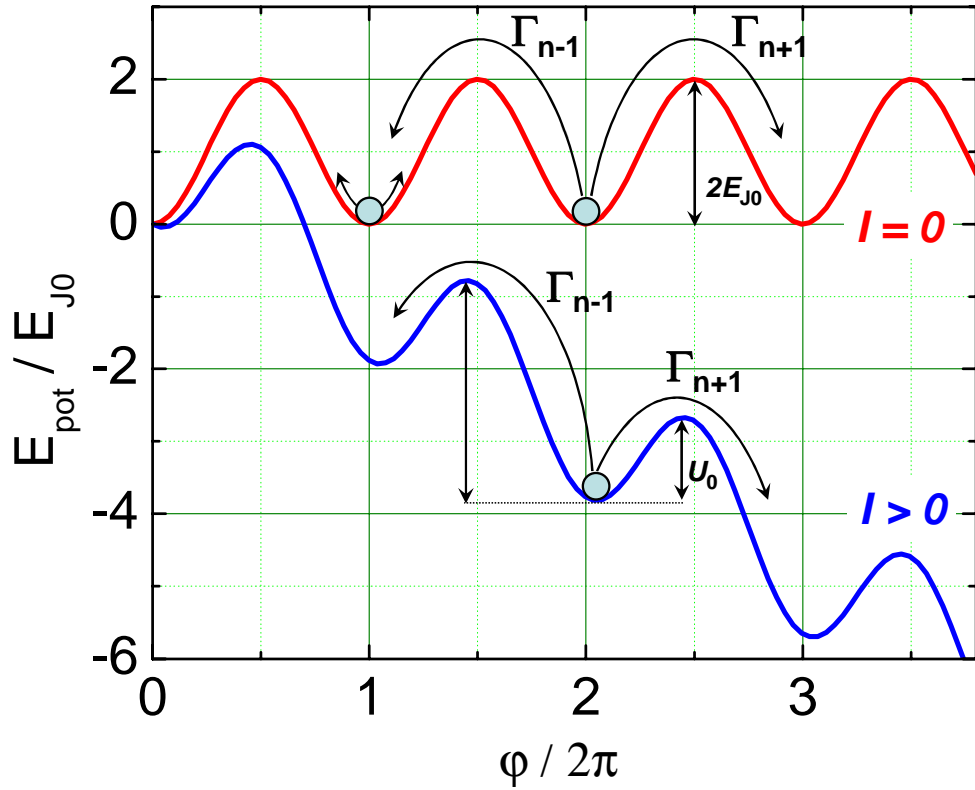


Figure 3.12: The thermally activated motion of the phase in the presence of thermal fluctuations for zero applied current and a finite applied current $I < I_c$. Small fluctuation result in fluctuations around the potential minimum. Large fluctuations result in a finite probability to escape into one of the adjacent phase states.

$$\Delta\phi = \phi'_n - \phi_n = \pi - 2\arcsin(i) \quad (3.2.47)$$

of the potential well surrounding the point ϕ_n (compare (2.1.10) and Fig. 2.3 in section 2.1.3).

If the fluctuations become larger and $\langle\bar{\phi}^2\rangle$ becomes comparable to $(\Delta\phi)^2$, there is a finite probability for the phase to escape from the local minimum of the potential well to one of the adjacent states $\phi_{n\pm 1}$. This probability can be characterized by the rates $\Gamma_{n\pm 1}$ or the corresponding lifetimes $\tau_{n\pm 1} = \hbar/\Gamma_{n\pm 1}$. This is shown in Fig. 3.12. The escape of the phase to one of the adjacent minima results in a $\pm 2\pi$ change of the phase. Whereas for zero applied external current we have $\Gamma_{n+1} = \Gamma_{n-1}$ and therefore the time-averaged change of the phase difference, $\langle\dot{\phi}\rangle$, is equal to zero, there is a net time-averaged change $\langle\dot{\phi}\rangle \neq 0$ for $I \neq 0$, since now $\Gamma_{n+1} \neq \Gamma_{n-1}$. Once the phase has escaped from the potential minimum the further evolution of the phase difference strongly depends on the damping of the junction.

In order to quantify the effect of thermal fluctuations we have to calculate the rates $\Gamma_{n\pm 1}$ as a function of the applied bias current and the intensity of the fluctuations. The simplest result can be again obtained in the framework of the RSJ model, when the Langevin equation has the form

$$I = I_c \sin \phi + \frac{1}{R_N} \frac{\Phi_0}{2\pi} \frac{d\phi}{dt} + C \frac{\Phi_0}{2\pi} \frac{d^2\phi}{dt^2} + I_F . \quad (3.2.48)$$

As the general theory of Brownian motion^{20,21} shows, this equation is equivalent to the following **Fokker-Planck equation**:^{22,23,24}

$$\frac{1}{\omega_c} \frac{\partial \sigma}{\partial t} + \frac{\partial}{\partial \varphi} (\sigma v) + \frac{1}{\beta_C} \frac{\partial}{\partial v} (\sigma [f(\varphi) - v]) = \frac{\gamma}{\beta_C^2} \frac{\partial^2 \sigma}{\partial v^2}. \quad (3.2.49)$$

Here^{25,26}

$$f(\varphi) = -\frac{1}{E_{J0}} \frac{\partial U(\varphi)}{\partial \varphi} = \frac{I}{I_c} - \sin \varphi \quad (3.2.50)$$

is the effective normalized force,

$$v = \frac{d\varphi/dt}{\omega_c} = \frac{V}{I_c R_N} \quad (3.2.51)$$

the effective normalized momentum, and $\sigma(v, \varphi, t)$ is the probability density of finding the system at a fixed point (φ, v) in phase space at the time t . After σ is found from (3.2.49), the statistical average of every variable $X(\varphi, v, t)$ can be calculated as

$$\langle X \rangle(t) = \iint_{-\infty}^{+\infty} \sigma(\varphi, v, t) X(\varphi, v, t) d\varphi dv. \quad (3.2.52)$$

For small fluctuations (3.2.49) has the simple static ($d\sigma/dt = 0$) solution

$$\sigma(v, t) = \mathcal{F}^{-1} \exp \left(-\frac{G(\varphi, \sigma)}{k_B T} \right) \quad \text{with} \quad (3.2.53)$$

$$\mathcal{F} = \iint_{-\infty}^{+\infty} \exp \left(-\frac{G(\varphi, \sigma)}{k_B T} \right) d\varphi dv, \quad (3.2.54)$$

²⁰H.A. Kramers, Physica **7**, 284 (1940).

²¹S. Chandrasekhar, Rev. Mod. Phys. **15**, 1 (1943).

²²A.D. Fokker, *Die mittlere Energie rotierender elektrischer Dipole*, Ann. Phys. **43**, 810 (1914).

²³M. Planck, *Über einen Satz der statistischen Dynamik und seine Erweiterung in der Quantentheorie*, Preuss. Akad. Wiss. (1917), p.324

²⁴The Fokker-Planck euqation has the form of a continuity equation in which the role of the flow in space is played by a quantity $J(\mathbf{r}, t)$ consisting of a drift and a diffusion flow. Depending on the meaning of the variable \mathbf{r} , it may be not only the diffusion in the configuration space but also diffusion in the space of velocities, diffusion of energy, diffusion of the phase of oscillation etc.

²⁵Yu. M. Ivanchenko, L.A. Zilberman, Sov. Phys. JETP **55**, 2359 (1968).

²⁶V. Ambegaokar, B.I. Halperin, Phys. Rev. Lett. **22**, 1364 (1969).

which is essentially the **Boltzmann distribution**. Here, $G = E - F \cdot x$ is the total energy with E the free energy. We see that we have a constant probability

$$p = \int_{-\infty}^{+\infty} dv \int_{\varphi \approx \varphi_n} \sigma(\varphi, v) d\varphi \quad (3.2.55)$$

to find the system in the n^{th} metastable state.

If the fluctuation are larger the transition rate $\Gamma_{n\pm 1}$ to the adjacent phase states becomes significant and p can change in time. The corresponding law describing the amount of phase slippage is simply

$$\frac{dp}{dt} = (\Gamma_{n+1} - \Gamma_{n-1}) p , \quad (3.2.56)$$

if $\omega_A/\Gamma_{n\pm 1} \gg 1$. Here, ω_A is the so-called **attempt frequency**. In most cases $\Gamma_{n+1} \gg \Gamma_{n-1}$. Then, in the limit $\omega_A/\Gamma_{n+1} \gg 1$ a universal expression can be derived for Γ_{n+1} and ω_A :^{27,28}

$$\Gamma_{n+1} = \frac{\omega_A}{2\pi} \exp\left(-\frac{U_0}{k_B T}\right) \quad (3.2.57)$$

with²⁹

$$\omega_A = \begin{cases} \omega_0 = \omega_p(1-i^2)^{1/4} & \text{for } \omega_0\tau \gg 1, \\ \tau^{-1} = \omega_c(1-i^2)^{1/2} & \text{for } \omega_0\tau \ll 1 \end{cases} . \quad (3.2.58)$$

Here, U_0 is given by (2.1.15) and ω_0 and ω_c are the plasma frequency and the characteristic frequency in the washboard potential tilt by the applied current $i = I/I_c$, respectively. Note that at $I = 0$ the attempt frequency ω_A is given by the plasma frequency ω_p , since this frequency represents the characteristic frequency at which the phase oscillates back and forth in the potential well. In the presence of a finite current, the potential is tilt and hence the characteristic frequency is not exactly the plasma frequency but by the frequency of small oscillations at around the minimum of the tilted washboard potential. It is evident that unless I is close to I_c we have $\omega_A \simeq \omega_p$ in good approximation. Note that in the limit of strong damping ($\beta_C = \omega_c\tau_{RC} \ll 1$) one has to replace the undamped plasma frequency by the characteristic frequency of an overdamped oscillator, namely $\omega_A = \omega_p\beta_C = \omega_p^2 R_N C = \omega_c$ (compare (3.1.14) in section 3.1.2).

²⁷H.A. Kramers, Physica 7, 284 (1940).

²⁸S. Chandrasekhar, Rev. Mod. Phys. 15, 1 (1943).

²⁹Using the notation $i = I/I_c$, the minimum of the resulting potential occurs at $\varphi = \arcsin(i)$ (compare (2.1.9)). Here, the curvature of the potential is $d^2U/d\varphi^2 = (\hbar I_c/2e)\cos\varphi = (\hbar I_c/2e)\sqrt{1-i^2}$ using the relation $\arcsin x = \arccos \sqrt{1-x^2}$. The classical frequency of small oscillations about the minimum is $\omega_A = \omega_p(1-i^2)^{1/4}$.

Underdamped Junctions: Reduction of I_c by Premature Switching

For $E_{J0} \gg k_B T$, the thermally activated escape from the potential minimum over the barrier height U_0 to the next minimum has a small probability $\propto \exp(-U_0(I)/k_B T)$ at each attempt.

The dependence of the barrier height on the applied current, $U_0(I)$, can be approximated well by

$$U_0(I) \simeq 2E_{J0} \left(1 - \frac{I}{I_c}\right)^{3/2}. \quad (3.2.59)$$

We see that $U_0 = 2E_{J0}$ for $I = 0$ and $U_0 \rightarrow 0$ for $I \rightarrow I_c$.

Since the barrier height goes to zero on approaching the critical current, the escape probability increases exponentially from a very small value $\sim \frac{\omega_p}{2\pi} \exp(-2E_{J0}/k_B T)$ at $I \ll I_c$ up to a large value $\sim \omega_p/2\pi$ at $I \simeq I_c$. Note that for an underdamped junction the phase will accelerate down the tilt washboard potential until it reaches its average velocity determined by the damping $\sim 1/R_N$ of the junction. That is, after the phase has escaped from the potential well at the current I , the junction voltage switches to the value IR_N .

Since the escape is a stochastic process, the exact escape current will be different every time ramping up the current. That is, we will measure a distribution of current values characterized by a width δI and a mean reduction ΔI_c below the critical current I_c obtained in the absence of any fluctuations. The determination of these values requires numerical calculations.³⁰ However, with the approximation (3.2.59) and the escape rate $\sim \frac{\omega_p}{2\pi} \exp(-U_0(I)/k_B T)$ the mean depression of I_c can be approximated by

$$\langle \Delta I_c \rangle \simeq I_c \left\{ 1 - \left[\frac{k_B T}{2E_{J0}} \ln \left(\frac{\omega_p \Delta t}{2\pi} \right) \right]^{2/3} \right\}. \quad (3.2.60)$$

Here, Δt is the time spent sweeping the applied current through the dense part of the distribution of observed critical current values. Since in experiments Δt is of the order of seconds and $\omega_p \sim 10^{10} \text{ 1/s}$, the logarithm typically is of the order of $\ln 10^{10} \simeq 23 \gg 1$. Since the logarithm is so large, it only weakly depends on the actual sweep rate of the applied current. Then, fluctuation effects cause a major reduction in I_c as soon as $k_B T$ is larger than about 5% of E_{J0} . One can further show that the width δI of the distribution is approximately given by the mean depression of I_c divided by the same logarithmic factor.

Overdamped Junctions: The Ambegaokar-Halperin Theory

When a thermal noise current is included into the driving term, **Ambegaokar** and **Halperin** showed³¹ that the simple IVC for overdamped Josephson junctions, $V = R_N \sqrt{I^2 - I_c^2}$ for $I > I_c$ is fundamentally modified. In particular, they found that the finite amount of phase slippage results in a nonvanishing junction voltage even in the limit $I \rightarrow 0$. The corresponding resistance is the so-called phase slip resistance

$$R_p = \lim_{I \rightarrow 0} \frac{\langle V \rangle}{I}. \quad (3.2.61)$$

³⁰T. Fulton, L.N. Dunkelberger, Phys. Rev. **B9**, 4760 (1974).

³¹V. Ambegaokar, B.I. Halperin, Phys. Rev. Lett. **22**, 1364 (1969).

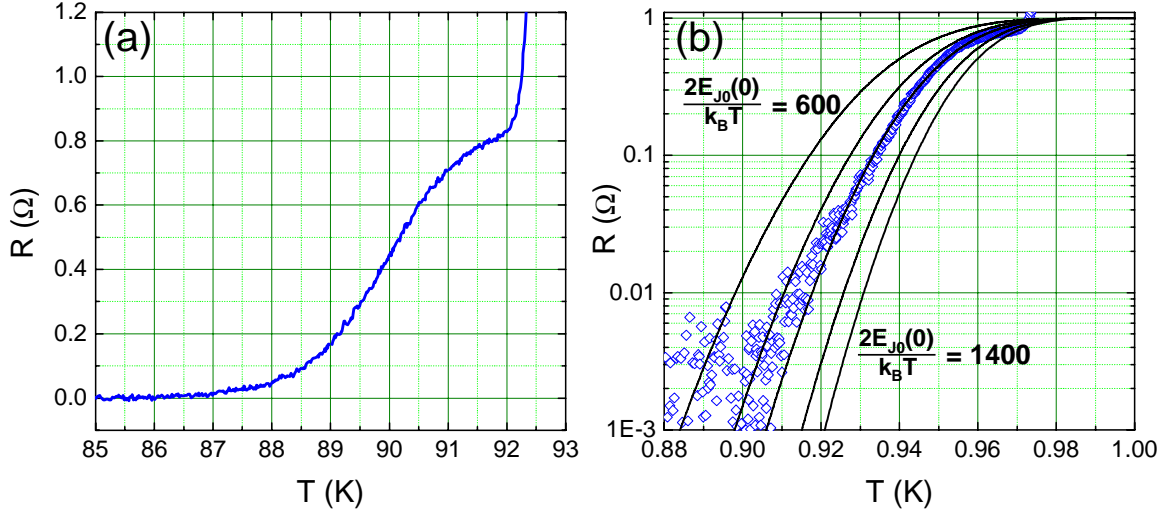


Figure 3.13: (a) Resistance versus temperature curve of a $\text{YBa}_2\text{Cu}_3\text{O}_7$ grain boundary Josephson junction showing the foot structure due to the thermally activated phase slippage. (b) Experimental $R_p(T)/R_N$ dependence (diamonds) as well as theoretical curves according to (3.2.62) and (3.2.63) for $\gamma_0(T) = \frac{\Phi_0 I_c(T)}{\pi k_B T} = \frac{2E_{J0}(0)}{k_B T} (1 - T/T_c)^2$ with $\frac{2E_{J0}(0)}{k_B T}$ ranging between 600 and 1400 (from R. Gross *et al.*, Phys. Rev. Lett. **64**, 228 (1990)).

This resistance has been calculated by **Ambegaokar** and **Halperin** for strong damping ($\beta_C \ll 1$). They obtained

$$R_p(T) = R_N \left\{ I_0 \left[\frac{\gamma_0(T)}{2} \right] \right\}^{-2} \quad \text{with} \quad (3.2.62)$$

$$\gamma_0(T) = \frac{2E_{J0}(T)}{k_B T} = \frac{\Phi_0 I_c(T)}{\pi k_B T}. \quad (3.2.63)$$

Here $I_0(x) = J_0(ix)$ is the modified Bessel function and we have used $U_0 = 2E_{J0}$ what is justified for $I \rightarrow 0$. For $E_{J0}/k_B T \gg 1$ the Bessel function dependence can be approximated by the exponential dependence $J_0(x) = e^x/2\pi\sqrt{x}$ resulting in

$$\frac{R_p(T)}{R_N} \propto E_{J0} \exp \left(-\frac{2E_{J0}}{k_B T} \right) \quad \text{or} \quad (3.2.64)$$

$$\langle \dot{\phi} \rangle \propto \frac{2eI_c R_N}{\hbar} \exp \left(-\frac{2E_{J0}}{k_B T} \right) = \omega_c \exp \left(-\frac{2E_{J0}}{k_B T} \right). \quad (3.2.65)$$

We see that the attempt frequency is given by the characteristic junction frequency ω_c and not by the plasma frequency. As already discussed above, this is caused by the strong damping ($\beta_C = \omega_c \tau_{RC} \ll 1$). In this case one has to replace the undamped plasma frequency by the characteristic frequency of an overdamped oscillator, namely $\omega_A = \omega_p \beta_C = \omega_p^2 R_N C = \omega_c$.

In terms of the tilt washboard potential model the phase particle in an overdamped Josephson junction diffuses over the barriers in a continuous process rather than making a single escape as in the underdamped limit. This difference occurs, since the strong damping brings the phase particle back into equilibrium in

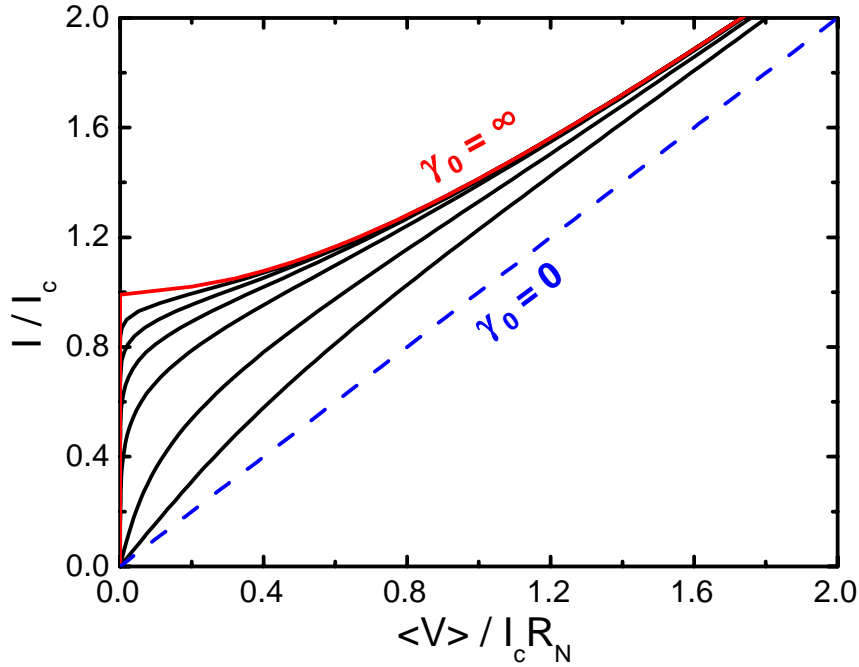


Figure 3.14: Current-voltage characteristics calculated according to (3.2.66) for a strongly overdamped Josephson junction ($\beta_C \ll 1$). The normalized barrier height was $\gamma_0 = 0, 1, 2, 5, 10, 20, 50$, and ∞ .

the next local minimum before it can diffuse to the next barrier. Therefore, it has no chance to run away as it was the case for the underdamped junction. The phase diffusion results in an activated nonlinear resistance.

Fig. 3.13 shows the temperature dependence of the normalized junction resistance, R_p/R_N , due to thermally activated phase slippage. The data are obtained for an overdamped $\text{YBa}_2\text{Cu}_3\text{O}_7$ grain boundary Josephson junction.³² The thermally activated phase slippage manifests itself as a foot structure in the $R(T)$ dependence of the Josephson junction. After the junction electrode become superconducting below the transition temperature T_c of the electrode material there is still a measurable resistance due to the thermally activated phase slippage of the junction. This resistance becomes vanishingly small only at a much lower temperature, at which the coupling energy $E_{J0}(T)$ has become sufficiently large to suppress the phase slippage. Also shown is a fit of the experimental data to equation (3.2.62). The fit can be used to determine the temperature dependence of the junction critical current $I_c(T)$. Actually, for $\text{YBa}_2\text{Cu}_3\text{O}_7$ grain boundary Josephson junctions the thermally activated phase slippage was used to determined the temperature dependence of the critical current close to T_c . A direct measurement of $I_c(T)$ close to the critical temperature is difficult because of the finite slope of the IVCs due to thermally activated phase slippage (see Fig. 3.14). Hence, it is impossible to define I_c as the current flowing without measurable resistance.

Thermally activated phase slippage causes a rounding of the IVCs of Josephson junctions at $I \sim I_c$. This is evident, because already at current values $I < I_c$ the phase can move down the tilt washboard potential due to thermal activation resulting in a finite voltage. The IVCs in the presence of thermally activated phase slippage are shown in Fig. 3.14. Of course the rounding strongly decreases with increasing γ_0 , that is, with increasing barrier height. Note that the small linear resistance at low currents is the single junction analog of the so-called ***thermally activated flux-flow*** resistance in bulk superconductors, in which the activation energy is thought to be the energy to move a fluxon rather than the energy for a phase slip in a single junction.

³²R. Gross, P. Chaudhari, D. Dimos, A. Gupta, G. Koren, *Thermally Activated Phase Slippage in High- T_c Grain Boundary Josephson Junctions*, Phys. Rev. Lett. **64**, 228 (1990).

According to Ambegaokar and Halperin, for strong damping ($\beta_C \ll 1$) the IVC can be calculated analytically giving

$$\langle V \rangle = \frac{2I_c R_N}{\gamma_0} \frac{e^{\pi\gamma_0 i} - 1}{e^{\pi\gamma_0 i}} \left\{ \int_0^{2\pi} d\varphi e^{-\gamma_0 i \varphi / 2} I_0 \left(\gamma_0 \sin \frac{\varphi}{2} \right) \right\}^{-1}, \quad (3.2.66)$$

where $i = \frac{I}{I_c}$.

We note that for small Josephson junctions ($L < \lambda_J$) the measurement of the resistance $R_p(T)$ also can be used to determine the magnetic field dependence of the critical current close to T_c . At constant temperature the magnetic field dependence of $R_p(T)$ is obtained to^{33,34}

$$R_p(B) = R_N \left\{ I_0 \left[\frac{\gamma_0(B)}{2} \right] \right\}^{-2} \quad \text{with} \quad (3.2.67)$$

$$\gamma_0(B) = \frac{2E_{J0}(B)}{k_B T} = \frac{\Phi_0 I_c(B)}{\pi k_B T}. \quad (3.2.68)$$

³³Stephan Schuster, Diploma Thesis, University of Tübingen (1993).

³⁴B. Mayer, R. Gross, S. Schuster, A. Beck, L. Alff, Appl. Phys. Lett. **62**, 783 (1993).

3.3 Secondary Quantum Macroscopic Effects

3.3.1 Quantum Consequences of the Small Junction Capacitance

In our discussion so far we have treated the Josephson junction as a classical system. Both the gauge-invariant phase difference φ and the charge $Q = CV$ have been treated as purely classical variables that in principle can be measured simultaneously with arbitrary precision.

In order to discuss the limits of this classical description let us consider a strongly underdamped junction. If the phase φ changes in time ($V \neq 0$), then the energy of the electric field is given by

$$K = \frac{1}{2}CV^2 = \frac{Q^2}{2C} = \frac{1}{2}E_{J0}\frac{\dot{\varphi}^2}{\omega_p^2} . \quad (3.3.1)$$

Here, $Q \equiv CV = \int Idt$. With the energy contribution K of the electric field and the potential energy $U_s = E_{J0}(1 - \cos \varphi)$ (compare (2.1.8)) of the junction we can express the total energy of the junction as

$$E = K + U_s = E_{J0}\left(1 - \cos \varphi + \frac{1}{2}\frac{\dot{\varphi}^2}{\omega_p^2}\right) . \quad (3.3.2)$$

We see that it is very convenient to use φ as a principle variable (coordinate) of the system. In this case $U_s(\varphi)$ should be interpreted as the potential energy and $K \propto \dot{\varphi}^2$ as the kinetic energy. Note that for an overdamped junction equation (3.3.1) does not make sense, since such junction is closely coupled to the environment through its normal current I_N and the energy is not conserved even over a short time.

Returning to the current-phase and voltage-phase relation describing the Josephson junction there is no doubt in their quantum nature. On the other hand, the structure of these equations contradicts basic quantum mechanical principles. We are assuming that all variables (observables) characterizing the state of the junction such as I , Q , V , φ , etc. can be measured simultaneously with arbitrary precision. Quantum mechanics, however, does not allow this and, in general, only the probability distribution of the variables can be calculated. From this we can conclude that the description of the Josephson junction by the current-phase and voltage-phase relation is at best an approximate description of a more precise quantum theory.

Following the recipes of quantum mechanics, we can just consider equation (3.3.2), $E = Q^2/2C + U_s(\varphi)$, to be the Hamiltonian of the junction. Using $Q = CV$ and making the operator replacement for the charge in the φ representation,³⁵ namely $Q/2e = N \rightarrow i\partial/\partial\varphi$, then the form of the Hamiltonian is

$$\mathcal{H} = E_{J0}(1 - \cos \varphi) - 4E_c \frac{\partial^2}{\partial \varphi^2} , \quad (3.3.3)$$

³⁵With $\frac{1}{2}E_{J0}\frac{\dot{\varphi}^2}{\omega_p^2}$ corresponding to $\frac{\hbar^2}{2M}\left(\frac{\partial}{\partial\varphi}\right)^2$ we obtain $\frac{\partial}{\partial\varphi} = CV/2e = Q/2e$ by using $M = (\hbar/2e)^2C$, $\omega_p^2 = 2eI_c/\hbar C$, $E_{J0} = \hbar I_c/2e$, and $\dot{\varphi} = (2e/\hbar)V$.

where $E_c = e^2/2C$ is the charging energy of the junction for a single electron charge. Note that this Hamiltonian describes only the Cooper pairs neglecting the quasiparticle degrees of freedom, which however is unimportant as soon as we consider the case $T = 0$.

The commutation rule for the operators φ and $Q/2e = -i\partial/\partial\varphi$ can be obtained from the general structure of the superconducting condensate wavefunction Ψ to

$$[\varphi, Q] = 2ie \quad \text{or} \quad [\varphi, N] = i, \quad (3.3.4)$$

where $N \equiv Q/2e$ is the deviation of the number of Cooper pairs in the junction electrodes from the equilibrium value. Equation (3.3.4) simply represents the uncertainty relation for the Cooper pairs:

$$\Delta N \cdot \Delta \varphi \geq 1. \quad (3.3.5)$$

Note that this relation is completely analogous to the uncertainty relation between the number of photons and the phase of coherent light.

Equations (3.3.3) and (3.3.4) allow us to calculate the deviations of the junction properties from those predicted by the “classical” “classical” description. These deviations are called ***secondary macroscopic effects*** to be distinguished from the ordinary or primary effects like the Josephson effect itself.^{36,37}

The degree of deviation from the classical description depends on the ratio of the two energies

$$\frac{\hbar\omega_p}{E_{J0}} = \sqrt{\frac{8E_c}{E_{J0}}}. \quad (3.3.6)$$

If $\hbar\omega_p \ll E_{J0}$, the energy levels of the system are localized near the bottom of the potential wells, that is, near the points $\varphi_n = 2\pi n$. For this case we can expand the $\cos \varphi$ in the potential energy U into a Taylor series with respect to small deviations $\tilde{\varphi} = \varphi - \varphi_n$ and neglect all terms except $\tilde{\varphi}^2/2 + \text{const}$. Then, the Hamiltonian is reduced to that of a harmonic oscillator with frequency ω_p and the energy eigenvalues

$$E_n = \hbar\omega_p \left(1 + \frac{1}{2}\right). \quad (3.3.7)$$

In order to get a feeling, in which cases the condition $\hbar\omega_p \ll E_{J0}$ or $E_c \ll E_{J0}$ holds for real Josephson junctions, we consider a planar tunnel junction of typical area $A_i = 10 \mu\text{m}^2$ with a tunneling barrier of thickness $d = 1 \text{ nm}$ and dielectric constant $\epsilon = 10$. The critical current density is $J_c = 100 \text{ A/cm}^2$ giving a coupling energy $E_{J0} \simeq 3 \times 10^{-21} \text{ J}$. With $\epsilon_0 = 8.8 \times 10^{-12} \text{ F/m}$ we obtain the junction capacitance $C = \epsilon\epsilon_0 A_i/d \simeq 9 \times 10^{-13} \text{ F}$ and, hence, $E_c \simeq 1.6 \times 10^{-26} \text{ J}$. We see, that for this typical junction area and current density the charging energy is by about 5 orders of magnitude smaller than the Josephson coupling energy. This is justifying our classical treatment of Josephson junctions in the previous section. However, we see that the classical treatment is no longer possible for very small junctions or junctions with very small critical current density. This is shown in Fig 3.15, where we have plotted the Josephson coupling energy and the charging energy as a function of the junction area for different values of the critical Josephson current density. For the typical current density $J_c = 100 \text{ A/cm}^2$ the charging energy

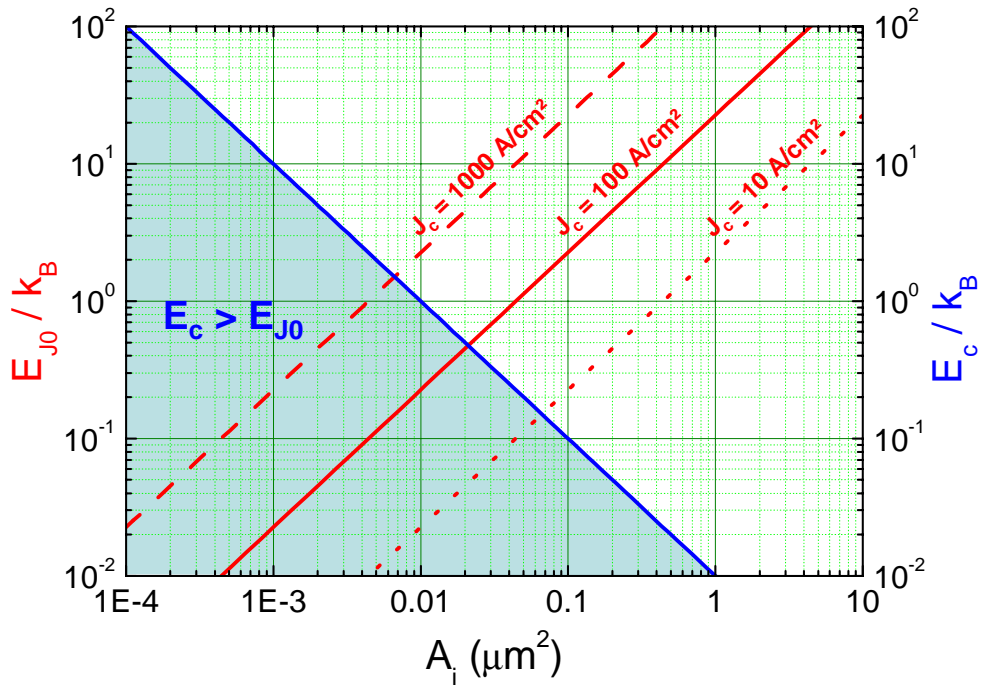


Figure 3.15: The Josephson coupling energy E_{J0} and the charging energy E_c plotted versus the junction area A_i for three different critical current densities J_c . Note that $E_{J0} \propto J_c \propto \exp(-2\kappa d)$ decreases exponentially with increasing thickness d of the tunneling barrier at constant junction area, whereas the charging energy $E_c \propto 1/C \propto d$ increases only linearly with increasing barrier thickness. We therefore have taken the charging energy the same for all three J_c values.

becomes comparable to the coupling energy at a junction area of about $0.01 \mu\text{m}^2$ corresponding to a capacitance of about 1 fF.

Our discussion shows that for $E_c/E_{J0} \ll 1$ the ground state of the system should be a narrowly peaked wavefunction centered at $\varphi = \varphi_n$ in order to minimize the dominating term E_{J0} . That is, the fluctuations in the phase are small. In contrast, for $E_c/E_{J0} \gg 1$, the term E_c is dominant and to minimize it in the ground state the wavefunction should approach a constant. That means, all values of the phase are equally probable. Since the problem is one-dimensional, it can be solved easily by numerical means. To get more insight into the physics we apply a variational approach to find an approximation to the ground state by using a trial function. For $E_c/E_{J0} \ll 1$, we use a gaussian trial function

$$\Psi(\varphi) \propto \exp\left(-\frac{\varphi^2}{4\sigma^2}\right), \quad (3.3.8)$$

where the rms spread σ in φ is chosen to minimize the expectation value of (3.3.3). For $E_c/E_{J0} \ll 1$, the minimum energy is

$$E = -E_{J0} \left[1 - \sqrt{\frac{2E_c}{E_{J0}}} \right]^2. \quad (3.3.9)$$

In the other limit, $E_c/E_{J0} \gg 1$, an appropriate trial function, which is periodic and satisfies the boundary conditions of zero slope at the edges of the cell, is

$$\Psi(\varphi) \propto (1 - \alpha \cos \varphi), \quad (3.3.10)$$

³⁶A.I. Larkin, K.K. Likharev, Yu.N. Ovchinnikov, Physica B **126**, 414 (1985).

³⁷A. Leggett, Suppl. Theor. Phys. **69**, 80 (1982).

which yields the approximate ground-state energy

$$E \simeq -\frac{E_{J0}^2}{8E_c} . \quad (3.3.11)$$

We see that in the limit $E_c/E_{J0} \gg 1$ the binding energy is of second order in E_{J0} , whereas it is of first order in the semi-classical limit of equation (3.3.9).

We finally note that in analogy with the periodic potential problem that leads to energy bands in crystals, we expect that the solution of (3.3.3) takes the form of Bloch waves

$$\Psi_q(\varphi) = u(\varphi) \exp(iq\varphi) , \quad (3.3.12)$$

where q is a “charge” or “pair number” variable and $u(\varphi)$ is periodic with period 2π . If only integer numbers of pairs are physically relevant, q is taking only integer values and Ψ would be periodic over 2π . However, q is a continuous variable, since it does not represent the total charge on an isolated piece of metal, but rather on the capacitor formed by the two junction electrodes. This charge can be varied continuously for example by a third gate electrode, which can change the charge in the junction region, although the tunnel current is restricted to the transfer of a discrete number of charges (e or $2e$ depending on whether one considers unpaired or paired electrons).

Quantum Fluctuations

Quantum mechanics shows that the classical theory of the harmonic oscillator coincides with the quantum one in all details but one: There is a finite motion of the quantum oscillator (quantum fluctuation) at the lowest energy level $n = 0$. These fluctuations can be described in a convenient way by including a Langevin force I_F to classical basic junction equation, which has the adequate statistical properties.^{38,39,40} If we assume that the junction environment is in thermal equilibrium, we can use the Callen-Welton fluctuation-dissipation theorem and write the spectral density of I_F as

$$S_I(f) = 2\pi S_I(\omega) = 2 \frac{E(\omega, T)}{R_N} . \quad (3.3.13)$$

Here, $E(\omega, T)$ is the average energy of the quantum oscillator with frequency ω at temperature T :

$$\begin{aligned} E(\omega, T) &= \frac{\hbar\omega}{2} + \hbar\omega \frac{1}{\exp\left(\frac{\hbar\omega}{k_B T}\right) - 1} \\ &= \frac{\hbar\omega}{2} \coth\left(\frac{\hbar\omega}{2k_B T}\right) . \end{aligned} \quad (3.3.14)$$

This expression describes the smooth transition from the **Johnson-Nyquist formula** (compare (3.1.15)) at low frequencies $\hbar\omega, eV$ to a purely quantum noise

$$S_I(\omega) = \frac{1}{2\pi} \frac{\hbar\omega}{R_N} \quad (3.3.15)$$

at very high frequencies ($\hbar\omega \gg k_B T, eV$).

³⁸H.B. Callen, T.E. Welton, Phys. Rev. **83**, 34 (1951).

³⁹I.R. Senitzky, Phys. Rev. **124**, 642 (1961).

⁴⁰M. Lax, Phys. Rev. **145**, 110 (1966).

3.3.2 Macroscopic Quantum Tunneling

One of the most convincing demonstrations of the quantum aspects of the Josephson effect is probably the observation of ***macroscopic quantum tunneling*** in an underdamped Josephson junction. The process of macroscopic quantum tunneling refers to the escape process of the “phase particle” from a minimum of the tilted washboard potential by tunneling through the barrier (see Fig. 3.16) rather than by thermal activation over the barrier as discussed in section 3.2.4. The process is called ***macroscopic*** because the tunneling quantity is not a single electron but the phase variable which describes the collective state of a large, macroscopic number of electrons.

Quantum effects usually are difficult to be observed on a macroscopic scale, since they involve microscopic quantities. Since in macroscopic quantum tunneling the systems switches from the zero voltage state with the phase variable trapped in a minimum of the tilted washboard potential to the voltage state, where the phase variable is running down the potential, the study of macroscopic quantum tunneling is a particularly sensitive technique to reveal quantum effects. The two states are easily to be distinguished. The only competing classical process is thermal activation over the barrier. However, this process can be frozen out by going to low enough temperatures. Another process preventing the observation of quantum effects is the presence of damping. It is reflected in the quantum hamiltonian by coupling the phase degree of freedom to an environmental hamiltonian with many degrees of freedom. In our discussion for simplicity we first neglect this coupling to the environment.

In the presence of a dc bias current, the Hamiltonian (3.3.3) is modified by the additional term $-\hbar I \varphi / 2e$. As already discussed before, the minimum of the resulting potential occurs at $\varphi = \arcsin i$ with $i = I/I_c$ (compare (2.1.9)). The curvature of the potential at the minimum is⁴¹.

$$\frac{\partial^2 U}{\partial \varphi^2} = E_{J0} \cos \varphi = E_{J0} \sqrt{1 - i^2} \quad (3.3.16)$$

and the classical frequency of small oscillations about the minimum is (compare (3.2.58))

$$\omega_A = \omega_p (1 - i^2)^{1/4}. \quad (3.3.17)$$

When solved quantum mechanically, the ground state wavefunction of a harmonic oscillator in such potential minimum is approximately gaussian, i.e. $\Psi \propto \exp(-c \cdot \tilde{\varphi}^2)$, where $\tilde{\varphi}$ is the deviation of the phase from the minimum value.⁴² However, there is one important difference between the harmonic oscillator solution and that for the tilted washboard potential: In contrast to the harmonic oscillator potential, for the tilted washboard potential the barrier is of finite width. Therefore, there is an exponentially small but finite tunneling amplitude through the barrier, which connects to an outgoing wave in the unbounded space. Therefore, the eigenstates are forming a continuum. However, only those states corresponding to the quasi-bound solutions have a high amplitude in the well of the potential. The energy width Γ of these states is given by \hbar/τ , where τ is the lifetime for the escape from the potential well.

In order to determine the wavefunction we have to solve the Schrödinger equation for the regions I to III in Fig. 3.16 and then match the solutions at the boundaries (wave matching method). However, since we are not interested in the detailed quantitative result, we disregard algebraic prefactors in the following and

⁴¹We use the relation $\arcsin x = \arccos \sqrt{1 - x^2}$

⁴²The wavefunction of the ground state of a harmonic oscillator is

$$\Psi_0 = C_0 \left(\frac{\mu \omega_0}{\pi \hbar} \right)^{1/4} \exp \left\{ -\frac{\mu \omega_0}{2\hbar} \tilde{\varphi}^2 \right\} e^{-i\omega_0 t/2}.$$

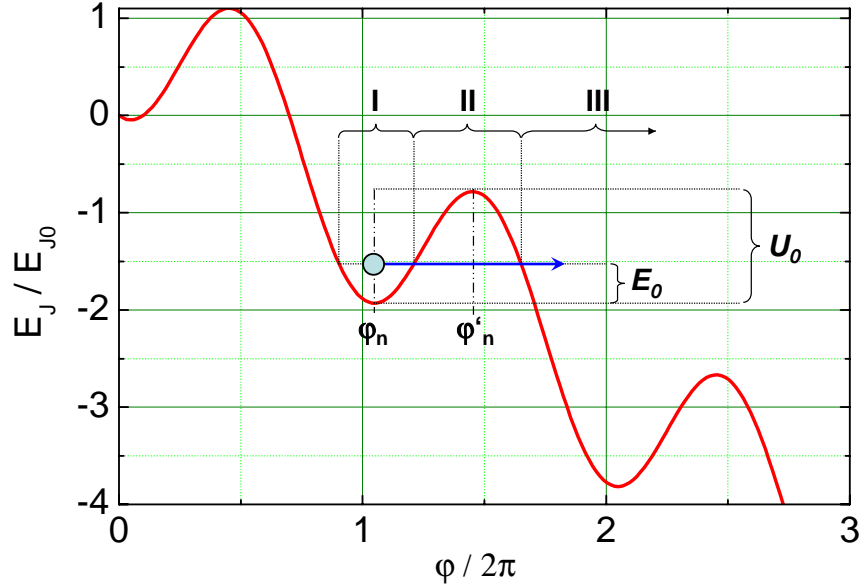


Figure 3.16: Macroscopic quantum tunneling of the gauge-invariant phase difference. U_0 is the barrier height and E_0 the energy of the “phase particle” with respect to the local minimum.

concentrate on the exponential factor, which dominates the transmission probability through the barrier. Within the WKB approximation method, in a one-dimensional situation the absolute square $|\Psi(x)|^2$ of the wavefunction of a particle with mass m and energy E decays in the barrier region as

$$|\Psi(x)|^2 \propto \exp \left\{ -\frac{2}{\hbar} \int_{\text{II}} \sqrt{2m[V(x)-E]} dx \right\}. \quad (3.3.18)$$

Here the integral extends over the region under the barrier (region II in Fig. 3.16). For a rough estimate we can use a constant average barrier height V_B of width Δx so that (3.3.18) becomes

$$|\Psi(x)|^2 \propto \exp \left\{ -\frac{2}{\hbar} \sqrt{2mV_B} \Delta x \right\}. \quad (3.3.19)$$

If $U(\varphi) \gg E_0 = \hbar\omega_0/2$ is satisfied, that is, if the ground state energy of the harmonic oscillator is much smaller than the barrier height, we can apply the quasi-classical WKB method to our problem. With respect to the Josephson junction problem we have to replace Δx by $\Delta\varphi$ and have to use $m = (\hbar/2e)^2 C$ (see (3.2.6)). Then we obtain

$$|\Psi(\varphi)|^2 \propto \exp \left\{ -\frac{2}{\hbar} \int_{\text{II}} \sqrt{2 \left(\frac{\hbar}{2e} \right)^2 C \left[U(\varphi) - \frac{\hbar\omega_0}{2} \right]} d\varphi \right\}. \quad (3.3.20)$$

With $U(\varphi) \gg \hbar\omega_0/2$ we can use the approximation $U(\varphi) - \frac{\hbar\omega_0}{2} \simeq U(\varphi)$. Again, for a rough estimate we can use a constant average barrier height U_0 of width $\Delta\varphi$ so that (3.3.20) becomes

$$|\Psi(\varphi)|^2 \propto \exp \left\{ -\sqrt{\frac{U_0}{E_c}} \Delta\varphi \right\} \quad (3.3.21)$$

with $E_c = e^2/2C$.

For small tilt angles of the washboard potential we usually (except for very small junctions) have $U_0 \simeq 2E_{J0} \gg E_c$ and $\Delta\varphi \simeq 2\pi$. Therefore, the transmission probability is very small. However, with increasing bias current both U_0 and $\Delta\varphi$ become smaller as

$$U_0 \simeq 2E_{J0}(1-i^2)^{3/2} \quad \text{and} \quad \Delta\varphi \simeq \pi\sqrt{1-i^2} \quad (3.3.22)$$

and the transmission probability can become significant.

In the following, we briefly give an estimate for the temperature T^* , at which the rate for macroscopic quantum tunneling becomes equal to that for thermal activation. Note that the rate for thermal activation is proportional to $\exp(-U_0/k_B T)$ and therefore also becomes exponentially large when increasing the bias current to the critical current. This already indicates that the temperature T^* should depend only weakly on the applied current. We start our discussion with $I \simeq 0$. In this limit, $U_0 \simeq 2E_{J0}$, $\hbar\omega_p = \sqrt{8E_{J0}E_c} \simeq 2\sqrt{U_0E_c}$. If we set $\delta\varphi \simeq \pi$, with these approximations we can rewrite (3.3.21) as

$$|\Psi(\varphi)|^2 \propto \exp\left\{-2\pi\frac{U_0}{\hbar\omega_p}\right\} \quad (3.3.23)$$

and the rates for macroscopic quantum tunneling and thermal activation become equal at the temperature

$$k_B T^* \simeq \frac{\hbar\omega_p}{2\pi}. \quad (3.3.24)$$

Taking into account the current dependent factors we see that with $\sqrt{U_0} \propto (1-i^2)^{3/4}$ and $\Delta\varphi \propto (1-i^2)^{1/2}$ the exponent in (3.3.21) scales with $(1-i^2)^{5/4}$, whereas the exponent in the Boltzmann factor $\exp(-U_0/k_B T)$ scales as $(1-i^2)^{3/2}$. That is, they differ by $(1-i^2)^{1/4}$, which exactly corresponds to the current dependence of the frequency ω_A for small oscillations around the minimum. Thus, for arbitrary currents below I_c we obtain the general result for the cross-over temperature

$$k_B T^* \simeq \frac{\hbar\omega_A}{2\pi} = \frac{\hbar\omega_p}{2\pi} (1-i^2)^{1/4}. \quad (3.3.25)$$

For a typical plasma frequency of the order of 10^{11}s^{-1} we obtain $T^* \sim 100\text{ mK}$. This temperature is easily accessible with dilution refrigerators.⁴³

Effect of Damping

In our previous discussion we have neglected the effect of damping. However, it has been found that damping strongly suppresses macroscopic quantum tunneling.⁴⁴ Due to the strong suppression of quantum tunneling the damped system follows the classical thermal activation behavior to lower temperatures.

⁴³We note that in a real experiments the rate for macroscopic quantum tunneling should also be large enough that a single event can be measured at least within the lifetime of the person doing the experiment. If a convenient rate required for an experiment is τ^{-1} , we have to satisfy also the criterion

$$\omega_A \exp\left\{-\sqrt{\frac{U_0}{E_c}} \Delta\varphi\right\} \geq \tau^{-1}.$$

With $\sqrt{U_0} \propto (1-i^2)^{3/4}$ this can of course always be done by using $i \simeq 1$. However, since due to technical reasons one usually has to use $i \leq 0.99$, this sets an upper limit for E_{J0}/E_c . Therefore, in most experiments junctions with small critical currents (typically smaller than $10\mu\text{A}$) and, hence, small E_{J0} are used.

⁴⁴H. Grabert, *Macroscopic Quantum Tunneling and Quantum Coherence in Josephson Systems*, in “Superconducting Quantum Interference Devices and their Applications”, H.-D. Hahlbohm and H. Lübbig eds., de Gruyter, Berlin (1985), p. 289.

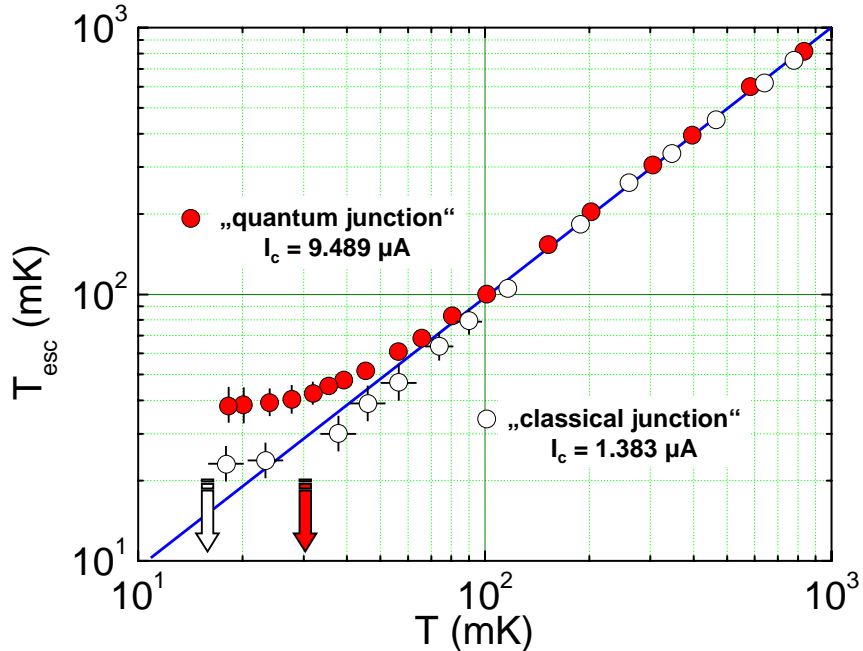


Figure 3.17: Temperature dependence of the escape rate described by an effective temperature for a “quantum junction” and a “classical junction”. The arrows mark the theoretically expected cross-over temperatures from thermal activation to macroscopic quantum tunneling (data after Martinis *et al.*, Phys. Rev. **B** 35, 4682 (1987)).

The crossover temperature T^* is in the presence of damping no longer given by (3.3.25) but by a similar expression, where ω_A has been replaced by a damping dependent frequency ω_R :

$$k_B T^* \simeq \frac{\hbar \omega_R}{2\pi} \quad (3.3.26)$$

with

$$\omega_R = \omega_A \left\{ \sqrt{1 + \alpha^2} - \alpha \right\} . \quad (3.3.27)$$

Here, $\alpha = 1/2R_N C \omega_A$ is a dimensionless damping parameter. Obviously, for $\alpha = 0$ we recover the result (3.3.24). For $\alpha \gg 1$, we obtain $\omega_R \simeq \omega_A/2\alpha = \omega_A^2 R_N C \ll \omega_A$. Hence, we obtain a much lower cross-over temperature T^* and the observation of macroscopic quantum tunneling is more difficult. The strong damping result can be understood by the fact that in the limit of strong damping one has to replace the undamped oscillation frequency ω_A around the minimum of the potential well by the characteristic frequency of an overdamped oscillator, namely by $\omega_A/2\alpha = \omega_A^2 R_N C = \omega_R$.

An experimental example is shown in Fig. 3.17, where the temperature dependence of the escape rate described by an effective temperature T_{esc} is plotted versus the sample temperature for a “quantum junction” and a “classical junction”. In the experiment the capacitance was chosen to put the sample into the lightly (quantum junction) and moderate damping regime (classical junction) in the presence of transmission line damping. Excellent agreement with theoretical predictions of the cross-over temperature was found. It is also seen that the escape temperature follows the sample temperature in the classical regime where thermal activation dominates. In the low temperature regime T_{esc} is a fictitious temperature, at which the classical thermal activation would yield the same escape rate as the actual quantum tunneling.

Phase Diffusion by Macroscopic Quantum Tunneling

An interesting situation occurs in the study of small junctions with small coupling energy and high resistance. In such junctions a finite resistance R_p is observed at low current, which is interpreted classically as resulting from phase diffusion. The temperature dependence of R_p is described at least qualitatively in terms of the classical thermally activated phase slippage (compare (3.2.62)). However, at very low temperature the data appear to bottom out at a finite, temperature independent phase slippage rate. Qualitatively this is what one would expect, if macroscopic quantum tunneling takes over below a certain cross-over temperature. Then a temperature independent value is expected for R_p determined by the rate of macroscopic quantum tunneling given by (3.3.21) with $U_0 = 2E_{J0}$ and $\Delta\varphi = \pi$. However, until now the validity of this interpretation is unclear.

3.4 Voltage State of Extended Josephson Junctions

In the previous sections we have assumed that the Josephson junction can be modelled as a lumped element. That is we have described the junction by integral quantities such as its maximum Josephson current. Such description is only possible for small Josephson junctions ($W, L < \lambda_J$) in the absence of an applied magnetic field. In this section we extend the discussion of extended Josephson junction in the zero voltage state (see section 2.2 and 2.3) to the finite voltage state.

3.4.1 Negligible Screening Effects

As we have done for the zero voltage state, for simplicity we first consider the case, where we can completely neglect the effect of the currents flowing in the junction electrodes. In this case the magnetic flux density in the junction is determined solely by the applied magnetic field: $\mathbf{B} = \mathbf{B}^{ex}$. Furthermore, the junction voltage V is given by the applied voltage V_0 throughout the junction. Then, the time dependence of the gauge-invariant phase difference is the same everywhere and given by the voltage-phase relation

$$\frac{\partial \varphi}{\partial t} = \frac{2e}{\hbar} V_0 = \omega_0 , \quad (3.4.1)$$

whereas the spatial variation is given by (3.4.7). Eqs.(3.4.1) and (3.4.7) are satisfied by a gauge-invariant phase difference given by

$$\varphi(z, t) = \varphi_0 + \omega_0 t + \frac{2\pi}{\Phi_0} B_y t_B \cdot z = \varphi_0 + \omega_0 t + k \cdot z . \quad (3.4.2)$$

This solution gives a periodic Josephson current distribution

$$J_s(z, t) = J_c \sin(\omega_0 t + k \cdot z + \varphi_0) \quad (3.4.3)$$

of exactly the same form as shown in Fig. 2.6. That is, the current distribution has the same form as the Josephson vortices in the zero voltage case except that in the case of finite voltage these vortices are moving along the z -direction with a velocity (compare section 2.2.6 and Fig. 2.12)

$$v_z = \frac{\omega_0}{k} = \frac{V_0}{B_y t_B} . \quad (3.4.4)$$

This motion of Josephson vortices is completely analogous to the motion of Abrikosov vortices in a type II superconductor.

3.4.2 The Time Dependent Sine-Gordon Equation

We now take into account the effect of the Josephson currents on the time-dependent electromagnetic fields. We consider a Josephson junction as shown in Fig.2.4. The barrier is in the yz -plane, the magnetic field is applied in y -direction resulting in phase variations along the z -direction. The applied current is flowing in the negative x -direction. The magnetic flux density in the junction results both from the externally applied field **and** the Josephson density and must satisfy Ampère's law. With $\mathbf{B} = \mu_0 \mathbf{H}$ and $\mathbf{D} = \epsilon_0 \mathbf{E}$ we obtain

$$\nabla \times \mathbf{B} = \mu_0 \mathbf{J} + \epsilon_0 \mu_0 \frac{\partial \mathbf{E}}{\partial t} . \quad (3.4.5)$$

Here, μ_0 and ϵ_0 are the permeability and permittivity in vacuum, respectively, and ϵ is the dielectric constant of the barrier material.

In contrast to section 2.2 and 2.3 we have now to take into account the term $\partial \mathbf{E} / \partial t$, which was zero in the zero voltage state of the junction. Then, for the geometry of Fig. 2.4 we obtain

$$\frac{\partial B_y(z,t)}{\partial z} = -\mu_0 J_x(z,t) - \epsilon \epsilon_0 \mu_0 \frac{\partial E_x(z,t)}{\partial t} . \quad (3.4.6)$$

Using

$$\frac{\partial \varphi(z,t)}{\partial z} = \frac{2\pi}{\Phi_0} t_B B_y(z,t) \quad (3.4.7)$$

we obtain

$$\frac{\partial^2 \varphi(z,t)}{\partial z^2} = -\frac{2\pi}{\Phi_0} t_B \left\{ \mu_0 J_x(z,t) + \epsilon \epsilon_0 \mu_0 \frac{\partial E_x(z,t)}{\partial t} \right\} . \quad (3.4.8)$$

Then, with $E_x = -V/d$, $J_x = -J_c \sin \varphi$ and $\partial \varphi / \partial t = 2\pi V / \Phi_0$ we can rewrite (3.4.8) as

$$\frac{\partial^2 \varphi(z,t)}{\partial z^2} = -\frac{2\pi}{\Phi_0} t_B \left\{ \mu_0 J_c \sin \varphi(z,t) + \epsilon \epsilon_0 \mu_0 \frac{\Phi_0}{2\pi d} \frac{\partial^2 \varphi(z,t)}{\partial t^2} \right\} . \quad (3.4.9)$$

With the definition (2.3.6) of the Josephson penetration depth, $\lambda_J \equiv \sqrt{\frac{\Phi_0}{2\pi \mu_0 t_B J_c}}$, we can rearrange this equation and obtain a wave equation for the junction known as the **time dependent Sine-Gordon equation**:

$$\frac{\partial^2 \varphi(z,t)}{\partial z^2} - \frac{1}{c^2} \frac{\partial^2 \varphi(z,t)}{\partial t^2} - \frac{1}{\lambda_J^2} \sin \varphi(z,t) = 0 . \quad (3.4.10)$$

Here,

$$\bar{c} = \sqrt{\frac{d}{\epsilon \epsilon_0 \mu_0 t_B}} = \frac{1}{\sqrt{\epsilon_0 \mu_0}} \sqrt{\frac{d}{\epsilon(2\lambda_L + d)}} = c \sqrt{\frac{1}{\epsilon(1 + 2\lambda_L/d)}} \quad (3.4.11)$$

is the velocity of the TEM mode in the transmission line formed by the two junction electrodes and the dielectric barrier named the **Swihart velocity**.⁴⁵ Since $\epsilon \sim 5 - 10$ and $2\lambda_L/d \sim 50 - 100$, the Swihart velocity is usually by more than an order of magnitude smaller than the velocity of light in vacuum. Furthermore, the wavelength is greatly reduced compared to free space. For example, microwaves at $f = 10$ GHz, which have a free-space wavelength of about 3 cm, would have a wavelength in the junction of only about 1 mm. This disparity of the wave velocities makes it difficult to couple electromagnetic energy in and out of the junction.

⁴⁵J.C. Swihart, J. Appl. Phys. **32**, 461 (1961).

3.4.3 Solutions of the Time Dependent Sine-Gordon Equation

The time dependent Sine-Gordon equation is nonlinear and has many interesting types of behavior. We only address a few simple cases. We restrict ourselves to quasi-onedimensional junctions having a width $W \ll \lambda_J$. We call these λ_J . We call these junctions *short* and *long*, if their and *large* compared to the Josephson penetration depth λ_J , respectively.

Short Junctions, Low Damping

In the short junction limit ($L \ll \lambda_J$) we can neglect the z variation of φ so that the Sine-Gordon equation reduces to

$$\frac{\partial^2 \varphi(z, t)}{\partial t^2} + \omega_p^2 \sin \varphi(z, t) = 0 \quad \text{with} \quad (3.4.12)$$

$$\omega_p^2 \equiv \frac{\bar{c}^2}{\lambda_J^2} . \quad (3.4.13)$$

This equation is equivalent to the differential equation (compare section 3.2) found from the RCSJ model approximation for zero damping ($G_N = 0$) and zero bias current ($I = 0$). This is expected, since for $L \ll \lambda_J$ the behavior of the lumped junction modelled by the RCSJ model should be recovered. Note that the definition $\omega_p^2 = 2eI_c/\hbar C$ is equivalent to the ω_p^2 value in (3.4.13) with $C/A_i = \varepsilon\varepsilon_0/d$, $I_c/A_i = J_c$ and $c^2 = 1/\varepsilon_0\mu_0$. Of course, the Sine-Gordon equation in the same way as the RCSJ model can be generalized by the inclusion of a damping term which is proportional to $\partial\varphi/\partial t$.⁴⁶ However, we will not discuss the case of finite damping here.

As already discussed in section 3.2, in the case of small amplitudes we can use the approximation $\sin \varphi \simeq \varphi$, that is, we can linearize the differential equation. In this case the solutions of (3.4.12) are plasma oscillations (compare (3.2.12)).

Finally, if λ_J is very large or the driving current is very small, we can neglect the term $\sin \varphi/\lambda_J^2$ and the Sine-Gordon equation reduces to the familiar linear wave equation

$$\frac{\partial^2 \varphi(z, t)}{\partial z^2} - \frac{1}{\bar{c}^2} \frac{\partial^2 \varphi(z, t)}{\partial t^2} = 0 . \quad (3.4.14)$$

The solutions of this equation are simply plane waves with velocity \bar{c} .

These electromagnetic waves will strongly couple to the Josephson currents, if the wave velocity \bar{c} matches the velocity v_z of the moving vortex pattern given by (3.4.4). This occurs, when the junction voltage is

$$V_{\text{Eck}} = \sqrt{\frac{d(2\lambda_L + d)}{\varepsilon}} \frac{B_y}{\sqrt{\varepsilon_0\mu_0}} = V_p \lambda_J k , \quad (3.4.15)$$

where we have used $\bar{c} = \omega_p \lambda_J$, $V_p = (\hbar/2e)\omega_p$ and $k = (\hbar/2e)t_B B_y$. The IVCs of Josephson junctions indeed show a current peak at the matching condition. This peak was first found by **R. E. Eck et al.**⁴⁷ and therefore is called the the *Eck peak*. The so-called *Eck voltage* corresponds to the to the frequency

$$\omega_{\text{Eck}} = \frac{2e}{\hbar} V_{\text{Eck}} = \omega_p \lambda_J k . \quad (3.4.16)$$

⁴⁶D.W. McLaughlin, A.C. Scott, Phys. Rev. A **18**, 1652 (1978).

⁴⁷R.E. Eck, D. J. Scalapino, B.N. Taylor, Phys. Rev. Lett. **13**, 15 (1964).

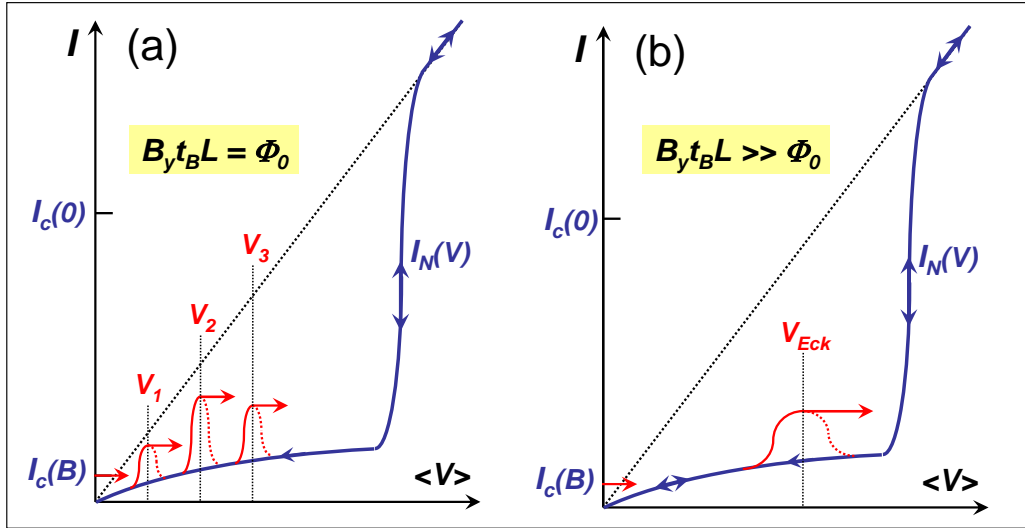


Figure 3.18: Schematic IVCs of a long Josephson tunnel junction at small damping and/or small magnetic field (a) showing the Fiske steps at voltages V_n and at medium damping and/or medium magnetic field (b) showing the Eck peak. Note that if the external source is a current bias, there will be horizontal jumps marked by the arrows, since the current is fixed by the external source.

The Eck peak can be interpreted as a result of the nonlinear interaction of the current wave given by (3.4.3) with the travelling electromagnetic wave of the same velocity. In fact the travelling wave of current (3.4.3) excites only the travelling wave of the same direction. When damping is low, the electromagnetic wave reflected at the open end of the junction transmission line can travel back almost without any loss of amplitude. Hence, a standing wave is formed. The Eck peak is therefore observed only at medium damping where the backward wave is significantly damped after reflection.

A related effect is the observation of steps in the IVCs as first found by **M. D. Fiske**.^{48,49} The **Fiske steps** occur at junction voltages V_n , where the frequency of the Josephson currents matches the frequencies

$$\omega_n = 2\pi f_n = 2\pi \frac{\bar{c}}{2L} n = \frac{\pi \bar{c}}{L} n \quad (3.4.17)$$

of the electromagnetic cavity modes, which can be regarded as standing wave modes. Note that the two junction electrodes separated by the insulating barrier can be regarded as a cavity with the eigenfrequencies given by (3.4.17). The Fiske steps occur at the voltages

$$V_n = \frac{\hbar}{2e} \omega_n = \Phi_0 \frac{\bar{c}}{2L} n = \Phi_0 \frac{\omega_p \lambda_L}{2L} n . \quad (3.4.18)$$

For a typical long junction with $L \sim 100 \mu\text{m}$ the first Fiske step occurs at frequencies of the order of 10 GHz so that the corresponding voltages are of the order of several tens of μV , which is much less than the gap voltage (e.g. $V_g \sim 3 \text{ mV}$ for Nb).

We briefly discuss the shape of the IVCs of underdamped extended junctions. For voltages that are not equal to V_{Eck} and V_n , the simple solution $J_s(z, t) = J_c \sin(\omega_0 t + k \cdot z + \phi_0)$ is a good approximation. This means that the time-average of the Josephson current vanishes, $\langle J_s \rangle = 0$, and that the IVCs are given by the ohmic line $I_N(V) = V/R_N$. However, at all dc voltages close to V_n the nonlinear interaction of the current waves (3.4.3) and the standing waves leads to narrow peaks (the Fiske steps) in the IVCs, whose

⁴⁸M.D. Fiske, Rev. Mod. Phys. **36**, 221 (1964).

⁴⁹D.D. Coon, M.D. Fiske, Phys. Rev. A **138**, 744 (1965).

height depends on the applied magnetic field and can be of the order of I_c (see Fig. 3.18). The Fiske modes appear at low damping. If the damping and/or the applied magnetic field is increasing, the width of the resonance peaks at V_n is increasing so that they are merging into a single Eck peak at V_{Eck} .

The linearized Sine-Gordon Equation: Josephson Plasma

Another class of solutions can be studied by linearizing the Sine-Gordon equation. Let

$$\varphi(z,t) = \varphi_0(z) + \varphi_1(z,t) , \quad (3.4.19)$$

where $\varphi_0(z)$ is a time independent solution and $\varphi_1(z,t)$ is a small deviation from this solution, i.e. $\varphi_1 \ll \varphi_0$. Then, a good approximation is

$$\sin \varphi \simeq \sin \varphi_0 + \varphi_1 \cos \varphi_0 . \quad (3.4.20)$$

Substitution into the Sine-Gordon equation and keeping only linear terms in φ_1 yields

$$\frac{\partial^2 \varphi_0}{\partial z^2} + \frac{\partial^2 \varphi_1(z,t)}{\partial z^2} - \frac{1}{\bar{c}^2} \frac{\partial^2 \varphi_1(z,t)}{\partial t^2} - \frac{1}{\lambda_J^2} \sin \varphi_0 - \frac{1}{\lambda_J^2} \cos \varphi_0 \varphi_1(z,t) = 0 . \quad (3.4.21)$$

With $\frac{\partial^2 \varphi_0}{\partial z^2} = \frac{1}{\lambda_J^2} \sin \varphi_0$ (φ_0 has to satisfy the time independent Sine-Gordon equation) we obtain

$$\frac{\partial^2 \varphi_1(z,t)}{\partial z^2} - \frac{1}{\bar{c}^2} \frac{\partial^2 \varphi_1(z,t)}{\partial t^2} - \frac{1}{\lambda_J^2} \cos \varphi_0 \varphi_1(z,t) = 0 . \quad (3.4.22)$$

If we further assume that φ_0 varies slowly over the scale that φ_1 changes, we can assume $\varphi_0 \simeq \text{const}$. In this case the solution is

$$\varphi_1(z,t) = \exp(-i[kz - \omega t]) \quad (3.4.23)$$

and ω has to satisfy the dispersion relation

$$\omega^2 = \bar{c}^2 k^2 + \omega_{p,J}^2 . \quad (3.4.24)$$

Here, $\omega_{p,J}$ is the Josephson plasma frequency and is given by

$$\omega_{p,J}^2 = \frac{\bar{c}^2}{\lambda_J^2} \cos \varphi_0 . \quad (3.4.25)$$

Note that for frequencies below $\omega_{p,J}$ the wave vector k is imaginary so that no propagating solutions exist. However, for $\omega > \omega_{p,J}$ modes will propagate and at $\omega = \omega_{p,J}$ the wavelength will be infinitely long just as it is for the plasma frequency in a metal. With the typical values $\bar{c} \sim 0.05c$ and $\lambda_J \sim 100 \mu\text{m}$ for Nb Josephson junctions we obtain a Josephson plasma frequency of about 10 GHz.

Large Junction Limit ($L \gg \lambda_J$), Solitons

The time dependent Sine-Gordon equation is invariant under the Lorentz transformation, in which \bar{c} plays the role of the velocity of light. This can be seen by its structure. An interesting type of solution for the (infinitely) long Josephson junction is the ***soliton*** or ***fluxon*** solution, which we already have discussed in section 2.3.2 for the stationary case. The solution has the form

$$\varphi(z, t) = 4 \arctan \left\{ \exp \left(\pm \frac{\frac{z-z_0}{\lambda_J} - \frac{v_z}{\bar{c}} t}{\sqrt{1 - \left(\frac{v_z}{\bar{c}}\right)^2}} \right) \right\}. \quad (3.4.26)$$

This solution maintains the value $\varphi = \pi$ at the moving point $z = z_0 + v_z t$ and goes from 0 to 2π as $[z - (z_0 + v_z t)]$ goes from $-\infty$ to $+\infty$ for the upper sign (“fluxon”) and vice versa for the lower sign (“anti-fluxon”). The solution represents a fluxon or anti-fluxon as shown in Fig. 2.13 moving with velocity v_z along the junction.

We note that other solutions exist for the infinitely long lossless junction representing fluxon-fluxon collisions, fluxon-anti-fluxon collisions, bound states, plasma waves etc.. Most of these solutions have been observed experimentally.^{50,51,52}

In order to discuss a simple example we consider the appearance of the so-called ***zero field steps*** in the IVCs of long Josephson junction at zero external field. When a propagating fluxon reaches the end of the junction transmission line, it is reflected back as an anti-fluxon. In a junction of length L , a full period for moving back and forth takes the time $T = 2L/v_z$. The associated phase change is 4π , since the passage of a fluxon and the return of an anti-fluxon both change φ by 2π . Thus, in the relativistic limit ($v_z \rightarrow \bar{c}$) reached at large bias current (large driving force), the dc voltage across the junction will be

$$V_{zfs} = \phi \frac{\hbar}{2e} = \frac{4\pi}{T} \frac{\hbar}{2e} = \frac{4\pi}{2L/\bar{c}} \frac{\hbar}{2e} = \frac{\hbar \bar{c}}{2eL}. \quad (3.4.27)$$

If n fluxons are present in the junction, the voltage will be n times larger. These constant voltage values are referred to as ***zero field steps***, because they are based on fluxons trapped in the junction in the absence of an external field.

⁵⁰R.A. Fulton, R.C. Dynes, Solid State Commun. **12**, 57 (1973).

⁵¹B. Duenholm, O.A. Levring, J. Mygind, N.F. Pedersen, O.H. Soerensen, M. Cirillo, Phys. Rev. Lett. **46**, 1299 (1981).

⁵²K. Nakajima, H. Mizusawa, Y. Sawada, H. Akoh, S. Takada, Phys. Rev. Lett. **65**, 1667 (1990).

Part II

Applications of the Josephson Effect

Chapter 4

Superconducting Quantum Interference Devices

Since the prediction and first experimental realization of pair tunneling in SIS systems, the technology of superconducting electronics has made much progress. Superconducting electronics based on the Josephson effect cover a large number of both analog and digital applications. The properties of Josephson tunnel junctions and their typical current-voltage characteristic (IVC) immediately suggest the following applications:

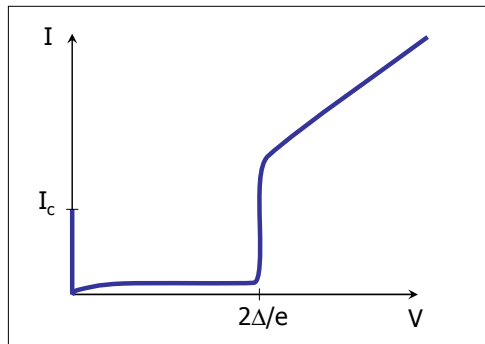


Figure 4.1: *

[IVC of tunnel junction] Schematic current-voltage characteristics (IVC) of a Josephson tunnel junction.

1. The maximum Josephson current depends on externally applied magnetic fields (see chapter 2), i.e. $I_c = I_c(B)$. The magnetic field dependence $I_c(B)$ is used in magnetic field sensors based on Superconducting Quantum Interference Devices (SQUIDs) as discussed in detail in chapter 4.
2. In an underdamped Josephson tunnel junction with $\beta_C \gg 1$ there is a bistable voltage state for $I < I_c$, namely the superconducting or **zero voltage state** and the **voltage state** with $V \sim V_g$. This bistability can be exploited in fast switching devices usable for digital circuit in Josephson computers (see chapter 5). The energy dissipation per switching process is expected to be very low.
3. The nonlinear IVC can be used in different kinds of mixers (Josephson- and QP-mixer) for frequencies up to several THz (see chapter 7).
4. The nonlinear dependence of the supercurrent on the phase difference across a Josephson junction leads to structures in the IVC with an applied ac-source (eg. Shapiro steps). The relation between

the ac frequency and the voltage/current steps can be utilized in voltage controlled oscillators (VCO) and in defining a voltage standard (see chapter 6).

The most important applications of Josephson junctions in analog and digital devices and circuits are discussed in the following chapters. We will start in this chapter with applications in superconducting quantum interference devices (SQUIDs).

4.1 Superconducting Quantum Interference Devices: SQUIDS

The discussion of the magnetic field dependence of the maximum Josephson current I_s^m as a function of the applied magnetic field in Chapter 2 already showed that there is a strong modulation of I_s^m with the applied field. Therefore, in principle a simple Josephson junction already can be used as a magnetic field sensor. However, for practical applications the sensitivity of such device is not high enough to compete with other techniques. The magnetic field dependence of the maximum Josephson current was found to have the shape of the diffraction pattern of a slit. The first minimum of the diffraction pattern is obtained, when the applied field generates one flux quantum in the junction area. Therefore, the sensitivity of the device is roughly $I_s^m/\Phi_0 = I_s^m/B_0 t_B L$, where $t_B L$ is the junction area threaded by the magnetic field. We immediately see, that we should increase the area $t_B L$ in order to increase sensitivity. Then, one flux quantum is generated already at a much smaller applied magnetic field.

The easiest way to increase the area threaded by the magnetic field is to use not only a single Josephson junction but a superconducting loop or cylinder containing one or more Josephson junctions. We will see that in this case the relevant area is determined by the cross-sectional area of the ring or cylinder and not the junction area. Devices consisting of a superconducting loop interrupted by one or more Josephson junction are denoted as *Superconducting Quantum Interference Devices* (SQUIDs). Hence, SQUIDs combine two physical phenomena, namely *flux quantization in superconducting loops* and the *Josephson effect*. Today SQUIDs are the most sensitive detectors for magnetic flux available. In essence, a SQUID is a flux to voltage converter providing a flux dependent output voltage with a period of one flux quantum. We will see that SQUIDs are very versatile. They can measure all physical quantities that can be converted into magnetic flux, for example magnetic field, magnetic field gradients, current, voltage, displacement, or magnetic susceptibility.

In this chapter we will discuss the underlying physics, the performance limits and some practical applications of SQUIDs. In doing so we will focus on two kinds of SQUIDs. The first, the so-called *direct current or dc-SQUID*¹ consists of two junctions connected in parallel on a superconducting loop. It is named dc-SQUID since it operates with a steady bias current. The second, *radio frequency or rf-SQUID*^{2,3} consists of a superconducting loop interrupted by a single junction. It operates with a radiofrequency flux bias. Historically, the dc-SQUID was used for magnetic measurements just after the first observation of macroscopic quantum interference in superconductivity.^{4,5} However, later in the late 1960s and early 1970s the rf-SQUID was preferred, mainly since it was easier to fabricate single junction interferometers using a simple point-contact. However, then in 1975 **J. Clarke** and co-workers showed that the energy sensitivity of dc-SQUIDs can be improved by using externally shunted junctions to values better than those of the rf-SQUID.⁶

¹R.C. Jaklevic, J. Lambe, A.H. Silver, J.E. Mercereau, *Quantum Interference Effects in Josephson Tunneling*, Phys. Rev. Lett. **12**, 159 (1964).

²J.E. Zimmermann, P. Thiene, J.T. Harding, *Design and Operation of Stable rf-biased Superconducting Point-contact Quantum Devices*, J. Appl. Phys. **41**, 1572 (1970).

³J.E. Mercereau, *Superconducting Magnetometers*, Rev. Phys. Appl. **5**, 13 (1970).

⁴J. Clarke, Phil. Mag. **13**, 115 (1966).

⁵R.L. Forgacs, A. Warnick, Rev. Sci. Instr. **18**, 214 (1967).

⁶J. Clarke, W.M. Goubau, M.B. Ketchen, Appl. Phys. Lett. **27**, 155 (1976); J. Low Temp. Phys. **25**, 99 (1976).

4.2 The DC SQUID

4.2.1 The Zero Voltage State

Two superconducting Josephson junctions can be combined in parallel as shown in Fig. 4.2 to obtain a superconducting quantum interference device known as the *direct current superconducting quantum interference device*. The two superconducting junctions, which we will consider as lumped elements, are connected in parallel and joined by a superconducting loop. The two junctions are assumed to have identical critical current I_c so that they are characterized by the current-phase relations $I_{s1} = I_c \sin \varphi_1$ and $I_{s2} = I_c \sin \varphi_2$. Applying Kirchhoff's law we obtain for the total current⁷

$$\begin{aligned} I_s &= I_{s1} + I_{s2} = I_c \sin \varphi_1 + I_c \sin \varphi_2 \\ &= 2I_c \cos\left(\frac{\varphi_1 - \varphi_2}{2}\right) \sin\left(\frac{\varphi_1 + \varphi_2}{2}\right). \end{aligned} \quad (4.2.1)$$

The gauge-invariant phase differences φ_1 and φ_2 can be found by considering the line integral along the contour shown in Fig. 4.2. We have to demand that the total phase change along the closed contour is $2\pi n$. Hence, in the same way as for the situation discussed in section 2.2.1 we obtain

$$\oint_C \nabla \theta \cdot d\ell = (\theta_{Q_b} - \theta_{Q_a}) + (\theta_{P_c} - \theta_{Q_b}) + (\theta_{P_d} - \theta_{P_c}) + (\theta_{Q_a} - \theta_{P_d}) = n2\pi \quad (4.2.2)$$

Using $\nabla \theta = \frac{2\pi}{\Phi_0} (\Lambda \mathbf{J}_s + \mathbf{A})$ (see (2.2.2)) and $\varphi = \theta_2 - \theta_1 - \frac{2\pi}{\Phi_0} \int_1^2 \mathbf{A} \cdot d\ell$ (see (2.2.3)) we obtain in analogy to section 2.2.1:

$$\theta_{Q_b} - \theta_{Q_a} = +\varphi_1 + \frac{2\pi}{\Phi_0} \int_{Q_a}^{Q_b} \mathbf{A} \cdot d\ell \quad (4.2.3)$$

$$\theta_{P_d} - \theta_{P_c} = -\varphi_2 + \frac{2\pi}{\Phi_0} \int_{P_c}^{P_d} \mathbf{A} \cdot d\ell \quad (4.2.4)$$

$$\theta_{P_c} - \theta_{Q_b} = \int_{Q_b}^{P_c} \nabla \theta \cdot d\ell = +\frac{2\pi}{\Phi_0} \int_{Q_b}^{P_c} \Lambda \mathbf{J}_s \cdot d\ell + \frac{2\pi}{\Phi_0} \int_{Q_b}^{P_c} \mathbf{A} \cdot d\ell \quad (4.2.5)$$

$$\theta_{Q_a} - \theta_{P_d} = \int_{P_d}^{Q_a} \nabla \theta \cdot d\ell = +\frac{2\pi}{\Phi_0} \int_{P_d}^{Q_a} \Lambda \mathbf{J}_s \cdot d\ell + \frac{2\pi}{\Phi_0} \int_{P_d}^{Q_a} \mathbf{A} \cdot d\ell. \quad (4.2.6)$$

Substitution of (4.2.3) – (4.2.6) into (4.2.2) yields

⁷We use $\sin \alpha + \sin \beta = 2 \sin\left(\frac{\alpha+\beta}{2}\right) \cos\left(\frac{\alpha-\beta}{2}\right)$.

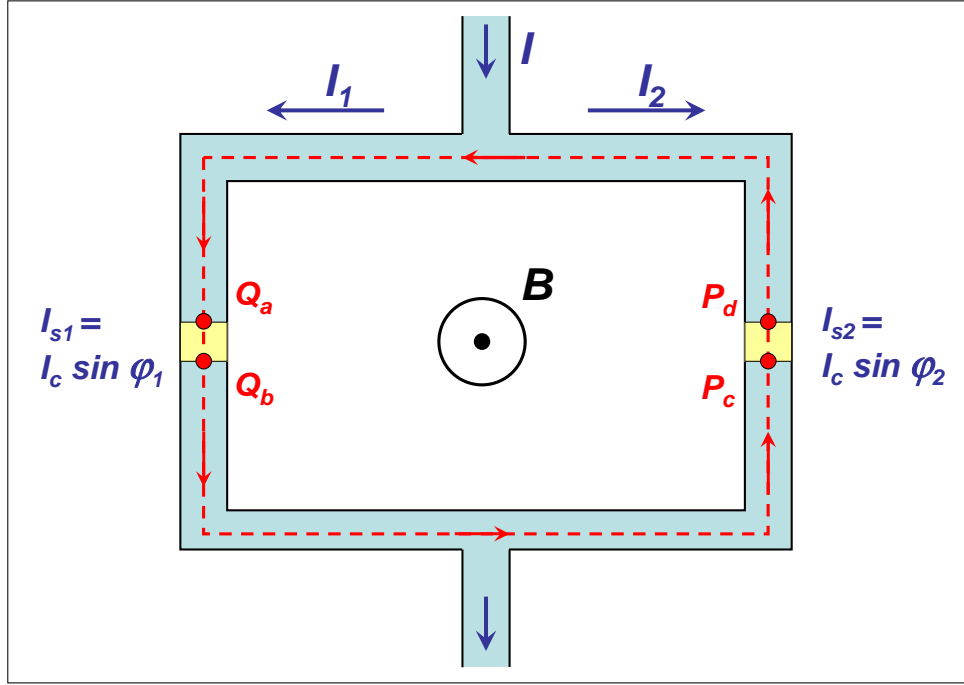


Figure 4.2: The dc-SQUID formed by two Josephson junctions intersecting a superconducting loop. The upper and the lower part of the loop can be represented by the macroscopic wave functions $\Psi_2 = \Psi_{20} \exp(i\theta_2)$ and $\Psi_1 = \Psi_{10} \exp(i\theta_1)$, respectively. The broken line indicates the closed contour path of the integration.

$$\varphi_2 - \varphi_1 = 2\pi n + \frac{2\pi}{\Phi_0} \oint_C \mathbf{A} \cdot d\ell + \frac{2\pi}{\Phi_0} \int_{Q_b}^{P_c} \Lambda \mathbf{J}_s \cdot d\ell + \frac{2\pi}{\Phi_0} \int_{P_d}^{Q_a} \Lambda \mathbf{J}_s \cdot d\ell . \quad (4.2.7)$$

The integration of \mathbf{A} is around a close contour and therefore is equal to the total flux Φ enclosed by the superconducting loop. The integration of \mathbf{J}_s follows the same contour C but excludes the integration over the insulating barrier. Furthermore, if the superconducting loop consists of a superconducting material with a thickness large compared to the London penetration depth λ_L , the integration path can be taken deep inside the superconducting material where the current density is negligible. Therefore, the two integrals involving the current density can be omitted and we obtain

$$\varphi_2 - \varphi_1 = 2\pi n + \frac{2\pi\Phi}{\Phi_0} . \quad (4.2.8)$$

Using this expression we can rewrite (4.2.1) as

$$I_s = 2I_c \cos\left(\pi \frac{\Phi}{\Phi_0}\right) \sin\left(\varphi_1 + \pi \frac{\Phi}{\Phi_0}\right) . \quad (4.2.9)$$

If the flux Φ threading the loop would be given by the flux Φ_{ext} due to the applied field, we would have solved the problem. Then, the maximum supercurrent of the parallel combination would be just given by

$$I_s^m = 2I_c \left| \cos\left(\pi \frac{\Phi}{\Phi_0}\right) \right|. \quad (4.2.10)$$

However, in many cases we have to take into account the finite inductance L of the superconducting loop. Then, the flux Φ threading the loop is given by the sum

$$\Phi = \Phi_{\text{ext}} + \Phi_L \quad (4.2.11)$$

due to the applied magnetic field and the currents flowing in the loop. If we assume that the two sides of the loop are identical, we can write the currents flowing in the two arms of the loop as

$$I_{s1} = \tilde{I} + I_{\text{cir}} \quad (4.2.12)$$

$$I_{s2} = \tilde{I} - I_{\text{cir}}, \quad (4.2.13)$$

where

$$\tilde{I} = \frac{I_{s1} + I_{s2}}{2} \quad \text{and} \quad I_{\text{cir}} = \frac{I_{s1} - I_{s2}}{2} \quad (4.2.14)$$

are the average current common in both arms and the current circulating in the loop, respectively. Note that only the latter generate a net magnetic flux in the loop with the total flux then given by

$$\begin{aligned} \Phi &= \Phi_{\text{ext}} + LI_{\text{cir}} = \Phi_{\text{ext}} + \frac{LI_c}{2} (\sin \varphi_1 - \sin \varphi_2) \\ &= \Phi_{\text{ext}} + LI_c \sin\left(\frac{\varphi_1 - \varphi_2}{2}\right) \cos\left(\frac{\varphi_1 + \varphi_2}{2}\right). \end{aligned} \quad (4.2.15)$$

Using (4.2.8), we can write the total flux threading the loop as an explicit function of Φ_{ext} and φ_1 :

$$\Phi = \Phi_{\text{ext}} - LI_c \sin\left(\pi \frac{\Phi}{\Phi_0}\right) \cos\left(\varphi_1 + \pi \frac{\Phi}{\Phi_0}\right). \quad (4.2.16)$$

We see that we have now two equations, (4.2.9) and (4.2.16), which determine the behavior of the dc-SQUID. These two equations have to be solved self-consistently. The maximum current I_s^m that can be sent through the SQUID at a given Φ_{ext} has to be found by maximizing (4.2.9) with respect to φ_1 ,

however, with the constraint given by (4.2.16). This problem has been solved first by **R. de Bruyn Ouboter** and **A.Th.A.M. de Waele**.⁸

In order to analyze limiting cases we introduce the so-called *screening parameter* β_L defined as

$$\beta_L \equiv \frac{2LI_c}{\Phi_0} . \quad (4.2.17)$$

This parameter represents the ratio of the magnetic flux generated by the maximum possible circulating current $I_{\text{cir}} = I_c$ and $\Phi_0/2$.

Negligible Screening: $\beta_L \ll 1$

In the case $\beta_L \ll 1$ the flux generated by the circulating current is small compared to the flux quantum and therefore can be neglected compared to Φ_{ext} . At a given Φ_{ext} the maximum supercurrent of the dc-SQUID is found by maximizing (4.2.9) with respect to φ_1 . From the condition $dI_s/d\varphi_1 = 0$ we obtain

$$\cos\left(\varphi_1 + \pi \frac{\Phi_{\text{ext}}}{\Phi_0}\right) = 0 . \quad (4.2.18)$$

Thus, at the maximum we have $\sin\left(\varphi_1 + \pi \frac{\Phi_{\text{ext}}}{\Phi_0}\right) = \pm 1$ and the maximum value of the supercurrent is found by taking the sign of the sine term. That is, we obtain the result

$$I_s^m \simeq 2I_c \left| \cos\left(\pi \frac{\Phi}{\Phi_0}\right) \right| . \quad (4.2.19)$$

which is of course equivalent to (4.2.10). As shown in Fig. 4.3, I_s^m is a periodic function of the external flux. Note that for a loop area of 2 mm^2 an applied field of 1 nT results in $\Phi_{\text{ext}} = \Phi_0$, that is, the periodicity of the curve corresponds to the very small field of 1 nT , which is more than four orders of magnitude smaller than the earth magnetic field.

Large Screening: $\beta_L \gg 1$

For large inductance L we have $LI_c \gg \Phi_0$ and the circulating current tends to compensate the applied flux. The loop of the SQUID looks more and more like the single loop formed by a superconducting wire. This situation was discussed already in section 1.2 when we discussed flux quantization in multiply connected superconductors. Consequently the total flux in the loop will tend to be quantized:

$$\Phi = \Phi_{\text{ext}} + LI_{\text{cir}} \simeq n\Phi_0 . \quad (4.2.20)$$

⁸ R. de Bruyn Ouboter, A.Th.A.M. de Waele, *Superconducting Point Contacts Weakly Connecting Two Superconductors*, Progress in Low Temp. Phys. VI, C.J. Gorter ed., Elsevier Science Publishers (1970).

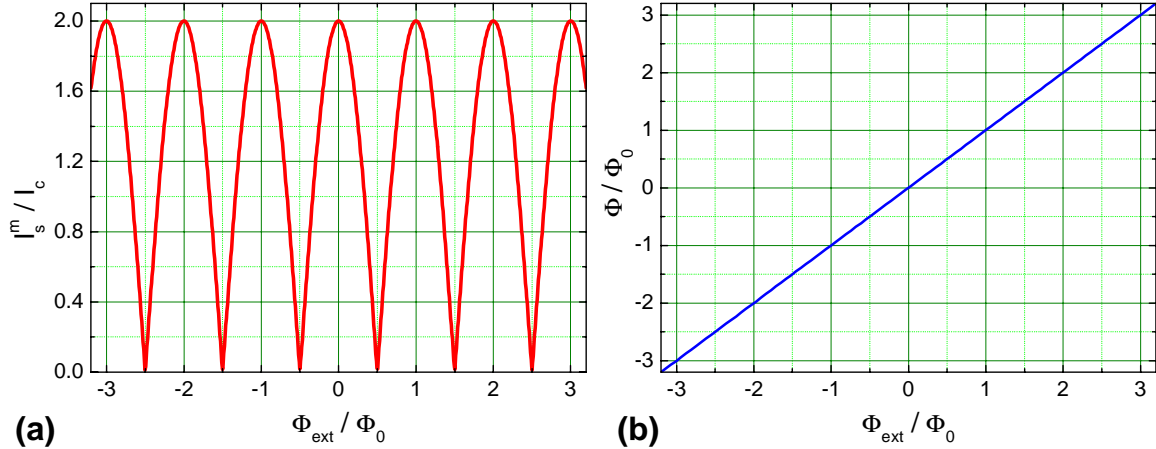


Figure 4.3: (a) The maximum supercurrent I_s^m plotted versus the applied magnetic flux Φ_{ext} for a dc-SQUID with two identical Josephson junctions in the limit $\beta_L \ll 1$. In (b) the flux threading the SQUID loop is plotted versus the applied flux Φ_{ext} .

Let us consider the case of large screening a bit more closely. The transport supercurrent through the SQUID is the sum of the currents passing junction 1 and 2:

$$I_s = I_c \sin \varphi_1 + I_c \sin \varphi_2 . \quad (4.2.21)$$

On the other hand, the circulating screening current is given by

$$I_{\text{cir}} = \frac{I_c}{2} (\sin \varphi_1 - \sin \varphi_2) . \quad (4.2.22)$$

Both (4.2.21) and (4.2.22) are constraint by the condition

$$\varphi_2 - \varphi_1 = 2\pi n + \frac{2\pi\Phi}{\Phi_0} . \quad (4.2.23)$$

Note that here the magnetic flux is the sum of the external flux Φ_{ext} and the flux $\Phi_{\text{cir}} = LI_{\text{cir}}$ due to the screening current. Given the applied current I and the total flux Φ we have two equations for the two phase differences $\varphi_{1,2}$ and hence can solve for them and finally for Φ_{cir} and Φ_{ext} . For example, if $I \approx 0$, we have $\varphi_1 \simeq -\varphi_2$ and obtain

$$\begin{aligned} \Phi_{\text{ext}} &= \Phi + LI_c \sin \left(\pi \frac{\Phi}{\Phi_0} \right) \quad \text{or} \\ \frac{\Phi_{\text{ext}}}{\Phi_0} &= \frac{\Phi}{\Phi_0} + \frac{\beta_L}{2} \sin \left(\pi \frac{\Phi}{\Phi_0} \right) . \end{aligned} \quad (4.2.24)$$

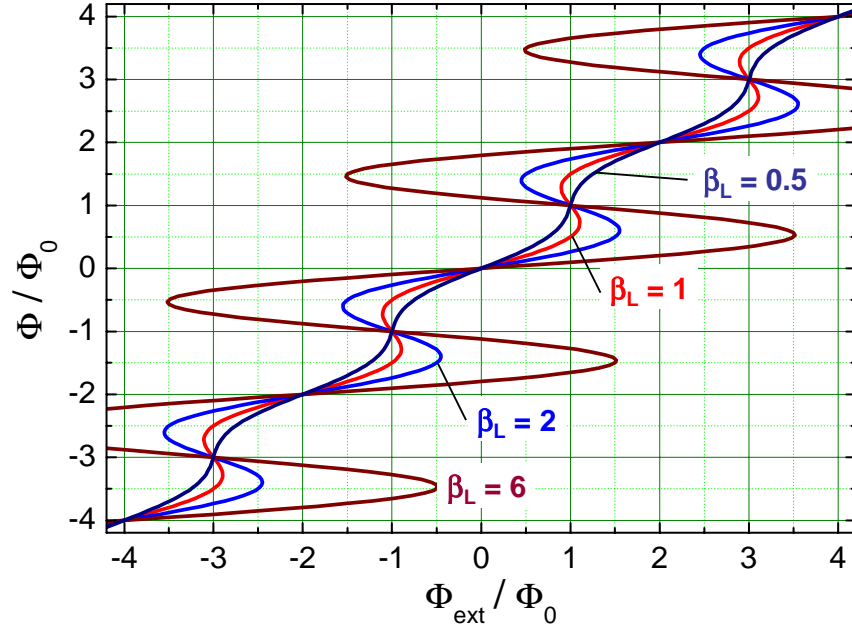


Figure 4.4: The total magnetic flux Φ plotted versus the applied magnetic flux Φ_{ext} for a dc-SQUID with two identical Josephson junctions for different values of the screening parameter β_L .

This relationship of course can be inverted to obtain Φ as a function of Φ_{ext} as shown in Fig. 4.4.

An interesting case occurs for $\Phi = n\Phi_0$, for which $\varphi_1 = \varphi_2 + n2\pi$, so that $I_{\text{cir}} = 0$ and $\Phi = \Phi_{\text{ext}}$. We see that the SQUID response to Φ_{ext} in integer multiples of Φ_0 is not affected by the screening. However, for practical application it is often required that the relation between Φ and Φ_{ext} is single-valued and non-hysteretic. As shown by Fig. 4.4 this is possible only for small values of the screening parameter β_L . This results from the fact that the maximum possible value of Φ_{cir} is LI_c . Since roughly speaking a multivalued relationship between Φ and Φ_{ext} can be avoided only for $|\Phi_{\text{cir}}| \leq \Phi_0/2$, we immediately see that this is equivalent to $LI_c \leq \Phi_0/2$ or $\beta_L = 2LI_c/\Phi_0 \leq 1$. A more detailed analysis shows that a hysteretic $\Phi(\Phi_{\text{ext}})$ dependence can be avoided for $\beta_L \leq 2/\pi$.

We still have to discuss the dependence of the supercurrent on the applied magnetic flux. From (4.2.20) we obtain for large β_L

$$I_{\text{cir}} \simeq -\frac{\Phi_{\text{ext}} - n\Phi_0}{L} . \quad (4.2.25)$$

We see that $I_{\text{cir}} \rightarrow 0$ for large L . Then, the applied current divides about equally in the two SQUID arms. The maximum current is obtained to $I_s^m \simeq 2I_c$. When n is initially zero, a small screening current $I_{\text{cir}} \simeq -\Phi_{\text{ext}}/L$ will flow to screen the applied magnetic field. Therefore, the current I_1 will tend to decrease and I_2 to increase with increasing Φ_{ext} . However, since $I_2 \leq I_c$, it will be fixed at I_c as I_1 decreases as

$$I_1 \simeq I_c - \frac{2\Phi_{\text{ext}}}{L} . \quad (4.2.26)$$

With this expression for I_1 and $I_2 \simeq \text{const}$ we obtain

$$I_s^m \simeq 2I_c - \frac{2\Phi_{\text{ext}}}{L} \quad \text{or} \quad (4.2.27)$$

$$\frac{I_s^m}{2I_c} \simeq 1 - \frac{2\Phi_{\text{ext}}}{\Phi_0} \frac{1}{\beta_L}. \quad (4.2.28)$$

We see that the modulation of the maximum supercurrent of the SQUID by the applied magnetic flux is strongly decreasing with increasing β_L roughly proportional to $1/\beta_L$.

4.2.2 The Voltage State

Practical dc-SQUIDs are not operated in the zero voltage state. They are operated at a constant bias current above the maximum supercurrent $I_s^m(0)$ at zero applied magnetic flux. That is, the SQUID is in the voltage state. We will show that in this situation the dc-SQUID produces an output voltage that is related to the applied magnetic flux.

Negligible Screening: $\beta_L \ll 1$, strong damping: $\beta_C \ll 1$

In order to discuss the dependence of the junction voltage on the applied magnetic flux we start with the limit of negligible screening. In this case the total flux in the SQUID loop is just given by the applied flux. We further assume that the junction capacitance is negligible small, that is, we consider the case of strongly overdamped Josephson junctions ($\beta_C \ll 1$) and that the two junctions are identical. Then, we only have to consider the Josephson current and the resistive current giving

$$\begin{aligned} I &= I_c \sin \varphi_1 + I_c \sin \varphi_2 + \frac{V}{R_N} + \frac{V}{R_N} \\ &= 2I_c \cos \left(\pi \frac{\Phi}{\Phi_0} \right) \sin \left(\varphi_1 + \pi \frac{\Phi}{\Phi_0} \right) + 2 \frac{V}{R_N}. \end{aligned} \quad (4.2.29)$$

Here, we have used (4.2.1) and (4.2.8). Let us define the new phase

$$\varphi = \varphi_1 + \pi \frac{\Phi}{\Phi_0} \quad (4.2.30)$$

and note that due $\Phi \simeq \Phi_{\text{ext}} = \text{const}$ we have

$$\frac{d\varphi}{dt} = \frac{d\varphi_1}{dt} = \frac{2\pi}{\Phi_0} V(t). \quad (4.2.31)$$

Then, we can rewrite (4.2.29) as

$$I = I_s^m(\Phi_{\text{ext}}) \sin \varphi + \frac{2}{R_N} \frac{2\pi}{\Phi_0} \frac{d\varphi}{dt} \quad (4.2.32)$$

with

$$I_s^m(\Phi_{\text{ext}}) = 2I_c \cos\left(\pi \frac{\Phi_{\text{ext}}}{\Phi_0}\right). \quad (4.2.33)$$

We see, that equation (4.2.32) represents the equation of a single Josephson junction with a maximum Josephson current that depends on the external flux. For a single junction we have used the pendulum as a mechanical analog. In the same way we can use two coupled pendula that are coupled to each other as the analog for the dc-SQUID. In the case of negligible screening ($\beta_L \ll 1$) the coupling of the two pendula is rigid as can be seen from (4.2.30) and they move with the same angular velocity as can be seen from (4.2.31). Note that the rigid coupling is no longer true for significant screening ($\beta_L \geq 1$).

Due to the equivalence of the dc-SQUID with a single junction having a flux dependent maximum Josephson current, the current-voltage characteristic of the dc-SQUID is just given by the RSJ-model result (3.2.20):

$$\langle V(t) \rangle = IR \sqrt{1 - \left(\frac{I_s^m(\Phi_{\text{ext}})}{I} \right)^2} = IR \sqrt{1 - \left[\frac{2I_c}{I} \cos\left(\pi \frac{\Phi_{\text{ext}}}{\Phi_0}\right) \right]^2} > 1. \quad (4.2.34)$$

The IVCs obtained according to this equation are shown in Fig. 4.5. It can be seen that the IVCs are periodic with the applied magnetic flux with the periodicity of a single flux quantum. Considering the time-averaged junction voltage as a function of the applied flux for different values of the bias current we see that these curves are also periodic with the same periodicity. Furthermore, the minima and maxima of the $\langle V \rangle(\Phi_{\text{ext}})$ always appear at the same flux values. Fig. 4.5 also shows the $\cos \pi \Phi_{\text{ext}} / \Phi_0$ dependence of the zero voltage supercurrent through the SQUID. Furthermore, it is seen that the maximum modulation of the time-averaged voltage with varying applied flux occurs for $I \simeq 2I_c$.

Finite Screening: $\beta_L \geq 1$, Intermediate Damping: $\beta_C \geq 1$

For practical SQUIDs the inductance L of the loop containing the Josephson junctions must be taken into account. As discussed already above, the loop area should be made large in order to increase the flux threading the SQUID at a given field value. However, a large loop area can not be obtained without increasing the loop inductance. Furthermore, for typical Josephson junctions we cannot neglect the displacement current due to the finite junction capacitance as well as the fluctuating noise current. In this general case the dc-SQUID circuit is governed by a set of time-dependent nonlinear equations that must be solved numerically.

The phase differences across the two junctions have to satisfy the following equations:^{9,10,11}

⁹C.D. Tesche, J. Clarke, *dc-SQUID: Noise and Optimization*, J. Low Temp. Phys. **27**, 301 (1977).

¹⁰J.J.P. Bruines, V.J. de Waal, J.E. Mooij, J. Low Temp. Phys. **46**, 383 (1982).

¹¹V.J. de Waal, P. Schrijner, R. Llurba, *Simulation and Optimization of a dc-SQUID with Finite Capacitance*, J. Low Temp. Phys. **54**, 215 (1984).

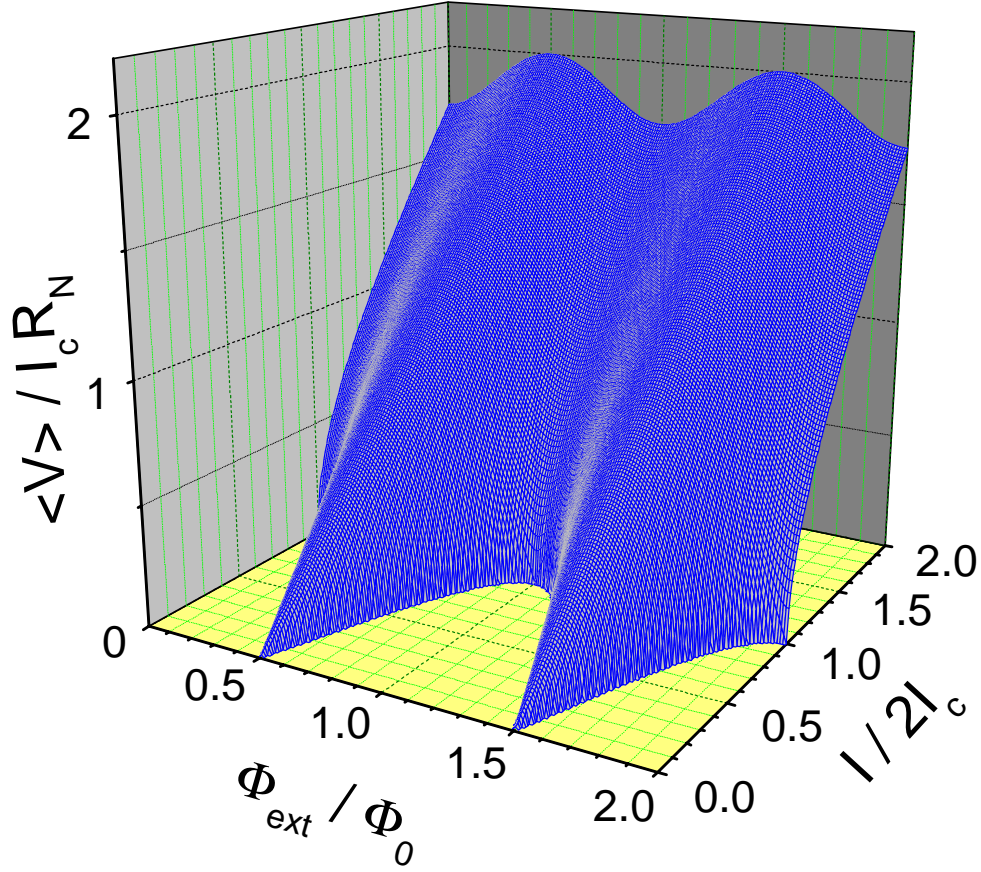


Figure 4.5: Current-voltage characteristics of a dc-SQUID in the limit $\beta_L \ll 1$ for different values of the applied magnetic flux Φ_{ext} for a dc-SQUID with two identical Josephson junction.

$$V = \frac{\Phi_0}{4\pi} \left(\frac{d\varphi_1}{dt} + \frac{d\varphi_2}{dt} \right) \quad (4.2.35)$$

$$2\pi n = \varphi_1 - \varphi_2 - 2\pi \frac{\Phi_{\text{ext}}}{\Phi_0} - 2\pi \frac{LI_{\text{cir}}}{\Phi_0} \quad (4.2.36)$$

$$\frac{I}{2} = \frac{\hbar C}{2e} \frac{d^2\varphi_1}{dt^2} + \frac{\hbar}{2eR_N} \frac{d\varphi_1}{dt} + [I_c \sin \varphi_1 + I_{\text{cir}}] + I_{F1} \quad (4.2.37)$$

$$\frac{I}{2} = \frac{\hbar C}{2e} \frac{d^2\varphi_2}{dt^2} + \frac{\hbar}{2eR_N} \frac{d\varphi_2}{dt} + [I_c \sin \varphi_2 - I_{\text{cir}}] + I_{F2} . \quad (4.2.38)$$

Equation (4.2.35) relates the SQUID voltage to the rate of change of phase. Note that for negligible screening we have $\frac{d\varphi_1}{dt} = \frac{d\varphi_2}{dt}$ and the usual voltage-phase relation is recovered. Considering the dc-SQUID as two coupled pendula, we already mentioned that the case of negligible screening is equivalent to a rigid coupling of the two pendula with their relative angle determined by the applied flux. In the case of finite screening the coupling between the pendula is no longer rigid and therefore the relative angle between the pendula is not fixed. Hence, we have $\frac{d\varphi_1}{dt} \neq \frac{d\varphi_2}{dt}$.

Equation (4.2.36) expresses the fluxoid quantization in the superconducting loop. We see that in contrast to negligible screening (compare (4.2.8)) we have to take into account also the flux LI_{cir} due to the finite inductance of the loop.

Equations (4.2.37) and (4.2.38) are Langevin equations coupled via I_{cir} . These coupled equations have to be solved numerically under the constraint given by (4.2.36) as a function of the screening parameter $\beta_L = 2LI_c/\Phi_0$, the Stewart-McCumber parameter $\beta_C = 2\pi I_c R_N^2 C / \Phi_0$ and the thermal noise parameter $\gamma = 2\pi k_B T / I_c \Phi_0$.

4.2.3 Operation and Performance of dc-SQUIDS

The principle of operation of a dc-SQUID is shown in Fig. 4.6. The two junctions, which are modelled by the RCSJ model, are connected in parallel on a superconducting loop with inductance L . In order to eliminate hysteretic IVCs, the Stewart-McCumber parameter of the junctions is restricted to $\beta_C \leq 1$. The IVCs of the SQUID depend on the applied magnetic flux as shown in Fig. 4.5 for $\beta_C = 0$ and $\beta_L = 0$. In Fig. 4.6b only the IVCs with the largest ($\Phi_{\text{ext}} = n\Phi_0$) and the smallest critical current ($\Phi_{\text{ext}} = (n + \frac{1}{2})\Phi_0$) are shown. When the SQUID is biased at a constant current $I > 2I_c$, the time-averaged voltage $\langle V \rangle$ of the SQUID varies periodically with the applied flux with period Φ_0 as shown in Fig. 4.6c.

For practical applications the flux threading the loop has to be measured with high resolution. Therefore, the SQUID is operated at the steepest part of the $\langle V \rangle(\Phi_{\text{ext}})$ curve, where the *flux-to-voltage transfer coefficient*

$$H \equiv \left| \left(\frac{\partial V}{\partial \Phi_{\text{ext}}} \right)_I \right| \quad (4.2.39)$$

is a maximum. We see that the dc-SQUID can be considered as a flux-to-voltage transducer, which produces an output voltage in response to small variations of the input flux.

The resolution of the SQUID can be characterized by the equivalent flux noise $\Phi_F(t)$, which has the power spectral density

$$S_\Phi(f) = \frac{S_V(f)}{H^2} \quad (4.2.40)$$

at a given frequency f . Here, $S_V(f)$ is the power spectral density of the voltage noise across the SQUID at a fixed bias current. The flux noise power spectral density is inconvenient for comparing the noise in SQUIDS with different values of the loop inductance. A more convenient characterization of the noise is to use the noise energy associated with $S_\Phi(f)$:

$$\epsilon(f) = \frac{S_\Phi(f)}{2L} = \frac{S_V(f)}{2LH^2}. \quad (4.2.41)$$

The noise energy of the dc-SQUID sets the energy resolution of the SQUID, which for practical applications should be as small as possible. For a given $S_V(f)$ we therefore have to maximize H and L . Just by using a plausibility consideration we see the following:

- Bias current I:** In order to maximize H we should choose a bias current just above $2I_c$, since here the modulation of the $\langle V \rangle(\Phi_{\text{ext}})$ curve is largest. Furthermore, the flux bias should be close to $(2n+1)\Phi_0/4$, since here H is maximum.

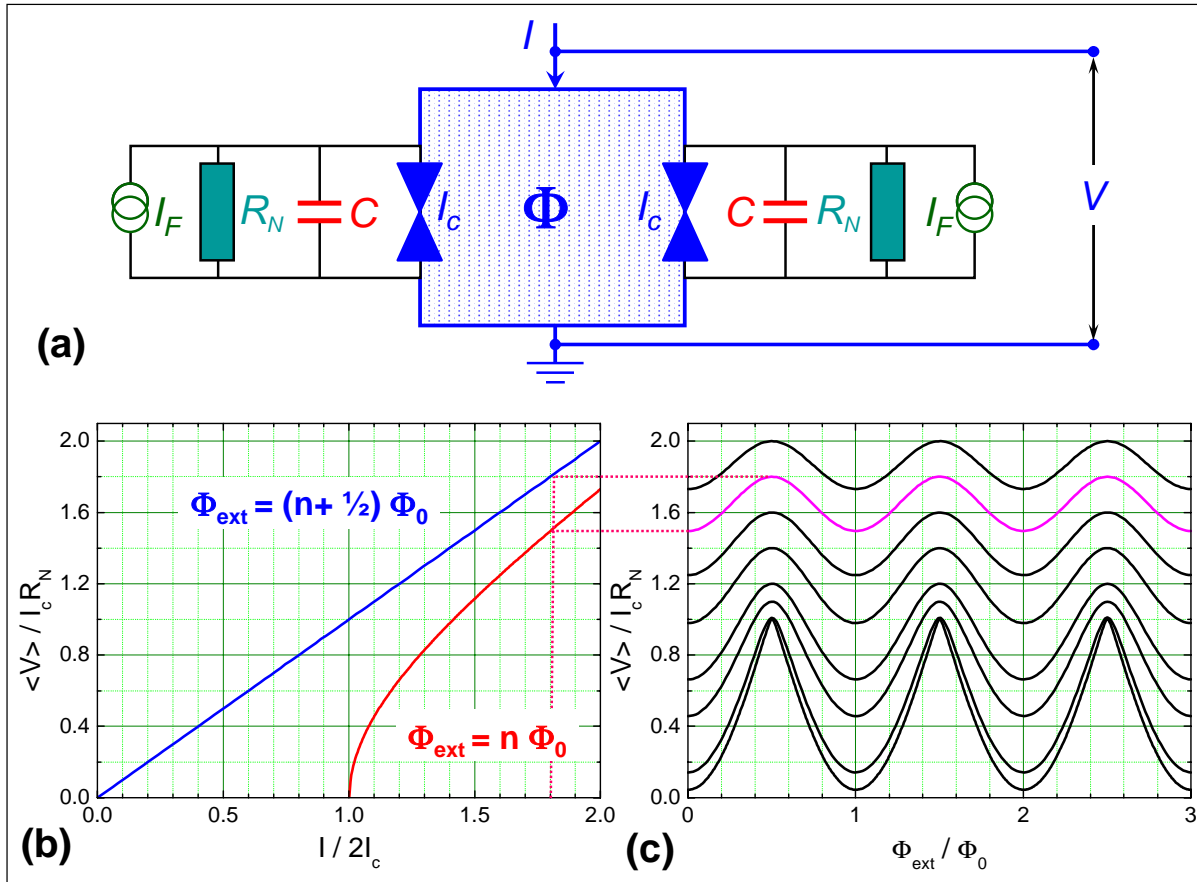


Figure 4.6: (a) The equivalent circuit of dc-SQUID, (b) the current-voltage characteristics for two different values of the applied magnetic flux ($\Phi_{\text{ext}} = n\Phi_0$ and $\Phi_{\text{ext}} = (n + 1/2)\Phi_0$) and (c) the time-average voltage plotted versus the applied flux for different values of the bias current ($I/2I_c = 1.01, 1.1, 1.2, 1.4, 1.6, 1.8$, and 2.0).

2. **Junction critical current I_c :** The junction critical currents should be much larger than the thermal noise current, or equivalently, the coupling energy $I_c\Phi_0/2\pi$ should be much larger than the thermal energy $k_B T$. By this a noise rounding of the IVCs as shown in Fig. 3.14 is avoided, which would deteriorate H . Computer simulations show that¹²

$$\frac{1}{5}I_c \gtrsim I_{\text{th}} \equiv \frac{2\pi k_B T}{\Phi_0} \quad (4.2.42)$$

is sufficient. At 4.2 K this condition, which is equivalent to asking for a sufficient coupling of the phases of the superconducting wavefunctions across the two Josephson junctions, implies that $I_c \gtrsim 1 \mu\text{A}$.

3. **The loop inductance L :** The loop inductance should be as large as possible for optimum sensitivity. However, at a given temperature T the thermal energy $k_B T$ causes a root mean square thermal noise flux in the loop, $\langle \Phi_l^2 \rangle^{1/2} = \sqrt{k_B T L}$. This noise flux should be considerably smaller than Φ_0 giving an upper bound for L . Again, computer simulations show that

¹²J. Clarke, R. Koch, *The Impact of High Temperature Superconductivity on SQUIDs*, Science **242**, 217 (1988).

$$5L \lesssim L_{\text{th}} \equiv \frac{\Phi_0^2}{2\pi k_B T} \quad (4.2.43)$$

is sufficient. This constraint, which is equivalent to asking for a sufficient coupling of the phase differences of the two junctions, implies that $L \lesssim 15 \text{ nH}$ at 4.2 K.

4. **The screening parameter β_L :** The screening parameter $\beta_L = 2I_c L / \Phi_0$ has to be smaller than unity to avoid hysteretic $\langle V \rangle(\Phi_{\text{ext}})$ curves. This condition can be easily satisfied by making L small. However, we already have seen that we should make L as large as possible to increase the SQUID sensitivity. Therefore, we should choose $\beta_L \simeq 1$, i.e. as large as possible. For $\beta_l \simeq 1$ and taking the smallest possible I_c value at 4.2 K, we obtain $L \simeq 1 \text{ nH}$, which is still well below the constraint given by (4.2.43).¹³
5. **The Stewart-McCumber parameter β_C :** The Stewart-McCumber parameter has to be smaller than unity in order to avoid hysteretic IVCs. For superconducting tunnel junctions, which intrinsically have large capacitance and hence $\beta_C \gg 1$, this is achieved by using an external shunt resistor smaller than the normal resistance of the junction. That is, in principle it is not a problem to satisfy the condition $\beta_C \leq 1$. However, using a small shunt resistor $R_{\text{shunt}} \ll R_N$ reduces the voltage amplitude of the $\langle V \rangle(\Phi_{\text{ext}})$ curves to $I_c R_{\text{shunt}} \ll I_c R_N$. Therefore, R_{shunt} should be as large as possible, that is we have to choose $\beta_C \simeq 1$.

The detailed value of the performance of the SQUID have to be evaluated by numerical simulations.^{14,15,16} These simulations show that the noise energy of dc-SQUIDs has a minimum for $\beta_L \simeq 1$, $\beta_C \simeq 1$, for a flux bias close to $(2n+1)\Phi_0/4$ and for a bias current I , for which the voltage modulation of the $\langle V \rangle(\Phi_{\text{ext}})$ curves is largest. Since the maximum voltage modulation is about $I_c R_N$ we have

$$H \simeq \frac{I_c R_N}{\Phi_0/2} \simeq \frac{R_N}{L} \quad (4.2.44)$$

for $\beta_L \simeq 1$. In the white noise regime¹⁷ the voltage noise of the SQUID can be estimated by splitting up the current noise power spectral density S_I into an in-phase part $S_I^{in} = 4k_B T / (R_N/2)$ and an out-of-phase part $S_I^{out} = 4k_B T / 2R_N$. Note that for the in-phase current fluctuations, which have the same direction in the two arms of the SQUID, the relevant resistance is $R_N/2$ due to the parallel connection of the two junction resistors. In contrast, for the out-of-phase part, which is in opposite direction in the two arms and results in a circulating current, the relevant resistance is $2R_N$ due to the series connection of the two junctions resistors for the circulating current. In a small signal analysis the voltage noise power spectral density due to the in- and out-of-phase current fluctuations is given by

¹³Note that for high temperature superconductor dc-SQUIDs the situation is different. Here, the operation temperature is about 20 times higher and therefore we have the constraint $I_c \gtrsim 20 \mu\text{A}$ and $L \lesssim 75 \text{ pH}$. For $\beta_L \simeq 1$ we obtain with $I_c \simeq 20 \mu\text{A}$ an inductance value $L \simeq 50 \text{ pH}$, which is close to the thermal constraint $L \simeq 75 \text{ pH}$.

¹⁴C.D. Tesche, J. Clarke, *dc-SQUID: Noise and Optimization*, J. Low Temp. Phys. **27**, 301 (1977).

¹⁵D. Drung, W. Jutzi, IEEE Trans. Magn. **21**, 330 (1985).

¹⁶D. Kölle, R. Kleiner, F. Ludwig, E. Dantsker, J. Clarke, *High-transition-temperature superconducting quantum interference devices*, Rev. Mod. Phys. **71**, 631 (1999).

¹⁷The low frequency regime, where $1/f$ noise dominates is not discussed here.

$$S_V(f) = S_I^{in}(f)R_d^2 + S_I^{out}(f)L^2 H^2 = \frac{4k_B T}{R_N} \left[2R_d^2 + \frac{L^2 H^2}{2} \right], \quad (4.2.45)$$

where R_d is the differential resistance at the operation point. With the optimum values $H \sim R_N/L$ and $R_d \sim \sqrt{2}R_N$ obtained from numerical simulations we obtain

$$S_V(f) \simeq \frac{4k_B T}{R_N} \left[4R_N^2 + \frac{R_N^2}{2} \right] = 18k_B T R_N, \quad (4.2.46)$$

The noise energy then can be estimated to

$$\varepsilon(f) = \frac{S_V(f)}{2LH^2} \simeq \frac{9k_B T L}{R_N} \simeq \frac{9k_B T \Phi_0}{2I_c R_N} \quad \text{for } \beta_L \simeq 1. \quad (4.2.47)$$

We see that the noise energy increases with temperature and decreasing $I_c R_N$ product of the Josephson junctions. If we eliminate R_N by using $\beta_C = 2\pi I_c R_N^2 C / \Phi_0 \simeq 1$ and if we also eliminate L by using $\beta_L = 2I_c L / \Phi_0 \simeq 1$ we obtain

$$\begin{aligned} \varepsilon(f) &\simeq 16k_B T \sqrt{\frac{LC}{\beta_C}} \\ &\simeq 16\sqrt{\pi}k_B T \sqrt{\frac{\Phi_0 C_s}{2\pi J_c}} = \frac{16\sqrt{\pi}k_B T}{\omega_p} \quad \text{for } \beta_L \simeq 1; \beta_C \simeq 1. \end{aligned} \quad (4.2.48)$$

Here, $C_s = C/A$ is the specific junction capacitance and $J_c = I_c/A$ is critical current density of the junction. We see that we can improve the performance of the dc-SQUID by reducing the temperature as well as by decreasing the capacitance and by increasing the critical current density, i.e. by increasing the plasma frequency of the Josephson junctions. Until today, a large number of dc-SQUIDS has been studied and it was found that their performance agrees well with the predictions of the numerical simulations. Today it is common to quote the noise energy of SQUIDS in units of $\hbar \simeq 10^{-34}$ Js. Best SQUIDS have a noise energy of only a few \hbar .

A recent result of a numerical simulation is shown in Fig. 4.7. Here, the reduced noise energy

$$\Sigma(f) = \frac{\varepsilon(f)}{\frac{2\Phi_0 k_B T}{I_c R_N}} \quad (4.2.49)$$

is plotted versus the dimensionless parameter

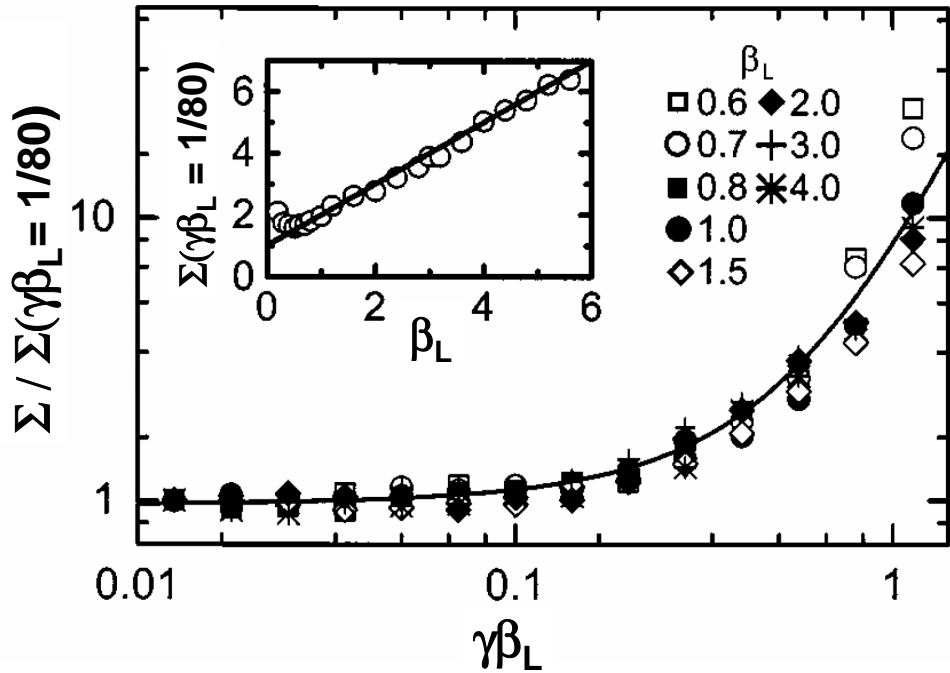


Figure 4.7: Calculated reduced energy resolution $\Sigma(\gamma\beta_L)$ normalized to $\Sigma(\gamma\beta_L = 1/80)$. Inset shows $\Sigma(\gamma\beta_L = 1/80)$ versus β_L (data from D. Kölle *et al.*, Rev. Mod. Phys. **71**, 631 (1999)).

$$\gamma\beta_L = \frac{2\pi k_B T}{I_c \Phi_0} \frac{2I_c L}{\Phi_0} = \frac{L}{\frac{\Phi_0^2}{2\pi k_B T}} \equiv \frac{L}{L_{\text{th}}} . \quad (4.2.50)$$

For $\gamma\beta_L \leq 0.2$, the reduced noise energy is almost constant, while for higher values of $\gamma\beta_L$ it increases rapidly. The rapid increase in noise energy arises from the rapid degradation of the transfer function with increasing $\gamma\beta_L = L/L_{\text{th}}$.

4.2.4 Practical dc-SQUIDs

Practical dc-SQUIDs do not only consist of the SQUID loop discussed so far, but also by an antenna and a room temperature electronics as schematically shown in Fig. 4.8. The antenna has both to transfer the quantity that has to be measured into magnetic flux and to couple this flux effectively into the SQUID loop. The SQUID itself acts as a flux-to-voltage transducer. The room temperature electronics has to amplify the voltage signal as well as to provide the current and flux bias.

The Washer Type dc-SQUID

Today dc-SQUIDs are based on thin film structures, which are patterned using optical and electron beam lithography. A major problem of such SQUIDs is to couple the magnetic flux of the antenna system effectively to the SQUID loop. This problem has been solved by **M.B. Ketchen** and **J.M. Jaycox**, who introduced the idea of depositing a spiral input coil on a dc-SQUID in a square washer geometry.^{18,19}

¹⁸M.B. Ketchen, J.M. Jaycox, *Ultra-low Noise Tunnel Junction dc-SQUID with a Tightly Coupled Planar Input Coil*, Appl. Phys. Lett. **40**, 736 (1982).

¹⁹J.M. Jaycox, M.B. Ketchen, *Planar Coupling Scheme for Ultra-low Noise dc-SQUIDS*, IEEE Trans. Magn. **17**, 400 (1981).

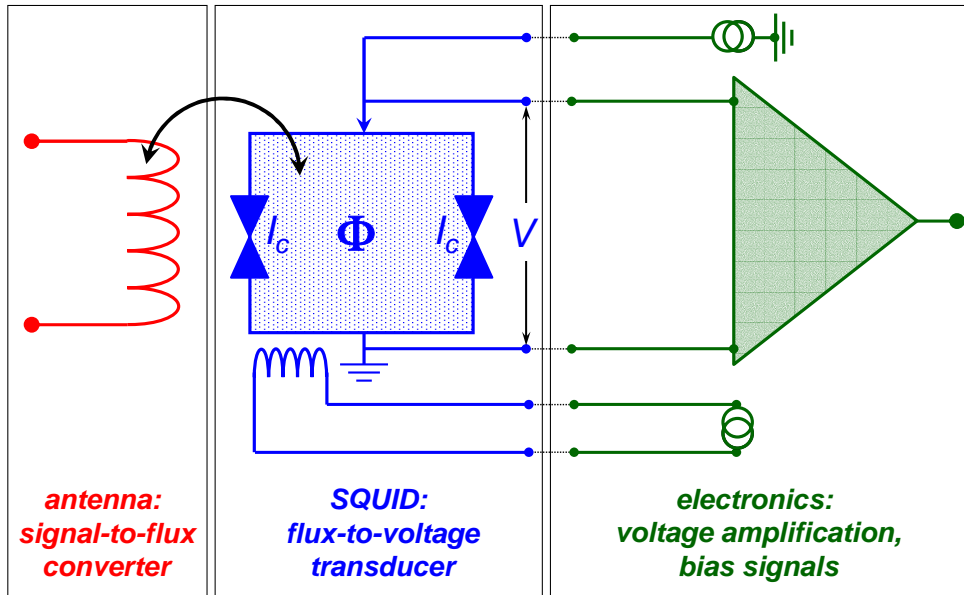


Figure 4.8: The practical dc-SQUID consisting of an antenna acting as a signal-to-flux converter, the SQUID loop acting as the flux-to-voltage transducer, and the room temperature electronics.

The thin film planar coil is separated from the SQUID washer only by a thin insulating layer. A typical washer type dc-SQUID is shown schematically in Fig. 4.9. The square washer forms the SQUID loop. It contains a narrow slit, which is closed by a superconducting line containing the two junctions, which are located at the outer rim of the washer.

Jaycox and Ketchen showed that a square washer with no slit and an inner and outer edge D and W has an inductance

$$L \simeq 1.25 \mu_0 D \quad (4.2.51)$$

in the limit $W \gg D$. Neglecting the parasitic inductance associated with the junctions, they found the following expressions for the inductance L_i of the spiral input coil, the mutual inductance M_i and the coupling coefficient α^2 between the spiral and the SQUID loop:

$$L_i \simeq n^2 L + L_s \quad (4.2.52)$$

$$M_i \simeq nL \quad (4.2.53)$$

$$\alpha^2 \simeq \frac{1}{1 + L_s/n^2 L} . \quad (4.2.54)$$

Here, L_s is the stripline inductance of the spiral coil. As an example, for $D = 20 \mu\text{m}$ we obtain $L \simeq 30 \text{ pH}$. For a 50 turn input coil we obtain $L_i \simeq 75 \text{ nH}$ ²⁰, $M_i \simeq 1.5 \text{ nH}$ and a coupling coefficient that typically ranges between 0.6 and 0.8. A specific problem of the washer-type dc SQUID geometry is the considerable capacitance between the spiral input coil and the square washer. This can result in LC -resonances. These resonances, in turn, result in structures in the IVCs, which can give rise to excess

²⁰The stripline inductance is insignificant for a 50 turn coil.

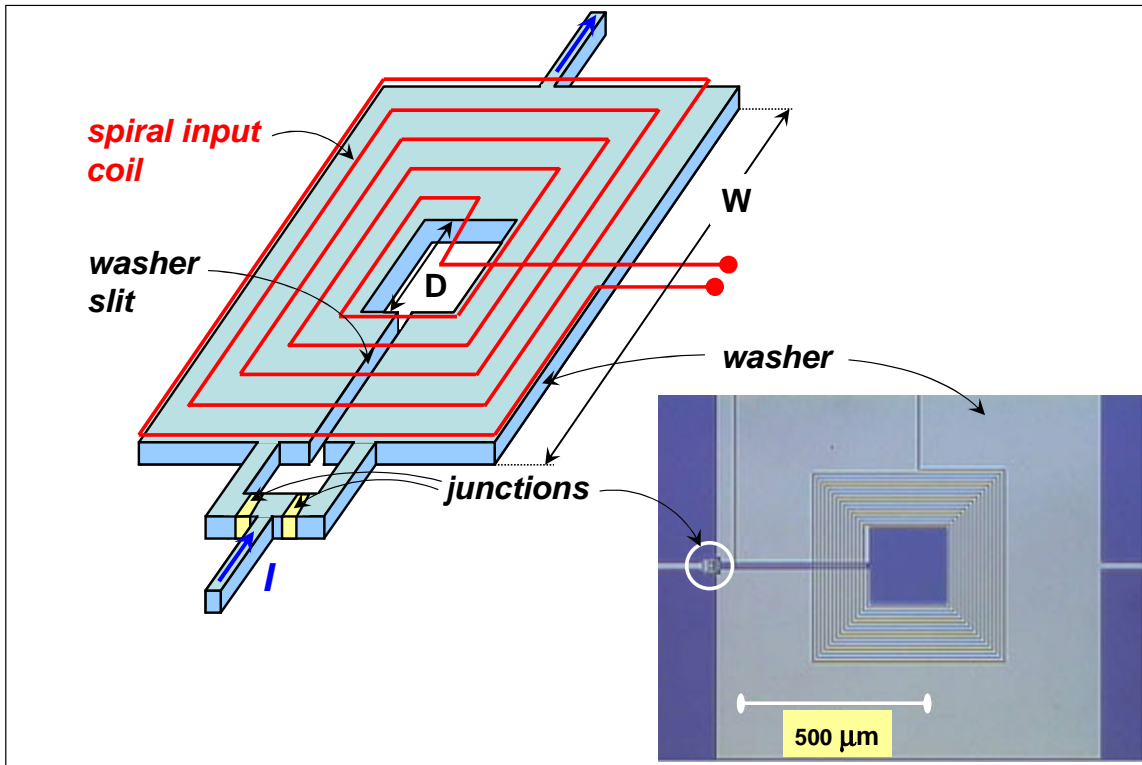


Figure 4.9: Sketch of the dc-SQUID using a square washer geometry and a planar spiral input coil. The inset shows an optical micrograph of a washer-type Nb dc-SQUID (by courtesy of J. Clarke).

noise. The effect of the LC -resonances can be reduced by reducing the number of turns on the washer and thereby reducing the parasitic capacitance (in this case an intermediate superconducting transformer can be used to couple in the signal). On the other hand, the shunt resistance of the junctions can be decreased thereby increasing the damping.

The Flux-Locked Loop Operation

The $\langle V \rangle(\Phi_{\text{ext}})$ curves of the dc-SQUID are nonlinear. Therefore, a linear relation between an input signal and the output voltage is obtained only in the small signal limit. This problem can be solved by using the SQUID in a feedback circuit as a null-detector for magnetic flux.²¹ One simply applies an oscillating magnetic flux with a peak-to-peak amplitude of about $\Phi_0/2$ and a frequency f_{mod} in the 100 kHz regime as shown in Fig. 4.10. If the quasistatic flux is exactly $n\Phi_0$, the resulting ac voltage is a rectified version of the input signal. That is, it contains only a $2f_{\text{mod}}$ frequency component. If this signal is detected by a lock-in amplifier referenced to the fundamental frequency f_{mod} , the resulting output voltage is zero. In contrast, if the quasistatic flux is $(n + \frac{1}{4})\Phi_0$, the voltage across the SQUID is at f_{mod} and the output signal from the lock-in amplifier will be maximum. Thus, increasing the flux from $n\Phi_0$ to $(n + \frac{1}{4})\Phi_0$ the lock-in output signal will increase, whereas it will increase in the negative direction on decreasing the flux from $n\Phi_0$ to $(n - \frac{1}{4})\Phi_0$.

The ac voltage across the SQUID is usually coupled to a low noise preamplifier via a cooled transformer, which results in an increase of the low SQUID impedance from R_d to $N^2 R_d$, where R_d is the differential resistance of the SQUID at the operation point and N the turns-ratio of the transformer. One also can use a cooled LC series resonant circuit, which provides an impedance $Q^2 R_d$, where Q is the quality of

²¹J. Clarke, W.M. Goubau, M.B. Ketchen, J. Low. Temp. Phys. **25**, 99 (1976).

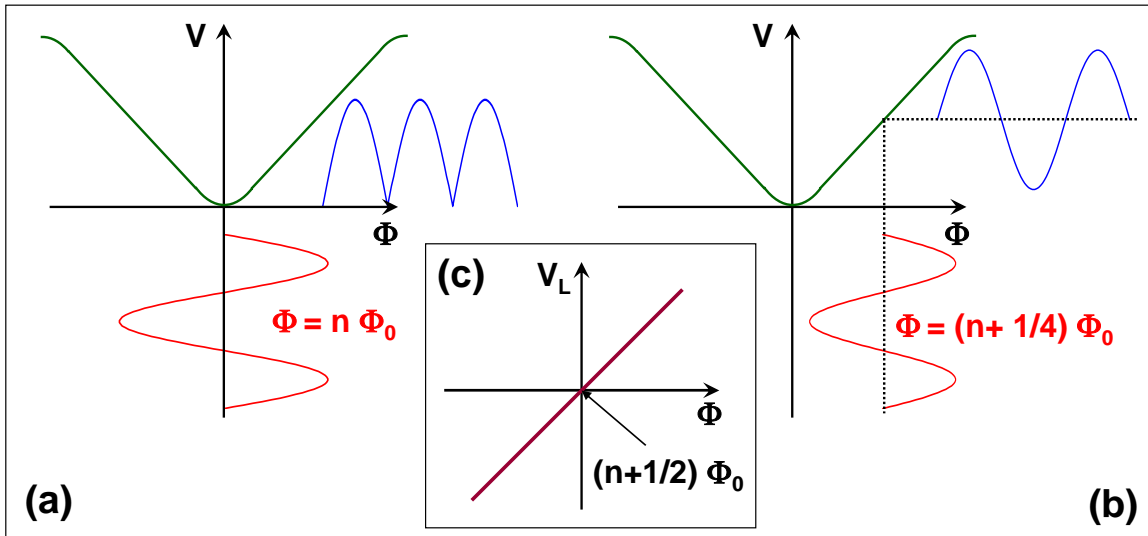


Figure 4.10: Flux modulation scheme for a dc-SQUID showing the voltage across the SQUID for $\Phi = n\Phi_0$ (a) and $\Phi = (n + \frac{1}{4})\Phi_0$ (b). Also shown is the output signal V_L of the lock-in amplifier versus the applied flux (c).

the tank circuit. The values of N or Q are chosen to obtain an optimum impedance match between the SQUID and the room temperature preamplifier.

Fig. 4.11 shows the equivalent circuit of a dc-SQUID operated in the *flux-locked loop*. An oscillator applies a modulating flux to the SQUID and also serves as the reference for the lock-in amplifier. After amplification, the ac voltage signal from the SQUID is phase sensitively detected by the lock-in amplifier. The output voltage V_L of the lock-in amplifier is sent to an integrator. The output voltage of the integrator is decreasing and increasing for negative and positive V_L , respectively. The output signal of the integrator is connected to the SQUID via a resistor R_f to the feedback coil L_f . If we are applying a small flux change $+\delta\Phi$ to the SQUID, the lock-in will generate a positive output voltage proportional to $\delta\Phi$. The positive output signal will cause an increase of the integrator output voltage, which in turn is causing an increase of the current through the feedback coil. The integrator voltage will increase until the current through the feedback coil is sufficient to compensate the small applied flux change. Then, the total flux coupled to the SQUID and, in turn, the lock-in signal is zero and the integrator output voltage stays constant. We see that the SQUID is operating as a null detector.

The change δV_{in} of the integrator output voltage is directly proportional to the flux change $\delta\Phi$. With the change of the feedback current $\delta I_f = \delta V_{in}/R_f$ and the flux induced by the feedback current, $\delta\Phi_f = k^2 L_f \delta I_f$ (here k^2 is the coupling constant between the feedback coil and the SQUID loop), we obtain from the condition $|\delta\Phi_f| = |\delta\Phi|$

$$\delta V_{in} = \frac{R_f}{k^2 L_f} \delta\Phi . \quad (4.2.55)$$

We see that the output signal increases with increasing feedback resistance. Furthermore, the output signal is linear with $\delta\Phi$ even if the flux change is several Φ_0 .

The typical modulation frequency of the flux-locked loop circuit is from 100 kHz to several MHz. Using suitable electronics a very high dynamic range up to several $10^7 \sqrt{\text{Hz}}$ and a signal bandwidth of up to 100 kHz can be achieved. An important quantity is the slew rate, which gives the speed at which the

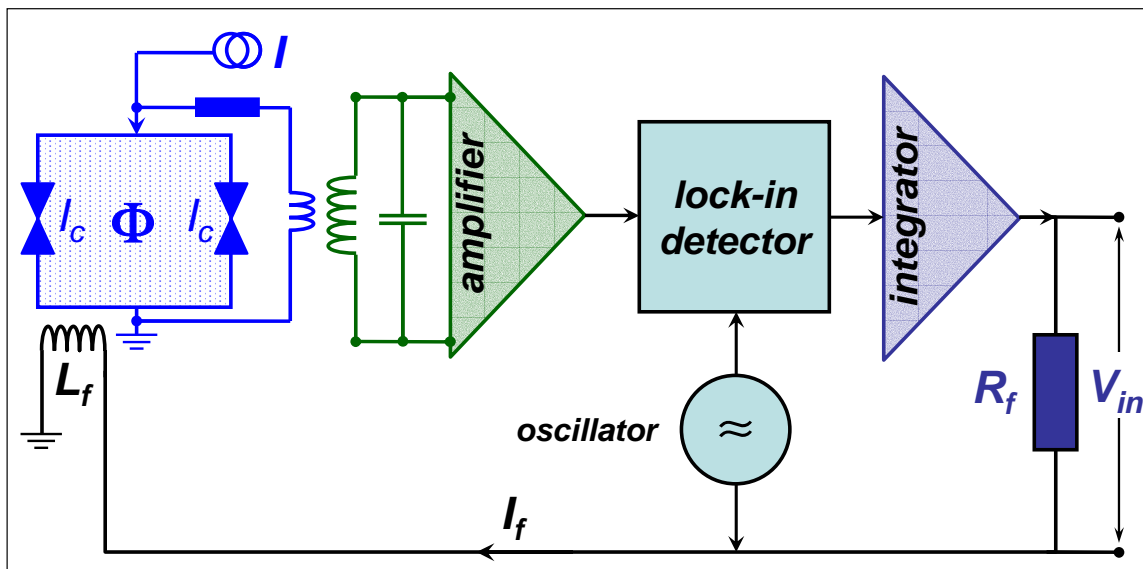


Figure 4.11: The modulation and feedback circuit of a dc-SQUID.

feedback circuit can compensate for rapid flux changes at the input. State of the art SQUID electronics has slew rates of up to $10^7 \Phi_0/\text{s}$.

4.3 Applications of SQUIDS

Both dc- and rf-SQUIDs are used as sensors in a broad assortment of instruments. In the following we briefly discuss some of them. Each SQUID instrument involves a specific antenna attached to the input of the SQUID. This antenna determines the quantity that is measured by the SQUID as shown in Fig. 4.12.

In using the SQUID in different applications involving different antenna at the input we should recognize that the presence of an input circuit influences both the signal and the noise properties of the SQUID. On the other hand, the SQUID reflects a complex impedance into the input. Furthermore, the SQUID represents a nonlinear device. Therefore, a full description of the interactions is complicated and we will not go into the details here. We only will concentrate on one important aspect that already was recognized in 1971 by **J.E. Zimmerman**.²² Suppose we are connecting a pick-up loop of inductance L_p to the input coil of the SQUID with inductance L_i to form a magnetometer as shown in Fig. 4.12. It is easy to show that the SQUID inductance L is thereby reduced to the value

$$L' = L \left(\frac{1 - \alpha^2 L_i}{L_i + L_p} \right), \quad (4.3.1)$$

where α^2 is the coupling coefficient between L and L_i . Here, we have neglected any stray inductances in the leads connecting L_i and L_p . The reduction in L tends to increase the transfer function ($H \sim R_N/L$ for the dc-SQUID) of the SQUID.

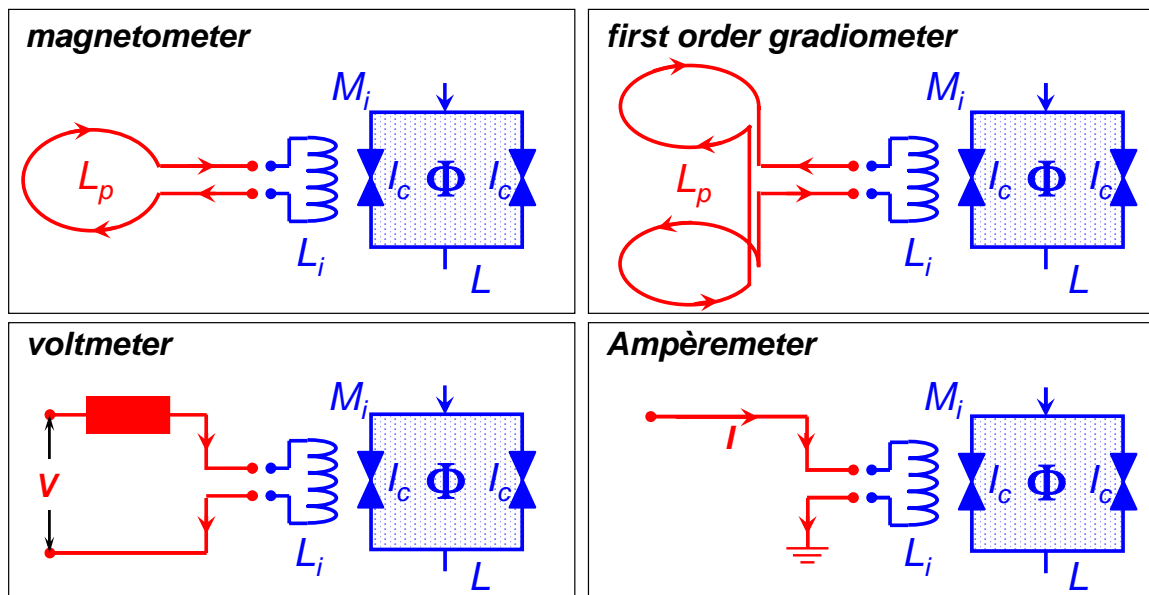


Figure 4.12: Different types of input antenna for superconducting quantum interference devices used in different applications. The input antenna converts the quantity to be measured into magnetic flux.

4.3.1 Magnetometers and Gradiometers

The probably most simple and straightforward SQUID instrument is the SQUID magnetometer. Here, a pick-up loop with inductance L_p is connected to the input coil of the SQUID forming a superconducting

²²J.E. Zimmerman, Sensitivity enhancement of SQUIDs through the use of fractional turn loops, *J. Appl. Phys.* **42**, 4483 (1971).

flux transformer. That is, a small flux change $\delta\Phi^p$ applied to the pick-up loop is causing a shielding current I_{sh} flowing through both the pick-up and the input coil. The current through the input coil generates magnetic flux that is coupled into the SQUID loop. Flux quantization requires that

$$\delta\Phi^p + (L_i + L_p)I_{sh} = 0 . \quad (4.3.2)$$

We have neglected the effects of the SQUID on the input circuit. The flux coupled into the SQUID operated in the flux locked loop is

$$\delta\Phi = M_i|I_{sh}| = \frac{M_i\delta\Phi^p}{L_i + L_p} , \quad (4.3.3)$$

where M_i is the mutual inductance between L_i and L .

In order to find the minimum detectable value of $\delta\Phi^p$, we equate $\delta\Phi$ to the equivalent flux noise of the SQUID. Defining S_Φ^p as the spectral density of the flux noise referred to the pick-up loop, we find

$$S_\Phi^p = \frac{(L_i + L_p)^2}{M_i^2} S_\Phi . \quad (4.3.4)$$

Introducing the equivalent noise energy referred to the pick-up loop, we obtain

$$\epsilon^p = \frac{S_\Phi^p}{2L_p} = \frac{(L_i + L_p)^2}{L_i L_p} \frac{S_\Phi}{2\alpha^2 L} = \frac{(L_i + L_p)^2}{L_i L_p} \frac{\epsilon}{\alpha^2} . \quad (4.3.5)$$

Analyzing (4.3.5) we see that it has the minimum value

$$\epsilon^p(f) = \frac{4\epsilon(f)}{\alpha^2} \quad (4.3.6)$$

for $L_i = L_p$. Thus, a fraction $\alpha^2/4$ of the energy in the pick-up loop is transferred to the SQUID. Here, we have neglected the noise currents in the input circuit and the fact that the input circuits reduces the SQUID inductance.

With the optimum flux resolution for $L_p = L_i$ we can give the corresponding magnetic field resolution $S_B^p(f) = S_\Phi^p(f)/(\pi r_p^2)^2$, where r_p is the radius of the pick-up loop. With $S_\Phi^p = 8\epsilon L_p/\alpha^2$ we obtain

$$S_B^p(f) = \frac{8L_p}{\alpha^2(\pi r_p^2)^2} \epsilon(f) \quad (4.3.7)$$

The inductance of the superconducting pick-up coil made from a wire with radius r_0 is given by $L_p = \mu_0 r_p [\ln(8r_p/r_0) - 2]$ and can be approximated by $L_p \simeq 5\mu_0 r_p$ over a wide range of values r_p/r_0 . Therefore, we obtain $S_B^p(f) \approx 4\mu_0 \varepsilon / \alpha^2 r_p^3$. This shows that we can increase the magnetic field resolution by increasing the radius of the pick-up loop while keeping $L_p = L_i$. In practice, of course there is a limitation due to the finite size of the cryostat used for cooling down the system. Taking $\varepsilon \simeq 10^{-28} \text{ J/Hz}$, $\alpha = 1$ and $r_p = 25 \text{ mm}$, we calculate $\sqrt{S_B^p} \simeq 5 \times 10^{-15} \text{ T}/\sqrt{\text{Hz}}$. This is a much better value than that achieved with non-superconducting magnetometers.

Chapter 5

Applications of the Josephson Effect in Digital Electronics

5.1 Superconductivity and Digital Electronics

Digital applications of the Josephson effect mainly aim in the direction of high-speed low power consumption computer systems. These applications are still under development because the scale/amount of technology required is much larger than that of analog applications. However, superconducting digital technology has been a leading technology for other applications such as SQUIDs, mixers, etc.. The fabrication technology for high-quality, reproducible Josephson junctions with low parameter spread and the required integration technology have been developed mainly for digital applications. These technologies have of course also greatly improved the performance of analog devices, i.e. integrated SQUID sensors.

Since there is extremely strong competition in the market of digital electronics, superconductivity must show up with significant advantages over conventional semiconducting electronics in order to compensate for several disadvantages implied by the superconducting state:

- Cooling is required: Since complicated integrated superconducting circuits most probably require Nb-technology cooling well below 9 K is necessary. This requires cooling by liquid helium or expensive cryocoolers. Higher operation temperature allowing for the use of liquid nitrogen or closed cycle refrigerators would be desirable. However, up to now there is no technology to realize high temperature superconductor (HTS) Josephson junctions and other circuit elements within the required margins of yield and parameter spread.
- The change-over to a new technology (e.g. from semiconductor to superconductor technology) involves huge financial investments for equipment and the development of the fabrication technology.
- New technologies for logic elements, packaging, power supply, ... have to be developed causing again significant costs.

5.1.1 Historical development

In this subsection we briefly address the historical development of superconducting digital circuits. Many ideas are quite old and never made it to the market place due to the dominating semiconductor technology.

1. Cryotron (1956):

In 1956 the cryotron was suggested. Here, the transition between the superconducting and normal state in a superconducting thin film was used for switching a current path. The major drawback of this device was the low switching speed of ~ 10 ns, which is due to the transition from the superconducting to the normal state. Such a thermal process is much slower than an electronic one.

2. Josephson Switching Device (1966):

Matisoo at IBM realized the first Josephson switching device in 1966 with sub-nanosecond switching speed. Since then IBM conducted a large program for developing a Josephson computer. This program was stopped in 1983. In the course of this program essential computer components including logic and memory circuits and systems have been developed as well as fabrication and packaging technologies. The two major reasons for the abandonment of the IBM project were the use of hardly reproducible Pb-alloy technology with large spreads in the junction critical currents.¹ together with the focus on latching logic gates based on underdamped Josephson junctions.

¹Furthermore, the Pb-alloy junctions are not stable enough at repeated thermal cycling

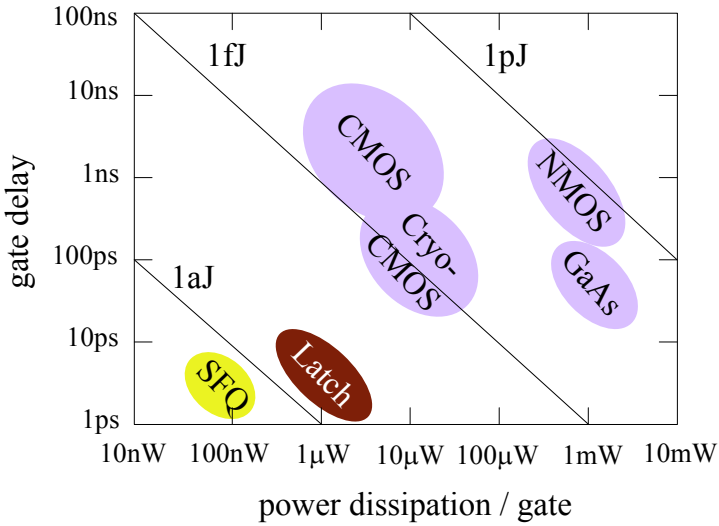


Figure 5.1: Comparison of device performance based on the delay-power relation for various devices. “Latch” stands for Josephson latching circuits, “SFQ” represents RSFQ-based gates. Josephson devices are superior in both propagation delay and power dissipation to any semiconducting devices.

The former problem nowadays has been solved through the Nb-technology, the latter by using the non-latching Rapid Single Flux Quantum (RSFQ) logic.

Stimulated by the IBM activities major Japanese computer companies (ETL, NEC, Hitachi, Fujitsu, NTT) started the *Japanese High Speed Computer project* in 1981, in which the Josephson device was selected to be one candidate (together with GaAs and HEMT) for the high-speed device to be used in future computer systems. These efforts continued even after the IBM project has been stopped and led to much progress in junction materials, devices and systems. The most important progress was the fabrication of Nb/Al₂O₃/Nb tunnel junctions instead of Pb-alloy junctions. These “refractory” junctions even allow the construction of circuits with LSI complexities. The Nb-technology also had a large impact on other Josephson applications (sensors, mixer, AD converter, . . .).

3. Rapid Single Flux Quantum (RSFQ) Logic (1985):

After the failure of the IBM project significant progress was achieved by the suggestion of the RSFQ (Resistive or Rapid Single Flux Quantum) logic. In RSFQ information is represented in a totally different way from that used in the latching voltage logic. Major advantages of RSFQ are (i) low power consumption, (ii) intrinsic memory, and (iii) very high speed.

5.1.2 Advantages and Disadvantages of Josephson Switching Devices

Pros:

- Josephson junctions switch fast with low power dissipation. In Fig. 5.1 delay-power characteristics of Josephson devices are compared with various semiconductor devices. The switching delays of Josephson devices are scattered below 10 ps. The power dissipation typically is in the range of 0.1 – 1 μ W which is two to three orders of magnitude less than for semiconductor devices. Low power dissipation is crucial for large scale integration, which in turn is important for reducing the wiring length and thus reducing the gate delay times. The dissipated energy per gate cycle is typically in the range of 10^{-18} – 10^{-17} J and hence by several orders of magnitude lower than for semiconductor devices.

- Superconducting matched striplines can be used for wiring chips and packagings. These transmission lines can transmit signals with very small loss or dissipation up to frequencies corresponding to the gap energy. The wave impedance of a microstrip line is given by

$$\rho[\Omega] = 60 \frac{\sqrt{t_I t_M}}{w \sqrt{\epsilon}} , \quad t_M = t_I + 2\text{Re}\delta \quad (5.1.1)$$

and can readily be made close to the Josephson junction resistance (which is of the order of its normal resistance). With a typical width $w \simeq 1 \mu\text{m}$ and an insulator thickness $t_I \simeq 0.3 \mu\text{m}$ a value $\rho \simeq 10 \Omega$ can be realized. The character of signal propagation in these lines is ballistic rather than diffusive and the contribution τ_i to the gate delay per gate is quite small ($\tau_i \simeq 10 \text{ ps}$ for lines as long as 1 mm). The absence of noticeable dispersion up to frequencies of 10^{12} Hz makes them the only means to transfer picosecond pulses along a chip.

- Refractory Josephson junctions can nowadays be fabricated reproducibly and easily using the Nb technology.

Cons:

- There are no feasible transistor-like 3-terminal devices so far.
- Due to the lack of a transistor like devices providing gain, integrated Josephson electronic circuits usually require a small parameter spread of the Josephson junctions.

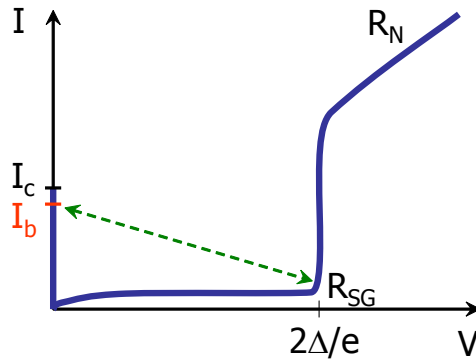


Figure 5.2: Schematic switching process of a Josephson tunnel junction along the load line.

5.2 Josephson Switching Gates

5.2.1 General requirements for Josephson switching devices

We first summarize the general requirements for switching devices usable for digital circuits:

- high *fan out*: a single switching gate should be capable of triggering N consecutive gates
- large operating margins for stable operation
- small size allowing for very large scale integration (VLSI)
- short switching time allowing for high clock frequency
- low power dissipation allowing for high integration capability
- input – output isolation allowing for directionality of logic signals

5.2.2 2-terminal and 3-terminal Devices

5.2.3 Operation Principle and Switching Times

Josephson switching gates usually make use of switching a tunnel junction between the superconducting state and the voltage state corresponding to the logical states “0” and “1”, respectively. Fig. 5.2 illustrates this switching from the “0” ($V = 0$) state along the load line to the “1” ($V = V_g$) state. The load line is defined by the load resistance R_L as depicted in Fig. 5.3. Initially, the junction is biased with a current $I_b < I_c$. If an input current I_g is added to I_b so as to exceed I_c the junction switches to the voltage state. R_L is chosen to be much smaller than the sub-gap resistance of the junction. Therefore, almost all of the current through the junction is transferred to the load after the junction switches.

As shown in the equivalent circuit for the Josephson junction in the right part of Fig. 5.3 the Josephson element can be replaced by a kinetic inductance L_s (see section 2.1.4)

$$L_s = \frac{\Phi_0}{2\pi I_c \cos \varphi(t)} = L_c \frac{1}{\cos \varphi(t)} \quad \text{with} \quad L_c = \frac{\hbar}{2eI_c} . \quad (5.2.1)$$

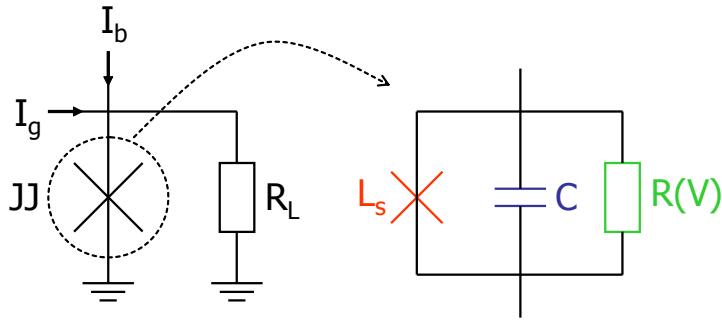


Figure 5.3: Simple Josephson switching device consisting of a single Josephson junction and the equivalent circuit of the Josephson junction.

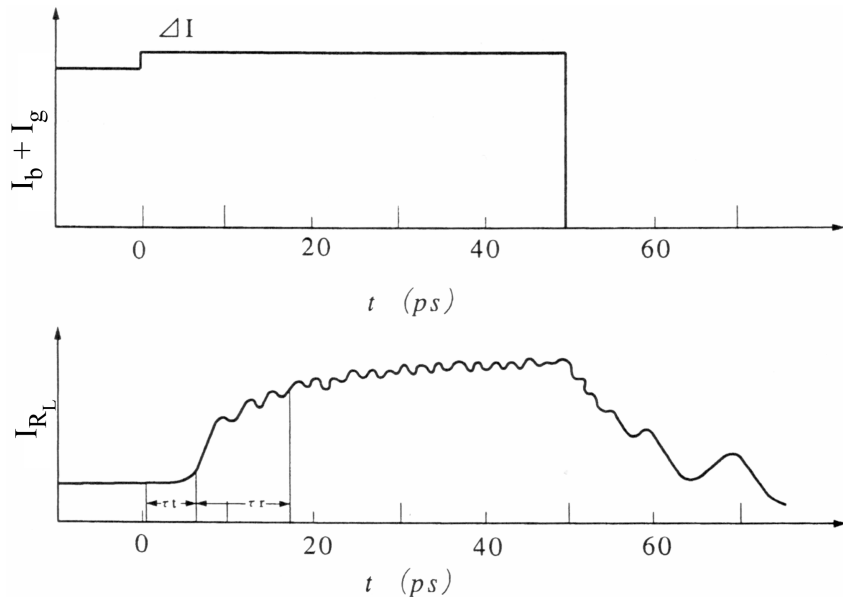


Figure 5.4: Output current waveform when the junction switches to the voltage state. The total switching delay is composed of two components: turn-on delay τ_t and rise time τ_r . The data are obtained with a computer simulation for a junction with critical current $I_c = 100 \mu\text{A}$, sub-gap resistance $R_{sg} = 150 \Omega$, normal resistance $R_n = 15 \Omega$, capacitance $C = 1 \text{ pF}$, and load resistance $R_L = 10 \Omega$. The bias current is stepped from I_c to $I_c + \Delta I = 1.1 \cdot I_c$.

5.2.4 Relevant Time Scales

Considering the switching process of the Josephson junction the following three characteristic times have to be considered (compare sections 3.1.1 and 3.1.2):

$$\tau_{RC} = RC \quad (5.2.2)$$

$$\tau_{RL} = \frac{L_c}{R} = \frac{\phi_0}{2\pi I_c R} = \tau_c = \frac{1}{\omega_c} \quad (5.2.3)$$

$$\tau_{LC} = \sqrt{L_c C} = \left(\frac{\phi_0 C}{2\pi I_c} \right)^{1/2} = \tau_p = \frac{1}{\omega_p} \quad (5.2.4)$$

The frequency range (operation window) of Josephson junction based on superconducting electronics is approximately limited by $\min[\omega_c, \omega_p]$. The switching of a junction is depicted in Fig. 5.4. The switching

delay mainly consists of two components: the “turn-on” delay τ_t and the “rise-time” τ_r required for charging the junction capacitance.

Turn-on Delay τ_t

In order to switch the junction the current has to be increased from $I_b < I_c$ by a value ΔI so that $I_b + \Delta I > I_c$. Initially, this current is not flowing through the junction (kinetic **inductance**) but through the capacitance C and the resistance R . τ_t is the characteristic time required for redirecting this current through the junction. It is given by

$$\tau_t = \sqrt{\tau_{RL}\tau_{RC}} = \sqrt{\frac{\phi_0}{2\pi} \frac{C}{\Delta I}} = \tau_{LC} \sqrt{\frac{I_c}{\Delta I}} \quad (5.2.5)$$

Equation (5.2.5) shows that τ_t is proportional to \sqrt{C} and $1/\sqrt{\Delta I}$. Small junction capacitances and high overdrive currents ΔI therefore decrease τ_t .

Rise Time τ_r :

The rise time is the time required to charge the junction capacitance. It is given by

$$\tau_r = RC, \quad (5.2.6)$$

where R is the total resistance given by $1/R = 1/R_J(V) + 1/R_L$. In order to transfer a large current to the load, R_L is usually chosen much smaller than the junction sub-gap resistance, so that $\tau_r = R_L C$. Since $I_c R_L \simeq V_g = 2\Delta/e$ the rise time can be written as

$$\tau_r = \frac{2\Delta C}{eI_c}. \quad (5.2.7)$$

Fig. 5.4 depicts a typical switching waveform obtained with a computer simulation. Typical values for Nb junctions are $J_c = 10^3 \text{ A/cm}^2$, $C/A \simeq 5 \mu\text{F/cm}^2$, $\Delta/I_c \simeq 0.1$, and $2\Delta/e \simeq 3 \text{ mV}$. This results in $\tau_t \simeq 4 \text{ ps}$ and $\tau_r \simeq 10 \text{ ps}$ comparable to the simulation results in Fig. 5.4. The total delay for Nb Josephson switching devices would then typically be $\tau = \tau_t + \tau_r \simeq 14 \text{ ps}$. Both τ_t and τ_r depend on the junction capacitance. Smaller delay times and faster switching can therefore be obtained by reducing the junction size.

Steering time

The steering time τ_{st} is required to redistribute the current in a circuit with an inductance L . From $V = 2\Delta/e = L\dot{I}$ we obtain with $\dot{I} = I_g/\tau_{st}$

$$\tau_{st} = \frac{LI_g e}{2\Delta}. \quad (5.2.8)$$

Usually LI_g is chosen to be much larger than Φ_0 . For $LI_g/\Phi_0 = 10$ the steering time $\tau_{st} \simeq 10 \text{ ps}$ is obtained for Nb junctions.

Conclusions on Delay Times

Summarizing our discussion on delay times we can state the following:

- τ_t , τ_r , and τ_{st} are of the order $\simeq 1 - 10 \text{ ps}$ for Josephson junction based on Nb technology. .
- Since $\tau_t \propto \sqrt{C/I_c}$ and $\tau_r \propto C/I_c$ it is advantageous to use junctions with low specific capacitance C/A and high critical current density I_c/A , where A is the junction area.

5.2.5 Power dissipation

The power dissipated when a Josephson junction switches from the superconducting state to the voltage state as shown in Fig. 5.2 is given by

$$P = \frac{V_g^2}{R_{sg}}, \quad (5.2.9)$$

where R_{sg} is the sub-gap resistance of the junction. For a Nb junction with a $R_{sg} \simeq 30 \Omega$ one obtains $P \simeq 3 \times 10^{-7} \text{ Watt}$, which amounts to an energy dissipation per switching cycle $E = P \cdot \tau \simeq 3 \times 10^{-18} \text{ J}$. This value has to be compared to values obtained for semiconducting device:

Si	$10^{-8} - 10^{-10} \text{ J}$
GaAs	$10^{-8} - 10^{-10} \text{ J}$
HEMT	$10^{-10} - 10^{-11} \text{ J}$
HTSL	$3 \times 10^{-15} \text{ J}$

For RSFQ (cf. section 5.4) $P\tau \simeq 10^{-18} \text{ Joule}$ is obtained, which would yield at an integration density of 10^7 gates/cm^2 a power dissipation per area of 1 W/cm^2 . Such power density can be easily removed by liquid helium. Note that for the same integration density the power density of semiconductor circuits is by several orders of magnitude larger giving severe problems with heat removal.

At a typical operation temperature $T/T_c \simeq 0.5$ of Josephson junction circuits the sub-gap resistance is determined by thermally activated quasiparticles resulting in $R_{sg} \simeq 10R_n$. The device application determines the minimum critical current I_c^{th} , which is needed for a reliable device operation². Since the I_cR_n product for SIS junction is a material parameter with $I_cR_n \simeq \Delta/e = V_g$ we obtain

$$R_{sg}^{th} \simeq \frac{V_g}{I_c^{th}} \times 10 = 30 \Omega \quad (5.2.10)$$

for $T = 4.2 \text{ K}$, $I_c^{th} = 100 \mu\text{A}$, and $V_g = 3 \text{ mV}$.

² I_c^{th} is given by the requirement that thermally induced switching to the voltage state should be negligibly small (compare section 3.2.4).

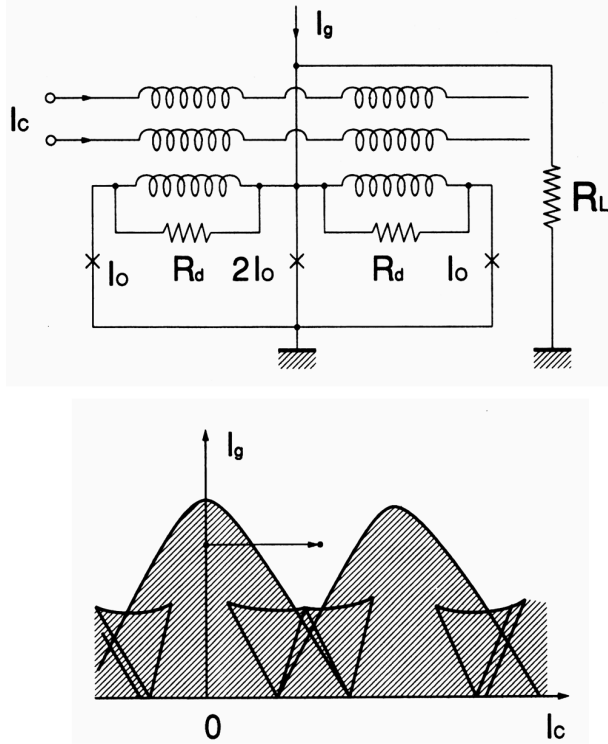


Figure 5.5: Top: equivalent circuit of a 3-Junction Interferometer Logic (JIL) gate. Bottom: threshold characteristics. R_d 's are damping resistors. The hatched region indicates the superconducting state.

5.3 Josephson Logic Gates

The Josephson switching device shown in Fig. 5.3 cannot be used in logic circuits because there is no input-output isolation. Therefore, it is very difficult to get directionality of the logic signal in the circuit (the current switched from one gate can flow in both forward and backward direction).

Different devices that have been suggested can be classified into two types according to the way they are controlled: (i) magnetically coupled gates and (ii) directly coupled gates.

5.3.1 Magnetically coupled gates

Magnetically coupled gates are essentially based on SQUIDs that are controlled by a magnetic field, which is generated by some overlapping control lines. A typical gate is the 3-Junction Interferometer Logic (JIL) gate,³ which is shown in Fig. 5.5 together with its threshold characteristics.⁴ When the control current I_{contr} applied to the control line is large enough, the gate switches to the voltage state. Three junction SQUIDs are used because of their wider operating margins. By choosing the SQUID critical currents $I_1 = I_3 = I_2/2$ the side lobes between the main lobes in the threshold characteristics are suppressed and a wider operating window is obtained, when the gate switches to the voltage state. Note that LC resonances, which may be excited in the circuit by the switching process, are suppressed by damping resistors R_d .

³M. Klein, IEEE J. Solid-State Circuits **13**, 593 (1978).

⁴The threshold characteristic corresponds to the dependence of the maximum bias current on the control current. In other words: the superconducting or zero voltage regime is separated from the finite voltage regime by the threshold curve.

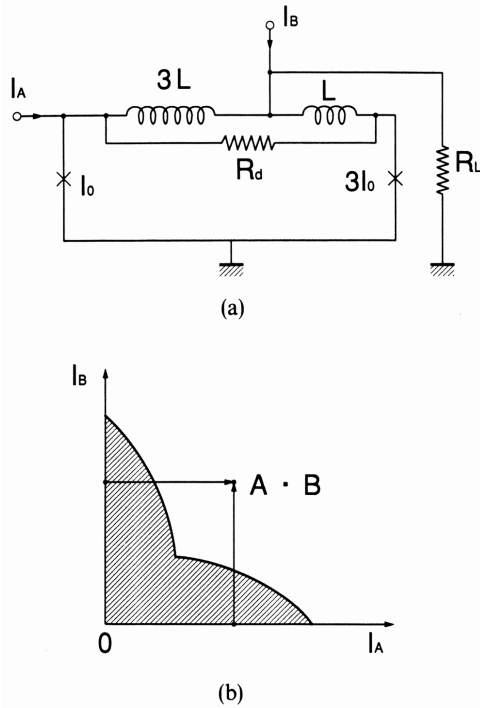


Figure 5.6: Equivalent circuit of the Current-Injection Device (CID) (a) and threshold characteristics (b). The threshold characteristics is symmetric in the two input currents I_A and I_B . Therefore, the CID could be used as an AND gate.

The Current Injection Device (CID),⁵ which is also based on SQUIDs is shown in Fig. 5.6. The CID is operated by direct current injection into the SQUID loop. The threshold characteristics can be made symmetric in the two input currents I_A and I_B by a proper choice of the circuit parameters. The CID gate switches to the voltage state with a broad operating window, if both input currents are applied simultaneously. Therefore, the CID can be used as an AND gate. The CID has no current isolation. JIL gates in front of a CID gate could be used as current isolation gates.

The operation of JIL and CID gates depends on rather large loop inductances. Therefore, the areas of these gates are rather large and a large scale integration of these devices is not possible.

5.3.2 Directly Coupled Gates

Directly coupled gates are controlled by direct injection of the input currents. Note that in the CID described above the magnetic field generated by the injected currents is used to operate the gate. That is why the CID is classified as a magnetically coupled gate. In directly coupled devices the inductances can be eliminated and the devices can be made small.

The first device named Josephson Atto Weber Switch (JAWS)⁶ is depicted in Fig. 5.7. The gate is biased with a current I_g below the critical current of junction J_1 , i.e. the current flows through J_1 and the gate stays in the superconducting state. An input current I_c through J_2 increases the current through J_1 to $I_g + I_c$, which switches J_1 to the voltage state. After J_1 has switched I_g flows through J_2 and a small resistor r_1 to the ground and J_2 also switches to the voltage state. As a result, I_g is transferred to a load resistor R_L and I_c flows through r_1 to the ground thus providing the current isolation.

⁵T. R. Gheewala, IBM J. Res. Dev. **24**, 130 (1980).

⁶T. A. Fuiton, Appl. Phys. Lett. **34**, 1876 (1979).

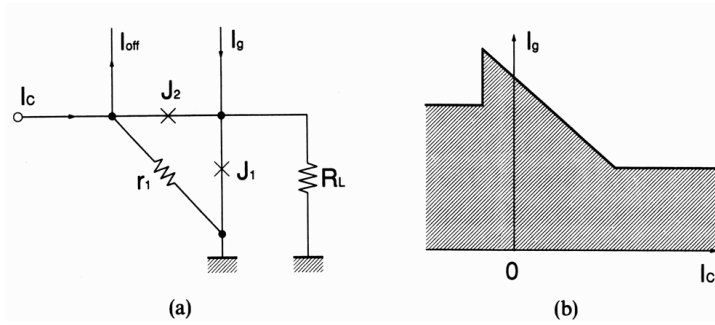


Figure 5.7: Equivalent circuit of the Josephson Atto Weber Switch (JAWS) gate (a) and its threshold curve (b). Input-output current isolation is achieved by the junction J_2 and the resistor r_1 .

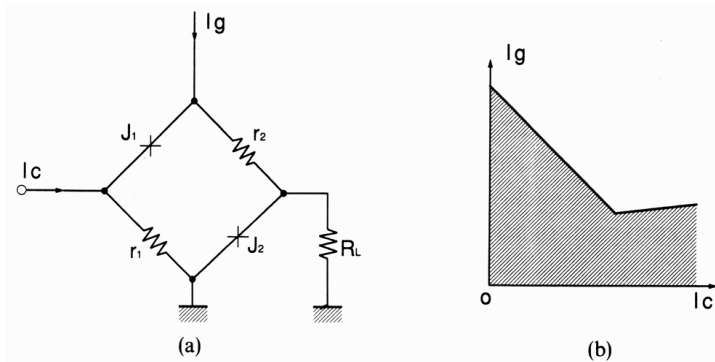


Figure 5.8: Equivalent circuit of the Directly Coupled Logic (DCL) gate (a) and its threshold curve (b).

Another current isolated gate is the Directly Coupled Logic (DCL) gate⁷ shown in Fig. 5.8. The operating principle is similar to that of the JAWS gate. For both the JAWS and DCL gate the threshold curves separating the superconducting from the voltage state have a slope $\Delta I_g / \Delta I_c = -1$. For higher slopes ($|\Delta I_g / \Delta I_c| > 1$) a higher sensitivity is obtained.

The gates shown in Fig 5.9 have higher sensitivity or gain compared to JAWS or DCL gates by inserting an additional Josephson branch. These gates are called Resistor Coupled Josephson Logic (RCJL)⁸ and

⁷T. R. Gheewala, in *Tech. Digest International Electron Device Meeting (IEDM)*, p. 482 (1979).

⁸J. Sone, Appl. Phys. Lett. **40**, 886 (1982).

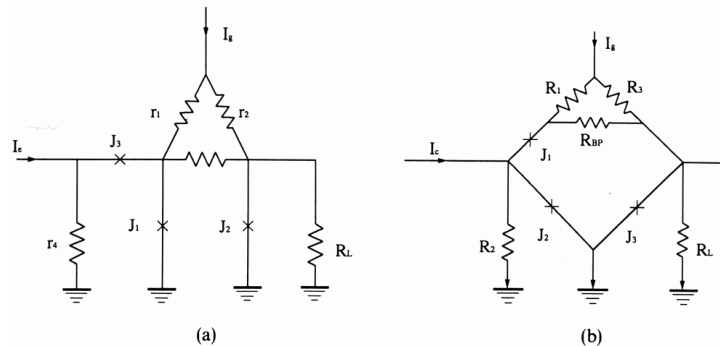


Figure 5.9: Equivalent circuits of the Resistor Coupled Josephson Logic (RCJL) (a) and Resistor Coupled Logic (RCL) gate (b). An additional Josephson branch (J_2 for RCJL and J_3 for RCL) enhances the sensitivity or gain compared to JAWS and DCL gates.

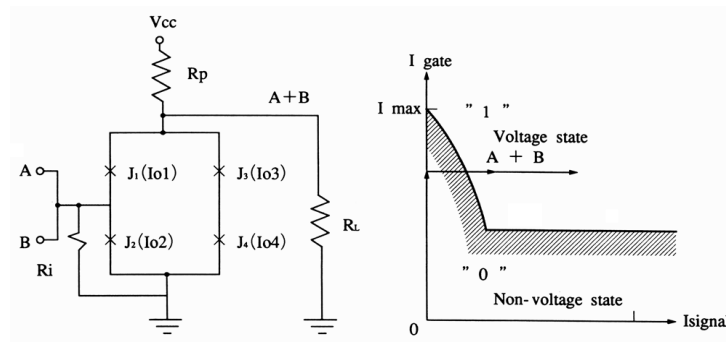


Figure 5.10: Equivalent circuit (a) and threshold curve (b) of the 4 Junction Logic (4JL) gate.

Resistor Coupled Logic (RCL)⁹.

The 4 Junction Logic (4JL)¹⁰ shown in Fig. 5.10 is constructed of 4 Josephson junctions, which are coupled in a loop. The essential feature of the 4JL gate is that the geometric loop inductance can be made as small as possible and therefore the threshold curve depends entirely on the phase differences across the junctions. The current isolation is realized by a small resistor at the input terminal and by making junction J_1 switch at the final stage of the switching sequence. Based on this 4JL concept an AND gate was realized.

The advantage of direct coupled gates over magnetically coupled gates is the elimination of the loop inductance. 4JL gates for example have been realized with a size of $1200 \mu\text{m}^2$, whereas a JIL gate based on the same design rules has an area of $4400 \mu\text{m}^2$.

Hybrid devices with both magnetic and direct coupled gates have also been investigated. In the Modified Variable Threshold Logic (MVTL)¹¹ the input current is first fed into a SQUID control line and then injected into the SQUID directly resulting in a very high sensitivity of the device.

5.3.3 Switching Delay of Logic Gates

gate	linewidth (μm)	switching time (ps)	power dissipation	junction
CIL	2.5	13	$2 \mu\text{W}$	Pb-alloy
JAWS	5	13		Pb-alloy
RCJL	5	10.3	$11.7 \mu\text{W}$	Pb-alloy
RCL	2	4.2		Pb-alloy
4JL	2.5	7	$4 \mu\text{W}$	Pb-alloy
DCL	1.5	5.6	$4 \mu\text{W}$	NbN/Pb-In
MVTL	1.5	2.5	$4 \mu\text{W}$	Nb/AlO _x /Nb

Table 5.1: Switching speeds for various logic gates

In Table 5.1 the logic delays measured for several gates are listed. The shortest delay of 2.5 ps was obtained for the MVTL fabricated with $1.5 \mu\text{m}$ Nb/AlO_x/Nb Josephson junctions. This should not suggest the superiority of the MVTL, because most of the experiments have been made at an early stage when only Pb-alloy junction technology was available. Gate delays could be significantly shorter for devices fabricated with modern Nb-technology.

⁹K. Hohkewa, Appl. Phys. Lett. **39**, 653 (1981).

¹⁰S. Takada, Jpn. J. Appl. Phys. Suppl. **19-1**, 601 (1981).

¹¹N. Fujimaki, Jpn. J. Appl. Phys. **24**, L1 (1985).

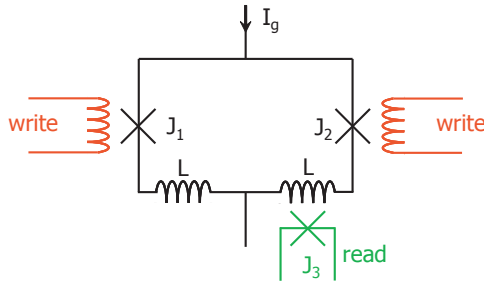


Figure 5.11: Equivalent circuit of the Non-Destructive Read-Out (NDRO) memory cell.

5.3.4 Memory cells

Memories are essential components of any computing system. Semiconducting memories rely on charges stored in capacitors. In superconducting devices persistent currents or magnetic fluxes in superconducting loops are used to store information. Magnetic fluxes are moved in and out of the loops by Josephson gates. The various memory cells can be divided into non-destructive (NDRO) and destructive (DRO) memory cells.

The information stored in non-destructive memory cells can be retrieved without changing the cell state. The NDRO cell is useful to realize cache memories that communicate directly with a CPU (here speed is important).

The earliest NDRO memory cell was suggested in 1969¹². Fig. 5.11 shows the schematic of a NDRO cell. Information is represented as flux enclosed in the loop (eg. “0”: no flux in the loop, “1”: one (or several) flux quanta in the loop). The cell is biased by a current I_g . For zero writing current the current through each of the junctions J_1 and J_2 is $I_g/2$ and no flux is written to the loop. A writing current different from zero results in a vanishing current through either J_1 or J_2 . After I_g is switched off, a circulating current in the loop represents a “1”. The junction J_3 is used to read out the cell. A circulating current in the loop switches the junction J_3 to the voltage state.

Fig. 5.12 shows the schematic layout of a Destructive Read-Out (DRO) memory cell¹³. The 2-junction SQUID has a threshold characteristic with overlapping regions of vortex modes where either of the states is stably maintained. In the DRO information is stored in a single flux quantum by using the mode overlapping region. When the operating point moves across the curve there are two different kinds of transitions: the vortex transition and the voltage transition. When the operating point crosses the dashed lines in Fig. 5.12 (vortex transition) the vortex mode is changed without generating a voltage (only a voltage spike is generated). When the operating point moves across the solid lines the cell generates a voltage. To write a “1” the currents I_x and I_y are used to move the operating point across the vortex transition along the arrow WR1 to the $n = 1$ state. To write “0” the operating point must be moved along WR0 to the $n = 0$ state. To read the cell the operating point is moved across the voltage transition line as depicted in Fig. 5.12. Only if the cell had been in the “1” state a voltage is generated. By reading out the cell the information stored in the cell is erased. Therefore, the cell content needs to be refreshed after each read-out process.

5.3.5 Microprocessors

Different elements such as logic gates, memory cells, address latches, decoders, power supply schemes, timing control circuits have to be functionally integrated to demonstrate the feasibility of Josephson

¹²W. Anacker, IEEE Trans. Magn. **5**, 968 (1969).

¹³H. H. Zappe, Appl. Phys. Lett. **25**, 424 (1974).

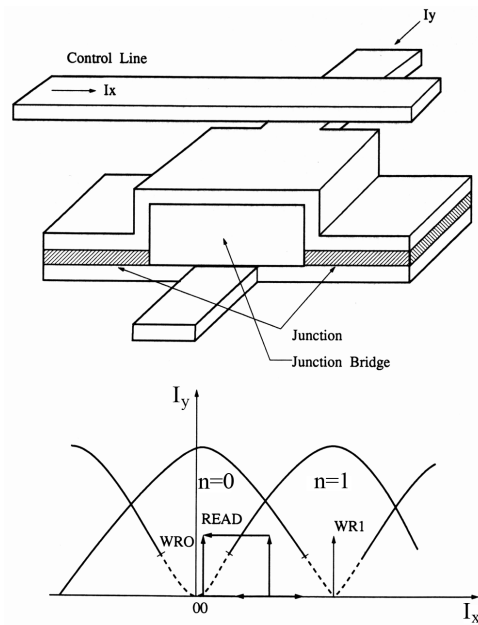


Figure 5.12: Schematic layout of a Destructive Read-Out (DRO) memory cell and its threshold characteristics.

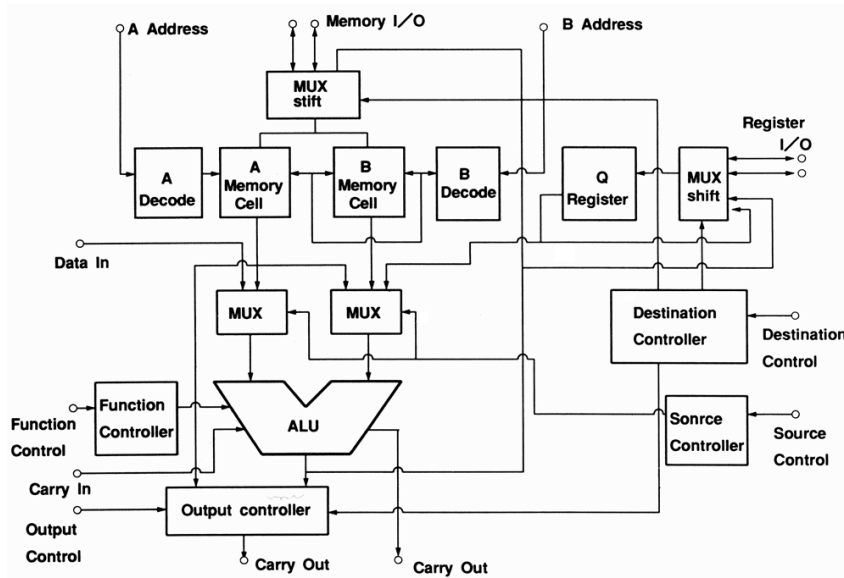


Figure 5.13: Block diagram of the 4 bit Josephson microprocessor.

computer systems. Fig. 5.13 shows the block diagram of an early 4 bit Josephson microprocessor,¹⁴ which is representative of a realistic computer model. The circuit consisting of 64 bit NDRO RAM, ALU, and control circuit was realized through 1841 gates using $2.5 \mu\text{m}$ Nb technology. A typical operation, a carry signal processed in the ALU transferred to the RAM, was performed with a maximum clock frequency of 770 MHz.

Table 5.2 shows various logic gates that have been realized using Josephson latching logic.

¹⁴S. Kotani, IEEE ISSCC Digest of Technical Papers, p. 150 (1988).

circuit	gate family	junction type	# of gates	performance	Ref.
8 bit adder	4JL	Pb-alloy	300	add time 300 ps	^a
8 bit adder	4JL	NbN/Oxide/NbN	364	add time 700 ps	^b
4 bit adder	RCJL	Pb-alloy	56	add time 172 ps	^c
4 bit multiplier	4JL	NbN/Oxide/NbN	652	mult. time 1 ns	^d
4 bit multiplier	RCJL	Pb-alloy	249	mult. time 280 ps	^e
4 bit multiplier	JTHL	Nb/AlO _x /Nb	104	mult. time 210 ps	^f
16 bit multiplier	MVTL	Nb/AlO _x /Nb	828	mult. time 1.1 ns	^g

^aH. Nakagawa, in “Extended Abstracts of 15th Conf. on Solid-State Devices and Materials”, p. 137 (1983).

^bS. Kosaka, IEEE Trans, Magn. **21**, 102 (1985)

^cJ. Sone, in “Technical Digest Int. Electron Device Meeting (IEDM)”, p. 765 (1982)

^dS. Kosaka, IEEE Trans, Magn. **21**, 102 (1985)

^eJ. Sone, IEEE Solid-State Circuits **20**, 1056 (1985)

^fH. Hatano, in “ISSCC Digest of Tech. Papers”, p. 196 (1986)

^gS. Kotani, IEEE J. Solid-State Circuits **22**, 98 (1987)

Table 5.2: Performance of various logic gates

5.3.6 Problems of Josephson Logic Gates

Josephson logic gates based on underdamped Josephson junctions (as discussed in the preceding sections) pose a number of severe problems:

- The first attempts to fabricate logic gates were based on unreliable Pb-alloy technology (large parameter spread, unstable against repeated thermal cycles). Modern Nb-technology provided a significant improvement for the junction quality and reproducibility.
- Josephson logic is a latching logic, i.e. switching the junction back to the $V = 0$ state can not be achieved by switching off the control current. This leads to several complications:
 - an ac power supply is needed
 - problem of punch through limits clock frequencies to below ~ 1 GHz
 - a global timing scheme is needed
 - junctions switch to the voltage state very fast ($0 \rightarrow 1$: 1-10 ps), switching back is slow ($1 \rightarrow 0$: 1 ns).
- There is no transistor-like 3-terminal device providing significant amplification.

In order to reliably switch the junction from the voltage state back to the superconducting state a small negative current has to be applied. This generates the probability of switching from $V = V_g$ to the non-defined state $V = -V_g$ (“punch through”). In order to minimize the punch through probability, the current ramp for resetting the Josephson junction has to be slowed down. This results in a slowed down $1 \rightarrow 0$ switching.

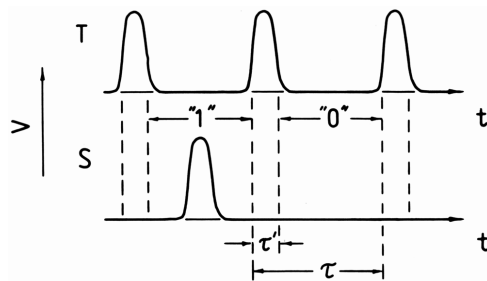


Figure 5.14: Representation of binary units in the RSFQ logic circuits. The signal pulses S are allowed to arrive during the whole clock period τ except some close vicinity τ' of the clock pulses.

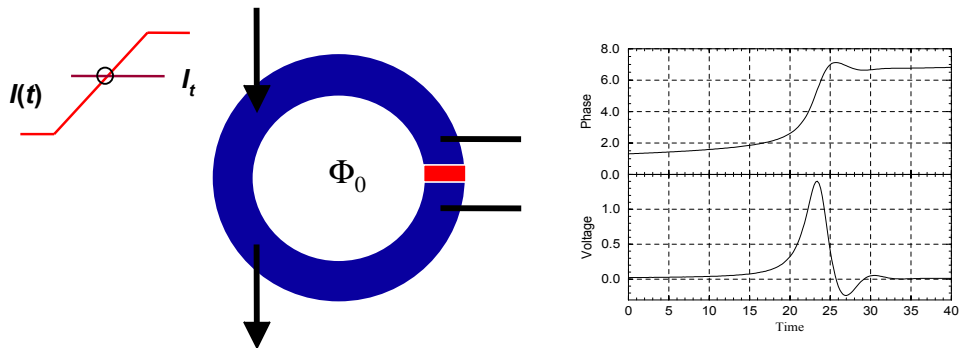


Figure 5.15: Generation of an SFQ pulse in a Josephson junction loop.

5.4 RSFQ Logic

To overcome the limitations of the Josephson latching logic the Resistive or Rapid Single Flux Quantum (RSFQ) logic has been proposed¹⁵. This logic family is based on a totally different representation of information. The information is transferred generally through two lines (cf. Fig. 5.14), one carrying short (quasi)periodic clock pulses T, while the other carries the bit pulses S. A binary “1” is characterized by the arrival of a single S pulse between two consecutive T pulses, whereas the absence of a S pulse denotes a “0”. In Josephson junction circuits this representation is very natural if single flux quantum (SFQ) pulses of the form

$$\int V dt = \phi_0 \quad (5.4.1)$$

are used in both the S and T line. Such pulses can be readily generated and reproduced/amplified either by single overdamped Josephson junctions or by simple circuits consisting of such junctions. Fig. 5.15 illustrates the generation of an SFQ pulse by applying a bias current $I(t)$ to a Josephson junction loop (SQUID). When the current exceeds some value I_t a flux quantum enters (leaves) the loop through the junction and a voltage pulse according to (5.4.1) is generated as illustrated in the right part of the plot.

The specific properties of the RSFQ logic are:

- nonlatching logic

¹⁵K. K. Likharev, in “SQUID ’85” (H.-D. Hahlbohm and H. Lübbig, eds.), p. 1103 (1985).

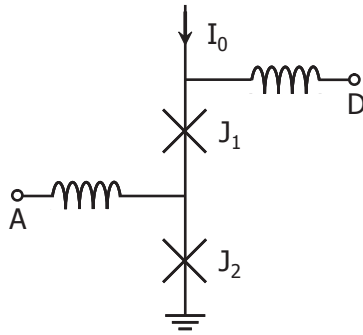


Figure 5.16: RSFQ buffer/amplification stage.

- clock frequencies up to several 10 GHz
- requirement of overdamped Josephson junctions
- low power consumption ($P\tau \simeq 10^{-18}$ J per bit)

5.4.1 RSFQ Buffer/Amplifier Stage

Fig. 5.16 shows a very simple RSFQ circuit, the buffer amplifier stage. The junctions are dc-current biased below their critical currents. If a short pulse arrives at A it induces a 2π switching of the Josephson phase of junction J₂. This switching produces the standard SFQ pulse at the output terminal D. The input pulse may be weaker than the standard pulse, so that the circuit provides some amplification. On the other hand, if the pulse arrives at terminal D, junction J₁ generates a 2π pulse because of its lower critical current. Thus, no SFQ pulse passes to the input A of the circuit, it performs the function of a one-directional buffer as well.

5.5 Recent Developments

5.5.1 RSFQ Logic

The following text is taken from “RSFQ technology: circuits and systems” by D. Brock, Hypres inc.:

(Demand from telecommunication and computer area for above 100 GHz systems) For traditional three-terminal semiconducting transistor devices a cutoff frequency approaching 1 THz is needed to achieve a throughput of the order of 100 GHz for small application specific ICs (ASICs). Such performance requirements are beginning to reach the limits of the physical properties of semiconductors¹⁶. Furthermore, it has been noted that the rate of innovation in semiconductor materials and devices has dramatically slowed down and that virtually no improvement in device speed is anticipated beyond the next five years¹⁷. To sustain the historical performance growth in the electronics industry, a radically new IC technology (one that is scalable and addresses the problems of both device speed and interconnect delay) must be identified and nurtured, while keeping cost in mind.

RSFQ technology, based on low-temperature superconductors, has the potential to leapfrog the performance of traditional silicon and III-V compound semiconductors. ICs with sub-micron RSFQ static digital frequency dividers have already been fabricated and operated in laboratories at over 750 Gb/s¹⁸. These achievements represent faster demonstrated electronic circuit speeds than any other technology has predicted to date, even through computer simulations. Prototype RSFQ circuits made with modest research-grade 2-3 μm linewidth niobium (Nb) fabrication processes have demonstrated circuits such as those shown in the following table.

circuit type	circuit metric(s)
toggle flip flop	144 GHz
4-bit shift register	66 GHz
6-bit flash ADC	20 GHz
1:8 demultiplexor (synchronous)	20 Gb/s
1-bit half-adder	23 GHz
8 × N bit serial multiplier	16 GHz
128-bit auto-correlator	16 GHz
2-bit counter	120 GHz
1-kbit shift register	19 GHz
6-bit transient digitizer	16 Gb/s
1:2 demultiplexor	95 Gb/s
2-bit full-adder	13 GHz
14-bit digital comb filter	20 GHz
time-to-digital converter	31 GHz

Because RSFQ logic uses the lossless ballistic transmission of digital data (fluxons) near the speed of light, the wire-up nightmare that silicon designers face is substantially reduced. This scenario also allows the full speed potential of individual gates to be realized. Other features of this technology that make it suitable for growth into the traditional market include its compatibility with existing IC packaging techniques. These include compatibility with optical (fiber) signal input and output, a maturing multi-chip module (MCM) technology with multi-Gb/s digital data transfer between chips, and simple interface circuits to convert to and from both ECL logic and CMOS logic levels. RSFQ integrated

¹⁶M. Shultz, Nature **399**, 729 (1999); P. Packman, Science **285**, 2079 (1999)

¹⁷1999 SIA Roadmap

¹⁸W. Chen, Appl. Phys. Lett. **73**, 2817 (1998)

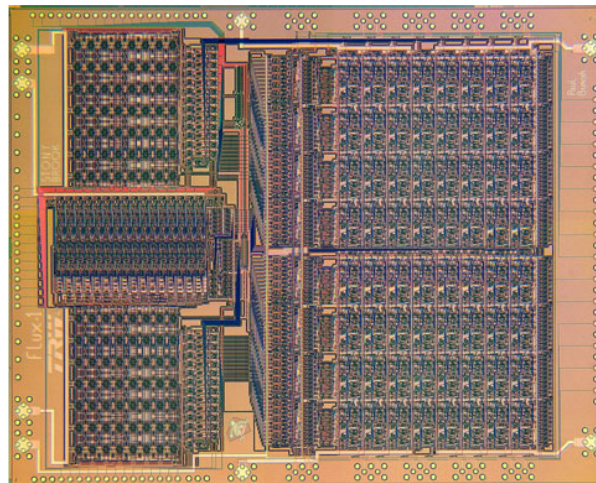


Figure 5.17: First superconducting 20 GHz 8-bit RSFQ microprocessor built in $1.75\text{ }\mu\text{m}$ Nb-technology designed at SUNY Stony Brook and fabricated using TRS's Nb-trilayer technology ("FLUX-1"). The MPU which uses 16 word instruction memory is fabricated from 70,000 Josephson junctions, consumes 14 mW and is designed to operate at 20 – 22 GHz.

circuits are made with standard semiconductor manufacturing equipment; however, there are many fewer mask layers (typically about 10) and the actual processing involves much less complex depositions¹⁹. Because RSFQ logic is an all thin-film technology, there are no doping profiles to calculate, no high-temperature drive-ins, no epitaxial growths or chemical-vapor depositions. These differences translate directly into reduced costs in the large-scale manufacture of RSFQ electronics. System-on-a-chip (SOC) architectures, containing both front-end analog circuitry, as well as digital processing blocks, are fundamental to enabling tomorrow's 100 GHz applications. This configuration presents extraordinary difficulties for semiconductors, due to crosstalk problems of interference between the analog and digital sections of the same chip. Because of the unique reliance on single quanta of magnetic flux to convey information, RSFQ are inherently more immune to this sort of crosstalk.

Novel developments in the Nb junction technology provide the shunt resistance for the shunting required to overdamp the junction without extra need of chip area thus paving the way for a VLSI integration level^{20,21}. At SUNY/Hypres RSFQ circuits with a complexity of > 1000 Nb/ AlO_x /Nb junctions have been realized for digital filter, correlator circuits²², and even for RSFQ microprocessors (cf. Fig. 5.17). Design methods developed for LTS and HTS RSFQ circuits, for Nb circuits even cell libraries, permit simulations of fairly complex circuits.

The GHz clocking of larger RSFQ circuits can no longer be accomplished by synchronous clocking as it is common practice up to now since the small relative time differences necessary for this clocking procedure can no longer be guaranteed over larger distances. A number of asynchronous clocking schemes have been proposed²³. Data-driven self timing was tested with success for the data exchange between 2 LTS shift registers at data rates up to 20 GBit/s²⁴. In a US project aiming at high speed data switches, a LTS clock recovery circuit²⁵ has been tested successfully at frequencies up to 35 GHz. In the same

¹⁹HYPRES, Inc., <http://www.hypres.com>; L. Ya, IEEE Trans. Magn. **23**, 1476 (1987)

²⁰H. Kohlstedt, in "Proc. Internat. Supercond. Electronics Conference (ISEC 97)", H. Koch and S. Knappe (eds.), Vol. 1, p. 254.

²¹M. Maezawa, Appl. Phys. Lett. **70**, 3603 (1997).

²²S. V. Polonsky, ISEC 1997 Vol. 1, p. 125

²³K. Gaj, ISEC 1997, Vol. 2 p. 299

²⁴Z. J. Deng, ISEC 1997, Vol. 2 p. 332.

²⁵V. Kaplunenko, Appl. Phys. Lett. **71**, 128 (1997).

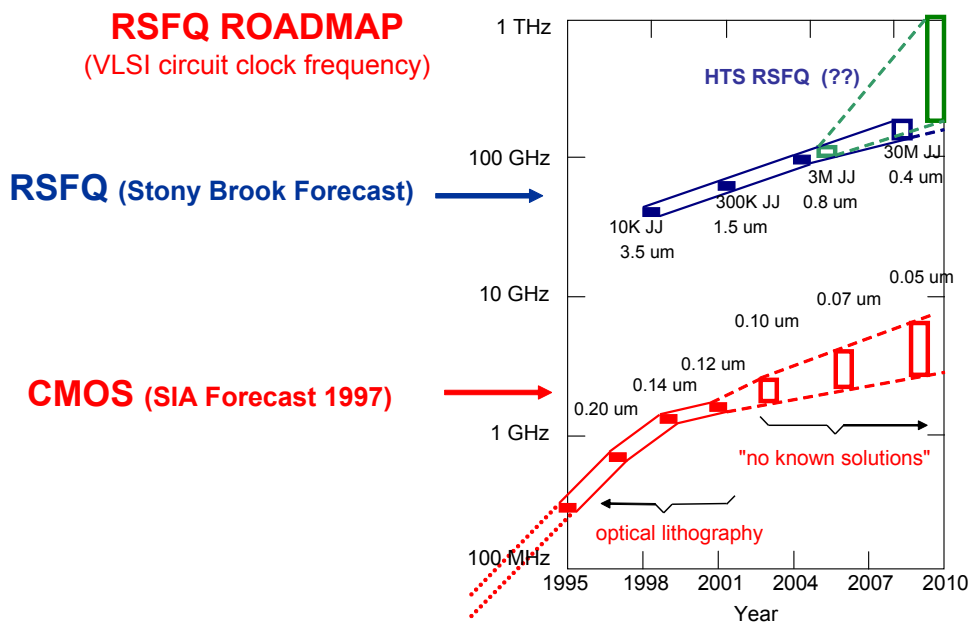


Figure 5.18: Roadmap for RSFQ digital electronics (as projected by K. K. Likharev, SUNY Stony Brook) compared to the SIA forecast for semiconducting CMOS electronics. The numbers below the symbols denote the technology linewidth. The major obstacle for advancing semiconducting electronics above several GHz is the high power dissipation.

project, an underdamped long Nb/A_xO₃/Nb junction was tested as soliton oscillator SFQ clock achieving a linewidth of 38 kHz at 12 GHz²⁶.

The projected potential of RSFQ circuits and their eventual superiority over semiconductor devices is illustrated in the roadmap for RSFQ digital electronics in fig. 5.18 (derived by K. K. Likharev, SUNY Stony Brook). The major obstacle for advancing semiconductor electronics above several GHz is the high power dissipation.

5.5.2 Latching Josephson Logic

The latching logic scheme was pursued in the IBM and the MITI Josephson computer projects as a close analog to the semiconductor logic implementation. The frequency limitation to clock frequencies ~ 1 GHz stems from the necessity to avoid a punch through. As many useful circuit designs have been developed for this logic scheme including interface circuits to semiconductor electronics, a *pragmatic* route to a rapid development of superconducting digital electronics must make use of these resources. This argument may be the reason for the continuation of development work, e.g. at NEC²⁷.

In the beginning of the 1990's despite the impressive technical results, MITI sponsors were ultimately disappointed that no operational systems resulted from the Josephson Computer Project. Because of this and the enthusiasm associated with the discovery of HTS, the LTS activities in Japan were abruptly scaled back at the conclusion of the project.

The evolution of the original LTS computer activities is discernible at three laboratories in Japan, with some continued effort on NbN junctions at ETL, data switch development at Hitachi and NEC, and refinements in RAM at NEC. Table 5.3 summarizes the status of the NEC memory work. Use of moats to

²⁶Y. M. Zhang, Appl. Phys. Lett. **71**, 1863 (1997).

²⁷Y. Hashimoto, ISEC 1997, Vol 2 p. 269.

control flux trapping has reduced the defects, and careful attention to the fabrication process has enabled the increase in size to 4 kbit organization and a reduction in critical path access time to below 400 ps. Using a shrink of design rules to submicron features, NEC recently demonstrated an $8.5 \times 8.5 \mu\text{m}^2$ cell which the researchers project to 1 Mb/cm^2 density (1997). Still, much effort remains to solve the memory deficiency of superconductive technology.

access time	380 ps
power dissipation	9.5 mW
bit yield	99.8 %
Josephson junctions	Nb/AlO _x /Nb
number of junctions	21.000
critical current density	3.3 kA/cm ²
minimum junction size	$2 \mu\text{m} \times 2 \mu\text{m}$
minimum line width	$1.5 \mu\text{m}$
cell size	$55 \mu\text{m} \times 55 \mu\text{m}$
RAM size	$4.5 \text{ mm} \times 4.5 \text{ mm}$

Table 5.3: Josephson 4 kbit RAM characteristics (Organization: 4096 word x 1 bit, NEC)

Chapter 6

The Josephson Voltage Standard

in Vorbereitung

Chapter 7

Microwave Sources and Detectors

in Vorbereitung

Chapter 8

Superconducting Quantum Bits

In section 3.3 we already have discussed the quantum consequences of the small capacitance of Josephson junctions leading to interesting secondary quantum macroscopic effects. The interest in macroscopic quantum effects in small capacitance Josephson junctions goes back to the 1980ies. The initial interest was to test whether or not the laws of quantum mechanics can be applied to macroscopic systems in a Hilbert space spanned by macroscopically distinct states.¹ The phase difference of the superconducting order parameter in a Josephson junction or the magnetic flux in a superconducting quantum interference devices were the degrees of freedom used in these studies. Although quantum phenomena such as macroscopic quantum tunneling and resonant tunneling of the phase difference could be demonstrated,^{2,3,4} it was impossible to observe coherent oscillations of the flux between two macroscopically different states, i.e. macroscopic quantum coherence.⁵

The field of macroscopic quantum coherence in superconducting systems received new attention in the last years, when it became obvious that Josephson circuits are interesting candidates for the realization of quantum bits (qubits). The vision that superconducting devices may serve as qubits in quantum information processing and that quantum logic operations could be performed by controlling gate voltages or magnetic fields stimulated an intensive research effort.^{6,7,8,9,10,11,12} Meanwhile there has been a tremendous progress in quantum state engineering in superconducting and other solid state systems. In particular, the quantum superposition of macroscopically distinct states, coherent oscillations and entangled states of several qubits have been observed. Superconducting Josephson systems are very promising, since they can be fabricated by established technologies and their control and measurement techniques

¹A. J. Leggett in *Chance and Matter*, edited by J. Souletie, J. Vannimenus, and R. Stora, Elsevier, Amsterdam (1987), p. 395.

²R. F. Voss, R. A. Webb, *Macroscopic quantum tunneling in a $1\mu\text{m}$ Nb Josephson junction*, Phys. Rev. Lett. **47**, 265 (1981).

³J. M. Martinis, M. H. Devoret, J. Clarke, *Experimental tests of the quantum behavior of a macroscopic degree of freedom: the phase difference across a Josephson junction*, Phys. Rev. **B 35**, 4682 (1987).

⁴R. Rouse, S. Han, J. E. Lukens, *Observation of resonant tunneling between macroscopically distinct quantum levels*, Phys. Rev. Lett. **75**, 1614 (1995).

⁵C. D. Tesche, *Can a noninvasive measurement of magnetic flux be performed with superconducting circuits?*, Phys. Rev. Lett. **64**, 2358 (1990).

⁶V. Bouchiat, *PhD Thesis*, Université Paris VI (1997).

⁷A. Snirman, G. Schön, Z. Hermon, *Quantum manipulations of small Josephson junctions*, Phys. Rev. Lett. **79**, 2371 (1997).

⁸D. Averin, *Adiabatic quantum computation with Cooper pairs*, Solid State Com. **105**, 659 (1998).

⁹L.B. Ioffe, V.B. Geshkenbein, M.V. Feigelman, A.L. Fauchére, G. Blatter, *Quiet sds Josephson junctions for quantum computing*, Nature **398**, 679 (1999).

¹⁰Y. Makhlin, G. Schön, A. Shnirman, *Josephson junction qubits with controlled couplings*, Nature **386**, 305 (1999).

¹¹J.E. Mooij, T.P. Orlando, L. Levitov, L. Tian, C.H van der Wal, S. Lloyd, *Josephson persistent current qubit*, Science **285**, 1036 (1999).

¹²Y. Nakamura, Y.A. Pashkin, J.S. Tsai, *Coherent control of macroscopic quantum states in a single Cooper pair box*, Nature **398**, 786 (1999).

are far advanced. Furthermore, superconducting qubits exploit the coherence of the superconducting state allowing the achievement of sufficiently long phase coherence times.

After giving a brief introduction to quantum information processing, in this chapter we discuss the realization of quantum bits by using superconducting Josephson junction devices.

8.1 Quantum Bits and Quantum Computers

8.1.1 Quantum Bits

Our today's classical computers represent the culmination of years of technological advancements beginning with the early ideas of **Charles Babbage** (1791-1871) and the creation of the first computer by the German engineer **Konrad Zuse** in 1941. Surprisingly however, the high speed modern computer is fundamentally not different from its gargantuan 30 ton ancestors, which were equipped with some 18 000 vacuum tubes and 500 miles of wiring. Although computers have become more compact and considerably faster in performing their task, the basic task remains the same: to manipulate and interpret an encoding of binary bits into a useful computational result. A bit is a fundamental unit of information, classically represented as a "0" or "1" in our digital computers. Each classical bit is physically realized through a macroscopic physical system, such as the magnetization on a hard disk or the charge on a capacitor. A document, for example, comprised of n -characters stored on the hard drive of a typical computer is accordingly described by a string of $8n$ zeros and ones. Herein lies a key difference between our todays classical computer and a quantum computer. Whereas a classical computer obeys the well understood laws of classical physics, a quantum computer is a device that harnesses physical phenomenon unique to quantum mechanics (especially quantum interference) to realize a fundamentally new mode of information processing.

Whereas classical computers operate with ***classical (c-) bits*** usually represented by "0" and "1", quantum computers operate with ***quantum (qu-) bits*** usually denoted as ***qubits***. Physically, a qubit can be represented by every two level quantum system. The basic properties of such systems are discussed in detail in Appendix E. With the basis states of a two level quantum system (e.g. a spin-1/2 system, see Appendix F)

$$|\phi_1\rangle = |0\rangle = |\uparrow\rangle = \begin{pmatrix} 1 \\ 0 \end{pmatrix} \quad (8.1.1)$$

$$|\phi_2\rangle = |1\rangle = |\downarrow\rangle = \begin{pmatrix} 0 \\ 1 \end{pmatrix} \quad (8.1.2)$$

we can define a single-qubit state in the following way:

A qubit $|\Psi\rangle$ is the superposition of two computational basis states

$$|\Psi(t)\rangle = a(t)|0\rangle + b(t)|1\rangle = \begin{pmatrix} a(t) \\ b(t) \end{pmatrix}. \quad (8.1.3)$$



Figure 8.1: Konrad Zuse 1945: Konrad Zuse was building the first binary digital computer Z1 in 1938. The first programmable electromechanical computer Z3 was completed in 1941. Zuse also developed the first algorithmic programming language called "Plankalkül".

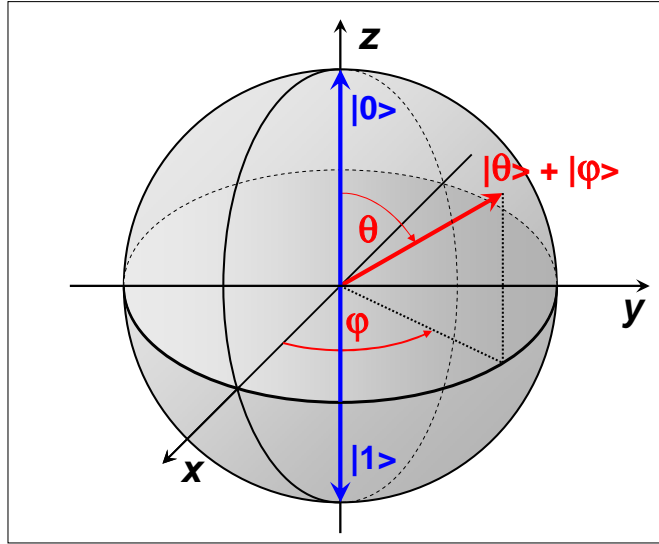


Figure 8.2: Representation of a qubit state as a vector on the Bloch sphere.

Here, $a(t)$ and $b(t)$ are complex amplitudes. If we are measuring the quantum state of a qubit, we obtain the result $|0\rangle$ with probability $|a(t)|^2$ and the result $|1\rangle$ with probability $|b(t)|^2$. Since the total probability must be unity, we have to satisfy the normalization condition

$$\langle \Psi(t) | \Psi(t) \rangle = |a(t)|^2 + |b(t)|^2 = 1 . \quad (8.1.4)$$

We see that the single-qubit exists in a continuum of states. It is a superposition of two basis states and therefore can be represented as a unit vector in a two-dimensional Hilbert space \mathcal{H}_2 . The key fact is that a qubit can exist not only in a state corresponding to the logical state “0” or “1” as in a classical bit, but also in states corresponding to a blend or superposition of these classical states. In other words, a qubit can exist as a zero, a one, or simultaneously as both 0 and 1, with a numerical coefficient representing the probability for each state. This may seem counterintuitive because everyday phenomenon are governed by classical physics, not quantum mechanics – which takes over at the atomic level.

A convenient way of representing of a qubit state is as a unit vector on the Bloch sphere as shown in Fig. 8.2. With the angles θ and φ the general state can be expressed as (compare Appendix D)

$$|\Psi\rangle = \cos \frac{\theta}{2} e^{-i\varphi/2} |0\rangle + \sin \frac{\theta}{2} e^{+i\varphi/2} |1\rangle . \quad (8.1.5)$$

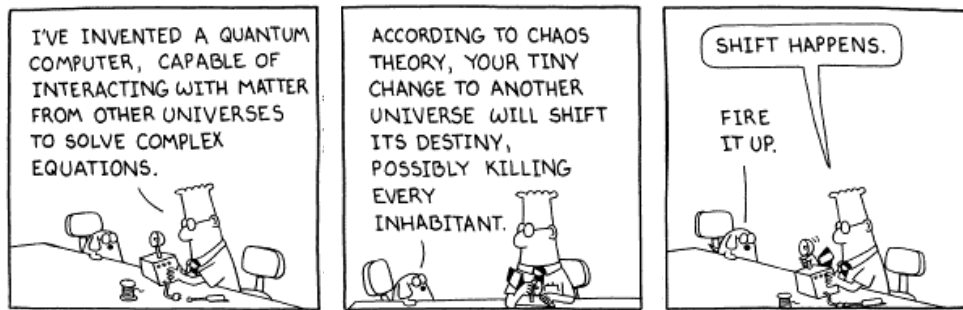
Note that this state is equivalent to the general state of a spin-1/2-system (compare (F.20) in Appendix F). In a measurement process one has to get information on the angles θ and φ .

The foundations of single- and two-qubit states and their manipulation by unitary operators are discussed in detail in Appendix D. There, also an introduction to classical one- and two-bit gates and their quantum counterparts is given.

8.1.2 Quantum Computing

Over the last decades the performance of computers has increased tremendously. This could lead us to suppose that there is no problem that is too complicated to be solved with a classical computer. However, this is not the case. Let us consider the very simple problem of about 150 spin 1/2 particle (e.g. electron).

If we want to do a quantum mechanical description of the state of these electrons, we will exceed the capacity of every conceivable classical computer. The reason for that is that the Hilbert space of the collective spin state of these 150 electrons has the dimension $2^{150} \simeq 10^{45}$. The corresponding density matrix would have 10^{90} elements. Since to our present knowledge the number of protons in our universe is just about 10^{90} , it is just impossible to build a classical computer with the required capacity. In contrast, a quantum computer would require only a few hundred quantum bits for the simulation of the 150 electrons. This simple example shows, that for the simulation of the quantum mechanics of many particle system quantum computers would be highly desirable.



In a classical computer, information is encoded in a series of ***classical bits***, and these bits are manipulated via ***Boolean logic gates*** arranged in succession to produce an end result. In a binary systems, the bits can only have two values usually denoted as “0” and “1”. Similarly, a quantum computer manipulates ***quantum bits*** by executing a series of ***quantum gates***, each a ***unitary transformation*** acting on a single qubit or pair of qubits (for details see Appendix D.3 and D.4). The quantum bits are realized by quantum mechanical two level system with the basis state denoted as $|0\rangle$ and $|1\rangle$ or $|\uparrow\rangle$ and $|\downarrow\rangle$ (see Appendix D to F). A basic difference between classical bits and quantum bits is the fact that the superposition principle allows superpositions of qubit values as entries into a register. An example for three qubits is given in Fig. 8.3. In general, for N qubits we can form 2^N superposition states, that is, the number of superposition states grows exponentially.

The second basic ingredient of a classical computer are ***Boolean logic gates***. In a quantum computer these classical gates are replaced by ***unitary operators***. It is well known that for a classical computer there exist universal sets of gates, that are sufficient to form all other possible gates. As discuss also in Appendix D.4, universal sets for classical gates are (NOT, AND) or the NAND gate alone. In complete analogy there exist sets of unitary operations allowing for the realization of all possible unitary operations. Usually, such set consists of the single bit rotation $U(\theta, \varphi)$ with $U(\theta, \varphi) = \cos \theta e^{-i\varphi/2}|0\rangle + \sin \theta e^{+i\varphi/2}|1\rangle$ (compare Appendix D.3), and a two-qubit-operation. Here, a common example is the ***controlled-NOT gate*** (compare (D.58) in Appendix D.4). With the single qubit rotation and the CNOT gate we can form every arbitrary unitary operation on N qubits allowing for the implementation of any algorithm. That is, in applying these gates in succession, a quantum computer can perform a complicated unitary transformation to a set of qubits in some initial state. The qubits can then be measured, with this measurement serving as the final computational result. A simple scheme how a quantum computer works is shown in Fig. 8.3.

Fig. 8.3 suggests that the operational principle of a classical and a quantum computer are quite similar: the successive application of gates (quantum gates) to a set of bits (qubits). This similarity in calculation between a classical and quantum computer affords that in theory, a classical computer can accurately simulate a quantum computer. In other words, a classical computer would be able to do anything a quantum computer can. So why bother with quantum computers? Although a classical computer can theoretically simulate a quantum computer, it is incredibly inefficient, so much that a classical computer is effectively incapable of performing many tasks that a quantum computer could perform with ease. The simulation of a quantum computer on a classical one is a so-called computationally hard problem,

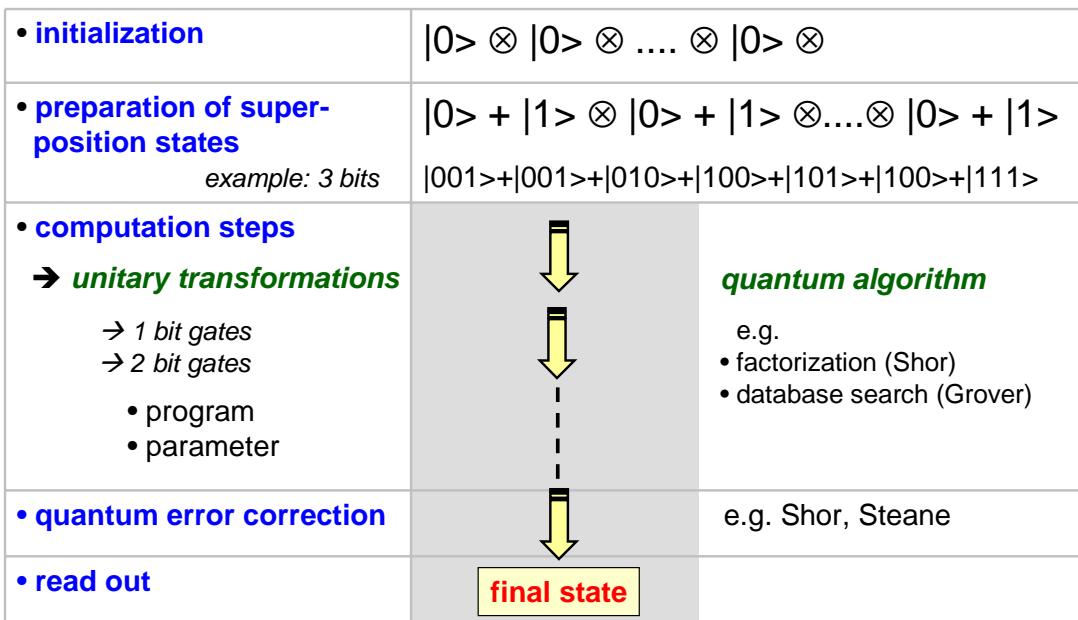


Figure 8.3: Simplified operational scheme of a quantum computer.

since the correlations among quantum bits are qualitatively different from correlations among classical bits. This was first pointed out by **John Bell**. Take for example a system of only 300 qubits, this exists in a Hilbert space of dimension $2^{300} \simeq 10^{90}$ (quantum complexity, see Appendix D.6) that in simulation would require a classical computer to work with exponentially large matrices (to perform calculations on each individual state, which is also represented as a matrix), meaning it would take an exponentially longer time than even a primitive quantum computer.

Richard Feynman was among the first to recognize the problem of handling the simulation of the quantum mechanics of many particle systems by a classical computer (already in 1981). At the same time he was pointing to the potential of quantum superposition for solving such problems much faster. As mentioned already above, a system of 300 qubits, which is impossible to simulate classically, represents a quantum superposition of as many as $2^{300} \simeq 10^{90}$ states. Each state would be classically equivalent to a single list of 300 ones and zeros. Any quantum operation on that system – a particular pulse of radio waves, for instance, whose action might be to execute a controlled-NOT operation on the 100th and 101st qubits – would simultaneously operate on all 2^{300} states. Hence, with one fell swoop, one tick of the computer clock, a quantum operation could compute not just on one machine state, as serial computers do, but on 2^{300} machine states at once! Eventually, however, observing the system would cause it to collapse into a single quantum state corresponding to a single answer, a single list of 300 ones and zeros, as dictated by the measurement axiom of quantum mechanics. The reason this is an exciting result is because this answer, derived from the massive quantum parallelism achieved through superposition, is the equivalent of performing the same operation on a classical super computer with $\sim 10^{90}$ separate processors, what is of course impossible. That is, by exploiting the massive parallelism of the coherent evolution of superpositions of states, quantum computers can perform certain tasks that no classical computer could do in an acceptable time.^{13,14}

Already between 1982 and 1985 **David Deutsch** provided the theoretical basis of the quantum computer by his work on quantum Turing machines. Although the early investigators in this field were naturally excited by the potential of the immense computing power, only very few people took that

¹³C. Bennett, *Quantum information and computation*, Physics Today **48**, 24 (1995).

¹⁴D. DiVincenzo, *Quantum Computation*, Science **270**, 255 (1995).

serious. Only when **Peter Shor**, a research and computer scientist at AT&T's Bell Laboratories in New Jersey, provided a specific application of a quantum computer by devising the first quantum computer algorithm, the field was widely recognized and then a very active hunt was on to find something interesting for a quantum computer to do. **Shor's algorithm** harnesses the power of quantum superposition to rapidly factorize very large numbers (on the order $\sim 10^{200}$ digits and greater) in a matter of seconds. The premier application of a quantum computer capable of implementing this algorithm lies in the field of **encryption**, where one common encryption code, known as RSA, relies heavily on the difficulty of factoring very large composite numbers into their primes. A computer which can do this easily is naturally of great interest to numerous government agencies that use RSA – previously considered to be “uncrackable” – and anyone interested in electronic and financial privacy.

Encryption, however, is only one application of a quantum computer. In addition, Shor has put together a toolbox of mathematical operations that can only be performed on a quantum computer, many of which he used in his factorization algorithm. Furthermore, Feynman asserted that a quantum computer could function as a kind of simulator for quantum physics, potentially opening the doors to many discoveries in the field. Currently the power and capability of a quantum computer is primarily theoretical speculation; the advent of the first fully functional quantum computer will undoubtedly bring many new and exciting applications.



Figure 8.4: Quantum Computing: What's it good for?

A Brief History of Quantum Computing

The idea of a computational device based on quantum mechanics was first explored in the 1970's and early 1980's by physicists and computer scientists such as **Charles H. Bennett** of the IBM Thomas J. Watson Research Center, **Paul A. Benioff** of Argonne National Laboratory in Illinois, **David Deutsch** of the University of Oxford, and the late **Richard P. Feynman** of the California Institute of Technology (Caltech). The idea emerged, when scientists were pondering the fundamental limits of computation. They understood that if technology continued to abide by Moore's Law, then the continually shrinking size of circuitry packed onto silicon chips would eventually reach a point, where individual elements would be no larger than a few atoms. Here, a problem arose because at the atomic scale the physical laws that govern the behavior and properties of the circuit are inherently quantum mechanical in nature, not classical. This then raised the question of whether a new kind of computer could be devised based on the principles of quantum physics.

Feynman¹⁵ was among the first to attempt to provide an answer to this question by producing an abstract model in 1982 that showed how a quantum system could be used to do computations. He also explained how such a machine would be able to act as a simulator for quantum physics. In other words, a physicist would have the ability to carry out experiments in quantum physics inside a quantum mechanical computer.

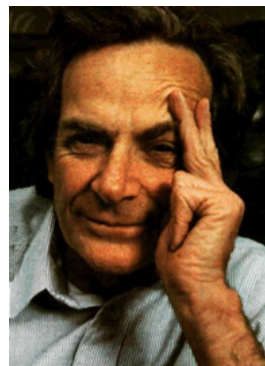
¹⁵R. P. Feynman, Int. J. Theor. Phys. **21**, 467 (1982).

Later, in 1985, Deutsch¹⁶ realized that Feynman's assertion could eventually lead to a general purpose quantum computer and published a crucial theoretical paper showing that any physical process, in principle, could be modelled perfectly by a quantum computer. Thus, a quantum computer would have capabilities far beyond those of any traditional classical computer. After Deutsch published this paper, the search began to find interesting applications for such a machine.

Unfortunately, all that could be found were a few rather contrived mathematical problems, until Shor¹⁷ circulated in 1994 a preprint of a paper in which he set out a method for using quantum computers to crack an important problem in number theory, namely factorization. He showed how an ensemble of mathematical operations, designed specifically for a quantum computer, could be organized to enable such a machine to factor huge numbers extremely rapidly, much faster than is possible on conventional computers. With this breakthrough, quantum computing transformed from a mere academic curiosity directly into a national and world interest.¹⁸



Peter W. Shor



Richard P. Feynman



Charles H. Bennett



David Deutsch

Figure 8.5: Some basic players in quantum computing.

8.1.3 Quantum Error Correction

Error correction is a well known process in classical information processing. For example, a parity bit is added to each data packet in protocols used for data transmission, where parity 0 and 1 state that the data packet has an even or odd number of "1", respectively. In this way one can check whether or not a single data bit or the parity bit has changed during transmission. If for example after transmission a single bit has changed from "1" to "0" or vice versa, the parity of the data packet does no longer correspond to the parity bit attached to the packet and one has to send the whole packet again. Obviously, such simple error correction protocol only protects against the change of an odd number of bits, whereas the change of an even number of bits remain undetected. More complicated protocols, for example the **Hamming protocol** allow for a far more extensive protection.¹⁹ In general, classical error correction operates by the judicious use of redundancy, that is, sending the same information many times. In this sense it is akin to making the system larger in order to make it more resistant to perturbations. However, the precise way in which the redundancy is introduced is very important. The type of redundancy, or encoding, employed must be carefully matched to the type of noise in the channel. Typically, one considers the case of random noise which affects different bits independently, but this is not the only possible case. The

¹⁶D. Deutsch, Proc. Roy. Soc. London, Ser. A **400**, 97 (1985).

¹⁷Shor, P. W., *Algorithms for quantum computation: Discrete logarithms and factoring*, in Proceedings of the 35th Annual Symposium on Foundations of Computer Science, IEEE Computer Society Press (1994).

¹⁸D. Deutsch, A. Ekert, *Quantum Computation*, Physics World, March (1998).

¹⁹F. J. MacWilliams and N. J. A. Sloane, *The Theory of Error-Correcting Codes*, North Holland, Amsterdam (1977).

encoding enables the most likely errors in the information to be identified and corrected. This corrective procedure is akin to active stabilization, and brings the associated benefits of powerful noise suppression.

Since qubits are representing superposition states $|\Psi\rangle = a|0\rangle + b|1\rangle$, it is not obvious that there are error correction protocols also for qubits. However, this is indeed the case. As has been shown by **Calderbank, Shor** and **Steane** there is even a direct relationship between classical and quantum error correction protocols.^{20,21,22,23}

To understand the application of the classical ideas to the quantum regime, it is best to start with a simple example. Thus, suppose we have a collection of spin-half particles, each of which is subject independently to random “flips” or amplitude errors $|0\rangle \rightarrow |1\rangle$, but which otherwise is stable (in particular, the precession is free of phase error). Whenever such a flip occurs, the relevant two-state system may become entangled with its environment. In order to stabilize a single qubit, in the general state $a|0_L\rangle + b|1_L\rangle$, we express it by means of three two-state systems, with the “encoding” $|0_L\rangle = |000\rangle$, $|1_L\rangle = |111\rangle$. Thus, the total initial state of the three spins is $a|000\rangle + b|111\rangle$. After a period of time, during which random flips may occur, the three-spin system is measured twice. The first measurement is a projection onto the two-state basis

$$\{ |000\rangle + |111\rangle + |001\rangle + |110\rangle, |010\rangle + |101\rangle + |100\rangle + |011\rangle \}$$

The second measurement is a projection onto the two-state basis

$$\{ |000\rangle + |111\rangle + |010\rangle + |101\rangle, |001\rangle + |110\rangle + |100\rangle + |011\rangle \}$$

Each measurement has two possible results, which we will call 0 and 1. Depending on which results R are obtained, an appropriate action is carried out: if $R = 00$, do nothing; if $R = 01$, flip the rightmost spin; if $R = 10$, flip the middle spin; if $R = 11$, flip the leftmost spin. If, during the time interval when the system was left to evolve freely, no more than one spin flipped, then this procedure will return the three-spin state to $a|000\rangle + b|111\rangle$. It is remarkable that this can be done without gaining information about the values of a and b and thus disturbing the stored quantum information. During the correction procedure, the entanglement between the system and its environment is transferred to an entanglement between the measuring apparatus and the environment. The qubit is actively isolated from its environment by means of this carefully controlled entanglement transfer. The above error correction technique is based on the simplest classical error correcting code. More advanced techniques can be deduced from more advanced known classical codes.

Before this discovery it seemed to be impossible to carry out a longer quantum algorithm in a reliable way, since already tiny errors would spread in such way that the final result would no longer have any meaning. It now has been discussed that quantum error correction could be even more powerful than classical error correction. So called interlinked quantum error correction protocols have been shown to allow for the implementation of arbitrary quantum algorithms, since in this case the probability for a wrong result is independent of the actual length of the algorithm.

In order to achieve an error tolerant operation of a quantum computer, the error probability per gate or measurement operation has to stay below a certain level. At present this threshold level is estimated to be about 10^{-4} per memory unit, gate or read out process.

²⁰P. W. Shor, Phys. Rev. A **52**, R2493 (1995).

²¹A. M. Steane, Phys. Rev. Lett. **77**, 793 (1996).

²²A. R. Calderbank and P. W. Shor, Phys. Rev. A **54**, 1098 (1996).

²³A. M. Steane, Proc. Roy. Soc. A **452**, 2551 (1996).

8.1.4 What are the Problems?

The field of quantum information processing has made numerous promising advancements since its conception. However, a few potentially large obstacles still remain that prevent us from just building a quantum computer that can rival today's modern digital computer. Among these difficulties, error correction, decoherence, and hardware architecture are probably the most formidable. Error correction is rather self explanatory, but what errors need correction? The answer is primarily those errors that arise as a direct result of decoherence, or the tendency of a quantum computer to decay from a given quantum state into an incoherent state as it interacts, or entangles, with the state of the environment. These interactions between the environment and qubits are unavoidable, and induce the breakdown of information stored in the quantum computer, and thus errors in computation. Before any quantum computer will be capable of solving hard problems, research must devise a way to maintain decoherence and other potential sources of error at an acceptable level. Thanks to the theory of quantum error correction, first proposed in 1995 and continually developed since, small scale quantum computers have been built. Probably the most important idea in this field is the application of error correction in phase coherence as a means to extract information and reduce error in a quantum system without actually measuring that system.

Today only a few of the benefits of quantum computation and quantum computers are readily obvious, but before more possibilities are uncovered theory must be put to the test. In order to do this, devices capable of quantum computation must be constructed. Unfortunately, quantum computing **hardware** is still in its infancy, whereas the theoretical concepts of quantum computing, the **software**, are already rather advanced. A solid state based hardware concept seems promising, since it allows scaling and the used of well developed fabrication techniques. However, it may be that the future of quantum computer hardware architecture is very different from what we know today. Nevertheless, the current research helps to provide insight as to what obstacles the future will hold for these devices.

8.2 Implementation of Quantum Bits

Quantum bits can be implemented with every two level quantum system as shown in Fig. 8.6. The properties of such systems are summarized in Appendix E and F. In practice, quantum information processing also requires the coherent manipulation of suitable quantum systems. The coherent manipulations of the qubits can be performed, if we have sufficient control over the fields and interaction terms in the Hamiltonian and if the decoherence in the considered quantum systems is small enough.

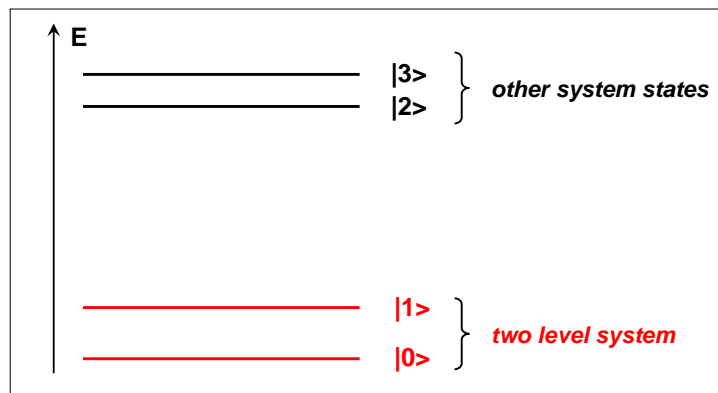


Figure 8.6: A qubit can be realized by a quantum mechanical two level system with the qubit representing the coherent superposition of the two discrete states: $|\Psi\rangle = a|0\rangle + b|1\rangle$. The only requirement is that all other states of the system are well separated from the states $|0\rangle$ and $|1\rangle$ in order to have an effective two-level system. Note that this requirement cannot be achieved for a harmonic potential, where all the states are equidistant.

As has been stressed by **DiVincenzo**,^{24,25} any physical system that is considered as a candidate for the implementation of quantum bits should satisfy the following criteria (DiVincenzo checklist):

1. **Qubits:** The system has to provide a well defined two-level quantum system. This implies that higher level states that are present in most real systems are not excited during qubit manipulations.
2. **Preparation of initial state:** It must be possible to prepare the initial state with sufficient accuracy.
3. **Decoherence:** The phase coherence time must be long enough to allow for a sufficiently large number (typically 10^4) of coherent manipulations. That is, the superposition states of the qubits are allowed to dephase only on time scales much longer than the elementary gate time.
4. **Quantum gates:** There must be sufficient control over the qubit Hamiltonian to perform the necessary unitary transformations, i.e. single- and two-qubit operations (see Appendix D.3). For this purpose it should be possible to control the fields at the sites of the qubits separately and to couple the qubits in a controlled way (e.g. by switching on and off the inter-qubit interactions). Then, the single- and two-qubit operations allow for the generation of arbitrary superpositions and nontrivially coupled states such as entangled states (see Appendix D.3 and D.4).
5. **Quantum measurement:** For read out of the quantum information a quantum measurement is needed. This can be either at the final stage or during the computation for the purpose of error correction.
6. **Scalability:** There should be the possibility to increase the number of qubits (scalability).

²⁴D. DiVincenzo, *The physical implementation of quantum computation*, Fortschr. Phys. **48**, 771 (2000).

²⁵D. DiVincenzo, in *Mesoscopic Electron Transport*, edited by L. Kouwenhoven, G. Schön, and L. Sohn, NATO ASI Series E: Applied Sciences No. 345, Kluwer Academic, Dordrecht (1997), p. 657.

With respect to requirement 1 we can state that there is a large number of physical systems that have been suggested as possible realizations of qubits and gates.²⁶ They are usually split up into non-solid state systems (e.g. ions in electromagnetic traps,^{27,28} nuclear magnetic resonance on ensembles of molecules in liquids,^{29,30} cavity QED systems,³¹ and neutral atoms in optical lattices) and solid state systems. Solid state devices including the above mentioned Josephson systems have the advantage of being more easily embedded into electronic circuits and scaled up to a larger number of qubits (requirement 6). Besides the Josephson systems, electronic states and spin states in quantum dots as well as impurity spins in semiconductors are further candidates. They can be manipulated by tuning potentials and barriers.^{32,33} Finally, electrons floating on liquid helium are discussed.

Besides the advantages of solid state systems with respect to ***scalability*** and embedding into electronic circuits, ***decoherence*** is a severe problem for solid state systems (requirement 3). Unavoidable for devices that have to be controlled externally are interactions with the environment. Due to the coupling to the environment the quantum state of the qubit gets entangled (see Appendix D.2) with the environmental degrees of freedom. As a consequence the phase coherence is destroyed after a time scale called the ***dephasing time***. Due to the large number of environmental degrees of freedom in solid state systems, decoherence is an important issue. Maintaining coherence of a quantum device throughout the manipulation processes is therefore the major challenge for practical quantum computing. We also note that the time evolution of the quantum state may be perturbed also by other sources such as inaccuracies in the preparation of the initial state, inaccuracies in the manipulations and uncontrolled couplings between qubits.

Quantum state engineering requires the ***coherent manipulation of quantum systems***. The manipulations can be performed, if we have sufficient control over the fields and interaction terms in the Hamiltonian. In order to discuss the requirements 4 and 5 we use a model Hamiltonian of a two-state quantum system (e.g. a spin system). We will see later that under certain conditions other systems such as “charge in a box” or “flux in a SQUID loop” effectively reduce to two-state systems. Since any single two-state quantum systems can be represented as a spin-1/2 system, in the following we write down the model Hamiltonian for this system. With the effective magnetic field \mathbf{B} the Hamiltonian for the manipulation can be written as (compare Appendix F.3)

$$\mathcal{H}_{\text{man}}(t) = -\frac{\hbar}{2}\gamma\mathbf{B}(t)\vec{\sigma} . \quad (8.2.1)$$

Here, $\vec{\sigma} = (\mathbf{X}, \mathbf{Y}, \mathbf{Z})$ are the Pauli spin matrices in the space of states $|\uparrow\rangle$ and $|\downarrow\rangle$ (compare (D.25) in Appendix D.3) and γ the gyromagnetic ratio. These states form the basis states of a physical quantity (spin, charge, flux, ...) that has to be manipulated. Full control of the quantum dynamics of the spin is achieved, if the field $\mathbf{B}(t)$ can be switched arbitrarily. Actually, as shown in Appendix D, full control is already achieved, if only two field components³⁴ can be controlled, e.g. (compare (D.24) in Appendix D.3)

$$\mathcal{H}_{\text{man}}(t) = -\frac{\hbar}{2}\gamma B_z \mathbf{Z} - \frac{\hbar}{2}\gamma B_x \mathbf{X} . \quad (8.2.2)$$

²⁶S. Braunstein, H.-K. Lo eds., *Experimental Proposals for Quantum Computing*, Fortschr. Phys. **48**, 765 (2000).

²⁷J. I. Cirac, P. Zoller, *Quantum computation with cold trapped ions*, Phys. Rev. Lett. **74**, 4091 (1995).

²⁸C. Monroe, D.M. Meekhof, B.E. King, W. M. Itano, D.J. Wineland, *Demonstration of a fundamental quantum logic gate*, Phys. Rev. Lett. **75**, 4714 (1995).

²⁹D. Cory, A. Fahmy, T. Havel, *Ensemble quantum computing by NMR spectroscopy*, Proc. Natl. Acad. Sci. USA **94**, 1634 (1997).

³⁰N. Gershenfeld, I. Chuang, *Bulk spin resonance quantum computation*, Science **275**, 350 (1997).

³¹Q.A. Turchette, C.J. Hood, W. Lange, H. Mabuchi, H.J. Kimble, *Measurement of conditional phase shifts for quantum logic*, Phys. Rev. Lett. **75**, 4710 (1995).

³²B.E. Kane, *A silicon based nuclear spin quantum computer*, Nature **393**, 133 (1998).

³³D. Loss, D.P. DiVincenzo, *Quantum computation with quantum dots*, Phys. Rev. A **57**, 120 (1998).

³⁴If all three field components can be controlled, the topological or Berry phase of the systems can be manipulated as well.

If we want to manipulate a many-qubit system in order to perform quantum computing, we have to control the field at the sites of each spin separately. Furthermore, in addition to single-qubit operations we need two-qubit unitary operations (see Appendix D.3 and D.4). The latter require the coupling of two qubits. Including this coupling, the following model Hamiltonian seems to be suitable for a N -qubit system:

$$\mathcal{H}_{\text{man}}(t) = - \sum_{i=1}^N \frac{\hbar}{2} \gamma \mathbf{B}^i(t) \vec{\sigma}^i + \sum_{i \neq j} J_{\alpha\beta}^{ij}(t) \vec{\sigma}_\alpha^i \vec{\sigma}_\beta^j . \quad (8.2.3)$$

Here, the summation over the spin indices $\alpha, \beta = x, y, z$ is implied. Note that in this model Hamiltonian we have assumed a general form of the coupling between the qubits. In many cases simpler forms such as the pure Ising (ZZ), the XY (see Appendix D.3) or the Heisenberg coupling are sufficient.

In the model Hamiltonian we so far have neglected the measurement system and the coupling with the environment. This can be accounted for by the two extra terms $\mathcal{H}_{\text{meas}}$ and $\mathcal{H}_{\text{envir}}$, respectively, resulting in the total Hamiltonian

$$\mathcal{H}(t) = \mathcal{H}_{\text{man}}(t) + \mathcal{H}_{\text{meas}}(t) + \mathcal{H}_{\text{envir}} , \quad (8.2.4)$$

where we have assumed that the residual coupling to the environment is time independent. During the manipulation of the qubits the measurement device should be in the off-state, i.e. $\mathcal{H}_{\text{meas}} = 0$. Furthermore, the interaction with the environment should be as small as possible, since it results in dephasing and relaxation processes.

The ***preparation of the initial state*** (requirement 2) can be achieved by keeping the system at low temperatures so that it relaxes to the ground state. For a spin system this can be achieved for example by switching on a large field $B_z \gg k_B T$ for a sufficiently long time, while $B_x(t) = B_y(t) = 0$. Then, due to the residual interaction with the environment, each qubit relaxes into its ground state, e.g. $|\uparrow\rangle$ for a spin system. If we then switch off B_z we are left with the system in a well-defined pure ground state.

A typical experiment performed with qubits involves the preparation of the initial state, the switching of the fields $\mathbf{B}(t)$ and the coupling $J_{\alpha\beta}^{ij}(t)$ to achieve a specific unitary evolution of the qubit state, and the measurement of the final state.

8.3 Why Superconducting Qubits

On the first sight, microscopic systems seem to be ideal candidates for qubits, since they can be easily isolated from the environment thereby avoiding decoherence. However, the disadvantage of microscopic systems (e.g. ions in an electromagnetic trap) is usually scalability and the lack of simple embedding into other electronic circuits. That is, it is difficult to integrate many qubits into a more complex circuit in order to approach the vision of a practical quantum computer. Therefore, macroscopic quantum systems such as superconductors are attractive, since they offer more flexibility in scaling using standard integrated circuit technology. Until now several “macroscopic” qubits have been proposed that are based on nanostructured solid state electronic circuits, which are based either of semiconductor quantum dots or superconducting Josephson junctions.

As already mentioned above the large number of microscopic degrees of freedom in solid state devices makes it more difficult to achieve sufficiently long dephasing times. This is in particular a problem for charge based qubits, since the charge degree of freedom strongly couples to environmental degrees of freedom. Therefore, the use of isolated spins on quantum dots³⁵ or through the deliberate doping of semiconductors³⁶ seems more promising.

Quantum bits based on superconducting materials have particular advantages. First, the superconducting ground state is separated by an energy gap Δ of the order of meV from the quasiparticle excitation spectrum (see Fig. 8.7). Second, the superconducting state represents a non-degenerate macroscopic ground state and finally, superconducting metals have a large electron density resulting in a short screening length for perturbing background charges.

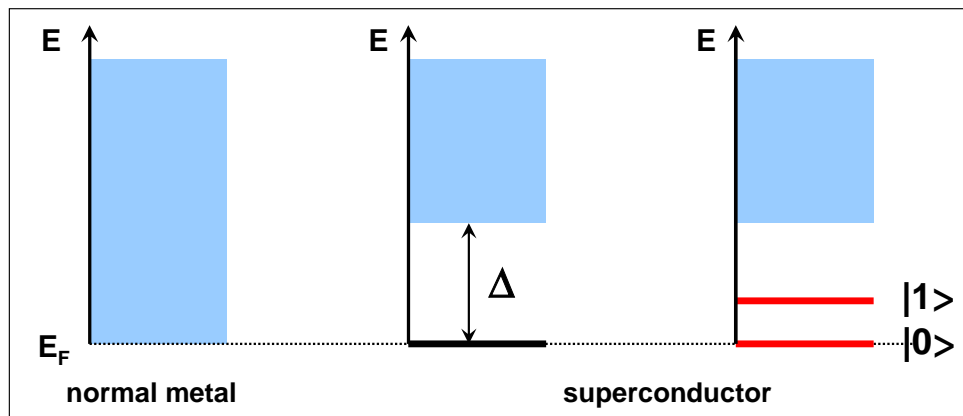


Figure 8.7: Advantage of superconductors for constructing solid state based quantum bits.

8.3.1 Superconducting Island with Leads

In order to get a feeling for the relevant energy scales for Josephson junction devices used for the realization of superconducting quantum bits we consider a superconducting island coupled to a superconducting lead via a Josephson junction that is characterized by an ideal Josephson element with Josephson inductance $L_J = \Phi_0/2\pi I_c$ (see (2.1.22)), normal resistance R_N and capacitance C as shown in Fig. 8.8. We can now consider the energy required to change the number N of Cooper pairs on the island by one and on the other hand the energy required to change the phase ϕ of the superconducting wave function by 2π .

³⁵D. Loss, D.P. DiVincenzo, *Quantum computation with quantum dots*, Phys. Rev. A **57**, 120 (1998).

³⁶B.E. Kane, *A silicon based nuclear spin quantum computer*, Nature **393**, 133 (1998).

The first is given by the charging energy

$$E_C = \frac{q^2}{2C} \quad (8.3.1)$$

with $q = 2e$. The latter is just the energy required to change the phase difference $\varphi = \phi_{\text{island}} - \phi_{\text{reservoir}}$ across the Josephson junction by 2π or, equivalently, to move a single flux quantum Φ_0 across the Josephson junction. This energy is given by the Josephson coupling energy $E_J = E_{J0}(1 - \cos \varphi)$ with the maximum value for $\varphi = \pi$ given by

$$2E_{J0} = \frac{\Phi_0 I_c}{\pi} = \frac{(\Phi_0/\pi)^2}{2L_J} . \quad (8.3.2)$$

As already discussed in section 3.3, there is an uncertainty relation $\Delta\phi \cdot \Delta \geq 1$ for the number N of Cooper pairs and the phase ϕ . Considering the two characteristic energy scales E_C and E_{J0} we can conclude the following:

- $E_C \gg E_{J0}$:

In this case large energy is required to change N . That is, the number N of Cooper pairs or the charge state of the island is well defined, whereas according to $\Delta\phi \cdot \Delta \geq 1$ the phase ϕ is completely smeared out.

- $E_C \ll E_{J0}$:

In this case a large energy is required to change the phase ϕ , whereas the energy for changing N is small. Then, Cooper pairs easily can enter and leave the island resulting in large fluctuation of N what, in turn, causes small fluctuations of ϕ and hence in a well defined phase.

Note that in this discussion we only considered the Cooper pairs and have completely neglected the quasiparticle degrees of freedom.

We also have to consider the effect of thermal and quantum fluctuations. Thermal fluctuation do not play any role as long as

$$E_{J0}, E_C \gg k_B T . \quad (8.3.3)$$

This condition can easily satisfied with respect to E_{J0} . For example, a Josephson junction with a maximum Josephson current $I_c = 100 \mu\text{A}$ (corresponding to a junction area of $10 \times 10 \mu\text{m}^2$ at a typical current density of $J_c = 100 \text{ A/cm}^2$) has a coupling energy $E_{J0} \simeq 3 \times 10^{-18} \text{ J}$ corresponding to $T \simeq 2300 \text{ K}$. For the charging energy this is more difficult. In order to have a charging energy corresponding a temperature of only 1 K, the capacitance has to be as small as only 1 fF. With a specific capacitance of Josephson tunnel junctions of typically $100 \text{ fF}/\mu\text{m}^2$, the junction area has to be as small as $0.1 \times 0.1 \mu\text{m}^2$ requiring advanced fabrication technology.

The effect of quantum fluctuations can be estimated from energy-time uncertainty relation $\Delta E \Delta t \geq \hbar$. For the charge and the phase channel the characteristic time scales are $R_N C$ and L_J/R_N , respectively. With the condition $\Delta E \ll E_C$ and $\Delta E \ll E_{J0}$ we obtain the conditions

$$R_N \gg h/q^2 \quad \text{for } \Delta E \ll E_C \quad (8.3.4)$$

$$R_N \ll h/q^2 \quad \text{for } \Delta E \ll E_J \quad (8.3.5)$$

respectively, with $q = 2e$. We see that the resistance $R_Q/4$, where $R_Q = h/e^2$ is the quantum resistance, separates the regimes, where quantum fluctuations of the charge and the phase are dominant.

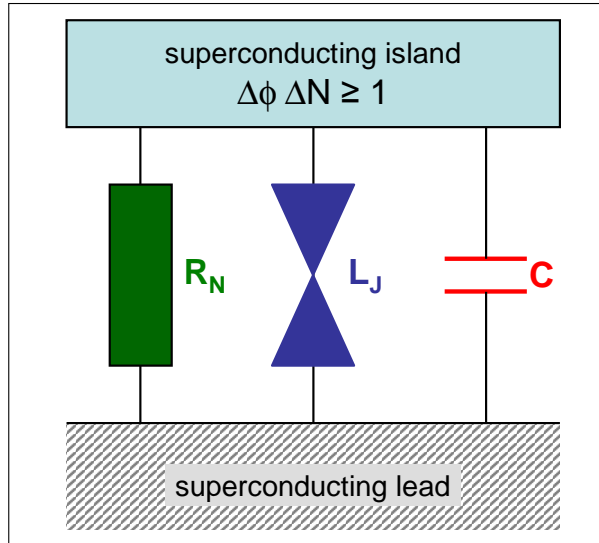


Figure 8.8: A superconducting island coupled to a superconducting lead (reservoir) via a Josephson junction characterized by an ideal Josephson element of Josephson inductance L_J , normal resistance R_N and a capacitance C .

A further characteristic energy scale of superconductors is the energy gap Δ . With the fact that the characteristic energy $eI_cR_N = eV_c \simeq \Delta$ we obtain

$$E_{J0} \simeq \frac{\hbar I_c}{2e} = \frac{\hbar}{2e^2 R_N} e I_c R_N \simeq \frac{R_Q}{4R_N} \Delta . \quad (8.3.6)$$

We see that for junctions with $R_N \gg R_Q/4$ we have $E_{J0} \ll \Delta$. Then one can always find a regime for which the two inequalities $E_{J0} \ll E_C \ll \Delta$ hold. The fact that Δ is the largest energy scale is often used in theoretical treatments. It allows to restrict to states of the island containing only an even number of electrons, which form Cooper pairs. The net charge Q on the island can then be written as $qN = 2eN$.

Part III

Appendix

Part IV

Anhang

A The Josephson Equations

The Josephson equations can be derived by considering two quantum systems that are weakly coupled. One starts with the completely uncoupled systems that are described by the macroscopic wave functions ψ_1 and ψ_2 . The time dependence of these wave functions is given by

$$\frac{\partial \psi_1}{\partial t} = -\frac{i}{\hbar} E_1 \psi_1 \quad (\text{A.1})$$

$$\frac{\partial \psi_2}{\partial t} = -\frac{i}{\hbar} E_2 \psi_2 . \quad (\text{A.2})$$

We now switch on a weak symmetric coupling of the two systems. In this case the time evolution of system 1 will also be determined by system 2 and vice versa. We account for this situation by introducing the coupling constant K in (A.1) and (A.1):

$$\frac{\partial \psi_1}{\partial t} = -\frac{i}{\hbar} [E_1 \psi + K \psi_2] \quad (\text{A.3})$$

$$\frac{\partial \psi_2}{\partial t} = -\frac{i}{\hbar} [E_2 \psi_2 + K \psi_1] . \quad (\text{A.4})$$

The coupling of the two systems means that Cooper pairs can be exchanged between the two systems, or equivalently, that the macroscopic wave functions are weakly overlapping (e.g. within the insulating barrier). The magnitude of the coupling constant is determined by the strength of the overlap.

Note that the coupling of two wave functions is very well known from molecules, e.g. the H_2^+ -molecule. However, in the case of two coupled superconductors the wavefunctions represent the whole ensemble of the superelectrons, whereas in a molecule the wavefunctions represent single electrons. Therefore, the amplitude of the superconducting wavefunction is proportional to the density of the superelectrons and the wavefunctions can be expressed as (compare (1.1.47) in section 1.1)

$$\psi_1 = \sqrt{n_1^*} e^{i\theta_1} \quad (\text{A.5})$$

$$\psi_2 = \sqrt{n_2^*} e^{i\theta_2} . \quad (\text{A.6})$$

Using these wavefunctions in (A.3) and (A.4) we obtain

$$\frac{\dot{n}_1^* e^{i\theta_1}}{2\sqrt{n_1^*}} + i\sqrt{n_1^*} e^{i\theta_1} \dot{\theta}_1 = -\frac{i}{\hbar} [E_1 \sqrt{n_1^*} e^{i\theta_1} + K \sqrt{n_2^*} e^{i\theta_2}] \quad (\text{A.7})$$

$$\frac{\dot{n}_2^* e^{i\theta_2}}{2\sqrt{n_2^*}} + i\sqrt{n_2^*} e^{i\theta_2} \dot{\theta}_2 = -\frac{i}{\hbar} [E_2 \sqrt{n_2^*} e^{i\theta_2} + K \sqrt{n_1^*} e^{i\theta_1}] . \quad (\text{A.8})$$

Separation into real and imaginary part yields

$$\frac{1}{2} \frac{\dot{n}_1^*}{\sqrt{n_1^*}} = \frac{K}{\hbar} \sqrt{n_2^*} \sin(\theta_2 - \theta_1) \quad (\text{A.9})$$

$$\frac{1}{2} \frac{\dot{n}_2^*}{\sqrt{n_2^*}} = \frac{K}{\hbar} \sqrt{n_1^*} \sin(\theta_1 - \theta_2) \quad (\text{A.10})$$

and

$$\imath \sqrt{n_1^*} \dot{\theta}_1 = -\frac{\imath}{\hbar} [E_1 \sqrt{n_1^*} + K \sqrt{n_2^*} \cos(\theta_2 - \theta_1)] \quad (\text{A.11})$$

$$\imath \sqrt{n_2^*} \dot{\theta}_2 = -\frac{\imath}{\hbar} [E_2 \sqrt{n_2^*} + K \sqrt{n_1^*} \cos(\theta_1 - \theta_2)] . \quad (\text{A.12})$$

In order to have current conservation we have to demand $\dot{n}_1^* = -\dot{n}_2^*$. For simplicity, we also assume two identical superconductors, that is $n_1^* = n_2^* = n^*$. Then, we obtain from (A.9) and (A.10)

$$\dot{n}_1^* = \frac{2K}{\hbar} n^* \sin(\theta_2 - \theta_1) = -\dot{n}_2^* . \quad (\text{A.13})$$

We have to recall that the change of the particle density in superconductor 1 multiplied by the volume of 1 just corresponds to the change of the particle number in superconductor 1 and, hence, the particle flow through the junction. In order to obtain the supercurrent I_s flowing from superconductor 1 to 2 we only have to multiply by the charge q^* of the superelectrons and obtain

$$I_s = I_c \sin(\theta_2 - \theta_1) \quad (\text{A.14})$$

with the maximum or critical Josephson current³⁷

$$I_c = \frac{2K \cdot q^*}{\hbar} V \cdot n^* . \quad (\text{A.15})$$

From (A.11) and (A.12) we obtain a differential equation for the temporal change of the phase difference $\theta_2 - \theta_1$. With $n_1^* = n_2^* = n^*$ we obtain

$$\frac{\partial}{\partial t}(\theta_2 - \theta_1) = \frac{1}{\hbar} (E_1 - E_2) . \quad (\text{A.16})$$

³⁷Note that in order to keep the density of superelectrons in the superconducting electrodes constant, the junction has to be attached to a current source. The current source supplies and removes charge from the two electrodes thereby keeping n^* constant.

We see that for $E_1 = E_2$ the phase difference between the two superconductors stays constant. However, if there is a constant electric field \mathbf{E} across the junction, the energy difference can be expressed as

$$E_1 - E_2 = q^* \int_1^2 \mathbf{E}(\mathbf{r}, t) \cdot d\ell \quad (\text{A.17})$$

and we recover the second Josephson equation (1.3.19).

B Imaging of the Maximum Josephson Current Density

...

C Numerical Iteration Method for the Calculation of the Josephson Current Distribution

...

D Foundations of Quantum Bits and Gates

D.1 What is a quantum bit ?

Classical computing is based on classical (c-) bits that are usually represented by “0” and “1”. Mathematically we have to deal with a binary variable

$$x \in \{0, 1\} \quad (\text{D.1})$$

with the property $x^2 = x$. Physically, these two states can be represented in different ways as for example by “charge on a capacitor” and “no charge on a capacitor”, by “magnetization direction to the left” and “magnetization direction to the right” or by “hole in the punch card” and “no hole in the punch card”. The bits are manipulated by classical single (e.g. NOT) or multiple bit gates (e.g. AND, NAND, OR, NOR, ...) as discussed in more detail in section D.4. For example, a two bit gate is transferring the two bits x and y with $(x, y) \in \{0, 1\}$ to $f(x, y)$ with $f(x, y) \in \{0, 1\}$.

Single-Qubit Systems

Whereas classical computers operate with *classical (c-) bits*, quantum computers operate with *quantum (qu-) bits* usually denoted as *qubits*. Physically, a qubit can be represented by every two level quantum system. With the basis states of a two level quantum system (e.g. a spin-1/2 system)

$$|\phi_1\rangle = |0\rangle = |\uparrow\rangle = \begin{pmatrix} 1 \\ 0 \end{pmatrix} \quad (\text{D.2})$$

$$|\phi_2\rangle = |1\rangle = |\downarrow\rangle = \begin{pmatrix} 0 \\ 1 \end{pmatrix} \quad (\text{D.3})$$

we can define a one qubit state in the following way:

A qubit $|\Psi\rangle$ is the superposition of two computational basis states

$$|\Psi(t)\rangle = a(t)|0\rangle + b(t)|1\rangle = \begin{pmatrix} a(t) \\ b(t) \end{pmatrix}, \quad (\text{D.4})$$

where $a(t)$ and $b(t)$ are complex amplitudes.

It is important to note that a and b are continuous analogue variables. If we are measuring the quantum state of a qubit, we obtain the result $|0\rangle$ with probability $|a(t)|^2$ and the result $|1\rangle$ with probability $|b(t)|^2$. Since the total probability must be unity we have the normalization condition

$$\langle\Psi(t)|\Psi(t)\rangle = |a(t)|^2 + |b(t)|^2 = 1. \quad (\text{D.5})$$

We see that the qubit exists in a continuum of states. It is a superposition of two basis states and therefore can be represented as a unit vector in a two-dimensional Hilbert space \mathcal{H}_2 .

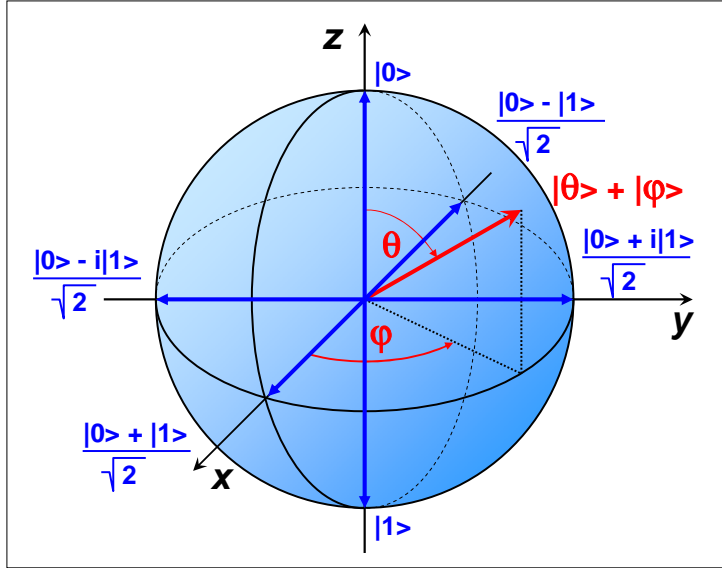


Figure D1: Geometrical representation of a qubit state as a vector on the Bloch sphere S^2 .

A general form of the one-qubit state satisfying (D.5) is given by

$$|\Psi(t)\rangle \equiv |\theta, \varphi\rangle = \cos \frac{\theta}{2} e^{-i\varphi/2} |0\rangle + \sin \frac{\theta}{2} e^{+i\varphi/2} |1\rangle = \begin{pmatrix} \cos \frac{\theta}{2} e^{-i\varphi/2} \\ \sin \frac{\theta}{2} e^{+i\varphi/2} \end{pmatrix}. \quad (\text{D.6})$$

The geometrical representation of the qubit state can hence be given by a point on the Bloch sphere S^2 as shown in Fig. D1.

We immediately can write down some special case for the qubit state $|\theta, \varphi\rangle$:

$$|\theta, \varphi\rangle = |0, \varphi\rangle = |0\rangle \quad (\text{D.7})$$

$$|\theta, \varphi\rangle = |\pi, \varphi\rangle = |1\rangle \quad (\text{D.8})$$

$$|\theta, \varphi\rangle = |\frac{\pi}{2}, 0\rangle = \frac{|0\rangle + |1\rangle}{\sqrt{2}} \quad (\text{D.9})$$

$$|\theta, \varphi\rangle = |\frac{\pi}{2}, \pi\rangle = \frac{|0\rangle - |1\rangle}{\sqrt{2}}. \quad (\text{D.10})$$

These states are also indicated in Fig. D1.

Note that there is an infinite number of possible qubit states. However, any measurement on the qubit state results in a collapse of the state and a reduction of the state to one of its basis states. Information on a and b is only obtained by performing measurements on an ensemble of identical qubits and a statistical analysis. This is a specific advantage of the use of quantum bits in quantum information processing: As long as the quantum system is not perturbed, i.e. as long as we do not perform any measurement, the state keeps all continuous variables for the description of the state. That is, the quantum system keep all possible options until the state is destroyed by a measuring process. This results in a massive quantum parallelism that can speed up computing processes.

The spin-1/2 system

Since spin systems have been widely studied and today's magnetic resonance techniques are capable to prepare a spin system in any state and let it evolve in time, it is quite common to adopt the language of

spin-1/2 systems to describe the preparation and manipulation of qubits (see Fig. D2). We also will often do so in the following. The spin state again can be considered as a vector on the Bloch sphere shown in Fig. D1. The controlled evolution of the spin state corresponding to the motion of the end point of the vector on the Bloch sphere can be obtained by applying control fields B_z and B_x or resonant microwave pulses to the system as discussed in more detail in Appendix F.

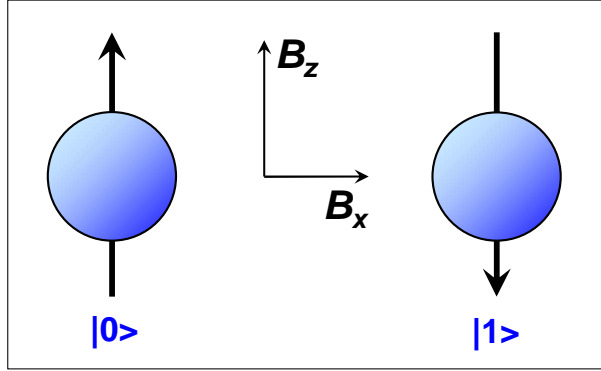


Figure D2: The spin-1/2 system as an example for a two-level quantum system. The two basis state $|0\rangle$ and $|1\rangle$ correspond to the two possible spin orientations $|\uparrow\rangle$ and $|\downarrow\rangle$ with respect to the quantization axis given by the magnetic field B_z . A perpendicular magnetic field B_x results in the mixing of the two basis states.

Two-Qubit Systems

It is instructive to consider first two classical bits. The four possible states of a *classical two-bit system* are

$$|\phi_1\rangle = |00\rangle = \begin{pmatrix} 1 \\ 0 \end{pmatrix} \otimes \begin{pmatrix} 1 \\ 0 \end{pmatrix} = \begin{pmatrix} 1 \\ 0 \\ 0 \\ 0 \end{pmatrix} \quad (\text{D.11})$$

$$|\phi_2\rangle = |01\rangle = \begin{pmatrix} 1 \\ 0 \end{pmatrix} \otimes \begin{pmatrix} 0 \\ 1 \end{pmatrix} = \begin{pmatrix} 0 \\ 1 \\ 0 \\ 0 \end{pmatrix} \quad (\text{D.12})$$

$$|\phi_3\rangle = |10\rangle = \begin{pmatrix} 0 \\ 1 \end{pmatrix} \otimes \begin{pmatrix} 1 \\ 0 \end{pmatrix} = \begin{pmatrix} 0 \\ 0 \\ 1 \\ 0 \end{pmatrix} \quad (\text{D.13})$$

$$|\phi_4\rangle = |11\rangle = \begin{pmatrix} 0 \\ 1 \end{pmatrix} \otimes \begin{pmatrix} 0 \\ 1 \end{pmatrix} = \begin{pmatrix} 0 \\ 0 \\ 0 \\ 1 \end{pmatrix}. \quad (\text{D.14})$$

These four states are also the basis states of a *quantum two-bit system*, which is given by the superposition of these basis states

$$|\Psi(t)\rangle = c_{00}(t)|00\rangle + c_{01}(t)|01\rangle + c_{10}(t)|10\rangle + c_{11}(t)|11\rangle = \begin{pmatrix} c_{00} \\ c_{01} \\ c_{10} \\ c_{11} \end{pmatrix}. \quad (\text{D.15})$$

measurement of 1. qubit		measurement of 2. qubit	
A	$P(A)$ remaining state	B	$P(B)$ remaining state
0	$ c_{00} ^2 + c_{01} ^2$ $ \Psi'\rangle = \frac{c_{00} 00\rangle + c_{01} 01\rangle}{\sqrt{ c_{00} ^2 + c_{01} ^2}}$	0	$\frac{ c_{00} ^2}{ c_{00} ^2 + c_{01} ^2}$ $ 00\rangle$
		1	$\frac{ c_{01} ^2}{ c_{00} ^2 + c_{01} ^2}$ $ 01\rangle$
1	$ c_{10} ^2 + c_{11} ^2$ $ \Psi'\rangle = \frac{c_{10} 10\rangle + c_{11} 11\rangle}{\sqrt{ c_{10} ^2 + c_{11} ^2}}$	0	$\frac{ c_{10} ^2}{ c_{10} ^2 + c_{11} ^2}$ $ 10\rangle$
		1	$\frac{ c_{11} ^2}{ c_{10} ^2 + c_{11} ^2}$ $ 11\rangle$

Table 1: Successive measurements on a two-qubit state showing the results A and B with the corresponding probabilities $P(A)$ and $P(B)$ and the remaining state after the measurement.

Similar as for the one-qubit system the four coefficients are complex, continuous and have to satisfy the normalization condition

$$\langle \Psi(t) | \Psi(t) \rangle = |c_{00}(t)|^2 + |c_{01}(t)|^2 + |c_{10}(t)|^2 + |c_{11}(t)|^2 = 1 . \quad (\text{D.16})$$

We see that the two-qubit state is a superposition of four basis states and therefore can be represented as a unit vector in a four-dimensional Hilbert space \mathcal{H}_4 . Note that for a n -qubit state the number of coefficients increases to 2^n .

If we are performing measurements on a two-qubit state, we are perturbing the qubit state. The results A and B with the respective probabilities $P(A)$ and $P(B)$ of successive measurements of the first and second qubit are summarized in Table 1.

We can now consider special states. If we assume for example that two of the four coefficients are zero, we obtain the following results for the measurement of the first (A) and the second qubit (B):

	$c_{00} = 0$	$c_{01} = 0$	$c_{10} = 0$	$c_{11} = 0$
$c_{00} = 0$	—	$A \equiv 1$	$B \equiv 1$	$B \equiv 1 - A$
$c_{01} = 0$	$A \equiv 1$	—	$B \equiv A$	$B \equiv 0$
$c_{10} = 0$	$B \equiv 1$	$B \equiv A$	—	$A \equiv 0$
$c_{11} = 0$	$B \equiv 1 - A$	$B \equiv 0$	$A \equiv 0$	—

These results directly follow from Table 1. If for example $c_{00} = c_{01} = 0$, the probability for the measurement result $A = 0$ is $P(A) = |c_{00}|^2 + |c_{01}|^2 = 0$. That is, that in a measurement we obtain always the result $A = 1$.

D.2 Entanglement

Entanglement is a new kind of correlations between two subsystems of a quantum system, which does not exist in classical physics (or classical probability). The term is a translation of the German “**Verschränktheit**”, coined by **Erwin Schrödinger** in 1935.³⁸ Both notations reflect well the efforts of understanding such correlations in classical terms. However, from the point of view of quantum theory such correlations are rather straightforward and, in fact, ubiquitous.

³⁸E. Schrödinger, *Die gegenwärtige Situation in der Quantenmechanik*, Die Naturwissenschaften **23** 807-812, 823-828, and 844-849 (1935).

Some correlations between quantum systems can be understood completely in classical terms: Suppose that two subsystems are prepared by two independent devices, whose operation may depend on the output of some classical random generator, which they both receive. In this case the source of the correlations is simply the classical random generator, and states produced in this way are called “classically correlated” or “separable”. The density operator of such a state is a convex combination of tensor products of density operators. All other states are called “entangled”. A simple example is a pure state, which happens not to be a product state. Since a pure state cannot be non-trivially decomposed into a convex combination of any other states, it also cannot be decomposed into products states, so it is not classically correlated. The fact that entangled states are not some bizarre but expendable feature of quantum mechanics but lead to observable effects, is shown most directly by Bell’s inequality. It is easy to show that these inequalities are satisfied by every classically correlated state, but they have been found violated in a series of now famous experiments.³⁹ Hence, these experiments directly confirm the existence of entangled states.

In the theory of Quantum Information entanglement is viewed as a resource needed to perform otherwise impossible tasks of information processing or computation. There is a variety of tasks for which entanglement plays an important role and, correspondingly, a variety of quantitative measures of entanglement. For pure states most of these reduce to the von Neumann entropy of the restricted density operators. This is a quantitative version of a crucial special feature of quantum mechanics, namely that pure states of composite systems may be mixed when restricted to a subsystem, as measured by the von Neumann entropy.

For mixed states there are many quantitative notions of entanglement, some of which are provably different. Probably only a few such quantities will turn out to be useful as the theory develops. But it is much too early to say which the interesting ones are.

As an example we consider the situations where the results A and B of a measurement on a two-qubit state are correlated. This is for example the case for the following normalized two-qubit states, which we obtain for $c_{01} = c_{10} = 0$ and $c_{00} = c_{11} = 0$:

$$\frac{c_{00}(t)|00\rangle + c_{11}(t)|11\rangle}{\sqrt{|c_{00}|^2 + |c_{11}|^2}} \quad \text{or} \quad \frac{c_{01}(t)|01\rangle + c_{10}(t)|10\rangle}{\sqrt{|c_{01}|^2 + |c_{10}|^2}}. \quad (\text{D.17})$$

It is obvious that by measuring the quantum state of the first qubit of these states we also fix the quantum state of the second qubit. Such states are called **Bell states** or **Einstein-Podolsky-Rosen (EPR) pairs**.⁴⁰ They represent **entangled states**.

³⁹A. Aspect, P. Grangier, G. Roger, *Experimental tests of realistic local theories via Bell’s Theorem*, Phys. Rev. Lett. **47**, 460-463 (1981); see also Phys. Rev. Lett. **49**, 91-94 (1982); Phys. Rev. Lett. **49**, 1804-1807 (1982).

⁴⁰A. Einstein, B. Podolsky, N. Rosen, *Can quantum mechanical description of physical reality be complete?*, Phys. Rev. **47** (1935).



Figure D3: Entanglement – an artist’s view.

In order to discuss entanglement a little bit more, we consider two quantum systems (such as two photon or two spins). If these two systems are not coupled, the wavefunction of the total systems is just given by the product of the two wavefunctions of the subsystems:

$$|0\rangle \cdot |1\rangle = |10\rangle \quad \text{or} \quad |1\rangle \cdot |0\rangle = |01\rangle . \quad (\text{D.18})$$

If there is a finite interaction between the subsystems, we obtain a coupling which is causing linear combinations of the wavefunction in (D.18). A well known example is

$$|\Psi\rangle = \frac{1}{\sqrt{2}} (|01\rangle - |10\rangle) , \quad (\text{D.19})$$

which corresponds to a spin singlet state for a spin system. Such linear combination of the product states is called ***entanglement***. The EPR pairs discussed above represent entangled states. An important mathematical property of entangled states is the fact that they cannot be expressed as a product of the basis states. The important physical property of entangled states is the fact that the measurement of the one-qubit state is fixing the measurement result of the other. We will discuss in section D.3 how we can produce entangled states by one- and two-qubit operations.

D.3 Qubit Operations

Unitarity

If we discuss possible manipulations of the qubit state we have to take into account the normalization condition (D.16). That is, during the time evolution of the qubit states we have to satisfy the normalization of the state. With the Schrödinger equation

$$i\hbar \frac{\partial}{\partial t} |\Psi\rangle = \mathcal{H} |\Psi\rangle \quad (\text{D.20})$$

the time evolution of the state can be expressed as

$$|\Psi(t)\rangle = \exp\left(-\frac{i}{\hbar} \mathcal{H} t\right) |\Psi(0)\rangle = \mathcal{U}(t) |\Psi(0)\rangle . \quad (\text{D.21})$$

Since we have to preserve normalization, we obtain

$$\langle \Psi(t) | \Psi(t) \rangle = \langle \Psi(0) | \mathcal{U}^\dagger(t) \mathcal{U}(t) | \Psi(0) \rangle = 1 . \quad (\text{D.22})$$

That is, we obtain the unitary condition

$$\mathcal{U}^\dagger(t) \mathcal{U}(t) = 1 \quad \rightarrow \quad \mathcal{U}^\dagger = \mathcal{U}^{-1} . \quad (\text{D.23})$$

We see that qubit operation in general have to be achieved with $n \times n$ unitary matrices with unit determinant. These matrices are forming the $\text{SU}(n)$ group. For a single-qubit we have to deal with the 2×2 matrices of the $\text{SU}(2)$ group.⁴¹

⁴¹Note that unitarity is the Hilbert space equivalent of rotation matrix orthogonality (isomorphism $\text{SU}(2) \leftrightarrow \text{SO}(3)$).

Single Qubit Operations

We use the spin-1/2 model system to discuss single-qubit operations. With the control fields B_z and B_x , which may be time dependent, the qubit Hamiltonian can be written in the spin-1/2 notation as

$$\mathcal{H} = -\mathcal{H}_z \mathbf{Z} - \mathcal{H}_x \mathbf{X} = -\frac{\hbar}{2}\gamma B_z \mathbf{Z} - \frac{\hbar}{2}\gamma B_x \mathbf{X}, \quad (\text{D.24})$$

where γ is the gyromagnetic ratio and the Pauli matrices in the space states $|\uparrow\rangle$ and $|\downarrow\rangle$ are given by

$$\vec{\sigma} = \{\mathbf{X}, \mathbf{Y}, \mathbf{Z}\} = \left\{ \begin{pmatrix} 0 & 1 \\ 1 & 0 \end{pmatrix}, \begin{pmatrix} 0 & -i \\ i & 0 \end{pmatrix}, \begin{pmatrix} 1 & 0 \\ 0 & -1 \end{pmatrix} \right\}. \quad (\text{D.25})$$

It is evident that the field B_z results in an energy splitting of the basis states $|\uparrow\rangle$ and $|\downarrow\rangle$ proportional to the applied magnetic field but does not mix these states. The magnetic field B_x in contrast results in a mixing of the basis state

A single-qubit operation can be performed, for example, by turning on the control field $B_x(t)$ for a time interval τ . As a result of this operation the quantum state evolves according to the unitary transformation

$$\mathcal{U}_x(\theta) = \exp\left(\frac{i\gamma B_x \tau}{2} \mathbf{X}\right) = \begin{pmatrix} \cos \frac{\theta}{2} & i \sin \frac{\theta}{2} \\ i \sin \frac{\theta}{2} & \cos \frac{\theta}{2} \end{pmatrix} = \cos \frac{\theta}{2} \mathbf{1} + i \sin \frac{\theta}{2} \mathbf{X}, \quad (\text{D.26})$$

where $\theta \equiv \gamma B_x \tau = \omega_x \tau$. For example, by proper choice of the time span τ we can achieve $\theta = \pi$ or $\theta = \pi/2$. This produces a spin flip (NOT operation) or an equal weight superposition of the spin states, respectively.

Switching on $B_z(t)$ for a time interval τ produces another basic single bit operation, namely a phase shift between $|\uparrow\rangle$ and $|\downarrow\rangle$. The unitary operation reads as

$$\mathcal{U}_z(\varphi) = \exp\left(\frac{i\gamma B_z \tau}{2} \mathbf{Z}\right) = \begin{pmatrix} e^{i\varphi/2} & 0 \\ 0 & e^{-i\varphi/2} \end{pmatrix}, \quad (\text{D.27})$$

where $\varphi \equiv \gamma B_z \tau = \omega_z \tau$. Note that with a sequence of these x - and z -rotations any unitary transformation of the qubit state can be achieved, that is, every position on the Bloch sphere can be accessed. There is no need to turn on B_y .

Two Qubit Operations

A two-qubit operation on two qubits i and j is induced by switching on a coupling $J^{ij}(t)$ for a time interval τ . According to (8.2.3) the coupling term can be expressed as

$$\mathcal{H}(t) = \sum_{i \neq j} J_{\alpha\beta}^{ij}(t) \vec{\sigma}_{\alpha}^i \vec{\sigma}_{\beta}^j, \quad (\text{D.28})$$

where the summation over the state (e.g. spin) indices α, β is implied. As an example we discuss the **XY** coupling of two spins:⁴²

$$\mathcal{H}(t) = J^{ij}(t) \vec{\sigma}_\alpha \vec{\sigma}_\beta = J^{ij}(\mathbf{XX} + \mathbf{YY}) = 2J^{ij} \begin{pmatrix} 0 & 0 & 0 & 0 \\ 0 & 0 & 1 & 0 \\ 0 & 1 & 0 & 0 \\ 0 & 0 & 0 & 0 \end{pmatrix}. \quad (\text{D.29})$$

In the basis $|\uparrow\uparrow\rangle, |\uparrow\downarrow\rangle, |\downarrow\uparrow\rangle, |\downarrow\downarrow\rangle$ the result is described by the unitary operator

$$\mathcal{U}^{ij}(\gamma) = \exp\left(\frac{i2J^{ij}\tau}{\hbar}(\mathbf{XX} + \mathbf{YY})\right) = \begin{pmatrix} 1 & 0 & 0 & 0 \\ 0 & \cos\delta & i\sin\delta & 0 \\ 0 & i\sin\delta & \cos\delta & 0 \\ 0 & 0 & 0 & 1 \end{pmatrix}, \quad (\text{D.30})$$

where $\delta = 2J^{ij}\tau/\hbar = 2\omega_{ij}\tau$. For $\delta = \pi/2$ the operation leads to a swap (exchange) of the states $|\uparrow\downarrow\rangle$ ($|10\rangle$) and $|\downarrow\uparrow\rangle$ ($|01\rangle$) and an additional multiplication by i . In contrast, for $\delta = \pi/4$ the operation transforms the state $|\uparrow\downarrow\rangle$ into an entangled state $\frac{1}{\sqrt{2}}(|\uparrow\downarrow\rangle + i|\downarrow\uparrow\rangle)$ (this is equivalent to the \sqrt{i} SWAP gate, see D.4).

It is evident that the qubit operations must be realized by unitary operators ($UU^\dagger = U^\dagger U = 1$). First, the normalization condition must be valid for the qubit state after the operation. Therefore, the absolute value of the determinant of the matrix must be unity. In this way we rotate the qubit vector on the Bloch sphere without changing its length. Second, the operation must be reversible, that is the matrix must be invertable. Note that classical computation is not reversible since heat is dissipated during the operations thereby making the computation thermodynamically irreversible. This is not possible for quantum computers, since the superposition of the quantum states must be maintained during the whole computational process. If heat would be dissipated in an uncontrolled way, the coherence of the quantum state would be lost.

We note that so far we only considered the sudden switching of $B_{z,x}^i(t)$ or $J^{ij}(t)$. This is called an ***non-adiabatic process***. However, one can also use other techniques to implement single or two qubit operations. For example, one can induce Rabi oscillations between different states of a qubit or a qubit pair by ac resonance signals. Furthermore, one can perform adiabatic manipulations of the qubits Hamiltonian to exchange different eigenstates with the occupations remaining unchanged.

D.4 Quantum Logic Gates

In the previous subsection we have shown how we can use unitary operators to realize manipulations of one- and two-qubit states. The details of the physical realization of an unitary operation such as

⁴²Note that for a **YY** coupling we obtain

$$\mathcal{H}(t) = J^{ij}\mathbf{YY} = J^{ij} \begin{pmatrix} 0 & 0 & 0 & -1 \\ 0 & 0 & 1 & 0 \\ 0 & 1 & 0 & 0 \\ -1 & 0 & 0 & 0 \end{pmatrix}$$

and for a **ZZ** coupling

$$\mathcal{H}(t) = J^{ij}\mathbf{ZZ} = J^{ij} \begin{pmatrix} 1 & 0 & 0 & 0 \\ 0 & -1 & 0 & 0 \\ 0 & 0 & -1 & 0 \\ 0 & 0 & 0 & 1 \end{pmatrix}.$$

the application of a magnetic field pulse or the way how one couples two qubits of course depend on the specific model system that is considered (e.g. spin, superconducting phase qubit, etc.). Quantum information theory, on the other hand, discusses quantum computation in a treatment that is independent of the physical system used to implement quantum computation. Here, the quantum algorithms are built out of standard single- and two-qubit gates. In the following we will discuss a several of them. In order to implement a quantum algorithm on a physical system we have to know how to express these standard gates in terms of the unitary operations specific to a physical system.

Single-Bit Gates

We first consider ***classical single-bit gates***. As shown in Fig. D4, a single-bit gate acting on the binary variable x is transferring this variable to the $f(x)$, which is again a binary variable:

$$x \rightarrow f(x) \quad \text{with} \quad x \in \{0, 1\} \quad \text{and} \quad f(x) \in \{0, 1\} . \quad (\text{D.31})$$

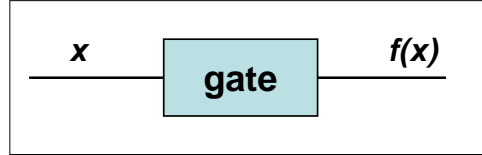


Figure D4: The classical-single bit gate.

Prominent examples for the classical single-bit gate are the NOT, IDENTITY or RESET gates:

$$\text{NOT} \quad f(x) = \text{NOT}(x) = 1 - x \quad (\text{D.32})$$

$$\text{IDENTITY} \quad f(x) = \text{IDENTITY}(x) = x \quad (\text{D.33})$$

$$\text{RESET} \quad f(x) = \text{RESET}(x) = 0 . \quad (\text{D.34})$$

Discussing the ***quantum realization of single-bit gates*** we have to use the unitary transformations discussed in the previous subsection:

Rotations about the x -axis are obtained by

$$\mathcal{U}_x(\theta) = \begin{pmatrix} \cos \frac{\theta}{2} & \imath \sin \frac{\theta}{2} \\ \imath \sin \frac{\theta}{2} & \cos \frac{\theta}{2} \end{pmatrix} = \cos \frac{\theta}{2} \mathbf{1} + \imath \sin \frac{\theta}{2} \mathbf{X} . \quad (\text{D.35})$$

We see that a rotation about the x -axis by an arbitrary angle θ interpolates between the classical gates IDENTITY and NOT. The quantum NOT gate (see Fig. D5)

$$\text{NOT} = \begin{pmatrix} 0 & 1 \\ 1 & 0 \end{pmatrix} = \mathbf{X} = e^{-\imath \frac{\pi}{2}} \mathcal{U}_x(\pi) \quad (\text{D.36})$$

permutes the basis vectors $|0\rangle \rightarrow |1\rangle$ and $|1\rangle \rightarrow |0\rangle$. We see that it can be realized (up to an unimportant overall phase factor) by the unitary operation (x -rotation) of (D.26) with a properly chosen time interval τ resulting in $\theta \equiv B_x \tau / \hbar = \pi$: $\mathcal{U}_x(\theta = \pi) = \imath \cdot \text{NOT}$.

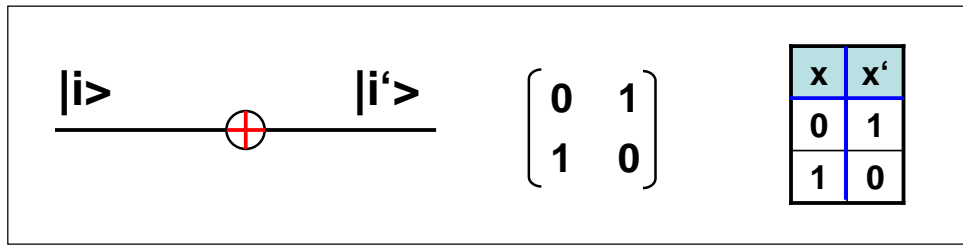


Figure D5: The quantum NOT gate with the corresponding unitary matrix and the truth table.

In contrast to classical computation in quantum logic there is a logic gate called $\sqrt{\text{NOT}}$, that when applied twice produces the NOT gate:

$$\sqrt{\text{NOT}} = \frac{1}{\sqrt{2}\iota} \begin{pmatrix} 0 & \iota \\ \iota & 0 \end{pmatrix} = \frac{1}{2} \begin{pmatrix} 1+\iota & -1+\iota \\ -1+\iota & 1+\iota \end{pmatrix} = \sqrt{\mathbf{X}} = e^{-\iota\frac{\pi}{4}} \mathcal{U}_x\left(\frac{\pi}{2}\right) \quad (\text{D.37})$$

This gate is also obtained by the unitary operation (x -rotation) of (D.26) with $\theta \equiv B_x \tau / \hbar = \pi/2$, more precisely $\mathcal{U}_x(\theta = \pi/2) = \sqrt{\iota} \cdot \sqrt{\text{NOT}}$.

Rotations of a one-qubit state about the z -axis are obtained by the unitary operation (compare (D.27))

$$\mathcal{U}_z(\varphi) = \begin{pmatrix} e^{i\varphi/2} & 0 \\ 0 & e^{-i\varphi/2} \end{pmatrix} = e^{i\frac{\varphi}{2}} \begin{pmatrix} 1 & 0 \\ 0 & e^{-i\varphi} \end{pmatrix}. \quad (\text{D.38})$$

The action on a qubit results in a relative phase shift φ

$$\mathcal{U}_z(\varphi)|0\rangle = |0\rangle \quad (\text{D.39})$$

$$\mathcal{U}_z(\varphi)|1\rangle = e^{-i\varphi}|1\rangle. \quad (\text{D.40})$$

Special cases are the **Z** gate

$$\mathbf{Z} = e^{-i\frac{\pi}{2}} \mathcal{U}_z(\pi) = \begin{pmatrix} 1 & 0 \\ 0 & -1 \end{pmatrix}, \quad (\text{D.41})$$

the **S** gate

$$\mathbf{S} = \sqrt{\mathbf{Z}} = \begin{pmatrix} 1 & 0 \\ 0 & i \end{pmatrix} = \begin{pmatrix} 1 & 0 \\ 0 & e^{i\frac{\pi}{2}} \end{pmatrix}, \quad (\text{D.42})$$

and the **T** gate

$$\mathbf{T} = \sqrt{\mathbf{S}} = \begin{pmatrix} 1 & 0 \\ 0 & e^{i\frac{\pi}{4}} \end{pmatrix}. \quad (\text{D.43})$$

The Hadamard gate is another important, essentially quantum mechanical, single bit gate defined as

$$H \equiv \frac{1}{\sqrt{2}} \begin{pmatrix} 1 & 1 \\ 1 & -1 \end{pmatrix} = \frac{\mathbf{X} + \mathbf{Z}}{\sqrt{2}} . \quad (\text{D.44})$$

This gate, which is composed of a y - and z -rotation transforms the basis vectors into superpositions:

$$H|0\rangle = \frac{1}{\sqrt{2}} (|0\rangle + |1\rangle) = |+\rangle \quad \text{and} \quad H|1\rangle = \frac{1}{\sqrt{2}} (|0\rangle - |1\rangle) = |-\rangle . \quad (\text{D.45})$$

The Hadamard gate is used to prepare a specific initial state. When applied to the ground state $|00\dots 0\rangle$, it provides an equally weighted superposition of all basis states:

$$H \otimes \dots \otimes H|0\dots 0\rangle = \frac{1}{2^{N/2}} \sum_{a_1\dots a_N=0,1} |a_1 \dots a_N\rangle . \quad (\text{D.46})$$

The terms in the sum can be viewed as binary representations of all integers from 0 up to $2^N - 1$. Therefore, the state (D.46) represents a superposition of all these integers. When this state is used as an input state for a quantum algorithm, it represents 2^N classical inputs. Due to the linearity of the quantum time evolution these inputs are processed simultaneously and the output is a superposition of 2^N classical results. This massive **quantum parallelism** is a key property of quantum computation and is responsible for the exponential speedup of certain quantum algorithms.

Two Bit Gates

We again first consider **classical two-bit gates**. As shown in Fig. D6, a two-bit gate acting on the binary variable (x,y) is transferring this variable to $f(x,y)$, which is again a binary variable:

$$(x,y) \rightarrow f(x,y) \quad \text{with} \quad (x,y) \in \{0,1\} \quad \text{and} \quad f(x,y) \in \{0,1\} . \quad (\text{D.47})$$

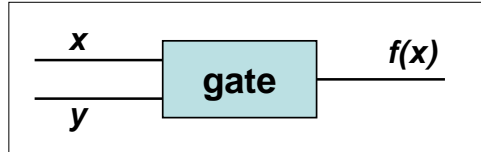


Figure D6: The classical two-bit gate.

Prominent examples for classical two-bit gates are

$$f(x,y) = (x \text{ AND } y) = xy \quad (\text{D.48})$$

$$f(x,y) = (x \text{ NAND } y) = \text{NOT}(x \text{ AND } y) = 1 - xy \quad (\text{D.49})$$

$$f(x,y) = (x \text{ OR } y) = x + y - xy \quad (\text{D.50})$$

$$f(x,y) = (x \text{ NOR } y) = \text{NOT}(x \text{ OR } y) = 1 + xy - x - y \quad (\text{D.51})$$

$$f(x,y) = (x \text{ EQUIV } y) = \delta_{xy} \quad (\text{D.52})$$

$$f(x,y) = (x \text{ XOR } y) = x \oplus y = \text{NOT}(x \text{ EQUIV } y) = 1 - \delta_{xy} . \quad (\text{D.53})$$

The truth table of these operations is given by

(x,y)	AND	NAND	OR	NOR	EQUIV	XOR
0 0	0	1	0	1	1	0
0 1	0	1	1	0	0	1
1 0	0	1	1	0	0	1
1 1	1	0	1	0	1	0

It is evident from Fig. D6 and the truth table that the two-bit gates discussed so far are *irreversible gates*. The difference between *reversible* and *irreversible* gates is shown in Fig. D7. After the operation we can no longer reverse the operation to determine the input states. That is, information is lost what is resulting in an increase of entropy by $\Delta S = k_B \ln 2$ (**Leo Szillard**, 1929). It can further be shown that not all of the logical gates are required. Only a small *universal set of gates* is necessary to construct all other gates. It can be shown that the NAND gate is sufficient to produce all other gates.

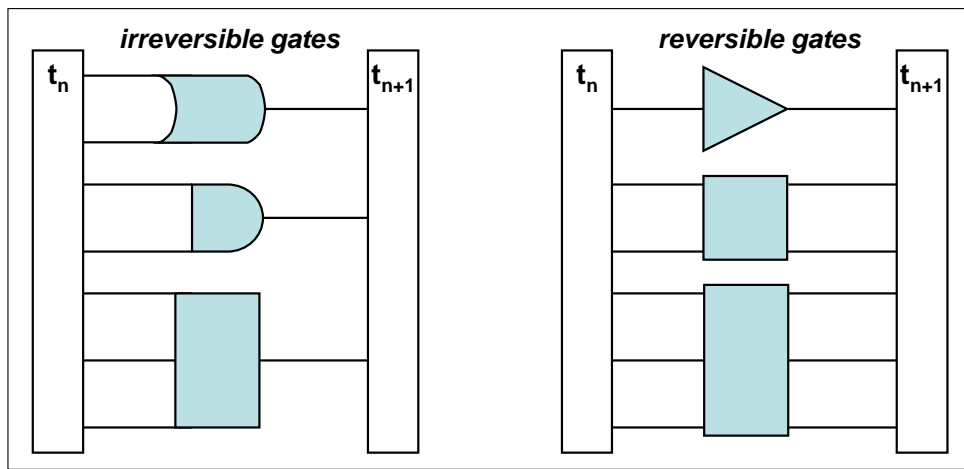


Figure D7: Irreversible (left) and reversible (right) gates.

In the 1970ies a *reversible classical logic* has been established (**Bennett**, 1973). The structure of a classical reversible gate is shown in Fig. D8. Reversibility is achieved by storage of the input bit x . A typical example is the controlled NOT (CNOT) gate corresponding to a reversible exclusive OR (XOR) gate as shown in Fig. D9a. The operation of the CNOT gate is defined as:

$$(x,y) \rightarrow \text{CNOT}(x,y) = (x, x \oplus y) = (x, 1 - \delta_{xy}) . \quad (\text{D.54})$$

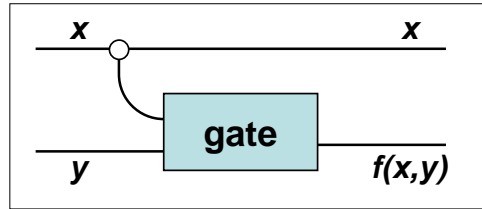


Figure D8: Reversible classical logic gate.

A further important reversible gate is the SWAP gate that interchanges x and y (see Fig. D9b):⁴³

⁴³Proof that $x \oplus (x \oplus y) \equiv y$:

$$\begin{aligned}
 (x, y) &\rightarrow (x, x \oplus y) \\
 (x, x \oplus y) &\rightarrow (x \oplus (x \oplus y), x \oplus y) = (y, x \oplus y) \\
 (y, x \oplus y) &\rightarrow (y, (x \oplus y) \oplus y) = (y, x) .
 \end{aligned} \tag{D.55}$$

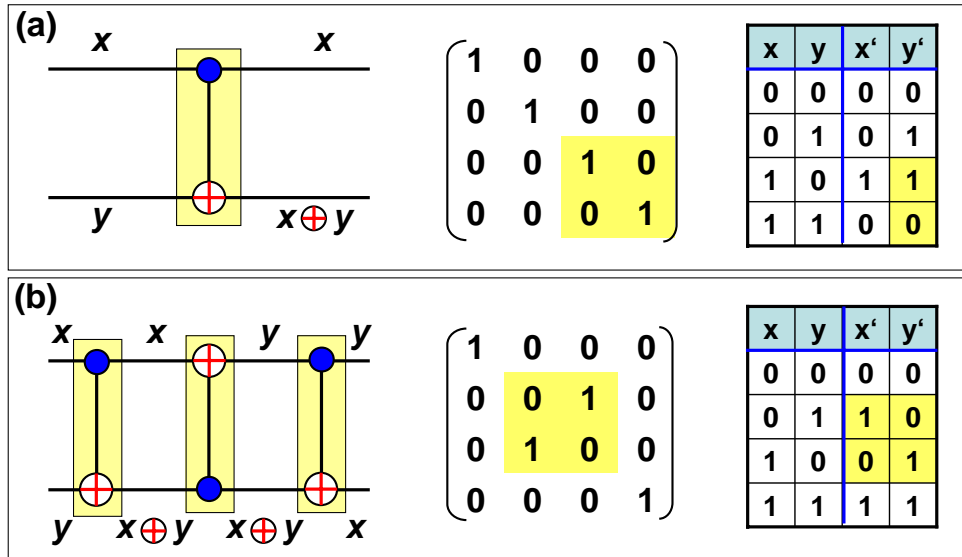


Figure D9: The reversible XOR (CNOT) gate (a) and the SWAP gate (b) with the corresponding matrix and truth tables.

We next have to discuss *two-bit quantum gates*. In the same way as for classical two-bit gates there exists a *universal set of two-qubit quantum gates* that is required to construct all other gates. It can be shown that the CNOT gate together with the one-qubit rotations \mathbf{X} , \mathbf{Y} , \mathbf{Z} , \mathbf{S} , \mathbf{T} ,... discussed above are sufficient to produce all other gates. That is, for the implementation of a quantum computer we only have to realize the CNOT gate and the single qubit rotations. With respect to two-bit quantum gates we therefore have to discuss mainly the CNOT gate.

Before describing the quantum CNOT gate we first introduce the more general controlled U (CU) gate shown in Fig. D10:

$$\text{CU } |ij\rangle = \text{CU } |i\rangle \otimes |j\rangle = |i\rangle \otimes \{\delta_{i0}|j\rangle + \delta_{i1}\mathcal{U}|j\rangle\} . \tag{D.56}$$

(x, y)	$x \oplus y$	$x \oplus (x \oplus y)$	y
0 0	0	0	0
0 1	1	1	1
1 0	1	0	0
1 1	0	0	1

Proof that $(x \oplus y) \oplus y \equiv x$:

(x, y)	$x \oplus y$	$(x \oplus y) \oplus y$	x
0 0	0	0	0
0 1	1	0	0
1 0	1	1	1
1 1	0	1	1

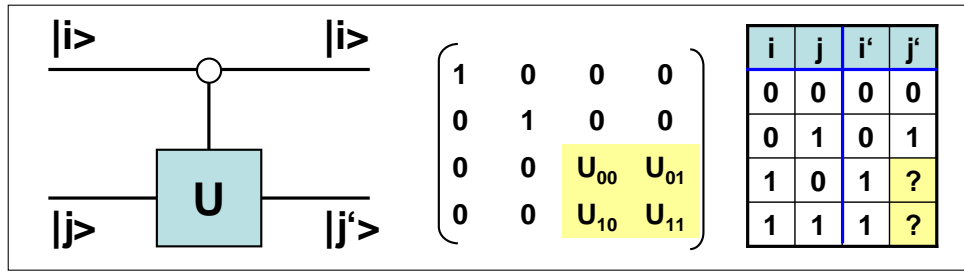


Figure D10: The controlled U gate.

In a 4×4 matrix representations the CU gate can be expressed as

$$\mathcal{U} = \begin{pmatrix} 1 & 0 & 0 & 0 \\ 0 & 1 & 0 & 0 \\ 0 & 0 & \mathcal{U}_{00} & \mathcal{U}_{01} \\ 0 & 0 & \mathcal{U}_{10} & \mathcal{U}_{11} \end{pmatrix} = \begin{pmatrix} 1 & 0 \\ 0 & \mathcal{U} \end{pmatrix}. \quad (\text{D.57})$$

The controlled NOT gate represents a special case of the CU gate with \mathcal{U} being the quantum NOT or X gate.⁴⁴ With (D.36) we obtain

$$\text{CNOT} = \begin{pmatrix} 1 & 0 & 0 & 0 \\ 0 & 1 & 0 & 0 \\ 0 & 0 & 0 & 1 \\ 0 & 0 & 1 & 0 \end{pmatrix} = \begin{pmatrix} 1 & 0 \\ 0 & \mathbf{X} \end{pmatrix}. \quad (\text{D.58})$$

The CNOT gate flips the second qubits only if the first qubits is in the $|1\rangle$ state.

A further example is the *controlled phase gate*

$$\text{C} - \varphi = \begin{pmatrix} 1 & 0 & 0 & 0 \\ 0 & 1 & 0 & 0 \\ 0 & 0 & 0 & 0 \\ 0 & 0 & 0 & e^{-i\varphi} \end{pmatrix} = \begin{pmatrix} 1 & 0 \\ 0 & e^{-i\varphi} \mathcal{U}_z(\varphi) \end{pmatrix}, \quad (\text{D.59})$$

which shifts the phase of state $|1\rangle$ of the second qubit when the first qubit is in the state $|1\rangle$.

As a further important two bit quantum gate we discuss the SWAP gate, which is produced by three CNOT gates in series:

⁴⁴The CNOT gate is therefore also called the CX gate.

Claim:

$$\text{CNOT } |ij\rangle = \text{CNOT } |i\rangle \otimes |j\rangle = |i\rangle \otimes \{\delta_{i0}|j\rangle + \delta_{i1}\text{NOT}|j\rangle\}.$$

Proof:

$$\begin{aligned} \text{CNOT } |i\rangle \otimes |j\rangle &= |i\rangle \otimes |1 - \delta_{ij}| \\ &= |0\rangle \otimes \{\delta_{00}|j\rangle + \delta_{01}\text{NOT}|j\rangle\} = |0\rangle \otimes |j\rangle \quad \text{for } i = 0 \\ &= |1\rangle \otimes \{\delta_{10}|j\rangle + \delta_{11}\text{NOT}|j\rangle\} = |1\rangle \otimes \text{NOT}|j\rangle \quad \text{for } i = 1. \end{aligned}$$

$$\text{SWAP} = \text{CNOT}_{12} \cdot \text{CNOT}_{21} \cdot \text{CNOT}_{12} = \begin{pmatrix} 1 & 0 & 0 & 0 \\ 0 & 0 & 1 & 0 \\ 0 & 1 & 0 & 0 \\ 0 & 0 & 0 & 1 \end{pmatrix}. \quad (\text{D.60})$$

and the $\sqrt{i\text{SWAP}}$ gate, “square root of the complex SWAP operation”

$$\sqrt{i\text{SWAP}} = \begin{pmatrix} 1 & 0 & 0 & 0 \\ 0 & \frac{1}{\sqrt{2}} & \frac{i}{\sqrt{2}} & 0 \\ 0 & \frac{i}{\sqrt{2}} & \frac{1}{\sqrt{2}} & 0 \\ 0 & 0 & 0 & 1 \end{pmatrix}. \quad (\text{D.61})$$

The result of the SWAP operation is

$$\text{SWAP}|i, j\rangle = |j, i\rangle. \quad (\text{D.62})$$

That is, the SWAP operation results in an exchange of the two input qubits $|i\rangle$ and $|j\rangle$. In contrast, the $\sqrt{i\text{SWAP}}$ operation transforms the state $|10\rangle$ into an entangled state $\frac{1}{\sqrt{2}}(|10\rangle + i|01\rangle)$.

The two-qubit gates can be realized by two-qubit operations as described in section D.3. We only consider the Hadamard and the CNOT gate. The Hadamard gate can be performed up to an overall phase factor as a sequence of the elementary operations \mathcal{U}_x and \mathcal{U}_z

$$H \propto \mathcal{U}_x(\theta = \frac{\pi}{4}) \mathcal{U}_z(\varphi = \frac{\pi}{4}) \mathcal{U}_x(\theta = \frac{\pi}{4}). \quad (\text{D.63})$$

However, it also can be performed faster by simultaneous switching of B_x and B_z (compare (D.26), (D.27) and (D.44)):

$$H \propto \exp\left(-i\frac{\pi}{2} \frac{\mathbf{X}+\mathbf{Z}}{\sqrt{2}}\right). \quad (\text{D.64})$$

The CNOT operation can be implemented by a combination of two-qubit gates \mathcal{U}^{ij} (see (D.30)) and several single-qubit gates:

$$\begin{aligned} \text{CNOT} \propto & \mathcal{U}_x^2\left(\frac{\pi}{2}\right) \mathcal{U}_z^2\left(-\frac{\pi}{2}\right) \mathcal{U}_x^2(-\pi) \mathcal{U}^{ij}\left(-\frac{\pi}{2}\right) \\ & \times \mathcal{U}_x^1\left(-\frac{\pi}{2}\right) \mathcal{U}^{ij}\left(\frac{\pi}{2}\right) \mathcal{U}_z^1\left(-\frac{\pi}{2}\right) \mathcal{U}_z^2\left(-\frac{\pi}{2}\right). \end{aligned} \quad (\text{D.65})$$

We see that it takes quite a number of elementary gates to perform the CNOT operation and optimization is required.

D.5 The No-Cloning Theorem

The term **cloning** in the quantum context, coined in the short paper by **Wootters** and **Zurek**,⁴⁵ reflects rather well the idea that there is a blueprint for quantum systems from which all its properties could be derived. However, the existence of a **Quantum Copier**, which would take one quantum system as input and produce two systems of the same kind, both of them indistinguishable from the input, is ruled out by the **no-cloning theorem**. So far, the **no-cloning theorem** has been stated only in a rather weak form, forbidding only *exact* cloning. Stronger forms give more detailed information: there is a finite error necessarily made by any putative cloner, and explicit bounds can be placed on this error.

Note that in classical systems cloning is easily possible. A special property of the classical CNOT operation is the fact that it can be used to copy bits:

$$\text{SWAP}(x, 0) = (x, x) . \quad (\text{D.66})$$

We can now try to use the quantum CNOT gate to make a copy of the single qubit state

$$|\Psi\rangle = a|0\rangle + b|1\rangle . \quad (\text{D.67})$$

With the two-qubit input

$$|\Psi, 0\rangle = |\Psi\rangle \otimes |0\rangle = a|00\rangle + b|10\rangle \quad (\text{D.68})$$

we obtain the following output after the quantum CNOT operation

$$\text{CNOT}|\Psi, 0\rangle = \text{CNOT}(a|00\rangle + b|10\rangle) = a|00\rangle + b|11\rangle . \quad (\text{D.69})$$

The copy of $|\Psi\rangle$ is however

$$|\Psi, \Psi\rangle = |\Psi\rangle \otimes |\Psi\rangle = a^2|00\rangle + b^2|11\rangle + ab|01\rangle + ab|10\rangle . \quad (\text{D.70})$$

That is,

$$\text{CNOT}|\Psi, 0\rangle \neq |\Psi, \Psi\rangle . \quad (\text{D.71})$$

This result is called the **no-cloning theorem** that says that an unknown quantum state cannot be copied.

D.6 Quantum Complexity

We have learnt that the quantum state of an n -qubit system is a vector in the 2^n dimensional Hilbert space. As an example, the state $|01001110\rangle$ is a basis vector in the 2^8 dimensional Hilbert space. In order to transform arbitrary quantum state $|\Psi\rangle$ into the new state $|\Psi'\rangle$ a unitary transformation \mathcal{U} is required:

$$|\Psi'\rangle = \mathcal{U}|\Psi\rangle , \quad (\text{D.72})$$

where \mathcal{U} is a $2^n \times 2^n$ complex matrix. If we are dealing for example with 100 qubits, a $2^{100} \times 2^{100}$ complex matrix is required ($2^{100} \simeq 10^{30}$). This problem is called **quantum complexity**.

⁴⁵W.K. Wootters and W.H. Zurek, *A single quantum cannot be cloned*, Nature **299**, 802 (1982).

D.7 The Density Matrix Representation

The density matrix allows the calculation of the expectation values of pure and mixed quantum states. The density matrix of a quantum state is defined as

$$\hat{\rho} = |\Psi\rangle\langle\Psi| . \quad (\text{D.73})$$

For a simple single-qubit state $|\Psi\rangle = a|0\rangle + b|1\rangle$ we obtain

$$\begin{aligned} |\Psi\rangle\langle\Psi| &= (|\Psi\rangle = a|0\rangle + b|1\rangle) \otimes (a^*\langle 0| + b^*\langle 1|) \\ &= aa^*|0\rangle\langle 0| + bb^*|1\rangle\langle 1| + ab^*|0\rangle\langle 1| + ba^*|1\rangle\langle 0| \\ &= \mathbf{P}_{00} + bb^*\mathbf{P}_{11} + ab^*\mathbf{P}_{01} + ba^*\mathbf{P}_{10} \end{aligned} \quad (\text{D.74})$$

with the fundamental projection 2D operators

$$\mathbf{P}_{00} = |0\rangle\langle 0| = \begin{pmatrix} 1 & 0 \\ 0 & 0 \end{pmatrix} = \frac{\mathbf{1} + \mathbf{Z}}{2} \quad (\text{D.75})$$

$$\mathbf{P}_{11} = |1\rangle\langle 1| = \begin{pmatrix} 0 & 0 \\ 0 & 1 \end{pmatrix} = \frac{\mathbf{1} - \mathbf{Z}}{2} \quad (\text{D.76})$$

$$\mathbf{P}_{01} = |0\rangle\langle 1| = \begin{pmatrix} 0 & 0 \\ 1 & 0 \end{pmatrix} = \frac{\mathbf{X} + i\mathbf{Y}}{2} \quad (\text{D.77})$$

$$\mathbf{P}_{10} = |1\rangle\langle 0| = \begin{pmatrix} 0 & 1 \\ 0 & 0 \end{pmatrix} = \frac{\mathbf{X} - i\mathbf{Y}}{2} . \quad (\text{D.78})$$

Rewriting these equation we obtain the density matrix as

$$\hat{\rho} = \frac{1}{2}(\mathbf{1} + \vec{v} \cdot \vec{\sigma}) \quad (\text{D.79})$$

with the Pauli matrices $\vec{\sigma}$ and

$$\vec{v} = \begin{pmatrix} v_x \\ v_y \\ v_z \end{pmatrix} = \begin{pmatrix} a^*b + b^*a \\ -i(a^*b - b^*a) \\ a^*a - b^*b \end{pmatrix} \quad (\text{D.80})$$

For the density matrix of the pure single-qubit states we obtain

$$\hat{\rho}_0 = |0\rangle\langle 0| = \begin{pmatrix} 1 & 0 \\ 0 & 0 \end{pmatrix} \quad (\text{D.81})$$

$$\hat{\rho}_1 = |1\rangle\langle 1| = \begin{pmatrix} 0 & 0 \\ 0 & 1 \end{pmatrix} . \quad (\text{D.82})$$

The result is shown in Fig. D11. We see that for the pure states there is a finite expectation value only for the respective state.

By applying the Hadamard gate we can generate a coherent superposition of the basis states (compare (D.45))

$$H|0\rangle = \frac{1}{\sqrt{2}}(|0\rangle + |1\rangle) = |+\rangle \quad \text{and} \quad H|1\rangle = \frac{1}{\sqrt{2}}(|0\rangle - |1\rangle) = |-\rangle . \quad (\text{D.83})$$

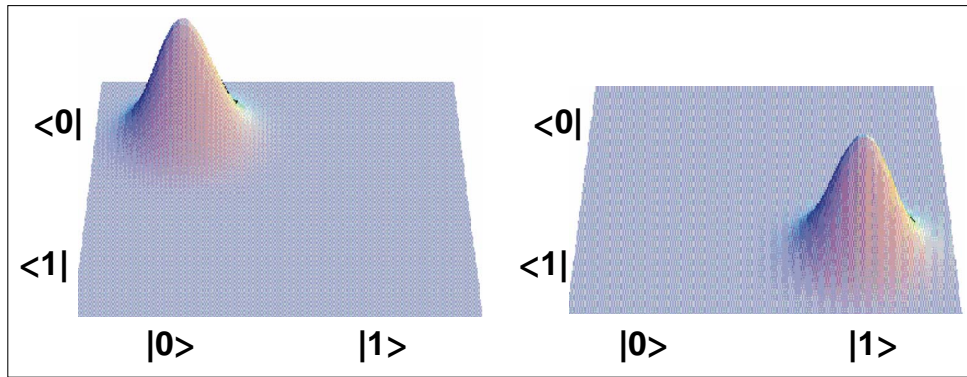


Figure D11: Graphical representation of the density matrices $\hat{\rho}_0$ (left) and $\hat{\rho}_1$ (right) for the pure single qubit states.

The corresponding density matrix is

$$\begin{aligned}
 \hat{\rho}_+ &= \frac{1}{2}(|0\rangle + |1\rangle) \otimes (\langle 0| + \langle 1|) \\
 &= \frac{1}{2}(|0\rangle\langle 0| + |0\rangle\langle 1| + |1\rangle\langle 0| + |1\rangle\langle 1|) \\
 &= \frac{1}{2} \mathbf{1} + \mathbf{X} .
 \end{aligned} \tag{D.84}$$

The result is shown in Fig. D12. We see that for the coherent superposition of the states achieved by the application of the Hadamard gate we obtain the same expectation value for the four possible configurations, since the Hadamard gate provides an equally weighted superposition of all basis states.

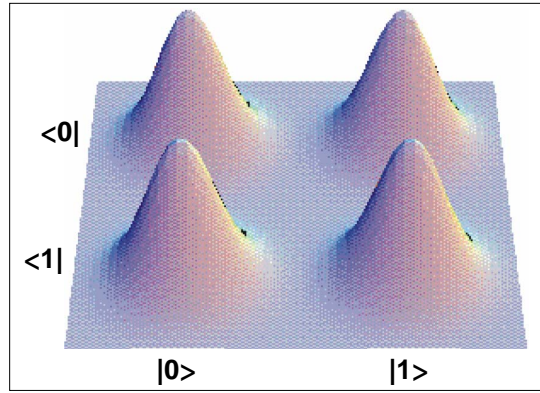


Figure D12: Graphical representation of the density matrix $\hat{\rho}_+$ for the coherent superposition of the basis states.

E Quantum Mechanical Two-Level Systems

We have seen that quantum bits can be represented by every two-level quantum system. There are numerous cases in physics, which can be in first order approximation treated simply as such kind of system. For example, a system with two states whose energies are close and differ very much from those of all other states of the system can be viewed as a two-level system. Therefore, we briefly summarize here the basic properties of quantum mechanical two-level systems. In particular we address the effect of an external perturbation as well as an internal interaction on the two states. The general treatment of a two-level system will provide some general and important ideas such as quantum resonance, oscillation between two levels etc..

E.1 Introduction to the Problem

We consider a system with a two-dimensional state space. As an orthonormal basis we choose the system of the two eigenstates $|\phi_1\rangle$ and $|\phi_2\rangle$ (cf. (D.2) and D.3)) of the Hamiltonian \mathcal{H}_0 , whose eigenvalues are E_1 and E_2 , respectively:

$$\mathcal{H}_0|\phi_1\rangle = E_1|\phi_1\rangle \quad (\text{E.1})$$

$$\mathcal{H}_0|\phi_2\rangle = E_2|\phi_2\rangle. \quad (\text{E.2})$$

We further take into account an external perturbation or interactions internal to the system, which are not contained in \mathcal{H}_0 , which is called the unperturbed Hamiltonian. The total Hamiltonian then becomes

$$\mathcal{H} = \mathcal{H}_0 + \mathcal{W} \quad (\text{E.3})$$

with the perturbation or coupling \mathcal{W} . The eigenvalues of \mathcal{H} are denoted by $|\Psi_+\rangle$ and $|\Psi_-\rangle$ with the corresponding eigenvalues E_+ and E_- :

$$\mathcal{H}|\Psi_+\rangle = E_+|\Psi_+\rangle \quad (\text{E.4})$$

$$\mathcal{H}|\Psi_-\rangle = E_-|\Psi_-\rangle. \quad (\text{E.5})$$

For simplicity, we will assume that \mathcal{W} is time-independent. In the basis of $\{|\phi_1\rangle, |\phi_2\rangle\}$ of the unperturbed eigenstates of \mathcal{H}_0 , the perturbation \mathcal{W} is represented by a Hermitian matrix

$$\mathcal{W} = \begin{pmatrix} \mathcal{W}_{11} & \mathcal{W}_{12} \\ \mathcal{W}_{21} & \mathcal{W}_{22} \end{pmatrix}. \quad (\text{E.6})$$

\mathcal{W}_{11} and \mathcal{W}_{22} are real and moreover $\mathcal{W}_{12} = \mathcal{W}_{21}^*$.

In the absence of any perturbation or coupling the possible eigenenergies of the system are E_1 and E_2 and the states $|\phi_1\rangle$ and $|\phi_2\rangle$ are stationary states, i.e. if the system is prepared in one of these states it stays there forever.

We now have to evaluate what happens if we are introducing a finite coupling \mathcal{W} . The consequences of the coupling are the following:

- E_1 and E_2 are no longer the possible eigenstates of the system.

If we are measuring the energy of the system only the two values E_+ and E_- are possible, which generally differ from E_1 and E_2 . Therefore, we first have to calculate the new eigenenergies E_+ and E_- in terms of E_1 and E_2 and the matrix elements \mathcal{W}_{ij} of the coupling \mathcal{W} . That is, we have to study the effect of the coupling on the position of the energy levels.

- $|\phi_1\rangle$ and $|\phi_2\rangle$ are no longer stationary states.

Since $|\phi_1\rangle$ and $|\phi_2\rangle$ are in general no longer eigenstates of the total Hamiltonian \mathcal{H} , they are no longer stationary states. If the system stays in the state $|\phi_1\rangle$ at the time $t = 0$, there is a certain probability $P_{12}(t)$ for finding the system in the state $|\phi_2\rangle$ at time t . That is, \mathcal{W} introduces transitions between the two unperturbed states. This justifies the name “coupling” for \mathcal{W} . The dynamic aspect of the effect of \mathcal{W} is the second problem we have to address.

Relation to Spin-1/2 Systems

It can be shown that the Hamiltonian \mathcal{H} has the same form as that of a spin 1/2 placed in a static magnetic field \mathbf{B} , whose components B_x , B_y and B_z are expressed in terms of E_1 and E_2 and the matrix elements \mathcal{W}_{ij} . That means that we can associate with every two-level system a spin 1/2 placed in a static field \mathbf{B} and described by a Hamiltonian of identical form. The spin is then called a *fictitious spin*. All results we are deriving in the following can then be interpreted in a simple geometric way in terms of a magnetic moment, Larmor precession and other concepts used for spin 1/2 systems. This geometrical interpretation often helps to get a helpful illustration of what is going on. For a discussion of the spin-1/2-system, see Appendix F.

E.2 Static Properties of Two-Level Systems

Eigenstates and Eigenvalues

We first write the Hamiltonian \mathcal{H} in the $\{|\phi_1\rangle, |\phi_2\rangle\}$ basis of the unperturbed eigenstates:

$$\mathcal{H} = \begin{pmatrix} \mathcal{H}_0 + \mathcal{W}_{11} & \mathcal{W}_{12} \\ \mathcal{W}_{21} & \mathcal{H}_0 + \mathcal{W}_{22} \end{pmatrix}. \quad (\text{E.7})$$

With $|\Psi\rangle = a|\phi_1\rangle + b|\phi_2\rangle$ we obtain the eigenvalue equation

$$\begin{pmatrix} E_1 + \mathcal{W}_{11} - E & \mathcal{W}_{12} \\ \mathcal{W}_{12}^* & E_2 + \mathcal{W}_{22} - E \end{pmatrix} \begin{pmatrix} a \\ b \end{pmatrix} = 0. \quad (\text{E.8})$$

Upon diagonalization of the matrix we find the eigenvalues

$$E_+ = \frac{1}{2}(E_1 + W_{11} + E_2 + W_{22}) + \frac{1}{2}\sqrt{(E_1 + W_{11} - E_2 - W_{22})^2 + 4|W_{12}|^2} \quad (\text{E.9})$$

$$E_- = \frac{1}{2}(E_1 + W_{11} + E_2 + W_{22}) - \frac{1}{2}\sqrt{(E_1 + W_{11} - E_2 - W_{22})^2 + 4|W_{12}|^2}. \quad (\text{E.10})$$

We immediately see that E_+ and E_- are identical to E_1 and E_2 for $W = 0$. The corresponding eigenvectors can be written as

$$|\Psi_+\rangle = \cos \frac{\theta}{2} e^{-i\varphi/2} |\phi_1\rangle + \sin \frac{\theta}{2} e^{+i\varphi/2} |\phi_2\rangle \quad (\text{E.11})$$

$$|\Psi_-\rangle = -\sin \frac{\theta}{2} e^{-i\varphi/2} |\phi_1\rangle + \cos \frac{\theta}{2} e^{+i\varphi/2} |\phi_2\rangle, \quad (\text{E.12})$$

where the angle θ and φ are given by

$$\tan \theta = \frac{2|W_{12}|}{E_1 + W_{11} - E_2 - W_{22}} \quad (\text{E.13})$$

$$W_{21} = |W_{21}| e^{i\varphi}. \quad (\text{E.14})$$

Interpretation

In order to discuss the above results we first will do a graphical representation of the effect of coupling. The most interesting effect of the perturbation \mathcal{W} is the fact that it possesses off-diagonal matrix elements $\mathcal{W}_{12} = \mathcal{W}_{21}^*$. If the off-diagonal terms would vanish, the eigenstates of \mathcal{H} would be the same as those of \mathcal{H}_0 and the new eigenenergies would be $E_1 + W_{11}$ and $E_2 + W_{22}$. Since the diagonal terms of the perturbation are not very interesting, we will assume $W_{11} = W_{22} = 0$ in the following. With this assumption the expression for the eigenenergies simplify to

$$E_+ = \frac{1}{2}(E_1 + E_2) + \frac{1}{2}\sqrt{(E_1 - E_2)^2 + 4|W_{12}|^2} \quad (\text{E.15})$$

$$E_- = \frac{1}{2}(E_1 + E_2) - \frac{1}{2}\sqrt{(E_1 - E_2)^2 + 4|W_{12}|^2} \quad (\text{E.16})$$

with

$$\tan \theta = \frac{2|W_{12}|}{E_1 - E_2} \quad 0 \leq \theta < \pi \quad (\text{E.17})$$

$$W_{12} = |W_{21}| e^{i\varphi}. \quad (\text{E.18})$$

By introducing the two parameters

$$E_m \equiv \frac{1}{2}(E_1 + E_2) \quad (\text{E.19})$$

$$\Delta \equiv \frac{1}{2}(E_1 - E_2) \quad (\text{E.20})$$

we obtain

$$E_+ = E_m + \frac{1}{2}\sqrt{\Delta^2 + 4|W_{12}|^2} \quad (\text{E.21})$$

$$E_- = E_m - \frac{1}{2}\sqrt{\Delta^2 + 4|W_{12}|^2}. \quad (\text{E.22})$$

We see that a variation of E_m corresponds to a shift of the eigenenergies E_+ and E_- along the energy axis. It can be further seen from (E.11) to (E.14) that the eigenstates $|\Psi_+\rangle$ and $|\Psi_-\rangle$ are not affected by changes of E_m . We therefore are not interested in the effect of E_m . In the following we will set the origin of the energy scale such that $E_m = 0$.

The influence of the parameter Δ is more interesting. In Fig. E1 we have plotted the variation of the eigenenergies E_+ , E_- , E_1 and E_2 as a function of the parameter $\Delta = (E_1 - E_2)/2$. It is evident that for E_1 and E_2 two straight lines are obtained with slopes $+1$ and -1 , respectively. According to (E.21) and (E.22), E_+ and E_- describe two branches of a hyperbola, which is symmetrical with respect to the $E = E_m$ and $\Delta = 0$ axis. The asymptotes of the hyperbola are the two straight lines associated with the unperturbed levels. The minimum separation between the two branches is $2|W_{12}|$. We immediately see that $E_+ \rightarrow E_1$ and $E_- \rightarrow E_2$ for $E_1 > E_2$ as well as $E_+ \rightarrow E_2$ and $E_- \rightarrow E_1$ for $E_1 < E_2$.

Discussing the effect of the coupling on the position of the energy levels we see the following: First, in the absence of any coupling the levels (E_1 and E_2) cross at the position ($E = E_m, \Delta = 0$). Under the effect of the off-diagonal coupling the two perturbed levels E_+ and E_- repel each other, i.e. the energy values

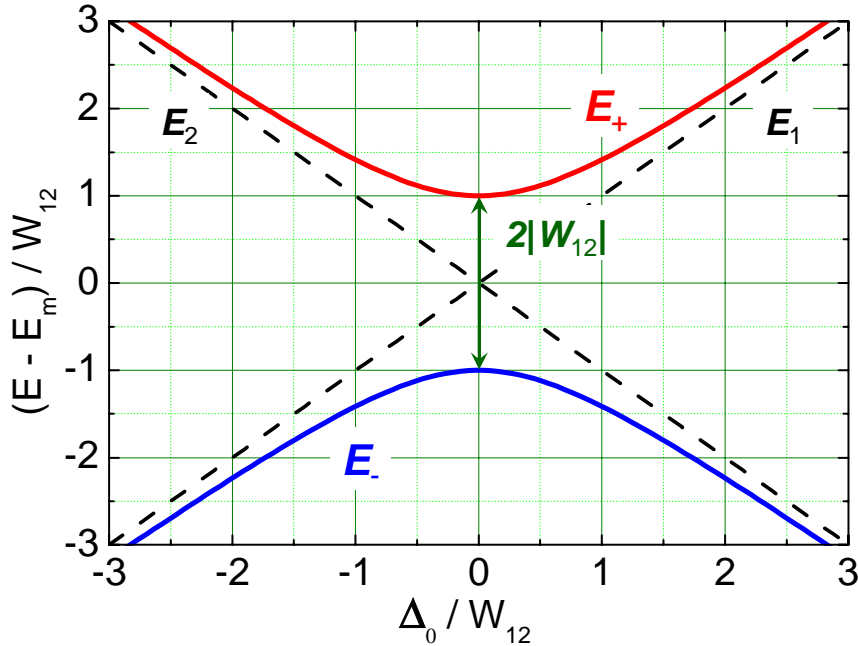


Figure E1: Variation of the eigenenergies E_+ and E_- as a function of the parameter $\Delta = (E_1 - E_2)/2$. Also shown are the energies E_1 and E_2 (dashed lines).

move further apart from each other, and we obtain the typical ***anti-crossing behavior***. We also see that for any Δ we have

$$|E_+ - E_-| > |E_1 - E_2| . \quad (\text{E.23})$$

This result is well known from other fields of physics. For example, in electronic circuit theory the coupling separates the normal frequencies.

Near the asymptotes we have $|\Delta| \gg |W_{12}|$ and the expressions (E.21) and (E.22) can be expanded into a power series in $|W_{12}/\Delta|$:

$$E_+ = E_m + \Delta \left(1 + \frac{1}{2} \left| \frac{W_{12}}{\Delta} \right|^2 + \dots \right) \quad (\text{E.24})$$

$$E_- = E_m - \Delta \left(1 + \frac{1}{2} \left| \frac{W_{12}}{\Delta} \right|^2 + \dots \right) . \quad (\text{E.25})$$

On the other hand, for Δ close to zero we obtain

$$E_+ = E_m + |W_{12}| \quad (\text{E.26})$$

$$E_- = E_m - |W_{12}| . \quad (\text{E.27})$$

From this we immediately see that the effect of coupling is more important when the two unperturbed levels have about the same energy. The effect is then of first order as seen from (E.26) and (E.27), whereas according to (E.24) and (E.25) it is of second order for $|\Delta| \gg |W_{12}|$.

We next have to discuss the effect of the coupling on the eigenstates. With the parameters E_m and Δ we can rewrite (E.17) as

$$\tan \theta = \frac{|W_{12}|}{\Delta} . \quad (\text{E.28})$$

That is, for strong coupling, i.e. $\Delta \ll |W_{12}|$, we have $\theta \simeq \pi/2$. In contrast, for weak coupling, i.e. $\Delta \gg |W_{12}|$, we have $\theta \simeq 0$. Then, at the center of the hyperbola when $E_1 = E_2$, ($\Delta = 0$) we have

$$|\Psi_+\rangle = \frac{1}{\sqrt{2}} \left[e^{-i\varphi/2} |\phi_1\rangle + e^{+i\varphi/2} |\phi_2\rangle \right] \quad (\text{E.29})$$

$$|\Psi_-\rangle = \frac{1}{\sqrt{2}} \left[-e^{-i\varphi/2} |\phi_1\rangle + e^{+i\varphi/2} |\phi_2\rangle \right]. \quad (\text{E.30})$$

Near the asymptotes, when $|\Delta| \gg |W_{12}|$ (weak coupling), we obtain in first order of $|W_{12}|/\Delta$:

$$|\Psi_+\rangle = e^{-i\varphi/2} \left[|\phi_1\rangle + e^{+i\varphi} \frac{|W_{12}|}{2\Delta} |\phi_2\rangle + \dots \right] \quad (\text{E.31})$$

$$|\Psi_-\rangle = e^{+i\varphi/2} \left[|\phi_2\rangle - e^{-i\varphi} \frac{|W_{12}|}{2\Delta} |\phi_1\rangle + \dots \right]. \quad (\text{E.32})$$

As expected, for weak coupling ($\Delta \ll |W_{12}|$) the perturbed states differ only slightly from the unperturbed ones. According to (E.31) the state $|\Psi_+\rangle$ differs from $|\phi_1\rangle$ only by the global phase factor $e^{-i\varphi/2}$ with an additional small contribution of the state $|\phi_2\rangle$. According to (E.32) the same is true for $|\Psi_-\rangle$. On the other hand, for strong coupling ($\Delta \gg |W_{12}|$) according to (E.29) and (E.30) the states $|\Psi_+\rangle$ and $|\Psi_-\rangle$ are very different from the unperturbed states $|\phi_1\rangle$ and $|\phi_2\rangle$, since they are linear superpositions of them with coefficients of the same modulus.

Quantum Resonance

We briefly discuss the case where the eigenenergies of \mathcal{H}_0 are two-fold degenerate, i.e. $E_1 = E_2 = E_m$. In this case the coupling W_{12} lifts the degeneracy as discussed above giving rise to a level with reduced energy. That means that if the ground state of a physical system is two-fold degenerate and all other levels are sufficiently far away any purely off-diagonal coupling between the corresponding states is causing a reduction of the ground state energy of the system.

There are many examples of this phenomenon such as the resonance stabilization of the benzene C_6H_6 molecule shown in Fig. E2. The ground state of the molecule includes three double bonds between neighboring carbons. The eigenfunctions $|\phi_1\rangle$ and $|\phi_2\rangle$ correspond to the two possible configurations of the double bonds shown in Fig. E2. By symmetry reasons we expect that the ground state energy of the system is $\langle \phi_1 | \mathcal{H} | \phi_1 \rangle = \langle \phi_2 | \mathcal{H} | \phi_2 \rangle = E_m$ resulting in a two-fold degenerate ground state. However, the off-diagonal matrix element $\langle \phi_1 | \mathcal{H} | \phi_2 \rangle$ is not zero resulting in a finite coupling between the states $|\phi_1\rangle$ and $|\phi_2\rangle$. This gives rise to two distinct energy levels with one having an energy lower than E_m . Therefore, the benzene molecule is more stable than we would have expected and the true ground state of the molecule is not represented by one of the two configurations shown in Fig. E2. The true ground state rather is a superposition of the two configurations.

Further examples are the ionized hydrogen molecule H_2^+ consisting of two protons and one electron. Again there are two possible configuration with the electron localized at proton 1 and proton 2 with degenerate energies. By a finite coupling of these two configurations we again obtain a states with reduced energy. In this state the electron is no longer localized at one of the protons but is delocalized. It is this delocalization which is by reducing the potential energy responsible for the chemical bond.

In chapter 8 as a further example we discuss a superconducting loop with an odd number of Josephson junctions. For half of a flux quantum in the loop there are two degenerate states with circulating currents in opposite direction. Again by a finite coupling a state with lowered energy is achieved given by a superposition of the two configurations.

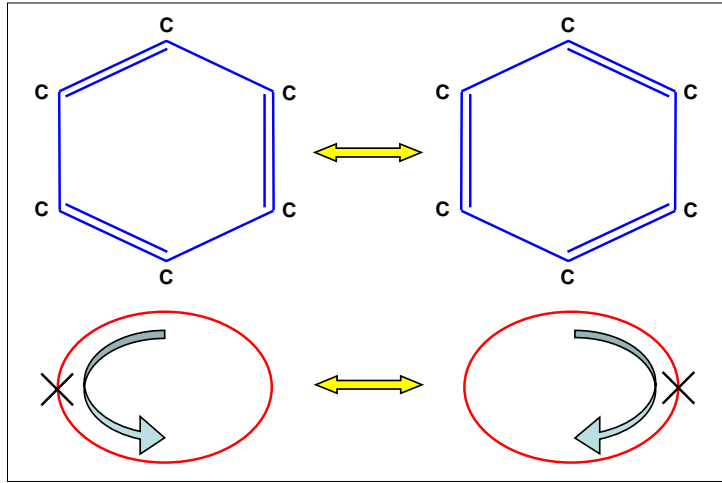


Figure E2: The two possible configurations of the double bonds in a benzene molecule (top) and of the circulating current in a superconducting loop containing a Josephson junction (bottom).

E.3 Dynamic Properties of Two-Level Systems

Time Evolution of the State Vector

We assume a state vector at the instant t given by the superposition

$$|\Psi(t)\rangle = a(t)|\phi_1\rangle + b(t)|\phi_2\rangle . \quad (\text{E.33})$$

The evolution of the state vector is determined by the Schrödinger equation

$$i\hbar \frac{d}{dt}|\Psi(t)\rangle = (\mathcal{H}_0 + \mathcal{W})|\Psi(t)\rangle = (\mathcal{H}_0 + \mathcal{W})(a(t)|\phi_1\rangle + b(t)|\phi_2\rangle) . \quad (\text{E.34})$$

By projecting this equation onto the basis vectors $|\phi_1\rangle$ and $|\phi_2\rangle$, we obtain (for $W_{11} = W_{22} = 0$):

$$i\hbar \frac{d}{dt}a(t) = E_1 a(t) + W_{12}b(t) \quad (\text{E.35})$$

$$i\hbar \frac{d}{dt}b(t) = W_{21}a(t) + E_2b(t) . \quad (\text{E.36})$$

For finite coupling ($|W_{12}| \neq 0$) we obtain a linear system of homogeneous coupled differential equations. In order to solve this system we have to look for the eigenvectors $|\Psi_+\rangle$ with eigenvalue E_+ and $|\Psi_-\rangle$ with eigenvalue E_- of the operator $\mathcal{H} = \mathcal{H}_0 + \mathcal{W}$, whose matrix elements are the coefficients of equations (E.35) and (E.36). We then have to decompose $|\Psi(0)\rangle$ in terms of $|\Psi_+\rangle$ and $|\Psi_-\rangle$ as

$$|\Psi(0)\rangle = \alpha|\Psi_+\rangle + \beta|\Psi_-\rangle , \quad (\text{E.37})$$

where α and β are determined by the initial conditions. We then have

$$|\Psi(t)\rangle = \alpha e^{-iE_+t/\hbar}|\Psi_+\rangle + \beta e^{-iE_-t/\hbar}|\Psi_-\rangle , \quad (\text{E.38})$$

which enables us to derive $a(t)$ and $b(t)$ by projecting $|\Psi(t)\rangle$ onto the basis states $|\phi_1\rangle$ and $|\phi_2\rangle$.

It can be shown that a system with the basis state given by (E.38) oscillates between the two unperturbed states $|\phi_1\rangle$ and $|\phi_2\rangle$. To demonstrate that we assume that $|\Psi(0)\rangle = |\phi_1\rangle$ and calculate the probability $P_{12}(t)$ of finding the system in the basis state $|\phi_2\rangle$ at the time t .

The Rabi Formula

We first express the state $|\Psi(0)\rangle = |\phi_1\rangle$ on the $\{|\Psi_+\rangle, |\Psi_-\rangle\}$ basis. By inverting the expressions (E.11) and (E.12) we obtain

$$|\Psi(0)\rangle = |\phi_1\rangle = e^{+i\varphi/2} \left[\cos \frac{\theta}{2} |\Psi_+\rangle - \sin \frac{\theta}{2} |\Psi_-\rangle \right] . \quad (\text{E.39})$$

Using the time evolution (E.38) we then obtain

$$|\Psi(t)\rangle = e^{+i\varphi/2} \left[\cos \frac{\theta}{2} e^{-iE_+ t/\hbar} |\Psi_+\rangle - \sin \frac{\theta}{2} e^{-iE_- t/\hbar} |\Psi_-\rangle \right] . \quad (\text{E.40})$$

The probability amplitude of finding the system in state $|\phi_2\rangle$ at time t is given by

$$\begin{aligned} \langle \phi_2 | \Psi(t) \rangle &= e^{+i\varphi/2} \left[\cos \frac{\theta}{2} e^{-iE_+ t/\hbar} \langle \phi_2 | \Psi_+ \rangle - \sin \frac{\theta}{2} e^{-iE_- t/\hbar} \langle \phi_2 | \Psi_- \rangle \right] \\ &= e^{+i\varphi/2} \sin \frac{\theta}{2} \cos \frac{\theta}{2} \left[e^{-iE_+ t/\hbar} - e^{-iE_- t/\hbar} \right] . \end{aligned} \quad (\text{E.41})$$

With this expression we obtain

$$\begin{aligned} P_{12}(t) &= |\langle \phi_2 | \Psi(t) \rangle|^2 = \frac{1}{2} \sin^2 \theta \left[1 - \cos \left(\frac{E_+ - E_-}{\hbar} t \right) \right] \\ &= \sin^2 \theta \sin^2 \left(\frac{E_+ - E_-}{2\hbar} t \right) . \end{aligned} \quad (\text{E.42})$$

Using the expression (E.15) and (E.16) for E_+ and E_- we can rewrite this equation to obtain the so called **Rabi formula**

$$P_{12}(t) = \frac{2|W_{12}|^2}{4|W_{12}|^2 + (E_1 - E_2)^2} \sin^2 \left[\sqrt{4|W_{12}|^2 + (E_1 - E_2)^2} \frac{t}{2\hbar} \right] . \quad (\text{E.43})$$

We see from (E.42) and (E.43) that $P_{12}(t)$ oscillates with the frequency $(E_+ - E_-)/\hbar$, which is the Bohr frequency of the system. We further see that $P_{12}(t)$ varies between zero and a maximum value equal to $\sin^2 \theta$, which is obtained for the times $t = (2n+1)\pi\hbar/(E_+ - E_-)$ with $n = 0, 1, 2, 3, \dots$ (see Fig. E3). According to (E.43) the value of $\sin^2 \theta$ as well as the oscillation frequency are functions of $|W_{12}|$ and $(E_1 - E_2)$.

For $E_1 = E_2$ we have $(E_+ - E_-)/\hbar = 2|W_{12}|/\hbar$. Then, according to (E.43) $P_{12}(t)$ has the maximum possible value of unity at the moments $t = (2n+1)\pi\hbar/2|W_{12}|$. That is, the system that is originally in the state $|\phi_1\rangle$ at $t = 0$ is in the state $|\phi_2\rangle$ at $t = \pi\hbar/2|W_{12}|$. Evidently any coupling between two states of equal energy causes the system to oscillate completely between the two states at a frequency proportional to the coupling. This phenomenon is known also for classical systems. For example, when we couple two pendulums of the same frequency by suspending them from the same support and we set only pendulum 1 into motion at $t = 0$, we will have after a certain time pendulum 1 in complete rest whereas pendulum 2 is oscillating with the initial amplitude of pendulum 1.

Fig. E3 shows that the oscillation period $(E_+ - E_-)/\hbar$ of $P_{12}(t)$ decreases when $(E_1 - E_2)$ increases due to a decrease of the parameter $\xi = |W_{12}|^2/(E_1 - E_2)^2$ at constant $|W_{12}|$. Note that for weak coupling

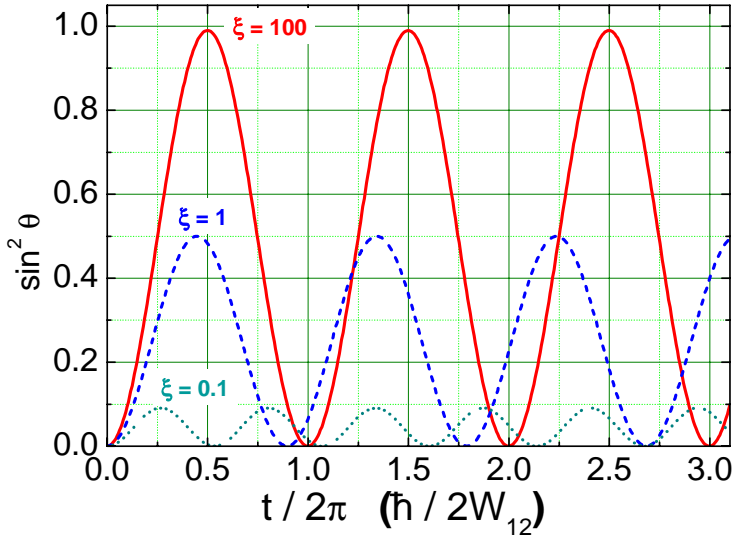


Figure E3: Variation of the probability P_{12} of finding the system in state $|\phi_2\rangle$ at time t , when it was in state $|\phi_1\rangle$ at $t = 0$. $P_{12}(t)$ is shown for three different values of the parameter $\xi = |W_{12}|^2/(E_1 - E_2)^2$ (weak coupling: $\xi \ll 1$, strong coupling: $\xi \gg 1$).

($|W_{12}| \ll E_1 - E_2$) we have $\xi \ll 1$ and hence $\sin^2 \theta$ becomes very small. This is not surprising, since in the case of weak coupling the state $|\phi_1\rangle$ is very close to the stationary state $|\Psi_+\rangle$ and therefore the system starting at state $|\phi_1\rangle$ evolves very little over time.

Above we have mentioned the H_2^+ molecule as an example for a two-level system. According to the result (E.43) we expect an oscillation of the electron between the two protons of the molecule at a frequency given by the Bohr frequency $(E_+ - E_-)/\hbar$ given by the two stationary states $|\Psi_+\rangle$ and $|\Psi_-\rangle$ of the molecule. This oscillation corresponds to an oscillation of the mean value of the electric dipole moment of the molecule. Therefore, when the molecule is not in a stationary state, an oscillating dipole field can appear. Such an oscillating dipole can exchange energy with an electromagnetic field of the same frequency. Hence, this frequency must be seen in the absorption and emission spectrum of the molecule. Of course, the same is true for a superconducting flux or charge qubit representing a two-level system. In many experiments the interaction of an electromagnetic field of varying frequency with the qubit has been measured showing absorption/emission features at the characteristic frequency $(E_+ - E_-)/\hbar$.

F The Spin 1/2 System

In this appendix we discuss the properties of a spin 1/2 system. Since all quantum mechanical two-level systems are equivalent to the spin 1/2 system the results derived in the following are quite general and can be transferred to other two-level systems using for the realization of quantum bits.

F.1 Experimental Demonstration of Angular Momentum Quantization

The quantization of the components of an angular momentum has been first demonstrated by **Stern** and **Gerlach** in 1922 in the ***Stern-Gerlach experiment***, where the deflection of a beam of neutral paramagnetic atoms (silver atoms in the first experiment) in an inhomogeneous magnetic field has been studied.

Classically, the Stern-Gerlach experiment can be understood as follows: Since the used atoms are neutral, they are not subject to the Lorentz force. However, as paramagnetic atoms they possess a magnetic moment \mathbf{m} and the resulting force can be derived by considering the potential energy

$$E_{\text{pot}} = -\mathbf{m} \cdot \mathbf{B} . \quad (\text{F.1})$$

From the basic course in physics we know that for an atom the magnetic moment \mathbf{m} and a total angular momentum \mathbf{J} is caused by (i) the motion of electrons about the nucleus (orbital moment \mathbf{L}) and (ii) the intrinsic magnetic moment or spin of the electrons (spin moment \mathbf{S}). In the case of silver atoms the total angular moment is simply equal to the spin moment of the single electron in the outermost shell, since this electron is an s -electron with zero orbital moment and the total spin and orbital moment of other electrons forming a completely filled shell is also zero. That is, the total angular moment of the silver atom is $\mathbf{J} = \mathbf{L} + \mathbf{S} = \mathbf{S}$ with $S = 1/2$.

We further know that for a given atomic level the magnetic moment is proportional to the angular moment

$$\mathbf{m} = \gamma \mathbf{J} \quad (\text{F.2})$$

with *gamma* the ***gyromagnetic ratio*** of the level under consideration. From (F.1) we immediately can derive the force exerted on the atom to

$$\mathbf{F} = \nabla(\mathbf{m} \cdot \mathbf{B}) , \quad (\text{F.3})$$

which is zero if the magnetic field is homogeneous. Furthermore, the magnetic field \mathbf{B} exerts a torque

$$\mathbf{D} = \mathbf{m} \times \mathbf{B} \quad (\text{F.4})$$

on the magnetic moment \mathbf{m} . The classical equation of motion of \mathbf{J} is (angular moment theorem)

$$\frac{d\mathbf{J}}{dt} = \mathbf{D} = \gamma \mathbf{J} \times \mathbf{B} \quad (\text{F.5})$$

or

$$\frac{d}{dt} \mathbf{m}(t) = \gamma \mathbf{m}(t) \times \mathbf{B} \quad (\text{F.6})$$

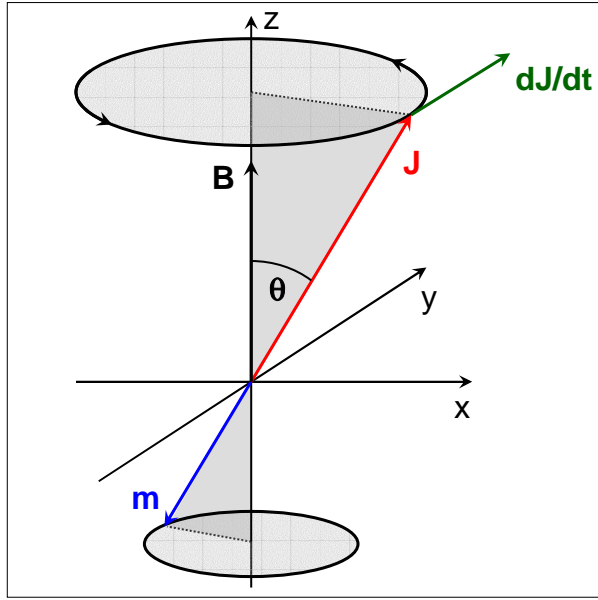


Figure F1: In a uniform magnetic field \mathbf{B} the magnetic moment \mathbf{m} of an atom, which is proportional to its total angular momentum \mathbf{J} , precesses around the field direction with constant angular velocity (Larmor precession).

Scalar multiplication of both sides of (F.6) by either $\mathbf{m}(t)$ or \mathbf{B} yields

$$\frac{d}{dt}[\mathbf{m}(t)]^2 = 0 \quad (\text{F.7})$$

$$\frac{d}{dt}[\mathbf{m}(t) \cdot \mathbf{B}] = 0 \quad (\text{F.8})$$

That is, the magnetic moment evolves with constant modulus and maintaining a constant angle with \mathbf{B} . The atom thus behaves like a gyroscope (see Fig. F1). The time derivative $\frac{d\mathbf{J}}{dt}$ is perpendicular to \mathbf{J} and \mathbf{B} and the angular moment therefore turns around the magnetic field direction with the angle θ between \mathbf{J} and \mathbf{B} remaining constant.

To calculate the force from (F.3) we can neglect in very good approximation the terms proportional to m_x and m_y and take m_z as constant. This can be done since the oscillation frequency due to the rotation of \mathbf{m} is so high that only time-averaged values of m_x and m_y can play a role in E_{pot} and these are both zero. Then, we obtain

$$\mathbf{F} = \nabla(m_z B_z) = m_z \nabla B_z . \quad (\text{F.9})$$

With $\mathbf{B} = (0, 0, B_z(z))$ also the components of ∇B_z along the x - and y -direction are zero. Then, the resulting force is parallel to z and proportional to m_z . In the Stern-Gerlach experiment the deflection of silver atoms in such magnetic field has been measured. Since the force is causing a deflection of the atoms in z -direction proportional to m_z and hence J_z , one would expect continuous distribution along z if the moments of the various atoms would be distributed homogeneously. In contrast, in the experiment only two spots have been observed showing that the moment m_z of the silver atoms can have only two distinct values $+m_z$ and $-m_z$.

F.2 Theoretical Description

We are now going to show how quantum mechanics describes the degrees of freedom of a spin 1/2 system. The idea is to give examples of kets and observables in order to show how physical predictions can

be extracted from them and how to distinguish clearly between the various stages of an experiment (state preparation, time evolution, measurement). We know that every physical quantity must be associated with an observable, i.e. a Hermitian operator whose eigenvalues can form a basis in the state space. We therefore must define the state space and the observables corresponding to the components S_x , S_y and S_z of a spin \mathbf{S} and, more generally, $S_u = \mathbf{S} \times \hat{\mathbf{u}}$, where $\hat{\mathbf{u}}$ is an arbitrary unit vector.

The Spin Space

From experiments it is known that with S_z we must associate an observable \mathcal{S}_z , which has the two eigenvalues $\pm\hbar/2$. We assume that these two eigenvalues are not degenerate. We further denote by $|\uparrow\rangle$ and $|\downarrow\rangle$ the corresponding orthonormal eigenvectors:

$$\mathcal{S}_z |\uparrow\rangle = +\frac{\hbar}{2} |\uparrow\rangle \quad (\text{F.10})$$

$$\mathcal{S}_z |\downarrow\rangle = -\frac{\hbar}{2} |\downarrow\rangle . \quad (\text{F.11})$$

The spin state space is the two-dimensional space S^2 spanned by its eigenvectors $|\uparrow\rangle$ and $|\downarrow\rangle$. The most general normalized vector in this space is a linear superposition of $|\uparrow\rangle$ and $|\downarrow\rangle$

$$|\Psi(t)\rangle = a(t)|\uparrow\rangle + b(t)|\downarrow\rangle \quad (\text{F.12})$$

with

$$|a(t)|^2 + |b(t)|^2 = 1 . \quad (\text{F.13})$$

Note that $|\Psi\rangle$ can be viewed as a vector on the Bloch sphere S^2 (see Fig. D1).

In the $\{|\uparrow\rangle, |\downarrow\rangle\}$ basis the matrices representing the observables \mathcal{S}_x , \mathcal{S}_y and \mathcal{S}_z are given by (we will not derive this result here)

$$\begin{aligned} \mathcal{S}_x &= \frac{\hbar}{2} \begin{pmatrix} 0 & 1 \\ 1 & 0 \end{pmatrix} & \mathcal{S}_y &= \frac{\hbar}{2} \begin{pmatrix} 0 & -i \\ i & 0 \end{pmatrix} & \mathcal{S}_z &= \frac{\hbar}{2} \begin{pmatrix} 1 & 0 \\ 0 & -1 \end{pmatrix} \\ \mathcal{S} &= \frac{\hbar}{2} \vec{\sigma} \end{aligned} \quad (\text{F.14})$$

with the Pauli spin matrices $\vec{\sigma} = (\mathbf{X}, \mathbf{Y}, \mathbf{Z})$. With the angles θ and φ defined in Fig. D1 we can write the component \mathcal{S}_u of \mathcal{S} along the unit vector $\hat{\mathbf{u}}$ as

$$\mathcal{S}_u = \mathcal{S} \cdot \hat{\mathbf{u}} = \mathcal{S}_x \sin \theta \cos \varphi + \mathcal{S}_y \sin \theta \sin \varphi + \mathcal{S}_z \cos \theta . \quad (\text{F.15})$$

Using (F.14) we easily find the matrix, which represents the corresponding observable $\mathcal{S}_u = \mathcal{S} \cdot \hat{\mathbf{u}}$ in the $\{|\uparrow\rangle, |\downarrow\rangle\}$ basis:

$$\begin{aligned} \mathcal{S}_u &= \mathcal{S}_x \sin \theta \cos \varphi + \mathcal{S}_y \sin \theta \sin \varphi + \mathcal{S}_z \cos \theta \\ &= \frac{\hbar}{2} \begin{pmatrix} \cos \theta & \sin \theta e^{-i\varphi} \\ \sin \theta e^{+i\varphi} & -\cos \theta \end{pmatrix} . \end{aligned} \quad (\text{F.16})$$

We now have to derive the eigenvalues and eigenvectors of the observables \mathcal{S}_x , \mathcal{S}_y and \mathcal{S}_u . The calculation using the matrices (F.14) is straightforward. For \mathcal{S}_u the eigenvalue equation $\mathcal{S}_u|\Psi\rangle = \lambda|\Psi\rangle$ with $|\Psi\rangle = a|\uparrow\rangle + b|\downarrow\rangle$ can be written as

$$\frac{\hbar}{2} \begin{pmatrix} \cos\theta - \lambda & \sin\theta e^{-i\varphi} \\ \sin\theta e^{+i\varphi} & -(\cos\theta + \lambda) \end{pmatrix} \begin{pmatrix} a \\ b \end{pmatrix} = 0 . \quad (\text{F.17})$$

It can easily be shown that this system is solved by $\lambda = \pm 1$ resulting in the eigenvalues $\pm\frac{\hbar}{2}$. More generally, it can be shown that \mathcal{S}_x , \mathcal{S}_y and \mathcal{S}_u have the same eigenvalues $\pm\hbar/2$ as \mathcal{S}_z . This result is expected, since in an experiment (e.g. a Stern-Gerlach experiment) it is always possible to make the axis defined by the magnetic field parallel to the x - and y -axis or parallel to $\hat{\mathbf{u}}$. Since all directions of space have the same properties, the same results are expected for all directions.

As for the eigenvectors of \mathcal{S}_x , \mathcal{S}_y and \mathcal{S}_u , we denote them by $|\pm\rangle_x$, $|\pm\rangle_y$ and $|\pm\rangle_u$, respectively, where the sign in the ket is that of the corresponding eigenvalue. The expansions of these eigenvectors in the $\{|\uparrow\rangle, |\downarrow\rangle\}$ basis is given by

$$|\pm\rangle_x = \frac{1}{\sqrt{2}}(|\uparrow\rangle \pm |\downarrow\rangle) \quad (\text{F.18})$$

$$|\pm\rangle_y = \frac{1}{\sqrt{2}}(|\uparrow\rangle \pm i|\downarrow\rangle) \quad (\text{F.19})$$

$$|+\rangle_u = \cos\frac{\theta}{2}e^{-i\varphi/2}|\uparrow\rangle + \sin\frac{\theta}{2}e^{+i\varphi/2}|\downarrow\rangle \quad (\text{F.20})$$

$$|-\rangle_u = -\sin\frac{\theta}{2}e^{-i\varphi/2}|\uparrow\rangle + \cos\frac{\theta}{2}e^{+i\varphi/2}|\downarrow\rangle . \quad (\text{F.21})$$

F.3 Evolution of a Spin 1/2 Particle in a Homogeneous Magnetic Field

We consider again a silver atom in a homogeneous magnetic field \mathbf{B}_0 as we have done in the classical treatment in section F.1. The classical potential energy of the magnetic moment \mathbf{m} related to the angular momentum $\mathbf{J} = \mathbf{S}$ is⁴⁶

$$E_{\text{pot}} = -\mathbf{m} \cdot \mathbf{B}_0 = -m_z B_0 = -\gamma B_0 S_z = \omega_0 S_z . \quad (\text{F.22})$$

It is easy to be seen that the quantity $\omega_0 \equiv -\gamma B_0$ has the dimension of an inverse time, i.e. of an angular velocity.

Going to a quantum mechanical treatment we must replace S_z by the operator \mathcal{S}_z and the classical energy by the Hamiltonian \mathcal{H} , which describes the evolution of the spin of the atom in the magnetic field \mathbf{B}_0 :

$$\mathcal{H} = \omega_0 \mathcal{S}_z . \quad (\text{F.23})$$

Since this operator is time independent, solving the corresponding Schrödinger equation is equivalent to solving the eigenvalue equation of \mathcal{H} . We immediately see that the eigenvectors of \mathcal{H} are those of \mathcal{S}_z :

$$\mathcal{H}|\uparrow\rangle = +\frac{\hbar\omega_0}{2}|\uparrow\rangle = E_\uparrow|\uparrow\rangle \quad (\text{F.24})$$

$$\mathcal{H}|\downarrow\rangle = -\frac{\hbar\omega_0}{2}|\downarrow\rangle = E_\downarrow|\downarrow\rangle . \quad (\text{F.25})$$

⁴⁶Note that for an electron with spin $S = 1/2$ we have $\mathbf{m} = -g_s \frac{e}{2m_e} \mathbf{S} = \gamma \mathbf{S}$. That is, $\gamma = -g_s \frac{e}{2m_e}$ is negative with $g_s \simeq 2$ the g -factor of the electron. The potential energy then is $E_{\text{pot}} = -\mathbf{m} \cdot \mathbf{B} = g_s \frac{e}{2m_e} \mathbf{S} \cdot \mathbf{B} = -\gamma S_z B_z$.

There are two energy levels E_{\uparrow} and E_{\downarrow} separated by the energy⁴⁷

$$\hbar\omega_0 = -\gamma\hbar B_0 . \quad (\text{F.26})$$

We next discuss the **Larmor precession** already mentioned in the classical treatment of section F.1. In order to do so let us assume that at $t = 0$ the spin is in the state

$$|\Psi(0)\rangle = \cos \frac{\theta}{2} e^{-i\varphi/2} |\uparrow\rangle + \sin \frac{\theta}{2} e^{+i\varphi/2} |\downarrow\rangle . \quad (\text{F.27})$$

It can be shown that any spin state could be put in this form. To calculate the spin state at a time $t > 0$ we can write

$$|\Psi(t)\rangle = \cos \frac{\theta}{2} e^{-i\frac{\varphi}{2}} e^{-iE_{\uparrow}\frac{t}{\hbar}} |\uparrow\rangle + \sin \frac{\theta}{2} e^{+i\frac{\varphi}{2}} e^{-iE_{\downarrow}\frac{t}{\hbar}} |\downarrow\rangle , \quad (\text{F.28})$$

since we already have expanded $|\Psi(0)\rangle$ in terms of the eigenstates of the Hamiltonian. Using the eigenvalues E_{\uparrow} and E_{\downarrow} we obtain

$$|\Psi(t)\rangle = \cos \frac{\theta}{2} e^{-i(\varphi+\omega_0 t)/2} |\uparrow\rangle + \sin \frac{\theta}{2} e^{+i(\varphi+\omega_0 t)/2} |\downarrow\rangle . \quad (\text{F.29})$$

We see that the presence of the magnetic field \mathbf{B}_0 introduces a phase shift between the coefficients of the kets $|\uparrow\rangle$ and $|\downarrow\rangle$, which is proportional to t .

Comparing (F.29) for $|\Psi(t)\rangle$ to the eigenket $|+\rangle_u$ of the observable $\hat{S} \cdot \hat{\mathbf{u}}$ (see (F.20)), we see that the direction $\hat{\mathbf{u}}(t)$ along which the spin component is $+\hbar/2$ is defined by the polar angles

$$\theta(t) = \theta \quad (\text{F.30})$$

$$\varphi(t) = \varphi + \omega_0 t . \quad (\text{F.31})$$

That is, the angle θ between $\hat{\mathbf{u}}(t)$ and the z -axis remains constant, while $\hat{\mathbf{u}}(t)$ rotates around the z -axis at an angular velocity $d\varphi/dt = \omega_0$. Thus, the quantum mechanical treatment also gives the precession of the spin around the direction of the magnetic field, which is denoted as the **Larmor precession**.

From the expression (F.23) for the Hamiltonian it is obvious that the observable S_z is a constant of the motion. Using the expression (F.29) it can be shown that the probabilities for obtaining $\pm\hbar/2$ in a measurement are time independent. Since the modulus of $e^{\pm i(\varphi+\omega_0 t)/2}$ is equal to 1, we obtain⁴⁸

$$\langle \Psi(t) | \mathcal{S}_z | \Psi(t) \rangle = \frac{\hbar}{2} \cos \theta . \quad (\text{F.32})$$

On the other hand, \mathcal{S}_x and \mathcal{S}_y do not commute with \mathcal{H} what can be easily shown by using the matrices in (F.14). We obtain

$$\langle \Psi(t) | \mathcal{S}_x | \Psi(t) \rangle = \frac{\hbar}{2} \sin \theta \cos(\varphi + \omega_0 t) \quad (\text{F.33})$$

$$\langle \Psi(t) | \mathcal{S}_y | \Psi(t) \rangle = \frac{\hbar}{2} \sin \theta \sin(\varphi + \omega_0 t) . \quad (\text{F.34})$$

We see that the mean values of the spin components behave as the components of a classical angular momentum of modulus $\hbar/2$ undergoing a Larmor precession.

⁴⁷For an electron we have $gamma = -g_s \frac{e}{2m_e}$ and hence $\hbar\omega_0 = +g_s \frac{e\hbar}{2m_e} B_0 = g_s \mu_B B_0$ with the Bohr magneton $\mu_B = \frac{e\hbar}{2m_e}$.

⁴⁸Here we have to use the equalities $\sin^2 \frac{\theta}{2} = \frac{1}{2}(1 - \cos \theta)$ and $\cos^2 \frac{\theta}{2} = \frac{1}{2}(1 + \cos \theta)$.

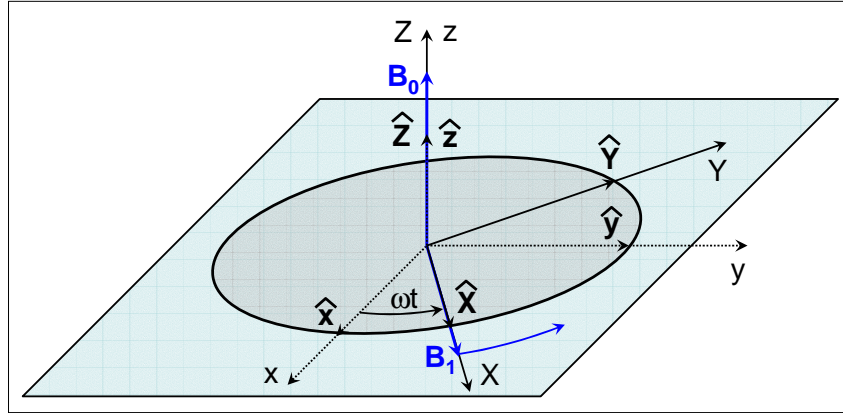


Figure F2: The absolute reference frame (dotted lines) and the rotating reference frame (solid lines). The magnetic field \mathbf{B}_0 is directed along the \hat{z} -direction. The rotating reference frame rotates about the \hat{z} -direction at an angular velocity ω . The direction $\hat{\hat{X}}$ is coincides with the direction of the rotating field $\mathbf{B}_1(t)$.

F.4 Spin 1/2 Particle in a Rotating Magnetic Field

Classical Treatment

We now discuss the situation, where in addition to the static magnetic field \mathbf{B}_0 we have an additional field $\mathbf{B}_1(t)$, which is perpendicular to \mathbf{B}_0 and rotates about \mathbf{B}_0 at constant amplitude with an angular velocity ω as shown in Fig. F2. The field amplitude are related to the two characteristic frequencies

$$\omega_0 = -\gamma B_0 \quad (F.35)$$

$$\omega_1 = -\gamma B_1 . \quad (F.36)$$

In order to analyze the behavior of a spin 1/2 system in such field we use a fixed coordinate system characterized by the unit vectors \hat{x} , \hat{y} and \hat{z} with the static magnetic field parallel to \hat{z} . We further introduce a rotating reference frame characterized by the unit vectors $\hat{\hat{X}}$, $\hat{\hat{Y}}$ and $\hat{\hat{z}}$, which is obtained from the fixed system by rotation through an angle ωt about \hat{z} . The direction $\hat{\hat{X}}$ corresponds to the direction of the rotating field $\mathbf{B}_1(t)$.

The equation of motion of the magnetic moment $\mathbf{m}(t)$ in the presence of the total field $\mathbf{B}(t) = \mathbf{B}_0 + \mathbf{B}_1(t)$ becomes (compare (F.6))

$$\frac{d}{dt} \mathbf{m}(t) = \gamma \mathbf{m}(t) \times [\mathbf{B}_0 + \mathbf{B}_1(t)] . \quad (F.37)$$

To solve this equation it is convenient to switch to the rotating reference frame. The velocity of the vector $\mathbf{m}(t)$ with respect to this rotating reference frame is

$$\left(\frac{d\mathbf{m}}{dt} \right)_{\text{rel}} = \frac{d\mathbf{m}}{dt} - \omega \hat{z} \times \mathbf{m}(t) . \quad (F.38)$$

With

$$\Delta\omega = \omega - \omega_0 \quad (F.39)$$

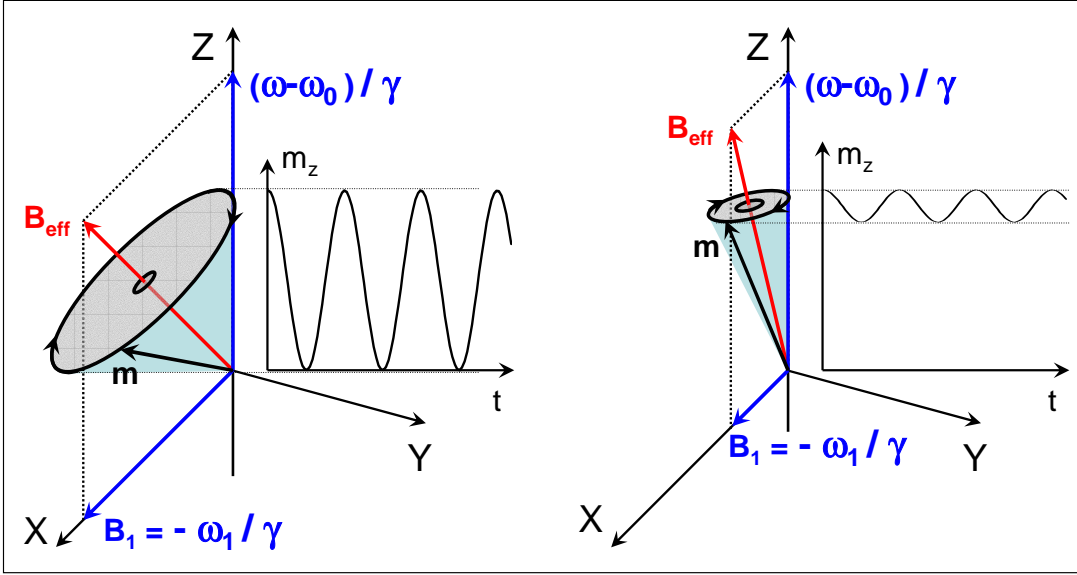


Figure F3: In the rotating reference frame the effective magnetic field \mathbf{B}_{eff} has fixed direction. The magnetic moment $\mathbf{m}(t)$ rotates about the direction of \mathbf{B}_{eff} with constant angular velocity: precession in the rotating reference frame. Also shown is the temporal oscillation of the Z-component of the magnetic moment. Left: close to resonance case, $\Delta\omega = \omega - \omega_0 \sim \omega_1$. Right: off-resonance case, $\Delta\omega = \omega - \omega_0 \gg \omega_1$.

we obtain

$$\begin{aligned} \left(\frac{d\mathbf{m}}{dt} \right)_{\text{rel}} &= \gamma \mathbf{m}(t) \times [\mathbf{B}_0 + \mathbf{B}_1(t)] - \omega \hat{\mathbf{z}} \times \mathbf{m}(t) \\ &= \mathbf{m}(t) \times [\Delta\omega \hat{\mathbf{Z}} - \omega_1 \hat{\mathbf{X}}] . \end{aligned} \quad (\text{F.40})$$

This equation can be solved easier, since the coefficients on the right hand side are now no longer time dependent. Moreover, the form of (F.40) is analogous to that of (F.6). Hence, the relative motion of the vector $\mathbf{m}(t)$ is therefore a rotation about an **effective field** \mathbf{B}_{eff} , which is static with respect to the rotating reference frame and given by (see Fig. F3)

$$\mathbf{B}_{\text{eff}} = \frac{1}{\gamma} [\Delta\omega \hat{\mathbf{Z}} - \omega_1 \hat{\mathbf{X}}] . \quad (\text{F.41})$$

In order to obtain the absolute motion of $\mathbf{m}(t)$ we have to combine the precession about \mathbf{B}_{eff} with the rotation about $\hat{\mathbf{z}}$ with the angular velocity ω .

We use the above discussion to understand the phenomenon of magnetic resonance. For this purpose let us consider a magnetic moment which is parallel to the field \mathbf{B}_0 at $t = 0$. The question is: What happens if we switch on the rotating field $\mathbf{B}_1(t)$? We first consider the case that the rotation frequency $\omega/2\pi$ of this field is very different from the natural frequency $\omega_0/2\pi$, so that $\Delta\omega = \omega - \omega_0 \gg \omega_1$. We immediately see from Fig. F3 that in this case the effective magnetic field is directed practically along $\hat{\mathbf{z}}$. The precession of $\mathbf{m}(t)$ about \mathbf{B}_{eff} then has a very small amplitude and hardly modifies the direction of the magnetic moment. That is, nothing happens.

The more interesting case is the resonance case, when $\omega \approx \omega_0$ and hence $\Delta\omega = \omega - \omega_0 \ll \omega_1$. In this case the angle between \mathbf{B}_{eff} and $\hat{\mathbf{z}}$ is large and the precession of the magnetic moment then has a large amplitude. Moreover, in the case of resonance, $\Delta\omega = 0$, \mathbf{B}_{eff} is directed along $\hat{\mathbf{X}}$ and the magnetic moment can be completely flipped.

Quantum Mechanical Treatment

With the two eigenvectors $|\uparrow\rangle$ and $|\downarrow\rangle$ of the projection \mathcal{S}_z of the spin onto the $\hat{\mathbf{z}}$ -direction the state vector of the system can be written as

$$|\Psi(t)\rangle = a(t)|\uparrow\rangle + b(t)|\downarrow\rangle . \quad (\text{F.42})$$

The Hamilton operator of the system is⁴⁹

$$\mathcal{H}(t) = -\mathcal{M} \cdot \mathbf{B}(t) = -\gamma \mathcal{S} \cdot [\mathbf{B}_0 + \mathbf{B}_1(t)] . \quad (\text{F.43})$$

With \mathbf{B}_0 parallel to \mathbf{z} and $\mathbf{B}_1(t)$ rotating in the xy -plane with angular frequency ω we obtain

$$\mathcal{H}(t) = \omega_0 \mathcal{S}_z + \omega_1 [\cos \omega t \mathcal{S}_x + \sin \omega t \mathcal{S}_y] . \quad (\text{F.44})$$

With the spin matrices (F.14) we obtain the matrix representing \mathcal{H} to

$$\mathcal{H}(t) = \frac{\hbar}{2} \begin{pmatrix} \omega_0 & \omega_1 e^{-i\omega t} \\ \omega_1 e^{+i\omega t} & -\omega_0 \end{pmatrix} . \quad (\text{F.45})$$

Using (F.42) and (F.45) we can write the Schrödinger equation as

$$i \frac{d}{dt} a(t) = \frac{\omega_0}{2} a(t) + \frac{\omega_1}{2} e^{-i\omega t} b(t) \quad (\text{F.46})$$

$$i \frac{d}{dt} b(t) = \frac{\omega_1}{2} e^{+i\omega t} a(t) - \frac{\omega_0}{2} b(t) . \quad (\text{F.47})$$

Equations (F.46) and (F.47) form a linear homogeneous system with time dependent coefficients. To solve this system it is convenient to switch again to the rotating reference frame. To do so, we define new functions by setting

$$\alpha(t) = e^{+i\omega t/2} a(t) \quad (\text{F.48})$$

$$\beta(t) = e^{-i\omega t/2} b(t) . \quad (\text{F.49})$$

Substitution of (F.48) and (F.49) into (F.46) and (F.47) gives

$$i \frac{d}{dt} \alpha(t) = -\frac{\Delta\omega}{2} \alpha(t) + \frac{\omega_1}{2} \beta(t) \quad (\text{F.50})$$

$$i \frac{d}{dt} \beta(t) = +\frac{\omega_1}{2} \alpha(t) + \frac{\Delta\omega}{2} \beta(t) . \quad (\text{F.51})$$

This is equivalent to

$$i\hbar \frac{d}{dt} |\tilde{\Psi}(t)\rangle = \tilde{\mathcal{H}} |\tilde{\Psi}(t)\rangle \quad (\text{F.52})$$

⁴⁹The expression $\mathcal{M} \cdot \mathbf{B}(t)$ symbolizes the scalar product $\mathcal{M}_x B_x(t) + \mathcal{M}_y B_y(t) + \mathcal{M}_z B_z(t)$, where \mathcal{M}_x , \mathcal{M}_y and \mathcal{M}_z are operators, while $B_x(t)$, $B_y(t)$ and $B_z(t)$ are numbers.

with

$$|\tilde{\Psi}(t)\rangle = \alpha(t)|\uparrow\rangle + \beta(t)|\downarrow\rangle \quad (\text{F.53})$$

and

$$\tilde{\mathcal{H}}(t) = \frac{\hbar}{2} \begin{pmatrix} -\Delta\omega & \omega_1 \\ \omega_1 & +\Delta\omega \end{pmatrix}. \quad (\text{F.54})$$

Thus, the transformation (F.48) and (F.49) has led to an equation, which is analogous to a Schrödinger equation, in which the Hamilton operator $\tilde{\mathcal{H}}$ plays the role of a time independent Hamiltonian. Note that $\tilde{\mathcal{H}}$ describes the interaction of a spin with a fixed field corresponding to the effective field introduced above. We therefore can conclude that the transformation (F.48) and (F.49) is the quantum mechanical analogue of the change from the fixed reference frame to the rotating reference frame.

Equation (F.52) is simple to solve. For a given $|\tilde{\Psi}(0)\rangle$ we can determine $|\tilde{\Psi}(t)\rangle$ by expanding $|\tilde{\Psi}(0)\rangle$ on the eigenvectors of $\tilde{\mathcal{H}}$, which can be calculated exactly. Since $\tilde{\mathcal{H}}$ does not depend explicitly on time, to find $|\tilde{\Psi}(t)\rangle$ at given $|\tilde{\Psi}(0)\rangle$ we simply can multiply the coefficients of the expansion on the eigenvectors by $e^{-iE_{\pm}t/\hbar}$, where E_{\pm} are the eigenvalues of $\tilde{\mathcal{H}}$ (for the eigenvalues compare appendix E.2). Finally, we go from $|\tilde{\Psi}(t)\rangle$ to $|\Psi(t)\rangle$ by using (F.48) and (F.49).

Rabi's Formula

We consider a spin residing in state $|\uparrow\rangle$ at $t = 0$, i.e. $|\Psi(0)\rangle = |\uparrow\rangle$. According to (F.48) and (F.49) this corresponds to

$$|\tilde{\Psi}(0)\rangle = |\uparrow\rangle. \quad (\text{F.55})$$

We are now interested in the probability $P_{\uparrow\downarrow}(t)$ of finding the spin in the state $|\downarrow\rangle$ at the time t . This probability is given by

$$P_{\uparrow\downarrow}(t) = |\langle\downarrow|\Psi(t)\rangle|^2 = |b(t)|^2 = |\beta(t)|^2 = |\langle\downarrow|\tilde{\Psi}(t)\rangle|^2. \quad (\text{F.56})$$

Here we have used the fact that $b(t)$ and $\beta(t)$ have the same modulus.

We see that we have to determine $|\langle\downarrow|\tilde{\Psi}(t)\rangle|^2$, where $|\tilde{\Psi}(t)\rangle$ is the solution of (F.52) under the initial condition (F.55). This problem has already been solved in section E.3. To use the results derived there we have to use the following correspondences:

$$\begin{aligned} |\phi_1\rangle &\simeq |\uparrow\rangle & |\phi_2\rangle &\simeq |\downarrow\rangle \\ E_1 &\simeq -\frac{\hbar}{2}\Delta\omega & E_2 &\simeq +\frac{\hbar}{2}\Delta\omega & W_{12} &\simeq +\frac{\hbar}{2}\omega_1. \end{aligned} \quad (\text{F.57})$$

With these replacements Rabi's formula (E.43) becomes

$$P_{\uparrow\downarrow}(t) = \frac{\omega_1^2}{\omega_1^2 + (\Delta\omega)^2} \sin^2 \left[\sqrt{\omega_1^2 + (\Delta\omega)^2} \frac{t}{2} \right]. \quad (\text{F.58})$$

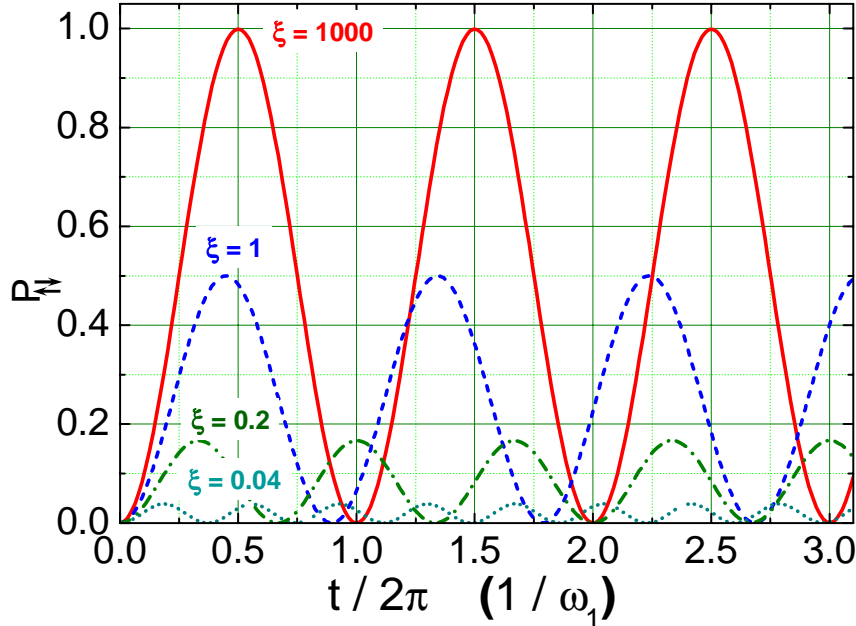


Figure F4: Variation of the probability $P_{\uparrow\downarrow}$ of finding a spin 1/2 system in the state $|\downarrow\rangle$ at time t , when it was in state $|\uparrow\rangle$ at $t = 0$. $P_{\uparrow\downarrow}(t)$ is shown for three different values of the parameter $\xi = \omega_1^2/(\Delta\omega)^2$. In resonance, $\Delta\omega \rightarrow 0$ and hence $\xi \rightarrow \infty$.

The probability is of course zero at $t = 0$ and then varies sinusoidally with time between the minimum value zero and the maximum value $\frac{\omega_1^2}{\omega_1^2 + (\Delta\omega)^2}$. We see, that for $|\omega_1| \ll |\Delta\omega|$ (this corresponds to the weak coupling case $|W_{12}| \ll E_1 - E_2$ in section E.3), $P_{\uparrow\downarrow}(t)$ remains almost zero as shown in Fig. F4. However, near resonance, i.e. for $\Delta\omega \simeq 0$, the oscillation amplitude of $P_{\uparrow\downarrow}(t)$ is large and becomes exactly 1 for $\Delta\omega = 0$ at the moments $t = (2n+1)\pi/\omega_1$ (see Fig. F4). This is in agreement with the result of our classical treatment. We find that at resonance a very weak rotating field is able to reverse the direction of the spin. We further note that the angular frequency of the oscillation of $P_{\uparrow\downarrow}(t)$ is $\sqrt{\omega_1^2 + (\Delta\omega)^2} = |\gamma\mathbf{B}_{\text{eff}}|$. In the rotating reference frame this oscillation corresponds to the projection of the precession of the magnetic moment about the effective field and is usually called **Rabi precession** or **Rabi oscillation**. We also would $P_{\uparrow\downarrow}(t)$ is $\sqrt{\omega_1^2 + (\Delta\omega)^2} \simeq \omega_1 \propto B_1$. That is, the oscillation frequency increases linearly with the amplitude of the rotating field.

G Literature

Superconductivity

1. M. Tinkham,
Introduction to Superconductivity,
McGraw-Hill, New York (1975).
2. P. de Gennes,
Superconductivity of Metals and Alloys,
Benjamin, New York (1966).
3. Werner Buckel,
Supraleitung — Grundlagen und Anwendungen,
VCH-Verlag, Weinheim (1994).
4. Vladimir Z. Kresin, Stuart A. Wolf,
Fundamentals of Superconductivity,
Plenum Press, New York (1990).
5. M. Cyrot, D. Pavuna,
Introduction to Superconductivity and High- T_C Materials,
World Scientific, Singapore (1992).
6. A. C. Rose-Innes, E. H. Rhoderick,
Introduction to Superconductivity,
Pergamon Press, Braunschweig (1969).
7. R. D. Parks (de.),
Superconductivity I and II,
Marcel Dekker Inc., New York (1969).
8. G. Rickayzen,
Theory of Superconductivity,
Interscience Publishers, John Wiley & Sons, New York (1965).
9. R. Schrieffer,
Theory of Superconductivity,
Benjamin, New York (1970).
10. F. London, H. London,
Superfluids, Vol.1, *Macroscopic Theory of Superconductivity*,
John Wiley & Sons, New York (1950)

Applications of Superconductivity

1. K. K. Likharev,
Dynamics of Josephson Junctions and Circuits,
Gordon and Breach Science Publishers, New York (1986).
2. T. P. Orlando, K. A. Delin,
Foundations of Applied Superconductivity,
Addison-Wesley, New York (1991).

3. A. Barone and G. Paterno,
Physics and Application of the Josephson Effect,
John Wiley & Sons, New York (1982).
4. Steven T. Ruggiero, David A. Rudman,
Superconducting Devices,
Academic Press, New York (1990).
5. Alan M. Kadin,
Introduction to Superconducting Circuits,
John Wiley & Sons, New York (1999).
6. T. van Duzer,
Principles of Superconducting Devices and Circuits,
Elsevier, New York (1981).
7. L. Solymar,
Superconductive Tunneling and Applications,
Chapman and Hall Ltd., London (1972).
8. V. L. Newhouse,
Applied Superconductivity,
John Wiley & Sons, New York (1964).
9. V. Kose,
Superconducting Quantum Electronics,
Springer, Heidelberg (1989).
10. J. Hinken,
Supraleiter-Elektronik,
Springer, Heidelberg (1988).

H SI-Einheiten

Das aus dem metrischen System weiterentwickelte Internationale Einheitensystem SI (*Système Internationale d'Unités*) enthält als die 7 Basiseinheiten *Meter* (m), *Kilogramm* (kg), *Sekunde* (s), *Ampère* (A), *Kelvin* (K), *Candela* (Cd) und *Mol* (mol). Hinzu kommen die beiden ergänzenden Einheiten *Radiant* und *Steradian*. Seit dem 01. 01. 1978 ist in der Bundesrepublik Deutschland die Verwendung des SI-Einheitensystems im amtlichen und geschäftlichen Verkehr gesetzlich vorgeschrieben.

Abgeleitete SI-Einheiten werden durch Multiplikation und Division aus den SI-Basiseinheiten, immer mit dem Faktor 1 (kohärent), gebildet.

Für viele abgeleitete SI-Einheiten wurden besondere Namen und Einheitenzeichen festgelegt, z.B. Newton (N) für die Einheit der Kraft und Volt (V) für die der elektrischen Spannung.

Das SI ist weltweit von der internationalen und nationalen Normung übernommen worden (z.B. ISO 1000, DIN 1301). In den EU-Mitgliedstaaten ist es die Grundlage für die Richtlinie über Einheiten im Messwesen (EU-Richtlinien 80/181 und 89/617).

Ausführliche Informationen zum SI Einheitensystem findet man bei der Physikalisch-Technischen Bundesanstalt unter <http://www.ptb.de> oder dem National Institut of Standards unter <http://www.physics.nist.gov>.

H.1 Geschichte des SI Systems

Bis kurz vor Mars war noch alles in Ordnung. Doch dann passierte das Unglück: Statt eine stabile Umlaufbahn einzunehmen, kam der Mars Climate Orbiter dem roten Planeten zu nahe und verglühte in seiner Atmosphäre. Das war im September 1999. Sofort begann eine fieberhafte Suche nach der Ursache für den Fehler. Das Ergebnis war kaum zu glauben: Die beiden NASA-Kontrollzentren in Denver und Pasadena hatten mit unterschiedlichen Maßeinheiten gerechnet: das eine Team in Metern und Kilogramm, das andere in Foot und Pound über ein Jahrhundert, nachdem sich die USA und 16 andere Staaten darauf geeinigt hatten, künftig nur noch das metrische System zu verwenden und 40 Jahre, nachdem nahezu weltweit die (auf dem metrischen System beruhenden) SI-Einheiten eingeführt waren.

Ein peinlicher Vorfall und ein eindrucksvolles Beispiel dafür, wie wichtig es ist, dass alle Welt mit gleichem Maß misst. *Für alle Welt, für alle Völker* dieses Motto wurde zur Zeit der Französischen Revolution geprägt, als in Frankreich die neue Längeneinheit "Meter" entstand. Das neue Maß wurde zur Grundlage des internationalen metrischen, dezimalen Maßsystems, das ein großes Durcheinander bei den Maßeinheiten beendete. Über die Einhaltung und Weiterentwicklung des metrischen Systems wachten die Organe der Meterkonvention. Ihr ausführendes Organ, die Generalkonferenz für Maß und Gewicht, tagte zum ersten Mal im Jahr 1889. Sie genehmigte Prototype für das Meter und das Kilogramm und verteilte sie an die Mitgliedstaaten. Auf den folgenden Treffen ging es vor allem um ein Ziel: ein neues internationales Einheitensystem zu schaffen. 1948 verabschiedete die 9. Generalkonferenz für Maß und Gewicht einen Entwurf für ein solches Einheitensystem, das zunächst auf sechs Basiseinheiten beruhte. Alle anderen Einheiten sind mit diesen Basiseinheiten ausschließlich über Multiplikation und Division verbunden. Der große Vorteil dieses Systems: Sämtliche Umrechnungsfaktoren fielen weg.

Die 10. Generalkonferenz für Maß und Gewicht im Jahr 1954 nahm die sechs Basiseinheiten offiziell an: Länge (Meter), Masse (Kilogramm), Zeit (Sekunde), elektrische Stromstärke (Ampere), thermodynamische Temperatur (Kelvin) und Lichtstärke (Candela). Eine siebte Basiseinheit, die der Stoffmenge (Mol), kam erst 1973 dazu. Sie wird heute üblicherweise an sechster Stelle genannt. Diese Änderung

der historisch gewachsenen Reihenfolge hat das Internationale Büro für Maß und Gewicht (Bureau International des Poids et Mesures, BIPM) veranlasst, um auszudrücken, dass die Entwicklung in der Optik möglicherweise zu einer Diskussion über die Candela als Basiseinheit führen wird.

Im Jahr 1960 bekam das neue System seinen Namen: *Système International d'Unités*, abgekürzt SI. Die 11. Generalkonferenz für Maß und Gewicht im Jahr 1960 vereinbarte, dass diese Abkürzung in allen Sprachen zu verwenden ist, und verabschiedete Vorsätze zur Bezeichnung der dezimalen Vielfache und Teile von Einheiten. In Deutschland wurde das neue System mit dem Gesetz über Einheiten im Messwesen (Einheitengesetz) vom 2. Juli 1969 und der Ausführungsverordnung zu dem Gesetz vom 5. Juli 1970 eingeführt. Seit dem 1. Januar 1978 sind die alten Einheiten in Deutschland verboten.

H.2 Die SI Basiseinheiten

Größe	Abkürzung	Name der Einheit	Symbol	Definition
Länge	<i>l</i>	Meter	m	Das Meter ist die Länge der Strecke, die Licht im Vakuum während der Dauer von $(1/299\,792\,458)$ Sekunden durchläuft.
Masse	<i>m</i>	Kilogramm	kg	Das Kilogramm ist die Einheit der Masse; es ist gleich der Masse des Internationalen Kilogrammprototyps (Ur-Kilogramm, 1889).
Zeit	<i>t</i>	Sekunde	s	Die Sekunde ist das $9\,192\,631\,770$ fache der Periodendauer der dem Übergang zwischen den beiden Hyperfeinstruktur niveaus des Grundzustandes von Atomen des Nuklids ^{133}Cs entsprechenden Strahlung.
elektrische Stromstärke	<i>I</i>	Ampère	A	Das Ampere ist die Stärke eines konstanten elektrischen Stromes, der, durch zwei parallele, geradlinige, unendlich lange und im Vakuum im Abstand von einem Meter voneinander angeordnete Leiter von vernachlässigbar kleinem, kreisförmigem Querschnitt fließend, zwischen diesen Leitern je einem Meter Leiterlänge die Kraft 2×10^7 Newton hervorrufen würde.
Temperatur	<i>T</i>	Kelvin	K	Das Kelvin, die Einheit der thermodynamischen Temperatur, ist der 273.16 -te Teil der thermodynamischen Temperatur des Tripelpunktes des Wassers.
Lichtstärke	<i>J</i>	Candela	cd	Die Candela ist die Lichtstärke in einer bestimmten Richtung einer Strahlungsquelle, die monochromatische Strahlung der Frequenz 540×10^{12} Hertz aussendet und deren Strahlstärke in dieser Richtung ($1/683$) Watt durch Steradian beträgt.

Fortsetzung auf nächster Seite

Fortsetzung von letzter Seite

Größe	Abkürzung	Name der Einheit	Symbol	Definition
Stoffmenge	n	Mol	mol	Das Mol ist die Stoffmenge eines Systems, das aus ebensoviel Einzelteilchen besteht, wie Atome in 0,012 Kilogramm des Kohlenstoffnuklids ^{12}C enthalten sind. Bei Benutzung des Mol müssen die Einzelteilchen spezifiziert sein und können Atome, Moleküle, Ionen, Elektronen sowie andere Teilchen oder Gruppen solcher Teilchen genau angegebener Zusammensetzung sein.
ergänzende SI Einheiten:				
ebener Winkel	ϑ	Radian	rad	
Raumwinkel	Ω	Steradian	sr	

H.3 Einige von den SI Einheiten abgeleitete Einheiten

Größe	Abkürzung	Name der Einheit	Symbol	SI-Einheit
Frequenz	v	Hertz	Hz	s^{-1}
Kreisfrequenz	ω	Radian/Sekunde		s^{-1}
Geschwindigkeit	v	Meter/Sekunde		m s^{-1}
Beschleunigung	a	Meter/Sekunde ²		m s^{-2}
Winkelgeschwindigkeit	ω	Radian/Sekunde		s^{-1}
Winkelbeschleunigung	α	Radian/Sekunde ²		s^{-2}
Kraft	F	Newton	N	
Energie	E	Joule	J	$\text{m}^2 \text{kgs}^{-2}$
Leistung	P	Watt	W	$\text{m}^2 \text{kgs}^{-3}$
Druck	p	Pascal	Pa	$\text{kg m}^{-1} \text{s}^{-2}$
Ladung	Q	Coulomb	C	As
Spannung (Potenzial)	U	Volt	V	$\text{m}^2 \text{kgs}^{-3} \text{A}^{-1}$
elektrische Feldstärke	E	Volt/Meter	V/m	$\text{mkgs}^{-3} \text{A}^{-1}$
elektrische Polarisation	P	Coulomb/Meter	C/m	As m^{-1}

Fortsetzung auf nächster Seite

Fortsetzung von letzter Seite

Größe	Abkürzung	Name der Einheit	Symbol	SI-Einheit
elektrische Flussdichte	<i>D</i>	Coulomb/Meter ²	C/m ²	Asm ⁻²
elektrischer Widerstand	<i>R</i>	Ohm	Ω	m ² kgs ⁻³ A ⁻²
elektrische Leitfähigkeit	σ	Siemens/Meter	S/m	m ⁻³ kg ⁻¹ s ³ A ²
magnetische Flussdichte	<i>B</i>	Tesla	T=Vs/m ²	kgs ⁻² A ⁻¹
magnetische Feldstärke	<i>H</i>	Ampère/Meter		A/m
magnetischer Fluss	Φ	Weber	Wb=Vs/m ²	m ² kgs ⁻² A ⁻¹
Selbstinduktion	<i>L</i>	Henry	H=Vs/Am ²	m ² kgs ⁻² A ⁻²
Wärmekapazität	<i>C</i>	Joule/Kelvin	J/K	m ² kgs ⁻² K ⁻¹
Entropie	<i>S</i>	Joule/Kelvin	J/K	m ² kgs ⁻² K ⁻¹
Enthalpie	<i>J</i>	Joule	J	m ² kgs ⁻²
Wärmeleitfähigkeit	λ	Watt/Meter Kelvin	W/m K	mkgs ⁻³ K ⁻¹

H.4 Vorsätze

Faktor	Bezeichnung	Abkürzung
10^{18}	Exa	E
10^{15}	Peta	P
10^{12}	Tera	T
10^9	Giga	G
10^6	Mega	M
10^3	Kilo	k
10^2	Hekto	h
10^1	Deka	da
10^{-1}	Dezi	d
10^{-2}	Zenti	c
10^{-3}	Milli	m
10^{-6}	Mikro	μ
10^{-9}	Nano	n
10^{-12}	Pico	p
10^{-15}	Femto	f
10^{-18}	Atto	a

H.5 Abgeleitete Einheiten und Umrechnungsfaktoren

In der Bundesrepublik Deutschland ist das Gesetz über Einheiten im Messwesen die Rechtsgrundlage für die Angabe physikalischer Größen in gesetzlichen Einheiten. Es verpflichtet zu ihrer Verwendung im geschäftlichen und amtlichen Verkehr. Die gesetzlichen Einheiten sind in den folgenden Tabellen farbig hinterlegt. Die Ausführungsverordnung zum Gesetz über Einheiten im Messwesen (Einheitenverordnung) verweist auf die Norm DIN 1301.

Länge, Fläche, Volumen

Einheit	Abkürzung	Umrechnung
Ångström	Å	$1 \text{ Å} = 10^{-10} \text{ m}$
Astronomische Einheit	AE	$1 \text{ AE} = 1.4960 \times 10^{11} \text{ m}$
Fermi	fm	$1 \text{ fm} = 10^{-15} \text{ m}$
inch	inch	$1 \text{ inch} = 0.254 \text{ m}$
foot	ft	$1 \text{ ft} = 0.3038 \text{ m}$
yard	yd	$1 \text{ yard} = 0.9144 \text{ m}$
mile	mile	$1 \text{ mile} = 1609 \text{ m}$
Lichtjahr	Lj	$1 \text{ Lj} = 9.46 \times 10^{15} \text{ m}$
Parsekunde	pc	$1 \text{ pc} = 30.857 \times 10^{15} \text{ m}$
Ar	a	$1 \text{ a} = 100 \text{ m}^2$
Hektar	ha	$1 \text{ ha} = 10^4 \text{ m}^2$
barn	b	$1 \text{ b} = 10^{-28} \text{ m}^2$
Liter	l	$1 \text{ l} = 10^{-3} \text{ m}^3$
gallon	gal (US)	$1 \text{ gal} = 3.7851 \times 10^{-3} \text{ m}^3$
barrel	bbl	$1 \text{ bbl} = 158.988 \times 10^{-3} \text{ m}^3$

Masse

Einheit	Abkürzung	Umrechnung
Atomare Masseneinheit	u	$1 \text{ u} = 1.660\,565\,5 \times 10^{-27} \text{ kg}$
Tonne	t	$1 \text{ t} = 1000 \text{ kg}$
metrisches Karat		$1 \text{ Karat} = 2 \times 10^{-4} \text{ kg}$
pound	lb	$1 \text{ lb} = 0.4536 \text{ kg}$
ounce	oz	$1 \text{ oz} = 1/16 \text{ lb} = 0.02835 \text{ kg}$

Zeit, Frequenz

Einheit	Abkürzung	Umrechnung
Tag	d	$1 \text{ d} = 86400 \text{ s}$
Stunde	h	$1 \text{ h} = 3600 \text{ s}$
Minute	min	$1 \text{ min} = 60 \text{ s}$
Jahr (tropisches)	a	$1 \text{ a} = 365.24 \text{ d} = 3.156 \times 10^7 \text{ s}$
Hertz	Hz	$1 \text{ Hz} = 1 \text{ s}^{-1}$

Temperatur

Einheit	Abkürzung	Umrechnung
Grad Celsius	°C	$T(\text{°C}) = T(\text{K}) - 273.15 \text{ (K)}$
Grad Fahrenheit	°F	$T(\text{°F}) = \frac{9}{5} T(\text{°C}) + 32$

Winkel

Einheit	Abkürzung	Umrechnung
Radian	rad	$1 \text{ rad} = 1 \text{ m/m}$
Grad	°	$1^\circ = (2\pi/360) \text{ rad} = 1.745 \times 10^{-2} \text{ rad}$
Winkelminute	'	$1' = 2.91 \times 10^{-4} \text{ rad}$
Winkelsekunde	''	$1'' = 4.85 \times 10^{-6} \text{ rad}$
Neugrad	gon	$1 \text{ gon} = 2\pi/400 \text{ rad}$

Kraft, Druck, Viskosität

Einheit	Abkürzung	Umrechnung
Newton	N	$1\text{ N} = 1\text{ kgm/s}^2$
Dyn	dyn	$1\text{ dyn} = 10^{-5}\text{ N} = 1\text{ gcm/s}^2$
Kilopond	kp	$1\text{ kp} = 1\text{ kg} \cdot \text{g} = 9.8067\text{ N}$
Pascal	Pa	$1\text{ Pa} = 1\text{ N/m}^2 = 1\text{ kg/ms}^2$
Bar	bar	$1\text{ bar} = 10^5\text{ Pa}$
Atmosphäre (physikalisch)	atm	$1\text{ atm} = 101\,325\text{ Pa}$
Atmosphäre (technisch)	at	$1\text{ at} = 98\,066\text{ Pa}$
Torr, mmHg	Torr	$1\text{ Torr} = 1\text{ mmHg} = 133.322\text{ Pa}$
Poise	P	$1\text{ P} = 0.1\text{ Pas}$
psi	lb/in ²	$1\text{ psi} = 6895.0\text{ Pas}$

Energie, Leistung, Wärmemenge

Einheit	Abkürzung	Umrechnung
Joule	J	$1\text{ J} = 1\text{ Nm} = 1\text{ kgm}^2/\text{s}^2$
Kilowattstunde	kWh	$1\text{ kWh} = 3.6 \times 10^6\text{ J} = 860\text{ kcal}$
Kalorie	cal	$1\text{ cal} = 4.187\text{ J}$
Erg	erg	$1\text{ erg} = 1\text{ g cm}^2/\text{s}^2 = 10^{-7}\text{ kgm}^2/\text{s}^2 = 10^{-7}\text{ J}$
Elektronenvolt	eV	$1\text{ eV} = 1.6022 \times 10^{-19}\text{ J}$ $1\text{ eV} \text{ entspricht } 11\,604\text{ K (E = k}_B\text{T)}$ $1\text{ eV} \text{ entspricht } 2.4180 \times 10^{14}\text{ Hz (E = h}\nu\text{)}$
Watt	W	$1\text{ W} = 1\text{ J/s} = 1\text{ kgm}^2/\text{s}^3$
Pferdestärke	PS	$1\text{ PS} = 735.6\text{ W}$

Elektromagnetische Einheiten

Einheit	Abkürzung	Umrechnung
Coulomb	C	$1\text{C} = 1\text{As}$
Volt	V	$1\text{V} = 1\text{J/As} = 1\text{kg m}^2/\text{As}^3$
Farad	F	$1\text{F} = 1\text{C/V} = 1\text{A}^2\text{s}^4/\text{kg m}^2$
Ohm	Ω	$1\Omega = 1\text{V/A} = 1\text{kg m}^2/\text{A}^2\text{s}^3$
Siemens	S	$1\text{S} = 1/\Omega$
Tesla	T	$1\text{T} = 1\text{Vs/m}^2 = 1\text{kg/As}^2$
Gauß	G	$1\text{G} = 10^{-4}\text{T}$
Oersted	Oe	$1\text{Oe} = (10^3/4\pi)\text{A/m}$, entspricht 1G ($B = \mu_0 H$)
Henry	H	$1\text{H} = 1\text{Vs/A} = 1\text{m}^2\text{kg/A}^2\text{s}^2$
Weber	Wb	$1\text{Wb} = 1\text{Vs} = 1\text{m}^2\text{kg/As}^2$
Maxwell	M	$1\text{M} = 10^{-8}\text{Wb}$

I Physikalische Konstanten

Fundamentalkonstanten treten im Netz der physikalischen Theorien als quantitative Verknüpfungspunkte dieser Theorien auf. So ist beispielsweise die Theorie der Hohlraumstrahlung über die Planck-Konstante h mit der Quantentheorie sowie über die Vakuum-Lichtgeschwindigkeit mit der Elektrodynamik und über die Boltzmann-Konstante k mit der Statistischen Mechanik verknüpft. Die Konstanten werden durch die Theorien nicht festgelegt, sie sind vielmehr experimentell so genau wie überhaupt nur möglich zu ermitteln. Denn die quantitativen Aussagen der Theorien können nur so genau sein, wie die Konstanten bekannt sind. Die möglichst genaue Kenntnis der Fundamentalkonstanten setzt aber eine möglichst genaue experimentelle Darstellung der im Internationales Einheitensystem (SI) definierten physikalischen Einheiten voraus. Dieser Sachverhalt bindet die Ermittlung der Werte der Fundamentalkonstanten eng an die Metrologie, die Wissenschaft vom genauen Messen, deren vornehmste und wichtigste Aufgabe die bestmögliche experimentelle Realisierung der definierten Einheiten ist.

Umgekehrt aber sind die Fundamentalkonstanten deshalb von besonderem Interesse für die Metrologie, weil sie selbst als ideale Einheiten dienen oder die ideale Basis für Einheiten bilden können. Schon heute werden sie zur Darstellung der SI-Einheiten herangezogen. Experimente zur Bestimmung einer Fundamentalkonstanten werden häufig direkt an metrologischen Instituten wie der Physikalisch-Technischen Bundesanstalt oder zumindest in enger Zusammenarbeit mit solchen Instituten ausgeführt.

Im Jahre 1999 hat die Task Group on Fundamental Constants des *Committee on Data for Science and Technology* (CODATA) des International Council of Scientific Unions (ICSU) einen neuen Satz von Fundamentalkonstanten erstellt und ihn zur einheitlichen Verwendung in Wissenschaft und Technik empfohlen. Dessen Werte sind das Ergebnis einer multivariaten Ausgleichsrechnung und beruhen auf Daten, die bis zum 31. Dezember 1998 publiziert vorlagen. Es ist geplant, zukünftig regelmäßig alle vier Jahre eine neue Ausgleichsrechnung unter Hinzuziehung neuer Daten vorzunehmen.

Eine Auswahl der wichtigsten Fundamentalkonstanten sind in der folgenden Tabelle zusammengefasst.
Quelle: Peter J. Mohr und Barry N. Taylor, *CODATA Recommended Values of the Fundamental Physical Constants 1998*, *Journal of Physical and Chemical Reference Data* **28**, No. 6, (1999) und *Reviews of Modern Physics* **72**, No. 2, (2000).

Physikalische Konstante	Symbol	Wert	Einheit	rel. Fehler
universelle Konstanten				
Lichtgeschwindigkeit	c	299 792 458	m/s	exakt
Plancksche Konstante	h	$6.626\,068\,76(52) \times 10^{-34}$	Js	7.8×10^{-8}
$h/2\pi$	\hbar	$1.054\,571\,596(82) \times 10^{-34}$ $6.582\,118\,89(26) \times 10^{-16}$	Js eVs	7.8×10^{-8} 3.9×10^{-8}
Gravitationskonstante	G	$6.673(10) \times 10^{-11}$	$\text{m}^3/\text{kg s}^2$	
Induktionskonstante, magnetische Feldkonstante	μ_0	$4\pi \times 10^{-7}$	N/A ²	exakt
Influenzkonstante, elektrische Feldkonstante, $1/\mu_0 c^2$	ϵ_0	$8.854\,187\,817\ldots \times 10^{-12}$	F/m	exakt

Fortsetzung auf nächster Seite

Fortsetzung von letzter Seite

Physikalische Konstante	Symbol	Wert	Einheit	rel. Fehler
Vakuumimpedanz $1/\mu_0 c^2$	Z_0	$376.730\,313\,461\dots$	Ω	exakt
Planck-Masse $\sqrt{\hbar c/G}$	m_P	$2.1767(16) \times 10^{-8}$	kg	7.5×10^{-4}
elektromagnetische Konstanten				
Elementarladung	e	$1.602\,176\,462(63) \times 10^{-19}$	C	3.9×10^{-8}
Magnetisches Flussquant $h/2e$	Φ_0	$2.067\,833\,636(81) \times 10^{-15}$	Vs	3.9×10^{-8}
von Klitzing Konstante h/e^2	R_K	$25\,812.807\,572(95)$	Ω	3.7×10^{-9}
Leitfähigkeitsquant $2e^2/h$	G_0	$7.748\,091\,696(28) \times 10^{-5}$	S	3.7×10^{-9}
Josephson-Konstante $2e/h$	K_J	$483\,597.898(19)$	Hz/V	3.9×10^{-8}
Bohrsches Magneton $e\hbar/2m_e$	μ_B	$9.274\,008\,99(37) \times 10^{-24}$ $5.788\,381\,749(43) \times 10^{-5}$ $1.399\,624\,624(56) \times 10^{10}$	J/T eV/T Hz/T	4.0×10^{-8} 7.3×10^{-9} 4.0×10^{-8}
Kernmagneton	μ_K	$5.050\,783\,17(20) \times 10^{-27}$ $3.152\,451\,238(24) \times 10^{-8}$ $7.622\,593\,96(31) \times 10^6$	J/T eV/T Hz/T	4.0×10^{-8} 7.6×10^{-9} 4.0×10^{-8}
atomare und nukleare Konstanten				
Feinstrukturkonstante	α	$7.297\,352\,533(27) \times 10^{-3}$		3.7×10^{-9}
$e^2/4\pi\epsilon_0\hbar c$	$1/\alpha$	$137.036\,999\,76(83)$		3.7×10^{-9}
Ruhemasse des Elektrons	m_e	$9.109\,381\,88(72) \times 10^{-31}$ $5.485\,799\,110(12) \times 10^{-4}$	kg u	7.9×10^{-8} 2.1×10^{-9}
Ruheenergie des Elektrons	$m_e c^2$	$5.109\,989\,02(21) \times 10^5$	eV	4.0×10^{-8}
Ruhemasse des Protons	m_p	$1.672\,621\,58(13) \times 10^{-27}$ $1.007\,276\,466\,88(13)$	kg u	7.9×10^{-8} 1.3×10^{-10}
Ruheenergie des Protons	$m_p c^2$	$9.382\,719\,98(38) \times 10^8$	eV	4.0×10^{-8}
Ruhemasse des Neutrons	m_n	$1.674\,927\,16(13) \times 10^{-27}$ $1.008\,664\,915\,78(55)$	kg u	7.9×10^{-8} 5.4×10^{-10}
Ruheenergie des Neutrons	$m_n c^2$	$9.395\,653\,30(38) \times 10^8$	eV	4.0×10^{-8}
Magnetisches Moment des Elektrons	μ_e	$9.284\,763\,62(37) \times 10^{-24}$	J/T	4.0×10^{-8}
	μ_e/μ_B	$1.001\,159\,652\,1869(41)$		4.1×10^{-12}
Magnetisches Moment des Protons	μ_p	$1.410\,606\,633(58) \times 10^{-26}$	J/T	4.1×10^{-8}
	μ_p/μ_B	$1.521\,032\,203(15)$		1.0×10^{-8}
	μ_p/μ_N	$2.792\,847\,337(29)$		1.0×10^{-8}

Fortsetzung auf nächster Seite

Fortsetzung von letzter Seite

Physikalische Konstante	Symbol	Wert	Einheit	rel. Fehler
Massenverhältnis Proton/Elektron	m_p/m_e	1836.152 6675(39)		2.1×10^{-9}
spezifische Ladung des Elektrons	e/m_e	$1.758\ 820\ 174(71) \times 10^{11}$	C/kg	4.0×10^{-8}
Rydberg-Konstante $\alpha^2 m_e c / 2h$	R_∞	10 973 731.568 549(83) $2.179\ 871\ 90(17) \times 10^{-18}$ 13.605 691 72(53)	1/m J eV	7.6×10^{-12} 7.8×10^{-8} 3.9×10^{-8}
Bohrscher Radius $\alpha / 4\pi R_\infty = 4\pi\epsilon_0\hbar^2 / m_e e^2$	a_B	$5.291\ 772\ 083(19) \times 10^{-11}$	m	3.7×10^{-9}
Klassischer Elektronenradius $\alpha^2 a_B$	r_e	$2.817\ 940\ 285(31) \times 10^{-15}$	m	1.1×10^{-8}
Compton Wellenlänge des Elektrons $h/m_e c$	λ_C	$2.426\ 310\ 215(18) \times 10^{-12}$	m	7.3×10^{-9}
physikalisch-chemische Konstanten				
Loschmidttsche Zahl, Avogadro Konstante	N_A	$6.022\ 141\ 99(47) \times 10^{23}$	1/mol	7.9×10^{-8}
Atomare Masseneinheit $\frac{1}{12} m(^{12}\text{C})$	u	$1.660\ 538\ 73(13) \times 10^{-27}$	kg	7.9×10^{-8}
Faradaysche Konstante $N_A e$	F	96 485.3415(39)	C/mol	4.0×10^{-8}
Gaskonstante	R	8.314 472(15)	J/mol K	1.7×10^{-6}
Boltzmann-Konstante	k_B	$1.380\ 6503(24) \times 10^{-23}$	J/K	1.7×10^{-6}
Molvolumen eines idealen Gases RT/p (bei $T = 273.15\text{ K}$, $p = 101\ 325\text{ Pa}$)	V_m	$22.413\ 996(39) \times 10^3$	m^3/mol	1.7×10^{-6}
Tripelpunkt des Wassers	T_t	273.15	K	
	T_0	272.16	K	
		0	$^\circ\text{C}$	
Stefan-Boltzmannsche Strahlungskonstante $(\pi^2/60)k_B^4/\hbar^3c^2$	σ	$5.670\ 400(40) \times 10^{-8}$	$\text{W}/\text{m}^2\text{K}^4$	7.0×10^{-6}
Wiensche Verschiebungskonstante $b = \lambda_{\max}T$	b	$2.897\ 7686(51) \times 10^{-3}$	m K	1.7×10^{-6}
fundamentale physikalische Konstanten – angenommene Werte				
Normaldruck	p_0	101 325	Pa	exakt
Standard Fallbeschleunigung	g	9.806 65	m/s^2	exakt
konventioneller Wert der Josephson-Konstante	K_{J-90}	483 597.9	Hz/V	exakt

Fortsetzung auf nächster Seite

Fortsetzung von letzter Seite

Physikalische Konstante	Symbol	Wert	Einheit	rel. Fehler
konventioneller Wert der von Klitzing-Konstante	R_{K-90}	25 812.807	Ω	exakt
